M.E.

JOURNAL OF THE
AEROSPACE SCIENCES

VOLUME 28 JULY 1961 NUMBER 7

PURDUE UNIVERSITY
JUL 3 1961
LIBRARY

MECHANICAL ENGINEERING
JUL 5 1961
LIBRARY

CONTENTS

An Investigation of Separated Flows—Part II: Flow in the Cavity and Heat Transfer ..... A. F. CHARWAT, C. F. DEWEY, JR., J. N. ROOS, AND J. A. HITZ 513

On Aircraft Maneuvers in the Vertical Plane Under Assumptions Leading to Easy Integrability of the Flight-Path Equations ..... F. EDWARD EHLERS AND GEORGES BRIGHAM 528

The Newtonian Approximation in Magnetic Hypersonic Stagnation-Point Flow ..... PAUL S. LYKOUDIS 541

Body Under Lifting Wing ..... C. F. CHEN AND JOSEPH H. CLARKE 547

A Summary of the Supersonic Pressure Drag of Bodies of Revolution ..... DEANE N. MORRIS 563

Buckling of a Finite-Length Cylindrical Shell Under a Circumferential Band of Pressure ..... B. O. ALMROTH AND D. O. BRUSH 573

Readers' Forum 579

Published by
INSTITUTE OF THE AEROSPACE SCIENCES, INC.

JOURNAL OF THE AEROSPACE SCIENCES

Editor: W. R. SEARS
Director, Graduate School of Aeronautical Engineering, Cornell University

Associate Editor: ROBERT R. DEXTER *Editorial Production Manager:* VEHIG S. TAVITIAN

Editorial Assistant: CAROL A. SCHAU

IAS Aerospace Technology Panels

Paul J. Burr, Technical Services Director, Coordinator

The members of the IAS Aerospace Technology Panels shown here are to be available, collectively or as individuals, to assist and advise IAS Committees, Sections, and staff members as to currently interesting and important technical topics related to their specialties and as to people most qualified to speak or write on such topics. The panels will also stimulate thought and scientific papers of potential value for the future, and they should be sensitive to technical activity of other professional groups, seeking through joint action the enlightenment of all having professional aerospace interests. Panel chairmen are indicated with an asterisk (*).

Aerodynamics and Fluid Mechanics
Lester Lees*
Seymour M. Bogdonoff
Dean R. Chapman
Antonio Ferri
Paul Germain
Wayland C. Griffith
Hans W. Liepmann
C. C. Lin
Henry T. Nagamatsu
W. R. Sears
John R. Sellars
R. T. Whitcomb
Hideo Yoshihara

Aeroelasticity
R. L. Bisplinghoff*
Y. C. Fung
I. E. Garrick
Martin Goland
Kurt H. Hohenemser
J. C. Houbolt
W. P. Jones
W. J. Mykytow
Robert F. Speaker

Biomedical Sciences
Brig. Gen. D. Flickinger, USAF*
W. Ross Adey
Capt. Wm. Augerson, USA
Hilding Bjurstedt
Stuart Bondurant
A. Scott Crossfield
Cdr. J. H. Ebersole, USN
W. R. Lovelace, II
Capt. Bruce Pinc, USAF
Stanley Roscoe

Communication
P. C. Sandretto*
K. C. Black
James M. Bridges
Harvard L. Hull
Leonard Jaffe
David S. Little
Cdr. D. O. Mann, USN
Paul Rosenberg
William Sen
Arnold Shostack
Teck A. Wilson

Control and Guidance
Robert N. Brown*
R. C. Berendsen
B. Paul Blasingame
S. F. Eyestone
Percy Halpert
B. J. O'Connor
Robert L. Roderick
S. F. Schmidt
O. Hugo Schuck
H. Philip Whitaker

Energy Conversion
David Altman*
Robert Bromberg
M. U. Clauser
J. Preston Layton
Frank Marble
G. H. Markstein
A. M. Rothrock
Milton M. Slawsky
Martin Summerfield
T. Y. Toong

Flight Mechanics
H. J. Kelley*
Malcolm J. Abzug
H. Julian Allen
A. E. Bryson, Jr.
T. N. Edelbaum
William C. House
George Leitmann
Bernard Maggin
Angelo Miele
John D. Nicolaides
Charles B. Westbrook

Instrumentation
R. H. Tripp*
Paul F. Bechberger
J. M. Hungerford
Mac Lowy
Walter McKay
M. David Prince
Charles P. Sonet
George I. Toumanoff
William A. Wildhack

Management
Edward A. Ledeen*
Garrett C. Covington, Jr.
Maj. Gen. Marvin C. Demler, USAF
Richard G. Folsom
Joel M. Jacobson
Boyd C. Myers
Sidney M. Robbins
Lewis A. Rodert
John H. Sidebottom
R. C. Siebold
Paul Torda

Meteorology
Thomas F. Malone*
Robert D. Fletcher
Henry T. Harrison
Joseph Kaplan
Donald T. Perkins
Herbert Riehl
Morris Tepper
Clayton Van Thullenar
Harry Wexler

Nuclear Applications
J. Donald Rauth*
Jack L. Armstrong
Robert W. Bussard
H. M. Dieckamp
Capt. R. L. Duncan, USN
Harold B. Finger
Donald J. Keirn
Frank E. Rom
Raymer E. Schreiber
D. Roy Shoults
T. B. Taylor

Operations
Benjamin S. Kelsey*
Maj. Gen. Otis Benson, USAF (MC)
Ernest A. Cutrell
Capt. E. E. Fawkes, USN
Melvin N. Gough
Franklin W. Kolk
Col. J. L. Marinelli, USA
Richard V. Rhode
W. E. Rhodes
M. B. Spaulding, Jr.
Maj. Gen. D. Yates, USAF

Propulsion Systems
Bruce T. Lundin*
Robert H. Boden
George W. Brady
David Cochran
Elliot Mitchell
Perry W. Pratt
C. C. Ross
John G. Wilder, Jr.
Maurice J. Zucrow

Space Physics
John C. Evvard*
Herbert Friedmann
Leo Goldberg
C. F. Hansen
Arthur Kantrowitz
Bruno Rossi
S. F. Singer
Leo Steg
Fred L. Whipple

Structures and Materials
Nicholas J. Hoff*
Samuel B. Batdorf
Bruno A. Boley
Pol Duwez
R. R. Heldenfels
Samuel Levy
George N. Mangurian
S. S. Manson
Nathan E. Promisel
Ernest E. Sechler

Support
Ernest G. Stout*
Albert D. Brown
Edward I. Brown
Col. Paul T. Cooper, USAF
P. J. Daniel
Paul Hartline
Donald R. Hill
Capt. N. D. Hodson, USN
Lt. Col. George L. Lovett
R. R. Malik
John McKenna
Gilbert Rolan
Richard A. Schmidt
William R. Owens

Vehicle Design
C. E. Pappas*
Ralph Alex
Adolph Burstein
C. H. Christenson
A. J. Eggers, Jr.
E. V. Marshall
Rene H. Miller
John R. Ragazzini
George S. Schairer
George S. Trimble, Jr.

SUBSCRIPTION RATES

JOURNAL OF THE AEROSPACE SCIENCES, Published Monthly. United States and Possessions: 1 Year, $15.00; Single Copies, $1.50. Foreign Countries Including Canada (American Currency Rates): 1 Year, $16.00; Single Copies, $1.50.

AEROSPACE ENGINEERING, Published Monthly. United States and Possessions: 1 Year, $5.00; Single Copies, $0.50. Foreign Countries Including Canada (American Currency Rates): 1 Year, $6.00; Single Copies, $0.50.

Notices of change of address, which should be sent at least 30 days prior to actual change of address, and correspondence regarding subscriptions should be sent to the Circulation Department, JOURNAL OF THE AEROSPACE SCIENCES, 2 East 64th Street, New York 21, N.Y.

Manuscripts for publication, proofs, and all correspondence should be addressed to the Editorial Office of the JOURNAL.

© Copyright, 1961, by the Institute of the Aerospace Sciences, Inc.

Publication Office, 20th and Northampton Sts., Easton, Pa. Second-Class Mail Privileges Authorized at Easton, Pa. Acceptance for mailing at a special rate of postage provided for in Section 1103, Act of October 3, 1917, authorized April 29, 1937.

JOURNAL OF THE AEROSPACE SCIENCES

VOLUME 28 JULY 1961 NUMBER 7

An Investigation of Separated Flows—Part II: Flow in the Cavity and Heat Transfer

A. F. CHARWAT,* C. F. DEWEY, JR.,** J. N. ROOS,‡ AND J. A. HITZ‡‡

University of California at Los Angeles

Summary

The first portion of this paper describes studies of the internal structure of the separated flow in a notch at a free-stream Mach number of 3. Observations include: flow visualization, spark-schlieren pictures of the fluctuations of the free shear layer, and studies of the diffusion of heat from sources placed in the separated region. The second part describes measurements of local heat transfer to the wall.

The external Mach number, the length-to-depth ratio of the cavity, the ratio of the oncoming boundary layer thickness to the notch depth (in the turbulent flow region), the thermal-to-momentum thickness ratio of the boundary layer and, finally, the geometry of the internal boundary of the separated region are varied as systematically as possible. On the basis of these observations, a simple model of the flow in and the heat transfer across the separated region is formulated.

Received March 16, 1960. Revised and received December 27, 1960.

* Associate Professor.

** Staff Member, Aeronutronic. Presently at California Institute of Technology.

‡ Research Assistant. Presently at Space Technology Laboratory.

‡‡ Research Engineer.

This investigation was sponsored by Aeronutronic, a Division of Ford Motor Company, under contract with the Bureau of Aeronautics, Department of the Navy, Contract No. as 58-688-C.

The support of the early phases of this research by the Research Committee of the Department of Engineering, University of California at Los Angeles, and of the heat transfer study by Aeronutronic, a division of Ford Motor Company, and the Bureau of Aeronautics, Department of the Navy, is gratefully acknowledged. We are indebted to Dr. J. Neustein and Dr. D. Altman for their interest and advice. Messrs. J. Campbel and P. Ono, senior students at the University, contributed portions of the experimental works; Mr. Khalil Seyrafi assisted in the reduction of the data. We are very indebted to the research technicians, Messrs. R. Roberson and J. Daughenbaugh, for their substantial contributions throughout all phases of this program.

Symbols

h = local heat-transfer coefficient
H = depth of notch
L = length of notch
L_{cr} = critical closure length
M_0 = Mach number in the free stream
P = pressure
q = heat flux per unit area to wall
Re = Reynolds number
St = Stanton number
S = distance to virtual origin of the boundary layer
T = temperature
T_{aw} = adiabatic wall recovery temperature
X = streamwise coordinate (along notch floor from separation corner)
Y = coordinate normal to free stream (origin at notch wall)
δ = boundary-layer thickness just ahead of notch
δ_s = thickness of the free shear layer at reattachment

Subscripts

f = reference flat plate
0 = free-stream conditions
w = wall condition
s = conditions at separation point
R = conditions at recompression point

Introduction

THE INFORMATION on heat transfer to and across separated regions is difficult to interpret because of differences in test conditions and in the geometry of the models—i.e., notches,[3,11,12] wakes, and separation steps in supersonic[13,14] and subsonic[4] flow, axisymmetric spike-induced compression wakes,[16] and various other complex separations[17,18]. General results indicate a drop in the heat transfer coefficient h after separation as compared to the value ahead of separation, and an increase of h near and behind recompression. The average over the whole cavity floor varies from 50 to

120 percent of that for an equivalent length of attached flow.

A theoretical analysis was proposed by Chapman[2] and applied by Larson.[12] This model treats the cavity as an isothermal "dead air" sink to which heat is transferred through the shear layer. The entire problem is assumed to lie in the transfer properties of this layer, which are estimated from an extension of an asymptotic solution of free jet mixing.[19]

The outstanding characteristic of this model is that it indicates a pronounced change of heat transfer to the cavity upon transition from laminar to turbulent flow in the shear layer. This is a consequence of the change of the shear layer profile, the sole transfer-rate-controlling element in the analysis. The absence of such an effect would constitute, in our opinion, a strong argument against the validity of the model.

Chapman's model disregards the resistance between the inner wall and the fluid in the cavity. There have been attempts to formulate the problem with more emphasis on the nature of the internal flow; Cole[20] considered the convection of heat around a vortex, but it is difficult to apply his analysis to a real case. Carlson[21] modified Chapman's work by assuming a velocity profile (in the form of a polynomial) both over a free shear layer and in the recirculated flow along the floor of the cavity. This assumption is entirely arbitrary and not substantiated by data.

None of the analyses mentioned above take into account the possibility that the flow may be unsteady and may involve a periodic "filling" and "emptying" of the cavity with fresh fluid. If this were the case, the transfer across the shear layer would no longer control the transfer of heat to or across the cavity. Furthermore, it would not be necessary that any of the aforementioned three mechanisms dominate over the others.

The foregoing arguments guided the planning of the present work. We attempted to investigate systematically many aspects of the flow and obtain insight into its true nature by a critical comparison of the results.

It was shown in Part I of this series,[1] in which the pressure field was discussed, that the flow will jump across a cutout to form an "open" cavity when the length-to-step-height ratio of the notch is less than a "critical" value, which is about 11 for turbulent flow in the Mach number range between 1.5 and 4. The similarity parameter which governs the pressure distribution in the "open" cavity regime is the ratio of cavity length to critical closure length, L/L_{cr}. There is a large decrease in L_{cr} upon transition from laminar to turbulent flow in the shear layer. Consequently, a cavity which is "open" in laminar flow may "close" upon transition to turbulence.

The present paper describes investigations of the internal flow in an "open" cavity. The results complement and explain the dynamic pressure traverses discussed in Part I and prove that there is a periodic inflow into the cavity. Also, measurements of local heat transfer to the wall are presented and discussed in terms of a model based on the observed unsteady structure of the flow.

Test Equipment and Measurements

Studies were made of the internal flow in a notch in the test section floor at a Mach number of 2.9. The boundary layer at separation was fully turbulent. The equivalent flat-plate Reynolds number was 1.5×10^6 and the ratio of the boundary layer thickness to the step height was approximately 0.4.*

The heat-transfer measurements were conducted in a specially designed wind tunnel. The test section was located in a flat plate replacing the plane of symmetry of a two-dimensional wedge-flow expansion nozzle. The nozzle was not contoured, but the expansion angle was small enough to ensure satisfactorily small gradients. The streamwise pressure variation per inch was always below 4 percent of the static pressure at the separation point.

Fig. 1 gives the configuration of the test block, which was made up of mutually insulated stainless steel modular elements. The insulation consisted of a 0.020-in. air gap and a 0.005-in. mica sheet. Matching cutouts in the modules formed an internal coolant passage. Each module was provided with an iron-constantan thermocouple junction located 0.003 in. below the test surface at the center of the element.

The wind tunnel operated at atmospheric stagnation pressure and stagnation temperatures between 50 and 600°F. Water was used in the internal coolant passage (heat flow to the wall); a few special tests (heat flux to the air) were run with steam circulated through the internal passage and atmospheric stagnation air temperature. The thermal resistance of the modules was such that the temperature drop across each could be maintained, typically, at around 100°. Under this condition instrument calibration errors were below 5 percent at $M = 2$ and below a maximum 10 percent at $M = 3.5$. Note that the use of the ratio h/h_f, where h_f is measured independently for each test, tends to eliminate such errors. Heat conduction between the modules and losses to the sidewall were neglected. An estimate of the possible error arising from this source indicates that the results are correct within 3 percent on the average, and within 10 percent under the worst conditions, that is, in regions of maximum streamwise temperature gradient. The modular construction was continued five modules beyond the test section proper.

All reference quantities (such as Mach number, stagnation temperature, Reynolds number, etc.) were determined in the free flow at the station corresponding to the separation point (beginning of the notch). The Reynolds numbers were calculated from measured boundary-layer thicknesses (equivalent flat-plate Reynolds numbers) by use of the relation:

$$\delta/S = 0.37Re^{-1/5} = 0.37(U_0S/\nu_0)^{-1/5} \qquad (1)$$

* This arrangement is the same as that used in reference 1.

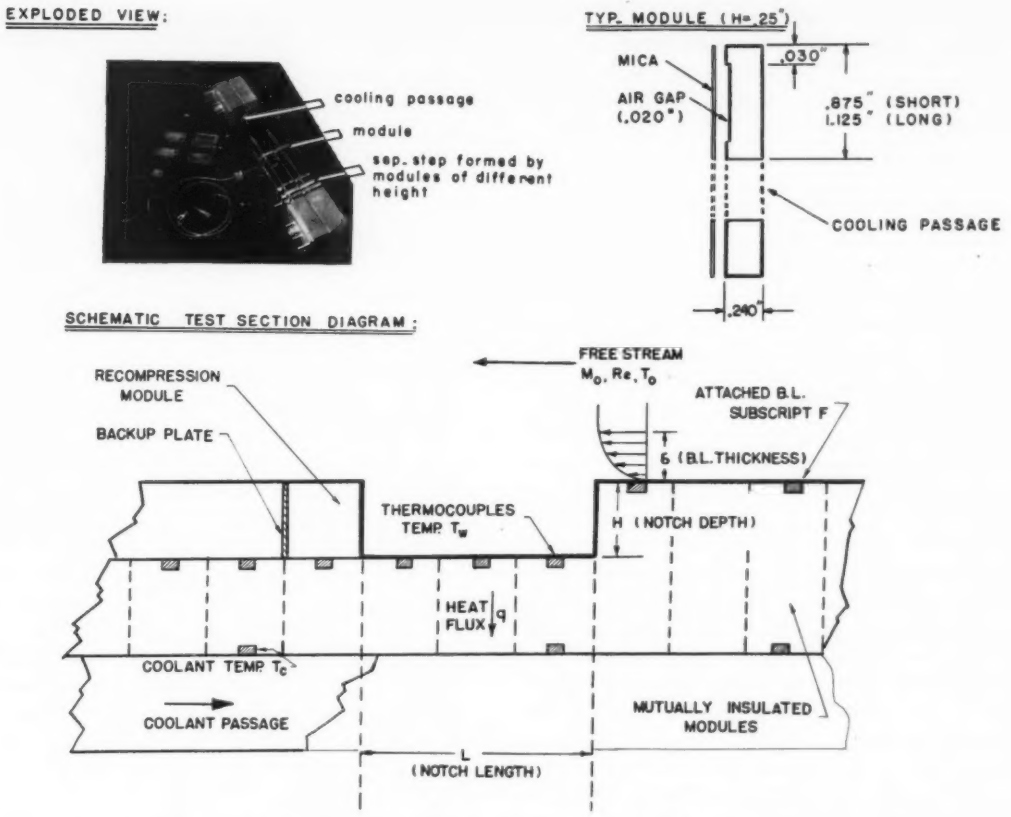

FIG. 1. Photograph of the test section (exploded view) and schematic diagrams of its construction.

The boundary layer was turbulent, and could be correlated to a good accuracy with a $^1/_7$-power velocity profile.

Flow Visualization

(A) *The Flow Near the Wall*

An oil film smeared on the floor of the cavity or a suspension of lampblack in kerosene injected into it (Fig. 2) were used to show the gross nature of the internal flow. It was found that all but the shortest notches ($L/H < 1.5$) contain a vortex at the separation corner and a distinct stagnation line separating it from the remainder of the flow. This vortex opposes the mean circulation in the cavity. Its "diameter" remains equal to H regardless of L. Another vortex exists at the recompression corner. Its diameter is equal to H. There is no stagnation line separating it from the central section of the cavity because the flow in that section is in the same (upstream) direction near the floor. Nevertheless, the complete lack of lampblack in the corner, as compared to the central section, bears evidence to the much larger velocity in this compression "vortex."

The fact that the velocities in the central zone are low and unsteady was demonstrated by introducing small bearing balls or drops of mercury into the open cavity near recompression. They rolled upstream slowly (at rates of the order of one inch per second), up to the separation vortex. (Sometimes they would then creep over to the corners driven by the three-dimensional flow pattern to be discussed.) The diameter of the balls had no noticeable effect on their acceleration as long as they were less than about $^1/_3$ of the notch depth. The motion of the balls was uneven and unsteady. The structure of the flow in an open cavity suggested by these observations, and confirmed by more elaborate measurements, is shown schematically in Fig. 18.

Fig. 2 shows an accumulation of the oil near the corners in longer notches, which indicates a three-dimensional shedding of the separation vortex. The location of the disturbance suggests a sidewall effect, which can be explained by considering the centrifugal force balance on a streamtube in the sidewall boundary layer, under the influence of the pressure distribution in the notch. A special model with fences separating out the sidewall boundary layer was tested. Fig. 2c shows a run in which oil is collected along a well-defined and uniformly two-dimensional line (vortex attached to the fences). However, this two-dimensional flow was found to be extremely sensitive to the alignment of the separation or recompression edges, to upstream nonuniformities, and even to transient disturbances.

Similar three-dimensional patterns were observed by all investigators who looked for them in notches,[3] free wakes,[6] and steps.[7] The question was raised whether two-dimensional cavity flow is fundamentally possible; our results indicate that it is, but only under extremely carefully controlled conditions.

(*b*) *Mass Exchange and Unsteadiness of the Flow*

Any detectable gas (ammonia, smoke) injected into the free flow upstream of the notch was found to penetrate into the cavity almost instantaneously. When injected into the cavity, the gas was immediately detected in the boundary layer downstream of recompression. When injection was interrupted, the concentration of the indicator in the cavity became zero very rapidly. There seems to be no doubt that there exists a strong exchange of mass between the cavity and the external flow.

Unsteady flow is demonstrated by the series of spark-schlieren pictures shown in Fig. 3. These are taken from a study to be published elsewhere,[9] which indicates that the shear layer forms a stationary space wave with wavelength approximately equal to H for all notch lengths and frequency proportional to M_0. This photographic technique did not yield clear results for the (turbulent) thick boundary-layer case, Fig. 3c; the pictures show that there is some wave radiation present, but it is too diffuse and random to have a definable space structure. On the basis of preliminary results, there is a limiting ratio of the thickness of the oncoming boundary layer to notch depth beyond which no radiation is observed. For laminar flow it was found to be $\delta/H = 0.3$. A study of turbulent flow is under way.

The results of which Fig. 3 is a sample show that the Stroudhal number based on notch depth (fU_0/H), rather than (fU_0/L),[26] is constant. As L increases the space-wave structure changes abruptly from one regime to the next which contains one more wave (of constant length).

Note the way in which the root of the shock segment at recompression in Fig. 3b *measurably* penetrates into the cavity. Such pictures indicate again that this is a periodic flow in and out of the cavity past the recompression step, rather than a potential wave motion like that on a stretched membrane.

Heat Diffusion Studies

For further study a method which is directly related to the fluid motion was chosen. The arrangement is shown in Fig. 4. A thin Nichrome wire was stretched across the cavity and heated electrically. A thermocouple junction was rotated at a fixed radius around the heat source, and the temperature difference (with and without current supply to the wire) was recorded as function of the polar angle around the source. Alternately, a separately supported thermocouple probe was introduced into the cavity and temperature distributions in Cartesian axes (Y and X) were obtained for selected positions of the heater wire.

(*a*) *Characteristics of the Method*

The diffusion of heat from a two-dimensional source in *uniform* turbulent flow results in a thermal wake described by[22]

$$(T - T_0) \simeq x^{-1/2} \exp(-Y^2/2\bar{Y}^2) \qquad (2)$$
$$\bar{Y}^2 = 2x\epsilon/U_0$$

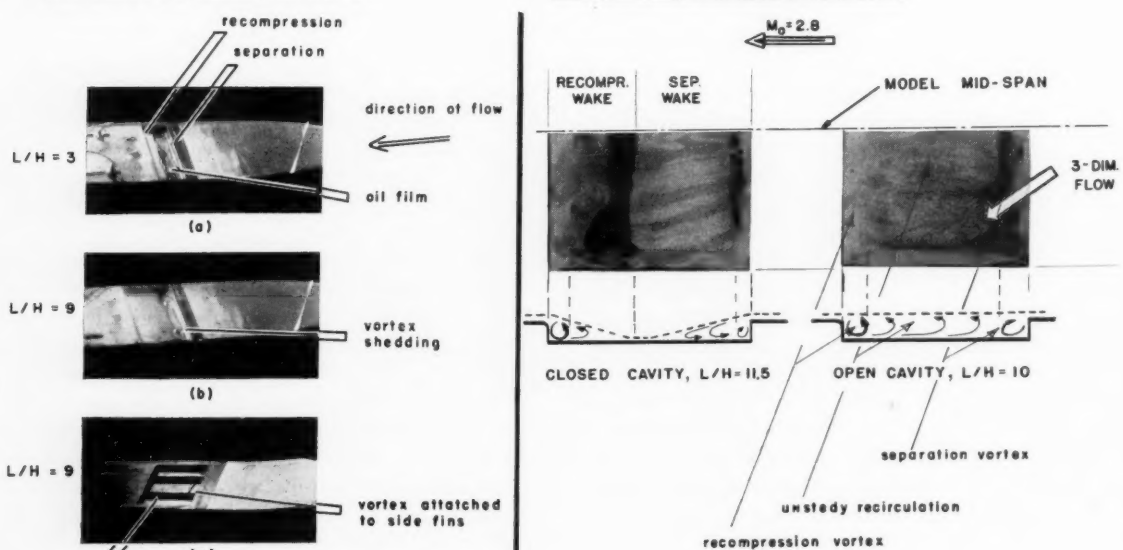

FIG. 2. Lampblack streaklines on the notch floor and oil-film visualization pictures for various configurations. (The light diagonal streaks in the separate wake picture are accidents of handling.)

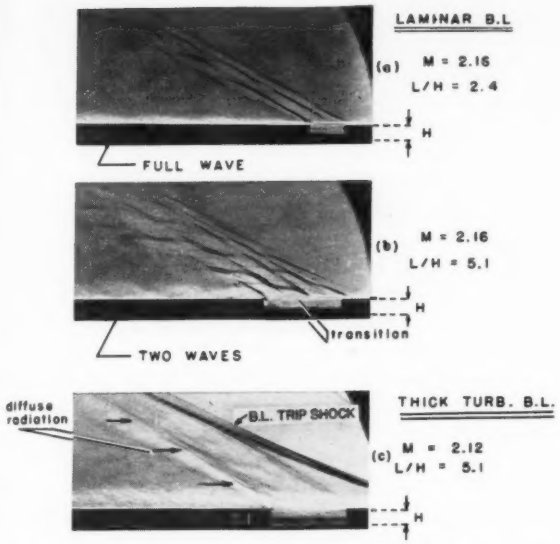

FIG. 3. Spark-Schlieren (5 μsec) photographs of wave radiation from cavities.

The coefficient of proportionality is evaluated from a heat balance, and ϵ is the turbulent "eddy diffusivity."[23]

Fig. 5 shows (polar) traverses in a uniform flow at two Mach numbers at a constant radius of 0.060 in. from the wire (0.010 in. diameter) for a fixed power dissipation. This constitutes a "calibration" of the system.

When the wire is placed in a *steady* but *nonuniform* flow the profile of the wake is different. With identical assumptions concerning the phenomenon, but with the mean velocity represented by

$$U_0 = U_0' + \gamma(Y) \tag{3}$$

one obtains for the profile of the thermal wake[24]

$$(T - T_0) \sim x^{-2/3} \exp\left[-(U_0' + \gamma Y)^3/q\epsilon\gamma x\right] \tag{4}$$

The *wake is skewed* and the temperature maximum is found to occur at a polar angle from the source

$$\alpha = \tan^{-1} U_0'/\gamma x \tag{5}$$

measured from the vector flow direction. Note that it is conceptually possible to reconstruct the velocity profile from sequences of such wake surveys by integration.

In vortical flow one must also consider the possible effect of recirculation. The argument can be set forth most clearly by discussing a specific example. At the top of Fig. 6 are shown polar traverses around both a heated and an unheated wire placed at the centerline of a long ($L/H = 10$) notch close to the floor (0.015 in. above it). The unheated traverse is symmetrical; in this case, the thermocouple records the adiabatic recovery temperature on (approximately) a cylinder (T_c). The temperature increased by about 10 degrees between the floor and the top of the traverse, indicating a higher velocity there, as expected. Also shown is $(T - T_c)$, the local difference between the readings with the source heated and unheated. A strong temperature lobe in the direction opposite to the external flow is found, indicating an upstream flow near the wall in the cavity; however, a relatively large lobe in the direction of the external flow is also found. The temperature must *decay in the direction of local flow*. *If the flow is steady* and the lobe on the downstream side of the wire is due to heated air being recirculated around the cavity, then the temperature must *decrease* upstream of the wire, but increase downstream of it. This is not the case, as shown by the lower portion of Fig. 6. One concludes that the back lobe is not due to recirculation but to a *reversal of the flow* during part of the time.

This striking result, confirmed by further tests, proves that the entire cavity is profoundly unsteady, not only in the sense of random "turbulent" fluctuations, but in the sense of definite reversals of the direction of the flow.

Consider the effect of the flow reversal further. When it occurs, the magnitude of the temperature difference measured at a given distance from a (constant power input) source can be, under proper conditions, *larger in the direction of the smaller velocity*. If one imagines a pulse with velocity V_F followed by one in the opposite direction with velocity V_B (for equal time), one finds from Eq. 2 that the magnitude of the average temperatures in the plane of the flow at equal distances from the source in one direction (subscript F) and in the other (subscript B) is:

$$(T_F - T_0)/(T_B - T_0) \sim \sqrt{V_B/V_F} \tag{6}$$

Consequently, the *direction of the larger diffusion lobe does not necessarily indicate the direction of mean mass flux*. To ascertain this one must compare the results with measurements of dynamic pressure; the larger pressure reading will indicate the direction of the time-averaged flow.

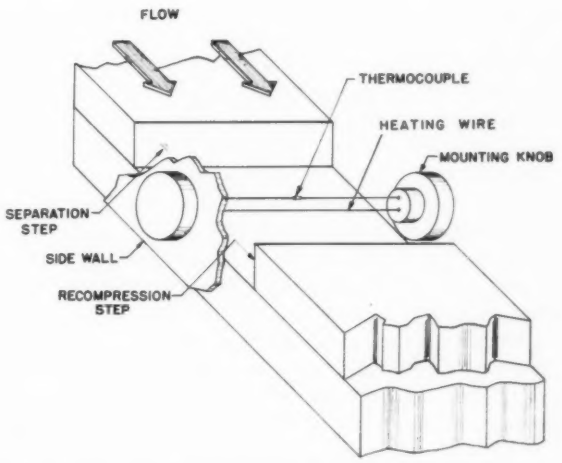

FIG. 4. Apparatus for surveys of diffusion from a two-dimensional heat source in the notch.

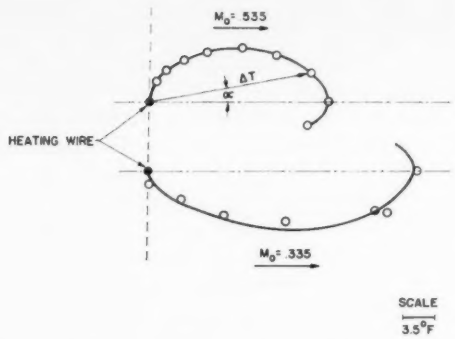

FIG. 5. Polar temperature traverses around a heated wire in free tunnel (subsonic flow) at two Mach numbers.

(*b*) *Heat Diffusion Tests at the Centerline of the Notch*

Fig. 7 shows a series of heat-diffusion polar surveys at different heights above the notch floor. They are presented in two groups for clarity. These results must be interpreted in conjunction with stagnation pressure surveys (see Fig. 18 of reference 1) keeping in mind the characteristics of the heated wake in nonsteady flow.

There is a layer of reverse flow near the floor (Fig. 7a) evidenced by the pronounced temperature lobe pointed upstream and the stagnation pressure readings which show flow in that direction. This flow is unsteady, and reverses part of the time, as evidenced by the existence of a smaller downstream-pointing lobe. The magnitude of the main lobe increases to a distance of 0.066 in. above the floor, indicating a decreasing velocity. At about 0.100 in., the forward and back lobes are almost equal in size*; this indicates that there is essentially no preferred direction of the flow. The height at which this happens coincides approximately with the height at which no definite dynamic pressure was recorded.

Above this layer one finds another layer (0.100 to 0.150 in. above the floor) in which stagnation pressure measurements show a downstream mean flow but the temperature surveys show an upstream-pointed lobe (Fig. 7b). This is not contradictory if one considers Eq. (6). The flow in this "buffer" layer reverses direction periodically. Physically, this suggests pulsations of the shear layer in and out of the cavity; when the shear layer dips in, the flow in the upper half of the cavity is entrained downstream; when it bends out, the flow in the cavity reverses. It confirms the spark photographs discussed previously.

Above the buffer layer, both pressure and heat-diffusion traverses indicate a strong downstream flow; this is the free shear layer proper.

Similar studies of heat diffusion were also made near the recompression and the separation step. However, the results were not interpretable. In both corners of the notch an almost uniform temperature was measured around the wire. These corners contain strong vortexes: recirculation and instability both contributed to the diffusion of heat. Consistent pressure surveys with which to monitor the interpretation could not be obtained.

Traverses were also made at several streamwise stations in the notch for fixed locations of the heated wire (at a fixed distance from the floor). From Fig. 8 we see that:

(a) The heat diffused from a wire in the recompression zone remains contained in a well-defined region occupied by the recompression vortex. It escapes into the free flow past the edge of the notch.

(b) The diffusion of heat from the wire at the centerline proceeds in both directions about equally, indicating a highly disturbed, direction-reversing flow.

(c) The heat from the wire in the separation corner remains in the low velocity separation vortex and diffuses from there downstream through the cavity.

(*c*) *Summary of Observations*

The diffusion studies did not yield quantitative information. They did, however, prove that the flow in the cavity is definitely unsteady. The inability to obtain a mass balance in the cavity from pressure measurements alone (see Fig. 18 of reference 1) is clarified. The cavity appears to contain a strong vortex at the recompression corner, and also a weaker one of opposite sign at the separation corner. The flow in the central section exhibits three vertical layers: a *reverse flow layer near the floor*, unsteady, relatively weak, but definitely in the upstream direction on the average; a *buffer layer* characterized by strong flow reversals with essentially no definite mass flux; and finally the *shear layer*.

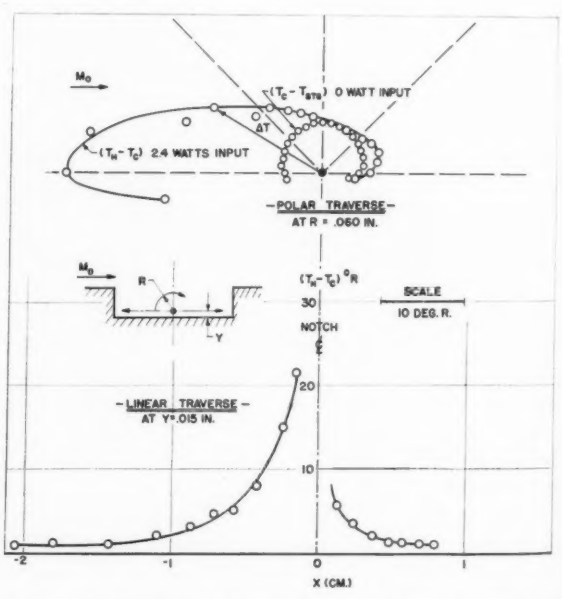

FIG. 6. Polar and linear heat diffusion surveys at the cavity centerline $L/H = 9$, $M_0 = 2.8$. Wire at $Y/H = 0.1$.

* The asymmetry in the temperature traverses is due to the gradients over the finite distance between the source and the thermocouple.

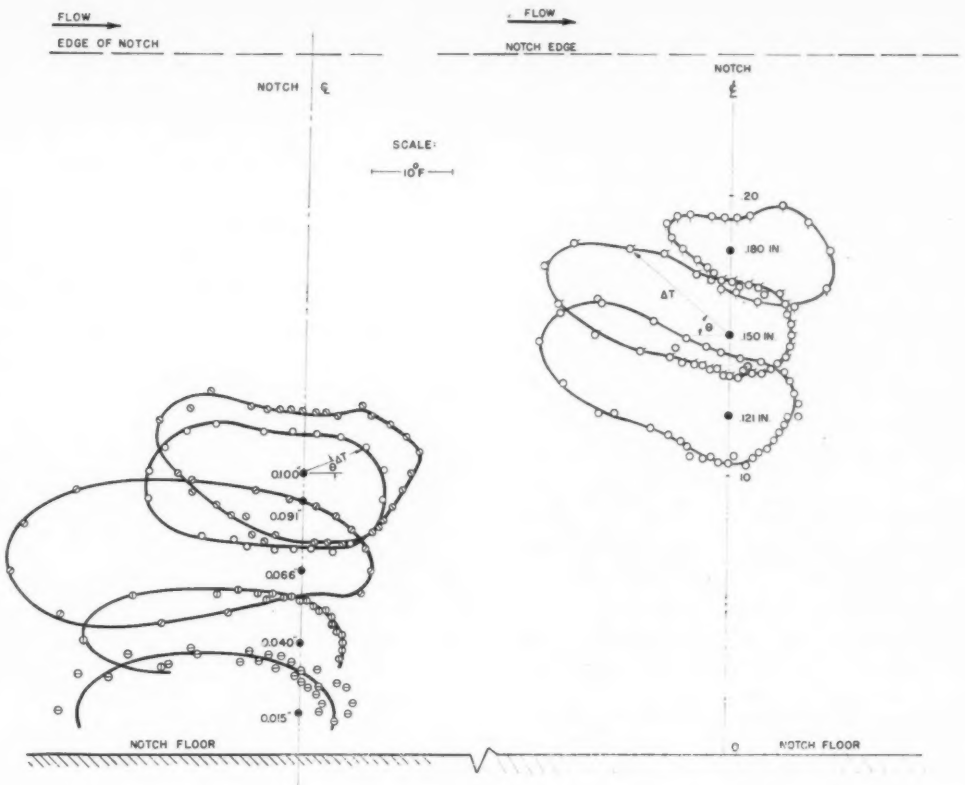

FIG. 7. Polar heat diffusion traverses at notch centerline at various distances from the floor (Y), $M_0 = 2.8$, and $L/H = 9$: (a) return flow layer, (b) buffer layer.

Heat Transfer Measurements

(*a*) *Experimental Method*

Practical considerations and analysis suggest a comparison of the transfer characteristics of separated regions with those of an "equivalent" attached boundary layer. In the present investigation the heat-transfer properties of the separated region are always referred to those of the attached boundary layer two to five notch depths ahead of separation, which were measured in each test. This station was chosen because the heat transfer is affected slightly by the expansion around the corner of the notch. The virtual distance from the origin of the oncoming boundary layer, S, as determined from traverses and Eq. 1, was long (about 30 in.) compared to the length of the notch (maximum 4 in.). Consequently, the Reynolds number and the heat transfer characteristic of the attached boundary layer (which depend on the one-fifth power of S) were almost constant over the length of the notch and could be unambiguously defined by their value at the reference station ahead of separation. There was a slight change in the boundary-layer thickness associated with each Mach number. Table 1 gives the pertinent conditions. In the subsequent discussion, the tests are referred to by the Mach number and the boundary-layer classification "thin" or "thick."

The use of the heat-transfer coefficient for the flat plate (h_f) just ahead of the notch for reference is obviously not universal because the history of the oncoming boundary layer is variable. In order to ascertain its possible influence, a comparison of the results for different upstream wall-temperature histories is shown in Fig. 9. The upper portion of the figure defines the conditions (obtained by changing the coolant distribution in the wall) while the lower portion shows corresponding ratios of local notch-floor heat-transfer coefficient to that of the standard station ahead of separation for a particular notch geometry and Mach number. This example shows a difference of approximately 10 percent in the ratio. It indicates that in the case of an *adiabatic* approaching boundary layer, such as in Larson's investigations,[12] a still lower ratio is to be expected and that, in general, the previous thermal history of the approaching flow does bear some influence on the problem.

It was questioned whether there is a difference between flow with heat transfer *to the wall* and flow with heat transfer *to the fluid* (such as was investigated in all

TABLE 1
Conditions for Heat Transfer Tests

Mach no. at separation (M_0)	δ/H Thin BL ($H = 0.50$ in.)	δ/H Thick BL ($H = 0.25$ in.)	Reynolds no. at separation $\times 10^{-6}$
2.1	0.85	1.7	4.8
2.9	1.08	2.16	3.6
3.5	1.14	2.27	2.3

other studies[11,12]). Two tests were conducted, in one of which the air was heated and the wall cooled (standard configuration) while in the other the air was at room stagnation temperature and the wall was heated (with saturated steam, 300°F). The heat transfer coefficient ratios of both tests were found to lie within the data scatter. However, the accuracy of the measurements was relatively low with so low an overall temperature potential (lower than in any standard tests by a factor of approximately 3 to 4).

All tests discussed subsequently were conducted under upstream conditions marked "standard" in Fig. 9a. Fig. 10a shows a summary of all the measurements of the flat-plate heat-transfer coefficient, defined as follows:

$$h_f = \frac{q_F}{(T_{aw} - T_w)} = K\frac{(T_w - T_c)}{(T_{aw} - T_w)} \qquad (7)$$

K is a proportionality constant involving the module geometry and the conductivity of the wall material. T_{aw} is the adiabatic wall recovery temperature computed from the relation:

$$\frac{T_{aw}}{T_0} = \eta_R + (1 - \eta_R)\left(1 + \frac{\gamma - 1}{2}M_0^2\right)^{-1} \qquad (8)$$

in which the recovery ractor η_R was assumed equal to the one-third power of the Prandtl number:

$$\eta_R = (Pr)^{1/3} \qquad (9)$$

Compared, for instance, with the Reshotko–Tucker[25] correlation, these data exhibit a somewhat larger decrease with M_0; at $M_0 = 2$ h_f is about 15 percent above and at $M_0 = 3.5$ it is about 30 percent below the values given by Eq. (34) of reference 25. The spread of the data includes all notch geometries, but there is no consistent effect of the notch L/H.

Rewriting Eq. 7, it is possible to check the unknown adiabatic wall recovery temperature* from tests at different stagnation temperatures:

$$\frac{q}{T_0} = \frac{h}{1 + (h/k)}\frac{(T_0 - T_c)}{T_0} - \frac{h}{1 + (h/k)}\left(1 - \frac{T_{aw}}{T_0}\right) \qquad (10)$$

All the data for a particular Mach number are shown in Fig. 10b plotted in this form. The correlation line shown is constructed using Eq. (9) to determine the intercept, and the mean value of the measured transfer coefficients (Fig. 10a) is used to determine the slope; it is seen that Eq. (9) is valid within the experimental accuracy.

However, Eq. (9) applies only to an attached boundary layer. It has been found in other investigations[3,4] that in the separated regions η_R differs somewhat (by 2 to 5 percent on the average), although the available data are not conclusive. In view of this uncertainty, we used a simpler heat-transfer coefficient h defined on the basis of the adiabatic recovery temperature *before* separation, T_{awf}. One has:

$$h = h_{loc.}\frac{T_{aw} - T_w}{T_{awf} - T_w} \qquad (11)$$

It is evident that for small heat-transfer rates ($T_w \to T_{aw}$) the ratio of this to the true local h in the cavity is

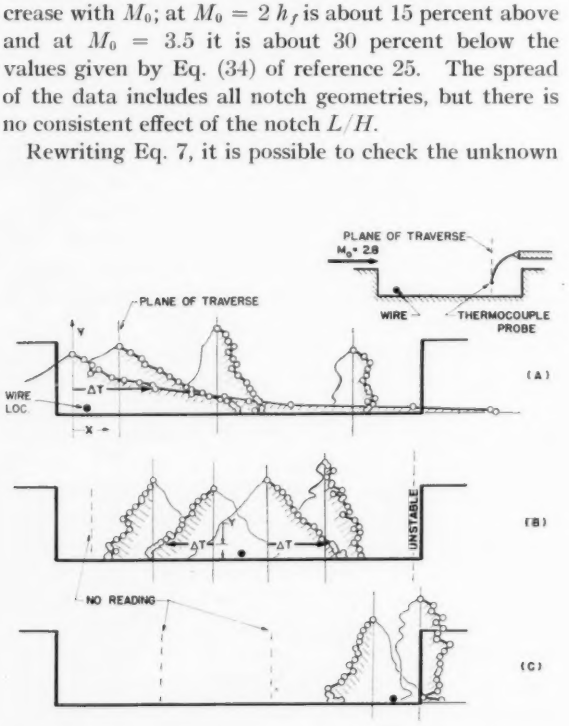

FIG. 8. Heat diffusion traverses at constant X/L, $M_0 = 2.8$, $L/H = 9$. Three locations of heat source (X/L) at $Y/H = 0.08$; centerline spanwise.

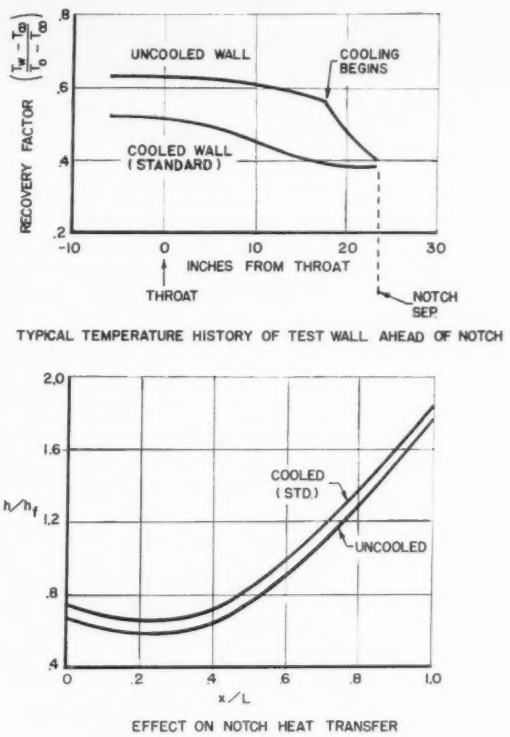

FIG. 9. The effect of the temperature history of the oncoming boundary layer on the heat transfer to the cavity at $M = 2.9$ and $L/H = 6$.

* The test set-up could not be insulated adequately so as to permit T_{aw} to be determined experimentally.

very sensitive to small variations in T_{aw}/T_{awf}. However, under the present test conditions, one would not expect the heat-transfer coefficient h to be in error by more than 5 to 10 percent of $h_{loc.}$ in the cavity.

(*b*) *Results*

Fig. 11 shows the distribution of the heat-transfer coefficient ratios over the floor of a (rectangular) notch at a fixed Mach number as a function of L/H for the thin and thick boundary-layer tests.

Individually, the curves show a drop below unity at the separation point, a minimum in the first half of the notch, and then a rise well above unity at the recompression step. The heat-transfer coefficient ratio increases with L/H near recompression, but decreases near separation. The "minimum" decreases with L/H and also shifts to a lower value of x/L. At $L/H = 9$ a "plateau" appears in the center of the notch, which is associated with the beginning of reattachment of the flow to the floor, and the "closure" of the cavity (the critical closure length ratio is about 11 for the small δ/H and about 12 for the large δ/H, see reference 1).

The effect of increasing δ/H is to shift the curve to higher h/h_f, while the curves remain qualitatively similar.

Fig. 12 shows a parametric representation of the behavior of the heat-transfer coefficient ratio in the domain of M_0 and L/H. The curves are for constant x/L except for the curves marked "minimum," which were drawn from values of the lowest the ratio h/h_f in the notch. This value is about 5 percent lower than that at the separation corner.* It is seen that the general level of the heat-transfer ratio is affected slightly by Mach number, less in the thin boundary-layer than in the thick boundary-layer tests. This is particularly noticeable at the station at 70 percent of the notch length. When the boundary layer is thin, this station is still essentially in the low-heat-transfer region of the notch, but when the boundary layer is thick, it is already affected by the rise towards the recompression point. This reflects strongly on the average heat transfer over the entire floor.

Fig. 13 shows data for a downstream-facing separation step (infinite L/H). The minimum value of the heat-transfer ratio occurs immediately behind separation. It is followed by a rise to a maximum of about 1.1 at a value of x/H at which one expects reattachment of the separated shear layer (see reference 1), and then decays to a value somewhat lower than unity as the equilibrium boundary layer is re-established. The final value below unity is to be expected, because the reattached boundary layer is thickened. There is a slight Mach number effect which may, however, be due to the δ/H effect associated with changes in M_0 (Table 1).

* The slight rise of h/h_f at separation is thought to be caused by the heat transfer to the cavity from the (noninsulated) inner vertical face of the separation step. The separation module is exposed to the attached boundary layer on its top surface and its temperature is higher than that of the first floor module.

The minimum h/h_f of Fig. 13 is consistent with the trend exhibited by the minimum lines of Fig. 12b with increasing L/H. The downstream-facing step under the thin-boundary-layer conditions could not be tested, but it is to be expected that the same general trend would be found with a minimum value at separation as low as $h/h_f \sim 0.2$ (see Fig. 16a).

Fig. 14 shows an integrated average heat-transfer coefficient ratio for the floor of the notch. It is seen that when the boundary layer is thin, the separated flow definitely "shields" the wall by a factor of about 2. This is drastically different in the case of a thick boundary layer. The changeover seems to occur for a value of the ratio δ/H of about one, the same limit that was found to differentiate between "thin" and "thick" boundary layer behavior in the pressure distribution. A slight Mach number effect is evident; again, this may reflect the influence of the variation in δ/H rather than in the free-stream Mach number proper.

In the foregoing, only the floor of the notch was considered. The overall heat transfer per unit *projected* area to a square ($H \times H$) section of the recompression step is presented in Fig. 15 for varying L/H and M_0. The step was made of high-conductivity material (brass) so that the surface temperature was nearly uniform,* and it was insulated from the backup plate

* The measurement does not, however, depend on this assumption.

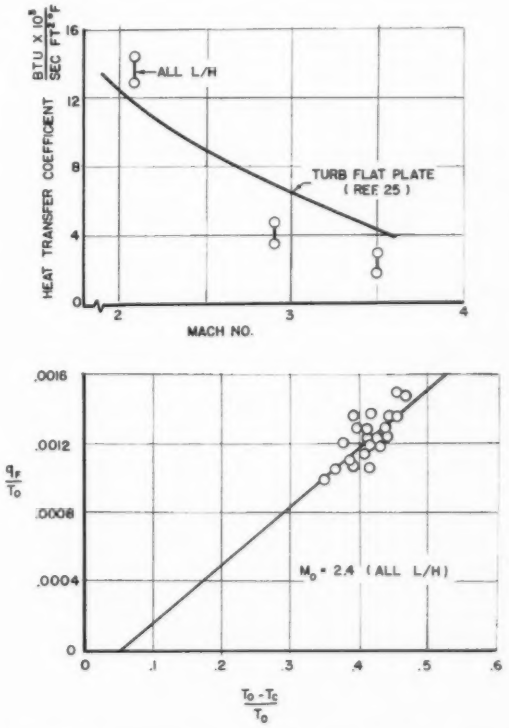

FIG. 10. Calibration tests: (a) heat-transfer coefficient ahead of separation; (b) correlation with assumed adiabatic recovery factor.

as shown in the sketch. The local temperature distribution and heat transfer over its surface could not be measured. We note that, while q_R/q_F based on projected area is higher than unity, when based on exposed area, it is less than unity for most of the tests.

A further study is shown in Fig. 16 for a specific L/H and M_0, including two different geometries of the step. The upper curve shows the heat transfer along the notch per unit *projected* area for both geometries, and the wedge-shaped step is seen to reduce this ratio. The lower curve shows the same data based on *exposed surface area;* on this basis the ratio is less for the square step. It seems that there exists a separation "bubble" immediately downstream of recompression, which is more pronounced for the rectangular corner and partly "shields" the wall. The use of projected surface is practically more significant: in terms of it the heat flux to the recompression zone is relatively high. It is decreased for slanted recompression steps. However, the shape of this step does not seriously affect the heat transfer either upstream in the notch or downstream.

Some measurements were also obtained in a double notch by removing the backup plate. The second notch is evidently somewhat affected by the first notch when the reattachment surface is short. The general level of heat transfer in the second notch is higher and the distribution exhibits a "bulge" near the center of the notch which does not exist when the oncoming flow is uniform. The difference between successive notches could be eliminated by lengthening the reattached zone between them.

Subsonic Flow

A limited number of tests were made in uniform subsonic flow with the same model. In general, there are no basic differences in the heat transfer to the notch in subsonic and supersonic flow, except that the transition from the "open" to the "closed" cavity regime is smoother, and the magnitudes of the coefficient ratio L/H are lower on the average, in subsonic flow. The same was found in the study of the pressure field. Fig. 17 shows a parametric map similar to that of Fig. 12, for $M_0 = 0.42$ and a thin boundary layer.

Discussion

The results of this study of heat transfer to cutouts in the boundary are in general agreement with trends already established in previous investigations (in particular, reference 12). Direct comparison of the data is difficult because of adjustments needed to compensate for the different experimental models and methods. However, when these differences are considered* one finds good agreement in the magnitudes of the numerical results.

The present work crystallized some of the secondary trends also, and threw light on the detailed structure of the flow. Between this work and the NACA program, the behavior of separated cavities in a restricted domain of Mach number, Reynolds number, cavity geometry, and initial conditions has become empirically fairly well known.

However, experiment failed to substantiate the validity of the shear layer model. Good agreement between the theory and experiment is found for the *laminar two-dimensional flow,* but this does not constitute a satisfactory argument. A theory which emphatically associates the entire heat transfer problem with the nature of the shear layer must be judged by how it responds to changes in the properties of the shear layer. Chapman's analysis can be said to provide a good correlation equation for *laminar* separations, but not for transitional and turbulent heat transfer through the cavity. Furthermore, the observed heat transfer gradients along the floor of a cavity are quite foreign to the model, and noting their magnitude one finds it difficult to neglect them.

As already mentioned in the Introduction, there are three transfer mechanisms at play: (a) conduction between the wall and the "dead air," (b) conduction through the shear layer, and (c) mass convection by exchange of fluid between the cavity and the external flow. It is not necessary that one of these mechanisms *dominate* the others either throughout the range of variables or at all, but such a hypothesis is the basis for postulating a simple "model." The Chapman–Larson assumption that (b) dominates does not check with experimental measurements, at least not in general. Carlson's analysis, which stresses (a), is simply too arbitrary; besides, the present measurements of the internal flow definitely disprove his particular assumption of the return-flow velocity profile. They indicate, to the contrary, that the conductivity of the wall film is very high due to an extremely turbulent unsteady and vortical flow. The mechanism (c) is introduced here for the first time. The observations reported earlier show that it is not a negligible effect, and it is reasonable to study the possibility that it dominates the heat transfer problem.

The Mass-Exchange Model

The cavity "breathes" at ultrasonic frequencies. During one half of the pulse mass is injected into it. Since the heat transfer to the wall inside the cavity is high, the excess fluid heats up to wall temperature and carries this heat away when ejected from the cavity during the ejection half of the pulse. The rate of heat exchange depends thus on the unsteady mass exchange. Schematically, the internal flow is as shown in Fig. 18. The mechanism is this: the separating streamline fluctuates to an extent $\pm\Delta$ about its mean position so that a mass dw is periodically fed into the cavity.

* For instance, reference 12 does not distinguish between the "floor" and the recompression step; the oncoming boundary layer is very thin; and caution must be exercised in interpreting the definition of the reference attached boundary layer.

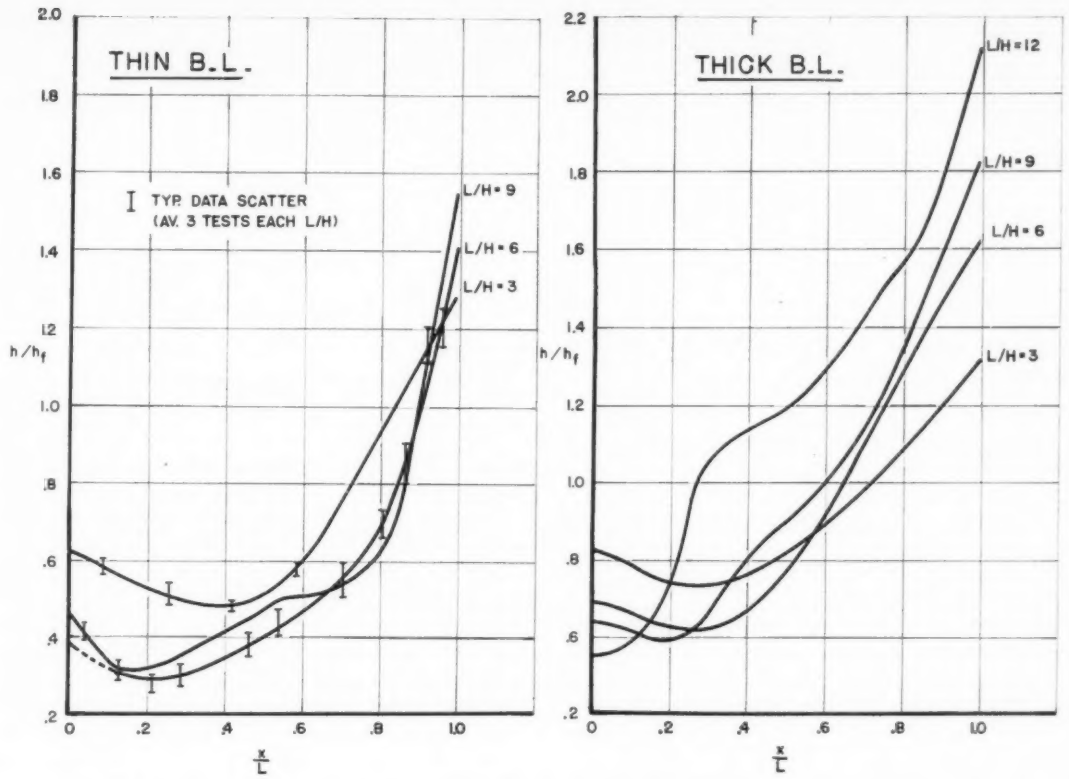

FIG. 11. Variation of the heat-transfer distribution on the floor of the cutout as function of L/H at $M_0 = 2.9$: (a) thin oncoming boundary layer; (b) thick oncoming boundary layer.

This fluid is recirculated around the recompression vortex, picked up in the shear layer, and discharged past the recompression point. The momentum impulse associated with the mass dw must be proportional to the centrifugal impulse of the mass dw whipped around the recompression vortex. This relation fixes the magnitude of the pulsation, assuming that the profile in the neighborhood of the mean streamline is known. A simple formulation of this mechanism is outlined in the Appendix. It leads to the following result for the mean heat transfer to the separated cavity:

$$St = \frac{q}{c_p U_0 (T_{aw} - T_w)} \sim \frac{1}{\phi} \frac{\delta_s}{L} \tag{12}$$

where δ_s is the thickness of the shear layer just ahead of recompression and ϕ is a function of the shear layer form describing its slope at the mean separating streamline:

$$\phi = \left[\frac{d(U/U_0)}{d(Y/\delta_s)} \right]_{Y=0} \tag{13}$$

Comparison With Experiment

Provided that the oncoming boundary layer is thin relative to the notch, the effect of it on the development of the free shear layer is small. The function ϕ is a universal function for *either* laminar or turbulent flow. From Chapman's laminar solution one finds:

$$\phi_L = 1.06 \tag{14}$$

For turbulent flow one finds, using Goertler's solution of free-jet mixing:

$$U/U_0 = \tfrac{1}{2}\{1 + \text{erf}\,(\sigma Y/x)\} \tag{15}$$

$$\phi \simeq 0.8 \tag{16}$$

The numerical values depend on how one defines δ_s, but it is obvious that the turbulent and the laminar values of ϕ are essentially equal. The entire effect of transition and Reynolds number is contained in δ_s/L, the growth rate of the free shear layer:

(a) Since upon transition to turbulence (at a fixed Re) δ_s/L certainly increases, one expects an increase in heat transfer. However, it seems reasonable to presume that the transitional thickening of a free shear layer would be of the same order of magnitude as the thickening of an attached boundary layer; therefore, *the ratio h/h_f would not be expected to change very much upon transition.* These results are borne out by the data.[12]

(b) In laminar flow $\delta_s/L \sim Re^{1/2}$, therefore

$$St_{\text{lam.}} \sim Re^{-1/2} \text{ and } (h/h_f)_{\text{lam.}} = \text{const.} \tag{17}$$

as verified by Larson's data.

(c) The rate of growth of a free shear layer in turbu-

lent flow is not well known. However, referring to the measurements of the thickness of the recompression profile presented in Part I of this series,[1] one finds that the "thin" boundary-layer data follow the trend $\delta_s/L \sim Re^{-2/5}$ very closely, so that Larson's result,

$$St_{\text{turb.}} \sim Re^{-2/5} \quad \text{and} \quad (h/h_f)_{\text{turb.}} \sim Re^{-1/5} \tag{18}$$

is consistent with this model as well as with the independent pressure measurements.

(d) Eq. 12 predicts no Mach number dependance in either laminar or turbulent flow, as long as the Mach number is low enough so that δ_s is not altered by compressibility effects. This is essentially in accord with the observations of Larson and with Fig. 14.

(e) Few theoretical arguments can be used in the case where the oncoming boundary layer is thick enough to influence the development of the shear layer. However, it seems certain that a thick boundary layer at separation will result in a thicker shear layer at recompression, that is, δ_s will increase with δ. Consequently, the heat transfer will increase. Fig. 14 bears out this conclusion.

(f) The trends shown by Fig. 9 relating to changes in thermal history of the oncoming flow are in qualitative agreement with the model. When the oncoming boundary layer is adiabatic, the fluid which penetrates the cavity is at a higher initial temperature, absorbs less heat from the cavity wall, and the heat transfer rate is decreased.

(g) Finally, the proposed structure of the flow inside the cavity is compatible with the observed distribution of heat transfer over the floor of the notch. One would expect the highest rate of heat transfer from the boundary to occur near the recompression zone, the remainder of the cavity contributing little to the exchange.

Limitation of the Model

The mass-exchange heat transfer model exhibits all the trends indicated by experimental data. Should one wish to extend the argument, the numerical values obtained from Eq. 12 (constant of proportionality in Eqs. A5 and A6 equal one, Chapman's laminar solution for δ_s/L, and Eq. 14) also check the measured Stanton numbers. However, these confirmations must be taken with reserve. The present model depends on the unsteadiness of the flow at the exclusion of the other mechanisms. Evidence of the existence of pulsation has been presented here (Fig. 6) and elsewhere,[10] but there is also evidence that not all cavities pulsate. For instance, preliminary work with cavities having slanted (wedge-shaped) recompression faces indicated[9] that no wave radiation occurred. In such cases, the

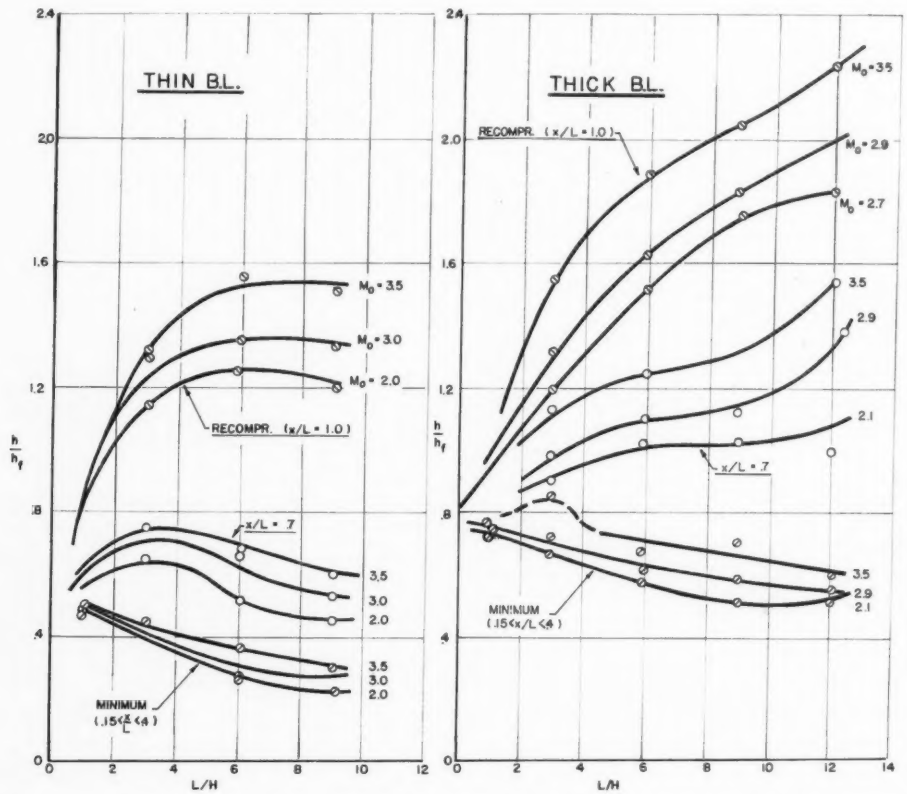

FIG. 12. Parametric map: heat-transfer coefficient ratio (minimum, maximum, and at $X/L = 0.7$) as function of L/H and M_0: (a) thin boundary layer; (b) thick boundary layer. (Note: points are averages over all tests.)

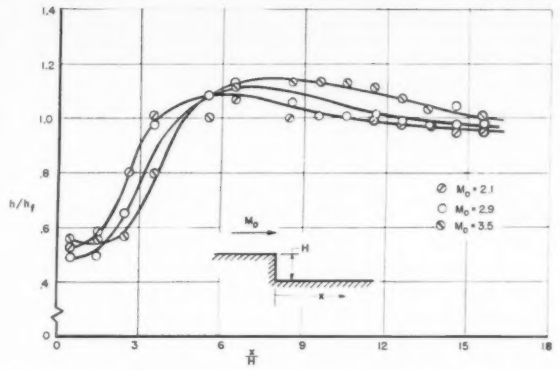

FIG. 13. Heat-transfer coefficient ratio behind a downstream-facing step. Thick boundary layer.

analytical model under discussion is clearly questionable.

One suspects that neither the Chapman–Larson "conduction" model nor the present mass-exchange model are sufficiently complete. Perhaps both mechanisms share in the process in varying proportions, depending on the geometry, and since their contribution to the transfer of heat is of the same order, it is difficult to distinguish between them. However, the present analysis seems to yield a more accurate semi-empirical correlation of the measurements over the entire range investigated to date than other models.

Concluding Remarks

The ratio of the heat transfer to an "open" cavity to that of an equivalent attached boundary layer is primarily a function of the thickness of the oncoming boundary layer. If it is thin (that is, less than one notch depth) the heat transfer ratio is reduced by a factor of approximately two; if it is thick, the heat transfer can be even increased.

However, the heat transfer per unit surface area is not necessarily the important criterion. The drag of a notched wall is an order of magnitude higher than that of an equivalent flat plate. Therefore, the heat transfer to a notched wall per unit drag is around $^1/_{20}$ of that to a plate. It is possible, subject to an extension of these findings to hypersonic Mach numbers, that this fact can be useful in re-entry problems.

It is proper to add that preliminary investigations of notches in the boundary of both supersonic and subsonic accelerating flows showed that the external pressure gradient has a strong influence on pressure and heat-transfer distributions. Some pressure measurements are reported in reference 26. Other measurements showed a twofold *increase* in heat transfer to the wall under these conditions. This is currently under investigation.

Appendix

If the shear layer dips in and out by a distance $y \pm \Delta$ (see Fig. 18) about its mean position ($y = 0$, $u = u_*$) as suggested by the results reported in the text, then there is an excess of momentum per pulse fed into the cavity, which is

$$dM = \rho \int_{-\Delta}^{+\Delta} u^2 dy - 2\rho u_*{}^2 \Delta = {}^2/_3 \rho \Gamma^2 \Delta^3 \quad \text{(A1)}$$

where the velocity in the neighborhood of the origin is assumed to vary linearly with distance:

$$u = u_* + \Gamma y \quad \text{(A2)}$$

This is associated with a periodic mass pulse

$$dw_+ = -dw_- = \rho \int_0^{\Delta} u \, dy - \rho u \Delta = \rho \Gamma \Delta^2 \quad \text{(A3)}$$

The impulse associated with the momentum transfer to the cavity and the centrifugal force due to the unbalance mass whipped around the recompression vortex must be in balance. The measurements of acoustic radiation suggest that the rim speed of the cavity vortex is proportional to the external flow velocity while its radius is of the order of the notch depth. Then on dimensional grounds*:

$$\frac{\text{Momentum impulse}}{\text{centrifugal impulse}} = \text{const.} = \frac{dM}{(dw\ U_0{}^2/H)\tau} \quad \text{(A4)}$$

where τ is the duration of the pulse governed by the circular frequency of the vortical motion,

$$\tau \sim H/U_0 \quad \text{(A5)}$$

* This dimensional argument does not take into account the effects of compressibility.

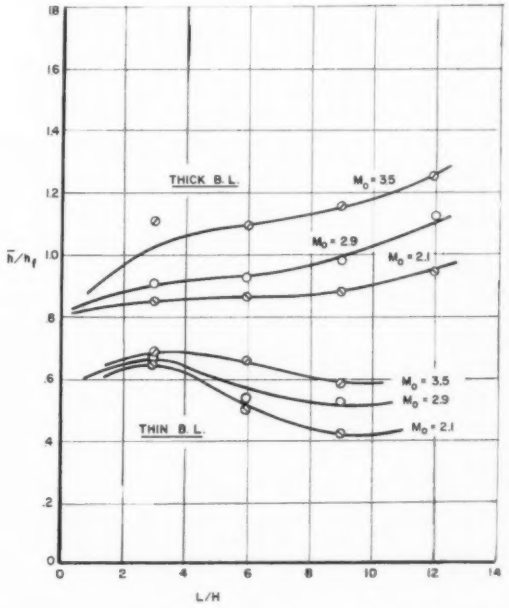

FIG. 14. Integrated average heat-transfer coefficient ratio for the floor of the cavity in the Mach number and L/H domains for thin and thick boundary layers.

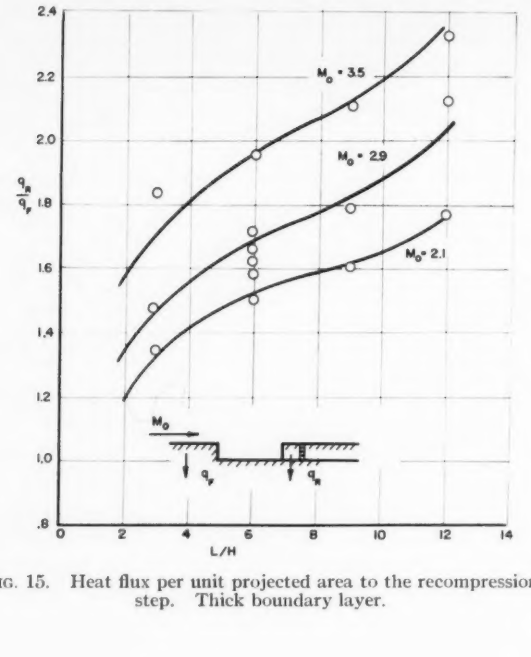

FIG. 15. Heat flux per unit projected area to the recompression step. Thick boundary layer.

so that one can relate the gradient of the shear-layer profile to the shear-layer thickness:

$$\Gamma = \left.\frac{dU}{dY}\right]_{Y=0} = \frac{U_0}{\delta_s}\frac{d(U/U_0)}{d(Y/\delta_s)} = \frac{U_0}{\delta_s}\phi \qquad \text{(A6)}$$

where δ_s is the thickness of the shear layer while ϕ is a shape factor discussed in the text.

Introducing these into Eq. (A4), one can solve for the unknown which is

$$\Delta \sim \delta_s/\phi \qquad \text{(A7)}$$

The unsteady mass exchange per pulse (note that the time-averaged mass flux per unit span to the cavity is, of course, zero) is:

$$dw \sim \rho U_0 \frac{\phi}{\delta_s}\left(\frac{\delta_s}{\phi}\right)^2 \sim \rho U_0 \frac{\delta_s}{\phi} \qquad \text{(A8)}$$

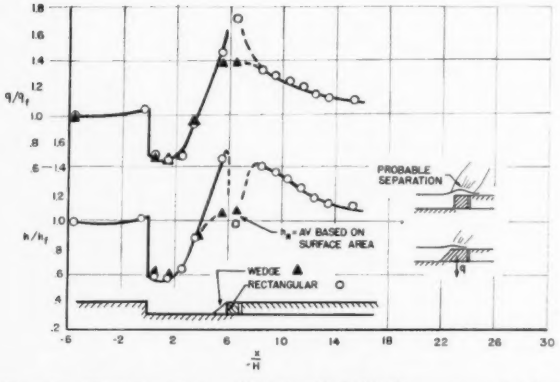

FIG. 16. Heat-transfer coefficient ratio behind recompression for a thick boundary layer and various geometries.

The heat absorbed and carried away by the fluid flowing through the cavity per unit span per second is

$$q = c_p dw(T_{aw} - T_w) \qquad \text{(A9)}$$

where T_{aw} is the temperature of the incoming fluid. For a cavity of the length L one has, using Eq. (A8):

$$St = \frac{q}{L(T_{aw} - T_w)C_p\rho U_0} = \frac{1}{\phi}\frac{\delta_s}{L} \qquad \text{(A10)}$$

or, relating the transfer properties of the cavity to those of an attached boundary layer just ahead of separation for which

$$St_f \sim Re^{-n}$$

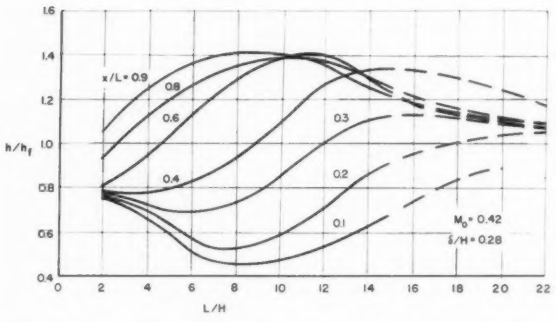

FIG. 17. Map of heat transfer to a cavity in subsonic flow: $M = 0.42$, $\delta/H = 0.28$, turbulent flow.

where n is 1/2 and 1/5 for laminar and turbulent flow, respectively, one has:

$$\frac{St}{St_f} = \frac{h}{h_f} = \frac{1}{\phi}\left(\frac{\delta_s}{L}\right)Re^n \qquad \text{(A11)}$$

It should be remembered that δ_s is the thickness of the shear layer and not the thickness of the approaching boundary layer, while Re relates to the characteristic of the boundary layer at the conditions selected as reference.

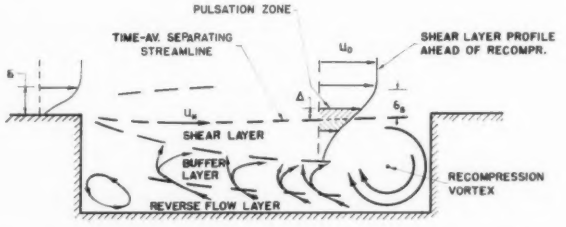

FIG. 18. Structure of the internal flow for the mass-exchange heat transfer model.

References

[1] Charwat, A. F., Roos, J. N., Dewey, C. F., and Hitz, J. A., *An Investigation of Separated Flows: Part I—The Pressure Field*, Journal of the Aerospace Sciences, Vol. 28, No. 6, pp. 457–470, June 1961.

[2] Chapman, D. R., *A Theoretical Analysis of Heat Transfer in Regions of Separated Flow*, NACA TN 3792, 1956.

[3] Thomman, H., *Measurements of Heat Transfer and Recovery Temperature in Regions of Separated Flow at a Mach Number of 1.8*, Report 82, Aero. Research Institute of Sweden, 1959.

[4] Seban, R. A., Emery, A., and Levy, A., *Heat Transfer to Separated and Reattached Turbulent Flows Obtained Downstream of a Surface Step*, WADC TR-56-217, 1956.

[5] Charwat, A. F., Roos, J. N., and Dewey, C. F., *Preliminary Results of an Experimental Investigation of Local Pressures and Heat Transfer in Regions of Separated Flow*, Dept. of Engr. Rept. No. 5983, University of California at Los Angeles, June 1959.

[6] Charwat, A. F., and Yakura, J. K., *An Investigation of Two-Dimensional Supersonic Base Pressures*, Journal of the Aeronautical Sciences, Vol. 25, No. 2, pp. 122–28, February 1958.

[7] Ginoux, J., *Experimental Evidence of Three-Dimensional Perturbations in the Reattachment of a Two-Dimensional Laminar Boundary Layer at $M = 2.05$*, Tech. Note No. 1, Training Center for Experimental Aerodynamics, Rhode St. Genese, Belgium, November 1958.

[8] Chapman, D. R., Kuehn, D. M., and Larson, H. K., *Investigation of Separated Flows in Supersonic and Subsonic Streams with Emphasis on the Effect of Transition*, NACA TN 3869, March 1957.

[9] Ginoux, J., and Charwat, A. F., *Pulsations of a Cavity in Supersonic Flow*, to be published.

[10] Krishnamurty, K., *Acoustic Radiation from Two-Dimensional Rectangular Cutouts in Aerodynamic Surfaces*, NACA TN 3487, 1955.

[11] Morozov, M. G., *Interaction Between a Supersonic Stream and a Rectangular Depression in a Flat Plate*, Soviet Technical Physics, Vol. 3, No. 1, January 1958 (in Russian: Zhur. Tekh. Fiz., Vol. 28, No. 1).

[12] Larson, H. K., *Heat Transfer in Separated Flows*, Journal of the Aero/Space Sciences, Vol. 26, No. 11, pp. 731–38, November 1959.

[13] Rabinowicz, J., *Measurements of Turbulent Heat Transfer Rates on the Aft Portion and Blunt Base of a Hemisphere Cylinder in the Shock Tube*, Jet Propulsion, pp. 615–20, September 1958.

[14] Powers, W. F., Stetson, K. F., Adams, M. C., *A Shock Tube Investigation of Heat Transfer in the Wake of a Hemisphere-Cylinder with Applications to Hypersonic Flight*, AVCO Research Report No. 30, August 1958.

[15] Gortler, H., *Berechung von Aufgaben der freien Turbulenz auf Grund eines neuen Näherungsansatzen*, ZAMM, Vol. 22, pp. 244–54, 1942.

[16] Bogdonoff, S. M., and Vas, I. E., *Exploratory Studies of a Spiked Body for Hypersonic Flight*, in *Proceedings of the 1958 Heat Transfer and Fluid Mechanics Institute* held at University of California; Stanford University Press, p. 187.

[17] Bloom, M. H., and Pallone, A., *Heat Transfer to Surfaces on the Neighborhood of Protuberances in Hypersonic Flow*, in *Proceedings of the 1957 Heat Transfer and Fluid Mechanics Institute* held at California Institute of Technology; Stanford University Press, p. 249.

[18] Carter, H. S., *Effect of Some External Crosswise Stiffeners on the Heat Transfer and Pressure Distribution on a Flat Plate at Mach Numbers of 0.77, 1.39 and 1.98*, NACA TN 4333, September 1958.

[19] Chapman, D. R., *Laminar Mixing of a Compressible Fluid*, NACA TN 1800, 1949.

[20] Cole, J. D., *Note on the Effect of Circulation in Heat Transfer*, Rand Research Memo No. 1351, September 24, 1954.

[21] Carlson, W. O., *Heat Transfer in Laminar, Separated, and Wake Flow Regions*, in *Proceedings of the 1959 Heat Transfer and Fluid Mechanics Institute* (held at University of California at Los Angeles); Stanford University Press, pp. 140–55.

[22] Goldstein, S., *"Modern Developments in Fluid Dynamics*, Vol. 1, Oxford University Press, 1938.

[23] Schubauer, G. B., *A Turbulence Indicator Utilizing the Diffusion of Heat*, NACA Rept. No. 524, 1935.

[24] Frost, B. A., *Turbulence and Diffusion in the Lower Atmosphere*, Proc. Roy. Soc. (London), Series A, Vol. 186, No. 1004, pp. 20–35, 1946.

[25] Reshotko, E., and Tucker, M., *Approximate Calculation of the Compressible Turbulent Boundary Layer with Heat Transfer and Arbitrary Pressure Gradient*, NACA TN 4154, 1959.

[26] Roos, J. N., *An Experimental Investigation in Regions of Separated Flow*, M.S. Thesis, Dept. of Engineering, University of California, Los Angeles, February 1959.

✦ ✦ ✦

A Reprint

Journal of the Aeronautical Sciences

Now entitled Journal of the Aerospace Sciences

Available

Volumes 1–5, 1934–1937/1938, paper bound set..... $140.00
Volumes 1–2, 1934–1935, single volumes, paper bound..... 20.00
Volumes 3–5, 1935/1936–1937/1938, single volumes, paper bound..... 35.00

In Preparation

Volumes 6–8, 1938/1939–1940/1941

(Reproduced with the permission of the original publisher, Institute of the Aerospace Sciences, Inc.)

Please address orders and inquiries to:

Johnson Reprint Corporation
111 Fifth Avenue, New York 3, N.Y.

On Aircraft Maneuvers in the Vertical Plane Under Assumptions Leading to Easy Integrability of the Flight-Path Equations

F. EDWARD EHLERS* AND GEORGES BRIGHAM**

Boeing Airplane Company

Summary

The differential equations for the flight path of an airplane in the vertical plane with constant acceleration of gravity are integrated in closed form under the following sets of assumptions:

(1) Net thrust-to-weight ratio and lift-to-weight ratio are constant.
(2) Centrifugal acceleration and net thrust-to-weight ratio are constant.
(3) Velocity and lift-to-weight ratio are constant.
(4) Angular velocity and net thrust-to-weight ratio are constant.

Graphs and tables of some of the solutions are provided.

Symbols

a = α/K
D = drag
g = acceleration of gravity
h = $\beta - \cos\theta$
h_0 = $\beta - 1$
K = number of g's of centrifugal acceleration
L = lift
t = time
T = thrust
v = velocity of airplane
v_0 = initial velocity for $\theta = 0$
v_1 = initial velocity for upside-down position, $\theta = \pi$
W = weight of airplane
(x, y) = Cartesian coordinates of airplane position
z = $1/K$
α = $(T - D)/W$, net thrust factor
β = L/W, load factor
σ = $g/v_0\omega$
ϕ = angle in radians defined by Eq. (9)
ϕ_1 = angle in radians defined by Eq. (22)
ψ = $(\alpha - \theta)\sqrt{z/2}$
ψ_0 = $\alpha\sqrt{z/2}$
ξ = gx/v_0^2
η = gy/v_0^2
τ = gt/v_0
} dimensionless variables
θ = angle of flight path measured with respect to x-axis as horizontal position
ω = angular velocity of airplane

Introduction

IN THE PRELIMINARY DESIGN OF AIRCRAFT, it is convenient to have simple means of estimating the flight path, angle, and speed of the aircraft undergoing some maneuvers in the vertical plane. For example, such problems may arise in the study of bomb-dropping techniques and of evasive tactics of fighter craft. Also, one may be concerned with the loss of altitude which an airplane must undergo in order to right itself from an upside-down position. To facilitate such investigations, some closed-form integrations of the equations of the flight path of an airplane have been obtained for the following sets of assumptions:

(1) Net thrust-to-weight ratio and load factor (lift-to-weight ratio) are constant.
(2) Centrifugal acceleration and net thrust-to-weight ratio are constant.
(3) Velocity and load factor are constant.
(4) Angular velocity and net thrust-to-weight ratio are constant.

These solutions may also be used in estimating more complicated flight paths by considering the load factor or net thrust factor, for example, as varying in a piecewise-constant manner, to approximate the desired continuous relation. Graphs and tables of some of the solutions are provided in dimensionless variables to facilitate use by the engineer.

Equations of Motion

Let θ be the angle between the flight path and the horizontal direction taken as the x-axis. Defining the lift L as the force on the airplane normal to the flight path and the thrust T and drag D as always tangent to the flight path yields the following equations of motion for the airplane:

$$dv/dt = g\,[(T - D)/W - \sin\theta] \tag{1}$$

$$v\,d\theta/dt = g(L/W - \cos\theta) \tag{2}$$

$$dx/dt = v\cos\theta, \quad dy/dt = v\sin\theta \tag{3}$$

where v is the speed of the airplane, W the weight, g the acceleration of gravity, and x and y are the Cartesian coordinates of the airplane position.

(I) Maneuvers With Constant Load Factor and Constant Net Thrust Factor

The Velocity as a Function of the Angle of Flight

If we assume that the airplane is flown in such a way that the load factor L/W and the net thrust factor

Received March 29, 1960.

* Mathematician, Mathematics Research Laboratory, Boeing Scientific Research Laboratories.

** Formerly, Operations Research Assistant, Sales and Contract Department, Transport Division; now Consultant, in operations research.

$(T - D)/W$ are maintained constant, then Eqs. (1) to (3) can be integrated in closed form. Let

$$(T - D)/W = \alpha$$

be the net thrust factor, and

$$L/W = \beta$$

the load factor. The equations of motion then become

$$dv/dt = g(\alpha - \sin\theta) \tag{4}$$

and

$$v\, d\theta/dt = g(\beta - \cos\theta) \tag{5}$$

Solving Eq. (5) for dt yields

$$dt = v\, d\theta/g(\beta - \cos\theta) \tag{6}$$

Eq. (4) now can be integrated if we replace dt in terms of θ and v by Eq. (6). This gives

$$dv/v = [(\alpha - \sin\theta)/(\beta - \cos\theta)]d\theta$$

$$dv/v = [\alpha d\theta/(\beta - \cos\theta)] - [(\sin\theta\, d\theta)/(\beta - \cos\theta)] \tag{7}$$

Integrating from 0 to θ yields

$$v/v_0 = [(\beta - 1)/(\beta - \cos\theta)]e^{\alpha\phi} \tag{8}$$

where

$$\phi = \frac{2}{\sqrt{\beta^2 - 1}} \tan^{-1}\left[\sqrt{\frac{\beta + 1}{\beta - 1}} \tan\frac{\theta}{2}\right] \tag{9}$$

and $v = v_0$ at $\theta = 0$.

The Coordinates as Functions of the Flight-Path Angle

The coordinates x and y are found as parametric equations in θ when dt in Eq. (3) is replaced with $d\theta$ by Eq. (6). Thus we have

$$x = \int_0^\theta [v^2 \cos\theta/g\,(\beta - \cos\theta)]\; d\theta$$

$$y = \int_0^\theta [v^2 \sin\theta/g\,(\beta - \cos\theta)]\; d\theta$$

Introducing the dimensionless variables

$$\xi = gx/v_0^2, \quad \eta = gy/v_0^2, \quad \tau = gt/v_0$$

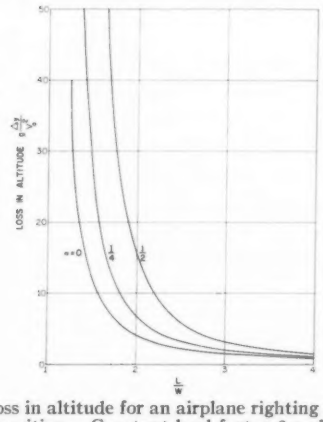

FIG. 1. Loss in altitude for an airplane righting itself from an upside-down position. Constant load factor β and constant net thrust factor α.

and eliminating v by Eq. (8), we obtain

$$\xi = h_0^2 \int_0^\theta [e^{2\alpha\phi} \cos\theta/h^3]\; d\theta \tag{10}$$

$$\eta = h_0^2 \int_0^\theta e^{2\alpha\phi} \sin\theta\; d\theta/h^3 \tag{11}$$

$$\tau = h_0 \int_0^\theta e^{\alpha\phi} d\theta/h^2 \tag{12}$$

where $h = \beta - \cos\theta$ and $h_0 = \beta - 1$.

The first step in evaluating the integrals in (10), (11), and (12) is to express them in terms of the functions of the form

$$F_n(\alpha, \theta) = \int_0^\theta e^{\alpha\phi}\, d\theta/h^n$$

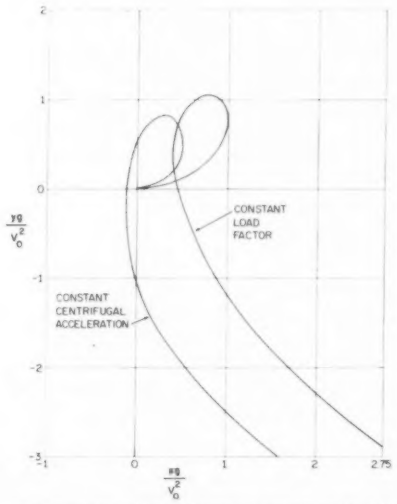

FIG. 2. Comparison of loop flown at constant load factor with loop flown at constant centrifugal acceleration. $\beta = K = 2$; $\alpha = 0.50$.

We then find a recurrence formula for the $F_n(\alpha, \theta)$ by repeated integration by parts, using the relation $d\phi = d\theta/h$. Since $(\cos\theta)/h = (\beta/h) - 1$, Eq. (10) can be written

$$\xi = h_0^2[\beta F_3(2\alpha, \theta) - F_2(2\alpha, \theta)] \tag{13}$$

Now

$$\int_0^\theta e^{2\alpha\phi} \sin\theta\, d\theta/h^3 = \frac{1}{2\alpha}\left[e^{2\alpha\phi} \sin\theta/h^2 - \int_0^\theta e^{2\alpha\phi}\, d\left(\frac{\sin\theta}{h^2}\right)\right]$$

Differentiation of $(\sin\theta)/h^2$ and use of the relation $(\cos\theta)/h = (\beta/h) - 1$ yields, for Eq. (11),

$$\eta = (h_0^2/2\alpha)[e^{2\alpha\phi} \sin\theta/h^2 - F_1(2\alpha, \theta) + 3\beta F_2(2\alpha, \theta) - 2(\beta^2 - 1)F_3(2\alpha, \theta)] \tag{14}$$

and for Eq. (12)

$$\tau = h_0 F_2(\alpha, \theta) \tag{15}$$

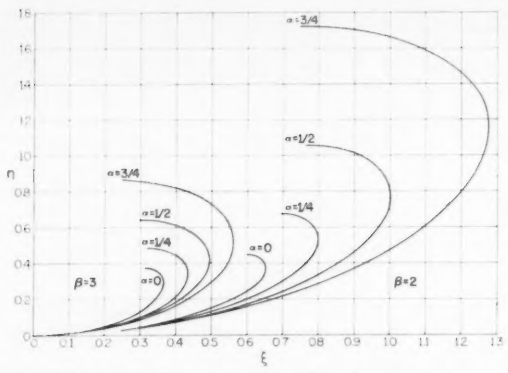

FIG. 3. Flight paths flown at constant load factor β and constant net thrust factor α. $\beta = 2, 3$; $\alpha = 0, 0.25, 0.50, 0.75$.

Consider first the function

$$F_1(\alpha, \theta) = \int_0^\theta e^{\alpha\phi}\, d\theta/h = \int_0^\theta e^{\alpha\phi}\ d\phi$$

This integrates easily to

$$F_1(\alpha, \theta) = (e^{\alpha\phi} - 1)/\alpha \tag{16}$$

The second integral becomes

$$F_2(\alpha, \theta) = \int_0^\theta e^{\alpha\phi}\, d\theta/h^2$$

$$= \frac{1}{\alpha}\left[e^{\alpha\phi}/h - 1/h_0 + \int_0^\theta e^{\alpha\phi} \sin\theta\, d\theta/h^2 \right]$$

$$= \frac{1}{\alpha}\left(e^{\alpha\phi}/h - 1/h_0 \right) + \frac{1}{\alpha^2}\left[e^{\alpha\phi} \sin\theta/h - \int_0^\theta e^{\alpha\phi} d\left(\frac{\sin\theta}{h}\right) \right]$$

Differentiation of $(\sin\theta)/h$ and use of the relation

$$(\cos\theta)/h = (\beta/h) - 1$$

yields

$$F_2(\alpha, \theta) = (1/\alpha)[(e^{\alpha\phi}/h) - (1/h_0)] + (1/\alpha^2)[e^{\alpha\phi} \sin\theta/h + \beta F_1(\alpha, \theta) - (\beta^2 - 1) F_2(\alpha,\theta)]$$

Solving for $F_2(\alpha, \theta)$ we finally obtain

$$F_2(\alpha, \theta) = \left\{ (e^{\alpha\phi}/h)(\alpha + \sin\theta) + \beta F_1(\alpha, \theta) - [\alpha/(\beta - 1)] \right\}/(\alpha^2 + \beta^2 - 1) \tag{17}$$

Similarly,

$$F_3(2\alpha, \theta) = \left\{ (e^{2\alpha\phi}/h^2)(\alpha + \sin\theta) - F_1(2\alpha, \theta) + 3\beta F_2(2\alpha, \theta) - [\alpha/(\beta - 1)^2] \right\}/2(\alpha^2 + \beta^2 - 1) \tag{18}$$

The flight path for which the thrust just balances the drag has special interest because of the simplicity of the formulas. When $\alpha = 0$, then

$$F_1(0, \theta) = \phi$$
$$F_2(0, \theta) = [\sin\theta/(\beta^2 - 1)h] + [\beta\phi/(\beta^2 - 1)]$$
$$\text{and } F_3(0, \theta) = [(\sin\theta/h^2) - \phi + 3\beta F_2(0, \theta)]/2(\beta^2 - 1)$$

Substituting in the relation for ξ and τ we obtain, after some simplification,

$$\xi = \left\{ [\beta(\beta - 1)/h] + [(\beta^2 + 2)/(\beta + 1)] \right\} \sin\theta \; 2(\beta + 1)h + [3\beta\phi/2(\beta + 1)^2] \tag{19}$$

and $$\tau = [\sin\theta/h(\beta + 1)] + [\beta\phi/(\beta + 1)] \tag{20}$$

The expression for η can be found more easily by setting $\alpha = 0$ in Eq. (11). Hence,

$$\eta = h_0^2 \int_0^\theta \sin\theta\, d\theta/h^3 = (1 - h_0^2/h^2)/2 \tag{21}$$

Downward Loop Under Constant Load Factor and Net Thrust Factor

A problem of practical interest is finding the loss in altitude and the increase in velocity for an upside-down airplane righting its position by means of a half loop. This information could be computed from the formulas of the previous sections, but for greater convenience we shall derive new formulas. We integrate Eqs. (7), (10), (11), and (12), replacing the lower limit by π, and h_0 by $\beta + 1$. The velocity is then given by

$$v = v_1[(\beta + 1)/(\beta - \cos\theta)]e^{\alpha\phi_1}$$

$$\text{where } \phi_1 = \frac{2}{\sqrt{\beta^2 - 1}} \tan^{-1}\left[-\sqrt{\frac{\beta - 1}{\beta + 1}} \cot\frac{\theta}{2} \right] \tag{22}$$

and v_1 is the velocity of the airplane at the horizontal upside-down position. The angle ϕ_1 will vary from 0 to $\pi/\sqrt{\beta^2 - 1}$ as θ varies from π to 2π. The relations for ξ, η, and τ are those of Eqs. (13), (14), and (15) except that h_0 is replaced by $\beta + 1$ and the functions $F_n(\alpha, \theta)$ are given by

$$F_n(\alpha, \theta) = \int_\pi^\theta e^{\alpha\phi_1}\, d\theta/h^n$$

with ϕ_1 defined in Eq. (22). Performing the integrations yields the same forms for $F_1(\alpha, \theta)$, $F_2(\alpha, \theta)$, and $F_3(2\alpha, \theta)$ as Eqs. (16), (17), and (18) with ϕ_1 replacing ϕ and $\alpha/(\beta + 1)$ and $\alpha/(\beta + 1)^2$ replacing $\alpha/(\beta - 1)$ and $\alpha/(\beta - 1)^2$, respectively.

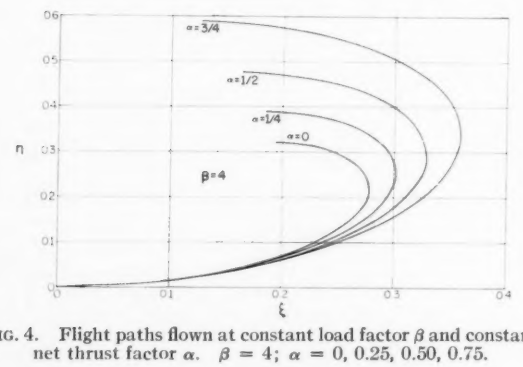

FIG. 4. Flight paths flown at constant load factor β and constant net thrust factor α. $\beta = 4$; $\alpha = 0, 0.25, 0.50, 0.75$.

The altitude lost by an airplane in righting itself is found for $\theta = 2\pi$. Hence

$$\eta = \frac{(\beta+1)^2}{2\alpha}\left[-F_1(2\alpha, 2\pi) + 3\beta F_2(2\alpha, 2\pi) - 2(\beta^2-1)F_3(2\alpha, 2\pi)\right]$$

where

$$F_1(2\alpha, 2\pi) = \frac{e^{2\alpha\pi/\sqrt{\beta^2-1}} - 1}{2\alpha}$$

$$F_2(2\alpha, 2\pi) = \left\{\left[\frac{2\alpha e^{2\alpha\pi/\sqrt{\beta^2-1}}}{(\beta-1)}\right] - \left[\frac{2\alpha}{(\beta+1)}\right] + \beta F_1(2\alpha, 2\pi)\right\}/4\alpha^2 + \beta^2 - 1$$

$$F_3(2\alpha, 2\pi) = \left\{\left[\frac{\alpha e^{2\alpha\pi/\sqrt{\beta^2-1}}}{(\beta-1)^2}\right] - \left[\frac{\alpha}{(\beta+1)^2}\right] - F_1(2\alpha, 2\pi) + 3\beta F_2(2\alpha, 2\pi)\right\}/2(\alpha^2+\beta^2-1)$$

For $\alpha = 0$, the loss in altitude reduces to

$$\eta = -\tfrac{1}{2}\left(\frac{\beta+1}{\beta-1}\right)^2 + \tfrac{1}{2}$$

A graph of altitude loss vs. β is shown in Fig. 1 for $\alpha = 0$, $\tfrac{1}{4}$, and $\tfrac{1}{2}$. The loss in altitude decreases with increasing β and increases with thrust, as we should expect.

(II) Maneuvers With Constant Centrifugal Acceleration and Constant Net Thrust

The Velocity as a Function of Flight-Path Angle

If the centrifugal acceleration is maintained constant during flight, then Eq. (2) becomes

$$v\, d\theta/dt = Kg \tag{23}$$

where K is a dimensionless constant. Eliminating dt from Eq. (4) by means of Eq. (23) yields

$$\int_{v_0}^{v} dv/v = \int_0^{\theta} (\alpha - \sin\theta)d\theta/K$$

Integrating gives

$$v/v_0 = \exp\left\{a\theta/K + (\cos\theta - 1)/K\right\}$$

or

$$v/v_0 = \exp\left\{a\theta + z(\cos\theta - 1)\right\} \tag{24}$$

where $a = \alpha/K$ and $z = 1/K$.

The Time of Flight as a Function of Flight-Path Angle

The time is found by integrating Eq. (23) with v given by Eq. (24). Thus, with $\tau = gt/v_0$, we get

$$\tau = z\int_0^{\theta} \exp\left\{a\theta + z(\cos\theta - 1)\right\} d\theta$$

To evaluate this integral we first expand $e^{z\cos\theta}$ in a Fourier series. Noting that $e^{z\cos\theta}$ is an even function of θ, we have

$$e^{z\cos\theta} = \sum_{n=0}^{\infty} a_n \cos n\theta$$

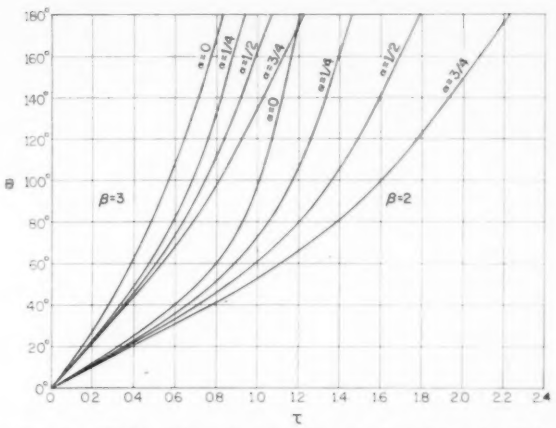

FIG. 5. Flight-path angle θ vs. dimensionless time τ for flight at constant load factor β and constant net thrust factor α. $\beta = 2.3$; $\alpha = 0, 0.25, 0.50, 0.75$.

where

$$a_0 = \frac{1}{\pi}\int_0^{\pi} e^{z\cos\theta}d\theta, \quad a_n = \frac{2}{\pi}\int_0^{\pi} e^{z\cos\theta}\cos n\theta\, d\theta, \; n > 0$$

These integrals can be expressed in terms of Bessel functions of imaginary argument by use of Eq. (4), p. 181, reference 2. Thus

$$a_0 = I_0(z), \qquad a_n = 2I_n(z)$$

The integral then becomes

$$\tau = ze^{-z}\left[I_0(z)\int_0^{\theta} e^{a\theta}\, d\theta + 2\sum_{n=1}^{\infty} I_n(z)\int_0^{\theta} e^{a\theta}\cos n\theta\, d\theta\right]$$

Since the series is absolutely convergent for all finite $K > 1$, we can integrate term by term. Hence,

$$\tau = ze^{-z}\{I_0(z)(e^{a\theta} - 1)/a + 2\sum_{n=1}^{\infty} I_n(z)\left[e^{a\theta}(a\cos n\theta + n\sin n\theta) - a\right](a^2+n^2)\} \tag{25}$$

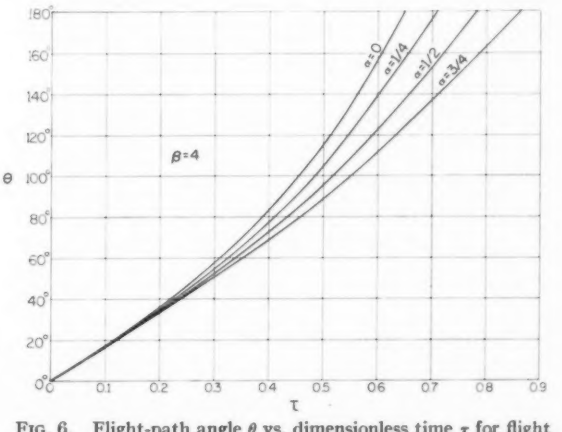

FIG. 6. Flight-path angle θ vs. dimensionless time τ for flight at constant load factor β and constant net thrust factor α. $\beta = 4$; $\alpha = 0, 0.25, 0.50, 0.75$.

TABLE 1

$\phi = (2/\sqrt{\beta^2 - 1}) \tan^{-1}[\sqrt{(\beta + 1)/(\beta - 1)} \tan(\phi/2)]$

θ	$\beta = 2$	$\beta = 3$	$\beta = 4$
0°	.0000000	.00000000	.00000000
10°	.1736561	.08704633	.05807968
20°	.3422650	.1728030	.1155818
30°	.5017389	.2561270	.1719792
40°	.6494999	.3361326	.2268358
50°	.7845022	.41224037	.2798304
60°	.9068986	.4841696	.3307644
70°	1.0176002	.5518939	.3795529
80°	1.1178973	.6155770	.4262086
90°	1.209196	.6755109	.4708197
100°	1.292872	.7320634	.5135302
110°	1.370185	.7856374	.5545199
120°	1.442270	.8366488	.5939929
130°	1.510062	.8854611	.6321304
140°	1.574592	.9326010	.6692512
150°	1.636566	.9783155	.7054765
160°	1.696763	1.023010	.7410589
170°	1.755517	1.067032	.7762137
180°	1.813792	1.110721	.8111558

The Altitude as a Function of Flight-Path Angle

The altitude is found by evaluating

$$\eta = \int_0^\theta (v/v_0) \sin\theta \, (d\tau/d\theta) \, d\theta$$

$$= z \int_0^\theta \exp\{2a\theta + 2z(\cos\theta - 1)\} \sin\theta \, d\theta$$

Integrating by parts, after noting that

$$d(e^{2z(\cos\theta - 1)})/d\theta = -2ze^{2z(\cos\theta - 1)} \sin\theta$$

we obtain

$$\eta = (1/2)\{1 - \exp[2a\theta + 2z(\cos\theta - 1)]\} + a \int_0^\theta \exp[2a\theta + 2z(\cos\theta - 1)] \, d\theta$$

This integral has the same form as the integral for the time τ, with $2z$ and $2a$ replacing z and a respectively. Then, following the same procedure used in evaluating τ leads to

$$\eta = (1/2)[1 - (v/v_0)^2] + e^{-2z}\left\{(1/2)I_1(2z)(e^{2a\theta} - 1) + 2a \sum_{n=1}^{\infty} \frac{I_n(2z)\, e^{2a\theta}(2a \cos n\theta + n \sin\theta) - 2a}{4a^2 + n^2}\right\} \quad (26)$$

The Range as a Function of Flight-Path Angle

Now the horizontal distance or range is given by

$$\xi = \int_0^\theta (v/v_0) \cos\theta (d\tau/d\theta) \, d\theta$$

or

$$\xi = z \int_0^\theta \exp[2a\theta + 2z(\cos\theta - 1)] \cos\theta \, d\theta$$

Using the Bessel expansion of $e^{2z\cos\theta}$, we obtain

$$\xi = ze^{-2z} \int_0^\theta e^{2a\theta}\left\{I_0(2z)\cos\theta + \sum_{n=1}^{\infty} I_n(2z)[\cos(n-1)\theta + \cos(n+1)\theta]\right\} d\theta$$

or combining like cosine terms, we get

$$\xi = ze^{-2z} \int_0^\theta e^{2a\theta}\left\{I_1(2z) + \sum_{n=1}^{\infty} [I_{n-1}(2z) + I_{n+1}(2z)] \cos n\theta\right\} d\theta$$

Finally, integrating term by term yields

$$\xi = ze^{-2z}\left\{(1/2a)I_1(2z)(e^{2a\theta} - 1) + \sum_{n=1}^{\infty} [I_{n-1}(2z) + I_{n+1}(2z)][e^{2a\theta}(2a \cos n\theta + n \sin n\theta) - 2a]/(4a^2 + n^2)\right\} \quad (27)$$

When $K > 1$ ($z < 1$), then the series for ξ, η, and τ converge very rapidly and only a few terms are needed, since

$$I_n(z) \sim z^n/n$$

The calculations of ξ, η, and τ are not as formidable as it might seem, since tables of $I_n(x)$ are given in reference 3. The functions $I_0(x)$ and $I_1(x)$ are also found in reference 2, and higher-order Bessel functions may be computed from the recurrence relation

$$I_{n+1}(x) = I_{n-1}(x) - (2n/x)I_n(x)$$

The Load Factor for a Turn at Constant Centrifugal Acceleration

The equations for the trajectory do not depend explicitly on the load factor β. Under constant centrifugal acceleration the load will vary as a function of θ. This is given by combining Eq. (23) with Eq. (5), which yields

$$\beta - \cos\theta = K$$

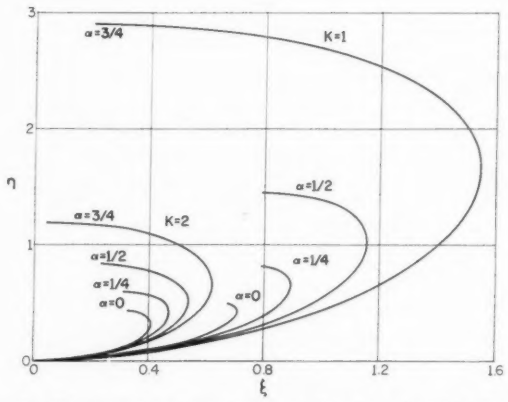

FIG. 7. Flight paths at constant centrifugal acceleration K and constant net thrust factor α $K = 1, 2$; $\alpha = 0, 0.25, 0.50, 0.75$.

or $$L/W = K + \cos\theta \tag{28}$$

The cos θ term gives the influence of gravity. The load factor is seen to vary between the limits of $K - 1$ in the upside-down horizontal position and $K + 1$ in the upright horizontal position.

The Long Climb Under Constant Centrifugal Acceleration

If $K \ll 1$, then the load factor for small angles is slightly larger than unity and the parameters a and z are large. The velocity is then approximated by

$$v/v_0 \cong e^{(a\theta - z\theta^2)/2}$$

$$\cong e^{za^2/2}\, e^{-z(a-\theta)^2/2}$$

sin e we are concerned only with small angles. The time of flight is given by the integration of

$$\tau \cong z e^{za^2/2} \int_0^\theta e^{-z(a-\theta)^2/2}\, d\theta$$

This integral can be expressed in terms of the error function

$$E_2 = \frac{2}{\sqrt{\pi}} \int_0^x e^{-t^2}\, dt$$

and becomes

$$\tau \cong \sqrt{\pi z/2}\; e^{za^2/2}[E_2(\psi_0) \mp E_2(\psi)] \tag{29}$$

where $\psi = (\alpha - \theta)\sqrt{z/2}$ and $\psi_0 = \alpha\sqrt{z/2}$

and the upper sign is taken when $\psi > 0$ and the lower sign when $\psi < 0$.
Similarly,

$$\xi = \int_0^\theta (v/v_0) \cos\theta\, (d\tau/d\theta)\, d\theta$$

$$\cong z e^{za^2} \left[\int_0^\theta e^{-z(a-\theta)^2}\, d\theta - \frac{1}{2} \int_0^\theta \theta^2 e^{-z(a-\theta)^2}\, d\theta \right]$$

$$\cong \sqrt{z}\, e^{za^2} \left[\int_{(a-\theta)\sqrt{z}}^{a\sqrt{z}} e^{-t^2}\, dt - \frac{1}{2} \int_{(a-\theta)\sqrt{z}}^{a\sqrt{z}} e^{-t^2} (a - t/\sqrt{z})^2\, dt \right]$$

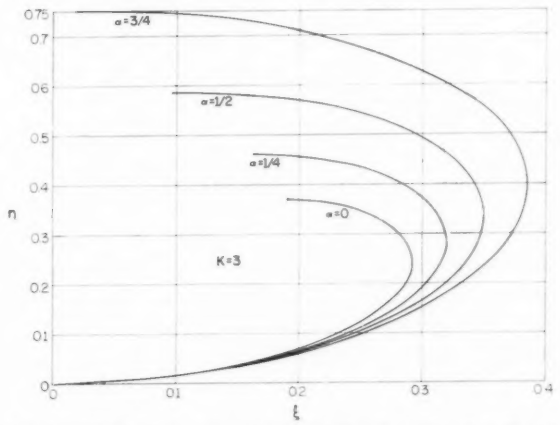

FIG. 8. Flight paths at constant centrifugal acceleration K and constant net thrust factor α. $K = 3$; $\alpha = 0, 0.25, 0.50, 0.75$.

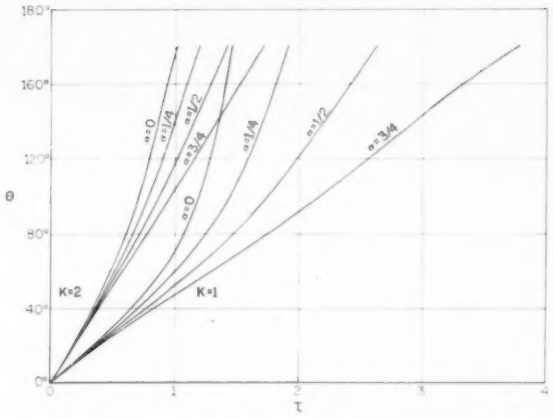

FIG. 9. Flight-path angle θ vs. dimensionless time τ for flight paths at constant centrifugal acceleration K and constant net thrust factor α. $K = 1, 2$; $\alpha = 0, 0.25, 0.50, 0.75$.

Integrating yields

$$\xi \cong \sqrt{z}\, e^{za^2} [1 - (a^2/2) - (1/4z)] \times [E(\sqrt{2}\psi_0) \mp E(\sqrt{2}\psi)] + (1/4)(\alpha + \theta) e^{z(2a\theta - \theta^2)} - (\alpha/4) \tag{30}$$

Also,

$$\eta \cong \int_0^\theta (v/v_0)\, \theta\, (d\tau/d\theta)\, d\theta$$

$$\cong z\, e^{za^2} \left[\int_{(a-\theta)\sqrt{z}}^{a\sqrt{z}} e^{-t^2} (a - t/\sqrt{z})\, dt \right]$$

$$\cong a\sqrt{z}\, e^{za^2} [E(\sqrt{2}\,\psi_0) \mp E(\sqrt{2}\,\psi) + (1 - e^{z(2a\theta - \theta^2)})/2 \tag{31}$$

These formulas are more amenable to calculation than the series of Bessel functions since they contain fewer terms and good tables of the error function are readily available (see reference 4, for example).

(III) Flight Path With Constant Velocity and Constant Load Factor

We shall now consider the maneuver with the velocity maintained constant. This is a realistic flight for a high-powered airplane over a limited portion of an upward loop, and for an airplane with speed brakes over a limited portion of downward loop, or for a transport plane which can use spoilers and extend its landing gear.

The assumption of constant velocity leads to a relation for the difference between thrust and drag in terms of the flight-path angle. From Eqs. (1) or (4) we have

$$(T - D)/W = \sin\theta$$

Eq. (5) becomes

$$g\, dt/v_0 = d\theta/(\beta - \cos\theta)$$

If β is assumed to be constant also, then for initial level flight this integrates to

$$\tau = \phi \tag{32}$$

TABLE 2

Flight paths for constant load factor β and constant net thrust factor α

($\beta = 2$; $\alpha = 0, 0.25, 0.50, 0.75$)

	$\beta=2,\ \alpha=0$				$\beta=2,\ \alpha=0.25$			
θ	ξ	η	τ	V/V_0	ξ	η	τ	V/V_0
0°	0.000	0.000	0.000	1.000	.00000	.00000	.00000	1.0000
10°	0.189	0.015	0.172	.992	.17865	.01574	.17658	1.0288
20°	0.322	0.055	0.335	.972	.35141	.06190	.35033	1.0274
30°	0.444	0.111	0.462	.943	.50044	.13107	.51230	.9996
40°	0.532	0.171	0.609	.910	.61630	.21175	.65681	.9532
50°	0.589	0.228	0.712	.879	.69831	.29325	.78180	.8964
60°	0.623	0.278	0.801	.850	.75129	.36835	.88791	.8363
70°	0.643	0.322	0.869	.823	.78199	.43357	.97728	.7779
80°	0.649	0.351	0.926	.806	.79680	.48811	1.05260	.7241
90°	0.653	0.375	0.973	.791	.80085	.53264	1.11652	.6765
100°	0.652	0.394	1.015	.778	.79782	.56846	1.17133	.6356
110°	0.646	0.409	1.047	.769	.79026	.59699	1.21918	.6014
120°	0.641	0.420	1.079	.762	.77982	.61951	1.26151	.5737
130°	0.635	0.429	1.103	.756	.76804	.63687	1.29980	.5519
140°	0.629	0.435	1.128	.752	.75409	.65057	1.33469	.5359
150°	0.623	0.439	1.148	.749	.73988	.66056	1.36757	.5253
160°	0.617	0.442	1.169	.747	.72515	.66751	1.39906	.5199
170°	0.610	0.444	1.193	.746	.70974	.67160	1.42951	.5196
180°	0.601	0.445	1.210	.745	.69396	.67297	1.45991	.5246

	$\beta=2,\ \alpha=0.50$				$\beta=2,\ \alpha=0.75$			
θ	ξ	η	τ	V/V_0	ξ	η	τ	V/V_0
0°	.00000	.00000	.00000	1.0000	.00000	.00000	.00000	1.0000
10°	.18669	.01668	.18049	1.0744	.19522	.01769	.18451	1.1220
20°	.38323	.06946	.36583	1.1191	.41893	.07806	.38224	1.2192
30°	.56714	.15508	.54581	1.1333	.64602	.18411	.58227	1.2847
40°	.72148	.26280	.71267	1.1213	.85169	.32798	.77497	1.3190
50°	.83868	.37948	.86219	1.0908	1.01924	.49512	.95383	1.3271
60°	.91939	.49412	.99326	1.0492	1.14225	.67017	1.11575	1.3162
70°	.96894	.59963	1.10692	1.0032	1.22227	.84088	1.26031	1.2938
80°	.99413	.69261	1.20527	.9575	1.26510	.99945	1.38874	1.2663
90°	1.00131	.77225	1.29075	.9153	1.27784	1.14191	1.50308	1.2383
100°	.99562	.83918	1.36577	.8781	1.26713	1.26698	1.60563	1.2133
110°	.98088	.89467	1.43243	.8471	1.23838	1.37493	1.69862	1.1932
120°	.95977	.94015	1.49259	.8227	1.19570	1.46677	1.78411	1.1799
130°	.93522	.97669	1.54802	.8051	1.14421	1.54358	1.86434	1.1743
140°	.90498	1.00602	1.59928	.7945	1.07901	1.60653	1.93967	1.1776
150°	.87325	1.02833	1.64839	.7909	1.00815	1.65630	2.01304	1.1906
160°	.83929	1.04435	1.69616	.7946	.92987	1.69316	2.08549	1.2144
170°	.80283	1.05397	1.74305	.8060	.84355	1.71590	2.15770	1.2499
180°	.76431	1.05731	1.79054	.8255	.74951	1.72402	2.23190	1.2991

where ϕ is defined in Eq. (9). The position coordinates are obtained by integrating

$$dx = v_0 \cos\theta\, dt = v_0^2 \cos\theta\, d\theta/g(\beta - \cos\theta)$$

and $$dy = v_0 \sin\theta\, dt = v_0^2 \sin\theta\, d\theta/g(\beta - \cos\theta)$$

Introducing dimensionless variables and integrating leads to

$$\xi = \phi - \theta \tag{33}$$

$$\eta = \log(h/h_0) \tag{34}$$

(IV) Maneuvers With Constant Angular Velocity and Net Thrust Factor

If the airplane follows a path with constant angular velocity, then the assumption of constant net thrust factor leads to simple formulas for the velocity, coordinates, and time along the flight path. Let $d\theta/dt = \omega$, a constant, then $\theta = \omega t$ and

$$dv/dt = g(\alpha - \sin\omega t) \tag{35}$$

$$v\omega = g(\beta - \cos\omega t) \tag{36}$$

The first equation can be integrated to give

$$v = v_0 + g\left[\alpha t - \frac{\cos \omega t - 1}{\omega}\right] \tag{37}$$

or, in dimensionless form,

$$v/v_0 = 1 + \sigma + \alpha\sigma\theta - \sigma \cos \theta \tag{38}$$

where $\sigma = g/v_0\omega$ is the ratio of the acceleration of gravity to the initial angular acceleration. With Eq. (37), Eq. (36) gives a relation for the load factor β as a function of time, net thrust factor, angular velocity, and initial speed. The coordinates are

$$x = \int_0^t v \cos \omega t \, dt, \qquad y = \int_0^t v \sin \omega t \, dt$$

which integrate to

$$x = (1/\omega)(v_0 + g/\omega + g\alpha t) \sin \omega t + (g\alpha/\omega^2)(\cos \omega t - 1) - (g/2\omega)t - (g/4\omega^2) \sin 2\omega t$$

$$y = (1/\omega)(v_0 + g/\omega + g\alpha t)(1 - \cos \omega t) + (g\alpha/\omega^2) \sin \omega t - (g/2\omega^2) \sin^2 \omega t$$

When the net thrust factor is zero, then v and y are periodic. The coordinate x has, in addition to its periodic component, a translation term $-gt/2\omega$. In

TABLE 3

Flight paths for constant load factor β and constant net thrust factor α

($\beta = 3$; $\alpha = 0, 0.25, 0.50, 0.75$)

	$\beta = 3$, $\alpha = 0$				$\beta = 3$, $\alpha = 0.25$			
θ	ξ	η	τ	V/V_0	ξ	η	τ	V/V_0
0°	0.000	0.000	0.000	1.000	.00000	.00000	.00000	1.0000
10°	0.082	0.007	0.073	.996	.08807	.00773	.08778	1.0143
20°	0.156	0.029	0.145	.985	.17333	.03055	.17483	1.0135
30°	0.221	0.060	0.213	.970	.24992	.06617	.25878	.9992
40°	0.272	0.099	0.276	.949	.31379	.11077	.33778	.9737
50°	0.311	0.140	0.336	.927	.36320	.15999	.41067	.9406
60°	0.337	0.180	0.391	.906	.39835	.20997	.47700	.9029
70°	0.354	0.217	0.442	.885	.42077	.25779	.53684	.8638
80°	0.362	0.250	0.487	.866	.43261	.30160	.59063	.8254
90°	0.364	0.278	0.528	.850	.43610	.34045	.63901	.7893
100°	0.364	0.301	0.571	.836	.43323	.37407	.68272	.7567
110°	0.360	0.321	0.605	.824	.42565	.40257	.72249	.7283
120°	0.355	0.337	0.642	.814	.41465	.42626	.75902	.7044
130°	0.349	0.350	0.675	.806	.40143	.44523	.79297	.6851
140°	0.345	0.359	0.720	.801	.38598	.46084	.82485	.6705
150°	0.335	0.366	0.765	.796	.36939	.47244	.85526	.6607
160°	0.328	0.371	0.772	.793	.35189	.48061	.88465	.6556
170°	0.320	0.374	0.801	.791	.33367	.48550	.91349	.6554
180°	0.313	0.375	0.833	.791	.31489	.48714	.94221	.6601

	$\beta = 3$, $\alpha = 0.50$				$\beta = 3$, $\alpha = 0.75$			
θ	ξ	η	τ	V/V_0	ξ	η	τ	V/V_0
0°	.00000	.00000	.00000	1.0000	.00000	.00000	.00000	1.0000
10°	.09001	.00796	.08874	1.0366	.09202	.00820	.08972	1.0594
20°	.18099	.03237	.17867	1.0583	.18911	.03431	.18263	1.1051
30°	.26622	.07208	.26724	1.0653	.28397	.07857	.27608	1.1357
40°	.34026	.12382	.35231	1.0592	.36979	.13863	.36768	1.1519
50°	.39978	.18320	.43235	1.0427	.44152	.21026	.45557	1.1559
60°	.44372	.24574	.50654	1.0191	.49644	.28854	.53856	1.1502
70°	.47274	.30770	.57465	.9915	.53400	.36882	.61608	1.1382
80°	.48856	.36635	.63689	.9626	.55515	.44735	.68809	1.1228
90°	.49335	.42000	.69374	.9346	.56173	.52144	.75490	1.1064
100°	.48925	.46779	.74586	.9087	.55587	.58938	.81704	1.0912
110°	.47816	.50943	.79393	.8864	.53964	.65021	.87516	1.0787
120°	.46164	.54496	.83867	.8682	.51485	.70351	.92995	1.0702
130°	.44139	.57420	.88079	.8548	.48377	.74860	.98221	1.0666
140°	.41689	.59869	.92078	.8466	.44509	.78702	1.03239	1.0689
150°	.39021	.61739	.95940	.8438	.40206	.81715	1.08142	1.0775
160°	.36135	.63085	.99715	.8467	.35445	.83934	1.12991	1.0934
170°	.33062	.63908	1.03460	.8557	.30262	.85321	1.17854	1.1173
180°	.29825	.64190	1.07230	.8713	.24682	.85804	1.22803	1.1501

dimensionless variables ξ, η, σ, and θ, the coordinates become

$$\xi = \sigma(1 + \sigma + \alpha\sigma\theta) \sin\theta + \alpha\sigma^2(\cos\theta - 1) - (\sigma^2/2)\theta - (\sigma^2/2) \sin 2\theta \quad (39)$$

$$\eta = \sigma(1 + \sigma + \alpha\sigma\theta)(1 - \cos\theta) + \alpha\sigma^2 \sin\theta - \sigma^2 \sin^2\theta \quad (40)$$

(V) Discussion of the Numerical Calculations and the Application of the Tables for Calculating More General Flight Paths

A comparison of the loop flown at constant load factor and net thrust factor with a loop flown at constant centrifugal acceleration and net thrust factor is provided in Fig. 2. The values of the parameters chosen for this figure are $\beta = K = 2$ and $\alpha = 1/2$. The path of constant centrifugal acceleration has greater lift in the flight path angles of 0° to 90° and 270° to 360° than the flight path of constant load factor, and less lift in the angles 90° to 270°. The evidence of this difference is easily seen in the two loops of Fig. 2. The loop with constant centrifugal acceleration covers less altitude and range than the loop with constant load factor. Level flight is attained at $\xi = 7.0$ and $\eta = -5.4$ for the constant centrifugal acceleration loop and at $\xi = 17.6$ and $\eta = -7.0$ for the constant load factor loop.

TABLE 4

Flight paths for constant load factor β and constant net thrust factor α

($\beta = 4$; $\alpha = 0, 0.25, 0.50, 0.75$)

	$\beta=4,\ \alpha=0$				$\beta=4,\ \alpha=0.25$			
θ	ξ	η	τ	V/V_0	ξ	η	τ	V/V_0
0°	0.000	0.000	0.000	1.000	.00000	.00000	.00000	1.0000
10°	0.058	0.005	0.048	.997	.04276	.00565	.05840	1.0095
20°	0.112	0.019	0.115	.990	.11503	.02028	.11649	1.0090
30°	0.160	0.042	0.170	.979	.16660	.04428	.17316	.9993
40°	0.200	0.070	0.222	.964	.21072	.07511	.22753	.9817
50°	0.231	0.101	0.270	.948	.24602	.11032	.27897	.9584
60°	0.254	0.133	0.315	.931	.27213	.14750	.32710	.9310
70°	0.268	0.166	0.356	.913	.28949	.18458	.37182	.9017
80°	0.276	0.194	0.393	.898	.29904	.21998	.41321	.8722
90°	0.278	0.219	0.428	.884	.30195	.25265	.45148	.8437
100°	0.275	0.242	0.457	.871	.29943	.28195	.48694	.8173
110°	0.271	0.261	0.487	.860	.29260	.30761	.51995	.7937
120°	0.261	0.278	0.512	.850	.28241	.32955	.55087	.7734
130°	0.254	0.291	0.547	.842	.26979	.34750	.58006	.7568
140°	0.243	0.302	0.563	.835	.25491	.36258	.60788	.7441
150°	0.231	0.310	0.593	.831	.23871	.37393	.63467	.7355
160°	0.220	0.316	0.608	.827	.22142	.38201	.66075	.7310
170°	0.207	0.319	0.629	.825	.20332	.38686	.68643	.7307
180°	0.194	0.320	0.650	.825	.18467	.38849	.71202	.7349

	$\beta=4,\ \alpha=0.50$				$\beta=4,\ \alpha=0.75$			
θ	ξ	η	τ	V/V_0	ξ	η	τ	V/V_0
0°	.00000	.00000	.00000	1.0000	.00000	.00000	.00000	1.0000
10°	.05929	.00522	.05883	1.0242	.06016	.00533	.05926	1.0393
20°	.11840	.02107	.11819	1.0386	.12189	.02191	.11992	1.0691
30°	.17380	.04689	.17694	1.0432	.18142	.04968	.18082	1.0891
40°	.22253	.08097	.23409	1.0391	.23524	.08735	.24089	1.0996
50°	.26257	.12095	.28888	1.0278	.28068	.13274	.29927	1.1023
60°	.29298	.16427	.34083	1.0113	.31607	.18322	.35534	1.0985
70°	.31369	.20855	.38970	.9915	.34080	.23611	.40875	1.0903
80°	.32535	.25186	.43547	.9702	.35504	.28908	.45937	1.0794
90°	.32898	.29273	.47829	.9491	.35957	.34023	.50726	1.0676
100°	.32575	.33021	.51839	.9293	.35542	.38816	.55262	1.0565
110°	.31682	.36371	.55612	.9117	.34374	.43191	.59573	1.0472
120°	.30322	.39294	.59181	.8972	.32561	.47085	.63693	1.0409
130°	.28614	.41735	.62584	.8864	.30246	.50408	.67661	1.0381
140°	.26547	.43819	.65857	.8796	.27378	.53284	.71511	1.0398
150°	.24263	.45419	.69038	.8773	.24156	.55541	.75289	1.0465
160°	.21780	.46578	.72162	.8797	.20591	.57203	.79032	1.0587
170°	.19135	.47286	.75267	.8872	.16726	.58237	.82785	1.0773
180°	.16362	.47528	.78388	.9001	.12601	.58595	.86591	1.1025

TABLE 5

Flight paths for constant centrifugal acceleration K and net thrust factor α

($K = 1$; $\alpha = 0, 0.25, 0.50, 0.75$)

	$K = 1$, $\alpha = 0$				$K = 1$, $\alpha = 0.25$			
θ	τ	ξ	η	V/V_0	τ	ξ	η	V/V_0
0°	.0000	.0000	.0000	1.0000	.0000	.0000	.0000	1.0000
10°	.1734	.1718	.0150	.9700	.1775	.1796	.0158	1.0288
20°	.3418	.3289	.0568	.8864	.3573	.3515	.0618	1.0272
30°	.5003	.4599	.1176	.7649	.5344	.5212	.1394	0.9970
40°	.6460	.5595	.1869	.6263	.7040	.6560	.2337	0.9423
50°	.7762	.6284	.2552	.4895	.8624	.7579	.3349	0.8703
60°	.8902	.6713	.3161	.3679	1.0075	.8268	.4330	0.7880
70°	.9883	.6948	.3657	.2682	1.1373	.8684	.5206	0.7029
80°	1.0717	.7053	.4043	.1915	1.2528	.8883	.5943	0.6203
90°	1.1420	.7078	.4324	.1353	1.3542	.8936	.6533	0.5449
100°	1.2011	.7062	.4522	.0956	1.4433	.8900	.6988	0.4784
110°	1.2509	.7027	.4659	2.0683	1.5218	.8808	.7331	0.4224
120°	1.2932	.6984	.4751	.0498	1.5913	.8692	.7581	0.3766
130°	1.3295	.6941	.4813	.0374	1.6537	.8564	.7764	0.3412
140°	1.3612	.6900	.4854	.0292	1.7112	.8434	.7892	0.3149
150°	1.3895	.6864	.4881	.0239	1.7642	.8298	.7989	0.2978
160°	1.4152	.6828	.4897	4.0207	1.8151	.8161	.8053	0.2889
170°	1.4397	.6795	.4906	8.0189	1.8658	.8021	.8090	0.2885
180°	1.4632	.6763	.4909	.0183	1.9027	.7877	.8104	0.2968

	$K = 1$, $\alpha = 0.50$				$K = 1$, $\alpha = 0.75$			
θ	τ	ξ	η	V/V_0	τ	ξ	η	V/V_0
0°	.0000	.0000	.0000	1.0000	.0000	.0000	.0000	1.0000
10°	.1813	.1878	.0167	1.0747	.1854	.1962	.0179	1.1228
20°	.3733	.3916	.0717	1.1211	.3906	.4289	.0806	1.2232
30°	.5709	.5937	.1662	1.1364	.6109	.6793	.1979	1.2953
40°	.7686	.7765	.2941	1.1219	.8348	.9280	.3725	1.3359
50°	.9611	.9271	.4425	1.0824	1.0752	1.1504	.5950	1.3463
60°	1.1452	1.0385	.6023	1.0239	1.3093	1.3298	.8513	1.3303
70°	1.3177	1.1107	.7569	0.9539	1.5386	1.4575	1.1242	1.2948
80°	1.4778	1.1494	.8987	0.8797	1.7644	1.5308	1.3966	1.2470
90°	1.6249	1.1603	1.0224	0.8069	1.9733	1.5522	1.6533	1.1949
100°	1.7597	1.1514	1.1265	0.7401	2.1829	1.5338	1.8926	1.1451
110°	1.8838	1.1288	1.2118	0.6824	2.3739	1.4776	2.1045	1.1029
120°	1.9987	1.0970	1.2801	0.6358	2.5636	1.3912	2.2905	1.0743
130°	2.1067	1.0594	1.3338	0.6014	2.7495	1.2780	2.4529	1.0615
140°	2.2094	1.0170	1.3765	0.5814	2.9351	1.1383	2.5957	1.0689
150°	2.3099	.9693	1.4096	0.5729	3.1243	.9674	2.7078	1.0806
160°	2.4103	.9156	1.4340	0.5806	3.3216	.7636	2.8072	1.1673
170°	2.5133	.8568	1.4501	0.6058	3.5338	.5156	2.8722	1.2719
180°	2.6228	.7897	1.4565	0.6511	3.7685	.2055	2.9039	1.4641

Graphs of the half loop—the flight-path angle range 0° to 180°—are shown in Figs. 3 and 4 for constant load factor and in Figs. 7 and 8 for constant centrifugal acceleration. The dimensionless times for these flight paths are shown in Figs. 5 and 6 and 9 and 10. The tabulations of the variables ϕ, ξ, η, τ, v/v_0 for values of the net thrust factor $\alpha = 0$, $1/4$, $1/2$, $3/4$ and for $\beta = 2, 3, 4$ and $K = 1, 2, 3$ are provided in Tables 1–7. The data for ξ, η, τ for the constant-velocity climb with constant load factors of $\beta = 2, 3, 4$ are given in Table 8 and plotted in Figs. 11 and 12 for $0 \leq \theta \leq 90°$.

More complicated flight paths may be estimated by use of these tables. For example, if the load factor must vary throughout a maneuver, an approximation to the true flight path may be found by considering the load factor to vary in a sequence of step functions approximating the true variation. By maintaining the velocity and angle continuous at each point of discontinuity of the load factor, we find the correct value of v_0 to use in determining the actual velocity and coordinates from the dimensionless variables v/v_0, $\Delta\xi$, and $\Delta\eta$ along the flight path. To illustrate the method of computing the coordinates, we assume that the aircraft flies at $\alpha = 1/4$ and $\beta = 2$ for $\theta = 0°$ to 20° and at $\alpha = 1/4$, $\beta = 3$ from 20° to 30°. Let the initial velocity be 100 mph; then we see from Table 2 that

TABLE 6

Flight paths for constant centrifugal acceleration K and net thrust factor α

($K = 2$; $\alpha = 0, 0.25, 0.50, 0.75$)

	$K=2,\ \alpha=0$				$K=2,\ \alpha=0.25$			
θ	τ	ξ	η	V/V_0	τ	ξ	η	V/V_0
0°	0.0000	0.0000	0.0000	1.0000	.0000	0.0000	.0000	1.0000
10°	0.0871	0.0864	0.0076	0.9924	.0876	0.0875	.0078	1.0143
20°	0.1728	0.1677	0.0285	0.9702	.1918	0.1738	.0343	1.0135
30°	0.2560	0.2396	0.0752	0.9352	.2640	0.2543	.0683	.9985
40°	0.3357	0.2993	0.1043	0.8896	.3501	0.3244	.1169	.9707
50°	0.4111	0.3451	0.1502	0.8364	.4335	0.3815	.1728	.9329
60°	0.4816	0.3780	0.1968	0.7788	.5097	0.4234	.2319	.8877
70°	0.5469	0.3997	0.2411	0.7196	.5850	0.4510	.2907	.8384
80°	0.6071	0.4096	0.2812	0.6615	.6599	0.4654	.3465	.7876
90°	0.6625	0.4128	0.3160	0.6066	.7268	0.4690	.3969	.7382
100°	0.7131	0.4102	0.3454	0.5561	.7888	0.4649	.4413	.6917
110°	0.7597	0.4040	0.3694	0.5112	.8473	0.4541	.4791	.6499
120°	0.8026	0.3950	0.3884	0.4724	.9023	0.4439	.5106	.6137
130°	0.8424	0.3847	0.4033	0.4398	.9542	0.4225	.5361	.5841
140°	0.8796	0.3735	0.4145	0.4135	1.0031	0.4036	.5563	.5612
150°	0.9147	0.3620	0.4226	0.3934	1.0516	0.3824	.5715	.5457
160°	0.9484	0.3503	0.4282	0.3791	1.0972	0.3595	.5824	.5375
170°	0.9811	0.3384	0.4313	0.3707	1.1458	0.3348	.5889	.5371
180°	1.0132	0.3266	0.4323	0.3679	1.1935	0.3082	.5911	.5448

	$K=2,\ \alpha=0.50$				$K=2,\ \alpha=0.75$			
θ	τ	ξ	η	V/V_0	τ	ξ	η	V/V_0
0°	0.0000	0.0000	0.0000	1.0000	0.0000	0.0000	0.0000	1.0000
10°	0.0889	0.0902	0.0073	1.0367	0.0899	**0.0923**	0.0081	1.0596
20°	0.1805	0.1783	0.0311	1.0588	0.1844	0.1912	0.0349	1.1060
30°	0.2733	0.2723	0.0746	1.0660	0.2824	0.2908	0.0818	1.1381
40°	0.3660	0.3532	0.1312	1.0592	0.3826	0.3812	0.1450	1.1558
50°	0.4578	0.4212	0.1992	1.0404	0.4839	0.4679	0.2301	1.1603
60°	0.5474	0.4740	0.2743	1.0119	0.5850	0.5347	0.3289	1.1534
70°	0.6343	0.5104	0.3526	0.9767	0.6851	0.5831	0.4296	1.1379
80°	0.7179	0.5309	0.4296	0.9379	0.7835	0.6142	0.5382	1.1167
90°	0.7979	0.5375	0.5027	0.8983	0.8885	0.6199	0.6423	1.0931
100°	0.8746	0.5318	0.5700	0.8603	0.9743	0.6153	0.7460	1.0701
110°	0.9482	0.5160	0.6297	0.8261	1.0669	0.5876	0.8387	1.0502
120°	1.0189	0.4922	0.6811	0.7974	1.1577	0.5470	0.9242	1.0365
130°	1.0873	0.4611	0.7257	0.7755	1.2478	0.4943	1.0004	1.0303
140°	1.1547	0.4246	0.7612	0.7625	1.3544	0.4288	1.0664	1.0339
150°	1.2208	0.3833	0.7907	0.7569	1.4282	0.3516	1.1315	1.0395
160°	1.2868	0.3376	0.8121	0.7620	1.5215	0.2628	1.1626	1.0804
170°	1.3542	0.2879	0.8252	0.7783	1.6176	0.1594	1.1891	1.1278
180°	1.4238	0.2338	0.8304	0.8069	1.7188	0.0426	1.1924	1.2100

for $\theta = 20°$

$$v/v_0 = 1.0274$$

or $v = 102.74$ mph. For $\beta = 3$, $\alpha = 1/4$, and $\theta = 20°$ (Table 3),

$$v/v_0 = 1.0135$$

Since these two values of v must agree, we choose $v_0 = 101.37$ for the $\beta = 3$ portion of the flight path. The position coordinates for $\theta = 20°$ from Table 2 are

$$\xi = 0.35141 \quad \text{and} \quad \eta = 0.06190$$

Since $v_0 = 100$ mph or 146.7 ft/sec, then

$$x = \frac{(146.7)^2(0.35141)}{(32.16)} = 235.2 \text{ ft}$$

$$y = 41.4 \text{ ft}$$

From Table 3 for $\beta = 3$ we find that the increments of the coordinates for $\theta = 20°$ to $\theta = 30°$ are

$$\Delta\xi = 0.24992 - 0.17333 = 0.07659$$
$$\Delta\eta = 0.06617 - 0.03055 = 0.03562$$

From this, we obtain

$$\Delta x = \frac{(148.7)^2(0.07659)}{(32.16)} = 52.7 \text{ ft}$$

$$\Delta y = 24.5 \text{ ft}$$

The coordinates at $\theta = 30°$ then become

$$x = 287.9 \text{ ft} \qquad y = 65.9 \text{ ft}$$

For ease in calculating the example, values of β were chosen such that the tables could be used directly. Solutions for intermediate values of β could be found by graphical or polynomial interpolation of the tabulated values. Lagrange's interpolation formula for the polynomial which passes through the three points (x_1, y_1), (x_2, y_2), and (x_3, y_3) is

$$y(x) = y_1L_1(x) + y_2L_2(x) + y_3L_3(x)$$

where

$$L_1 = (x - x_2)(x - x_3)/(x_1 - x_2)(x_1 - x_3)$$
$$L_2 = (x - x_1)(x - x_3)/(x_2 - x_1)(x_2 - x_3)$$
$$L_3 = (x - x_1)(x - x_2)/(x_3 - x_1)(x_3 - x_2)$$

For interpolating the three tables of $\eta(\theta)$ for $\beta = 2$, 3, and 4 we obtain

$$\eta(\theta,\beta) = \eta(\theta)|_{\beta\text{-}2}\,(1/2)(\beta - 3)(\beta - 4) - \eta(\theta)|_{\beta\text{-}3}(\beta - 2)(\beta - 4) + \eta(\theta)|_{\beta\text{-}4}\,(1/2)(\beta - 2)(\beta - 3)$$

The other variables can be interpolated by similar relations.

TABLE 7

Flight paths for constant centrifugal acceleration K and net thrust factor α

($K = 3$; $\alpha = 0, 0.25, 0.50, 0.75$)

	$K=3,\ \alpha=0$				$K=3,\ \alpha=0.25$			
θ	τ	ξ	η	V/V_0	τ	ξ	η	V/V_0
0°	.0000	.0000	.0000	1.0000	.0000	.0000	.0000	1.0000
10°	.0582	.0577	.0051	.9949	.0592	.0585	.0051	1.0095
20°	.1157	.1126	.0197	.9801	.1181	.1160	.0204	1.0091
30°	.1721	.1621	.0428	.9563	.1775	.1691	.0454	.9989
40°	.2269	.2044	.0722	.9250	.2352	.2160	.0778	.9804
50°	.2798	.2383	.1060	.8877	.2910	.2546	.1165	.9547
60°	.3303	.2634	.1417	.8465	.3453	.2839	.1586	.9237
70°	.3781	.2800	.1775	.8031	.3976	.3042	.2010	.8891
80°	.4237	.2893	.2118	.7592	.4479	.3156	.2444	.8529
90°	.4666	.2922	.2433	.7165	.4966	.3207	.2846	.8168
100°	.5071	.2898	.2714	.6762	.5416	.3160	.3218	.7821
110°	.5452	.2833	.2957	.6393	.5883	.3072	.3544	.7503
120°	.5815	.2737	.3160	.6066	.6321	.2940	.3830	.7222
130°	.6160	.2622	.3328	.5783	.6745	.2685	.4070	.6987
140°	.6489	.2489	.3460	.5550	.7151	.2578	.4266	.6804
150°	.6806	.2348	.3559	.5369	.7547	.2377	.4417	.6678
160°	.7115	.2199	.3628	.5238	.7937	.2128	.4526	.6611
170°	.7418	.2048	.3669	.5160	.8310	.1883	.4593	.6607
180°	.7718	.1895	.3682	.5134	.8694	.1633	.4616	.6670

	$K=3,\ \alpha=0.50$				$K=3,\ \alpha=0.75$			
θ	τ	ξ	η	V/V_0	τ	ξ	η	V/V_0
0°	.0000	.0000	.0000	1.0000	.0000	.0000	.0000	1.0000
10°	.0587	.0594	.0053	1.0242	.0615	.0603	.0054	1.0393
20°	.1191	.1194	.0215	1.0386	.1247	.1228	.0222	1.0695
30°	.1798	.1765	.0480	1.0435	.1971	.1845	.0511	1.0900
40°	.2405	.2282	.0862	1.0371	.2552	.2419	.0912	1.1013
50°	.3007	.2722	.1280	1.0268	.3210	.2916	.1412	1.1042
60°	.3598	.3069	.1774	1.0079	.3863	.3321	.1991	1.0998
70°	.4177	.3319	.2297	.9844	.4509	.3617	.2623	1.0899
80°	.4743	.3454	.2827	.9581	.5145	.3793	.3280	1.0764
90°	.5294	.3499	.3343	.9310	.5769	.3852	.3941	1.0612
100°	.5826	.3457	.3831	.9046	.6379	.3796	.4585	1.0461
110°	.6372	.3338	.4279	.8804	.6980	.3636	.5188	1.0332
120°	.6853	.3153	.4675	.8599	.7569	.3376	.5742	1.0239
130°	.7350	.2912	.5022	.8441	.8153	.3027	.6249	1.0195
140°	.7838	.2624	.5312	.8341	.8734	.2598	.6672	1.0225
150°	.8321	.2295	.5550	.8297	.9315	.2094	.7026	1.0330
160°	.8805	.1930	.5711	.8345	.9904	.1520	.7318	1.0505
170°	.9294	.1532	.5815	.8463	1.0509	.0881	.7463	1.0835
180°	.9793	.0951	.5853	.8667	1.1132	.0178	.7535	1.1260

TABLE 8

Flight paths for constant velocity and constant load factor

(β = 2, 3, 4)

	$\beta=2$			$\beta=3$			$\beta=4$		
θ	ξ	η	τ	ξ	η	τ	ξ	η	τ
0°	0.0000	0.0000	0.0000	0.0000	0.0000	0.0000	0.0000	0.0000	0.000
10°	0.1745	0.0151	0.3490	0.0885	0.0086	0.263	0.0595	0.0050	0.234
20°	0.3369	0.0586	0.686	0.1699	0.0298	0.519	0.1169	0.0199	0.466
30°	0.4814	0.1258	1.005	0.2464	0.0649	0.770	0.1674	0.0437	0.691
40°	0.6029	0.2103	1.301	0.3109	0.1107	1.009	0.2129	0.0751	0.911
50°	0.6985	0.3054	1.572	0.3633	0.1643	1.236	0.2493	0.1125	1.122
60°	0.7778	0.4055	1.825	0.4088	0.2231	1.456	0.2798	0.1542	1.327
70°	0.8163	0.5056	2.038	0.4313	0.2844	1.653	0.3023	0.1983	1.524
80°	0.8447	0.6024	2.241	0.4497	0.3459	1.846	0.3127	0.2433	1.709
90°	0.8472	0.6932	2.418	0.4552	0.4055	2.026	0.3152	0.2877	1.886

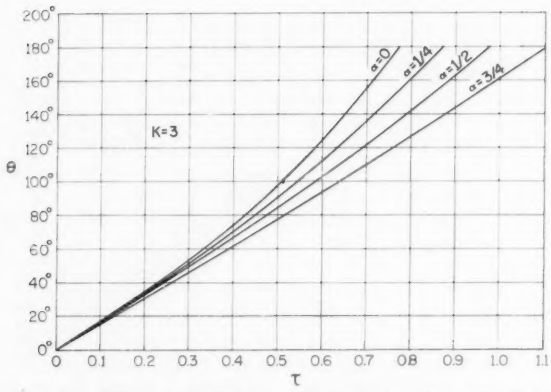

FIG. 10. Flight-path angle θ vs. dimensionless time τ for flight paths at constant centrifugal acceleration K and constant net thrust factor α. $K = 3$; $\alpha = 0, 0.25, 0.50, 0.75$.

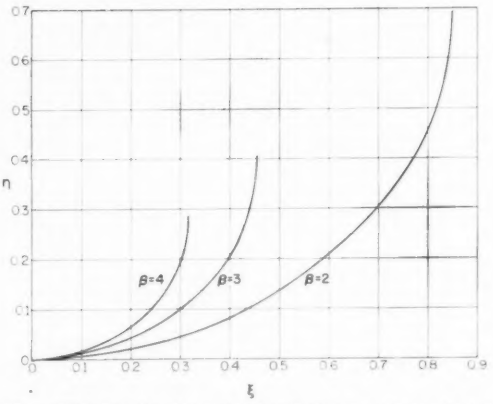

FIG. 12. Flight paths at constant velocity v_0 and constant load factor β. $\beta = 2, 3, 4$.

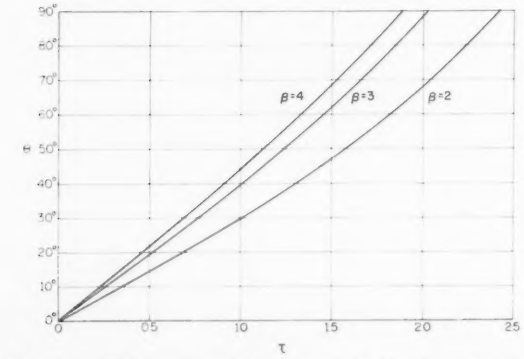

FIG. 11. Flight-path angle θ vs. dimensionless time τ for flight paths at constant velocity v_0 and constant load factor β. $\beta = 2, 3, 4$.

References

[1] Jahnke, E., and Emde, F., *Tables of Functions*, 1938 Edition, Dover Publications.

[2] Watson, G. N., *Treatise on Bessel Functions*, Second Edition, Cambridge University Press, 1948.

[3] British Association for the Advancement of Science, *Mathematical Tables, Vol. X, Bessel Functions—Part II: Functions of Positive Integer Order*, Cambridge University Press, 1952.

[4] National Applied Mathematics Laboratories, U. S. National Bureau of Standards, *Tables of the Normal Probability Functions*, Washington, D.C., U.S. Government Printing Office, 1953.

[5] Ehlers, F. Edward, *On Airplane Maneuvers Involving Constant Load Factor or Constant Centrifugal Acceleration*, Mathematical Note No. 165, Boeing Airplane Company, March 18, 1957.

✦ ✦ ✦

The Newtonian Approximation in Magnetic Hypersonic Stagnation-Point Flow†

PAUL S. LYKOUDIS*
Purdue University

Summary

The hypersonic flow of an electrically conducting fluid around the stagnation region of a sphere carrying a radial magnetic field is examined.

By assuming a Newtonian pressure distribution and constant density, the differential equation of the inviscid flow is integrated and a simple closed-form solution is obtained.

It is found that the ratio of the stand-off distances of the shock wave for the magnetic and nonmagnetic cases does not depend explicitly on the magnetic parameter S_s (ratio of the ponderomotive force to the free-stream inertia force) nor on the density ratio ϵ (the value at the free stream divided by the value behind the shock wave) but on the product $S_s\sqrt{\epsilon}$, at least for values of ϵ between 1/5 and 1/20.

The velocity gradient on the body is also calculated and the ratio of the magnetic to the nonmagnetic case is shown to depend on the parameter $S_s\sqrt{\epsilon}$.

The case of cylindrical shocks is also examined; the same general conclusions are drawn.

Symbols

B = magnetic inductance
C = coefficient of proportionality
C_p = pressure coefficient defined in Eq. (3)
J = current density
m = parameter defined in Eqs. (16) and (23)
P = positive root of the quadratic (15) or (22); physically, the inviscid nondimensional velocity gradient
p = pressure
Q = negative root of the quadratic (15) or (22)
R = radius of curvature
S_s = ratio of magnetic force over inertia force defined in Eq. (8)
U = free-stream velocity ahead of the shock wave
u = velocity in the x direction inside the shock wave
x = coordinate along the shock wave (see Fig. 1)
x_1 = coordinate inside the shock wave (see Fig. 1)
y = coordinate in the radial direction (see Fig. 1)
Z defined in Eq. (33)
ε defined in Eq. (12)
Δ = nondimensional stand-off distance $[= (R_s - R_b)/R]$
ϵ = density ratio across the shock wave $(= \rho_\infty/\rho)$
ζ defined in Eq. (34)
ρ = mass density
σ = coefficient of electrical conductivity

Subscripts

b refers to the radius of curvature of the body
e refers to the edge of the boundary layer
0 refers to the nonmagnetic case
s refers to the radius of curvature of the shock
∞ refers to conditions prevailing ahead of the shock wave
cyl. refers to the cylindrical case
sph. refers to the spherical case

A bar ($^-$) denotes a nondimensional parameter

Received March 30, 1960.

† This investigation was carried out by the author as consultant to The Midwest Applied Science Corp., Lafayette, Ind., for The Allison Division of General Motors Corp., Indianapolis, Ind.

This paper was presented at the Symposium on Engineering Aspects of Magnetohydrodynamics held at the University of Pennsylvania, February 18–19, 1960.

* Associate Professor, School of Aeronautical Engineering.

The author is indebted to this student, Mr. Chia-ping Yu, for the numerical calculations of this work.

(1) Introduction

When a vehicle with a blunt nose moves at hypersonic velocity, part of the kinetic energy associated with its motion is transformed, in the stagnation region, into thermal motion, a substantial fraction being used for the dissociation and to some extent ionization of the different species present.

An ionized gas is of course a good electrical conductor, and hence it is possible in the presence of electromagnetic fields to impart forces whose relative magnitude may be considerable in comparison with the inertia or viscous forces. It is well known that in the presence of a magnetic field fixed relative to the moving body, and acting perpendicularly to the oncoming flow, these forces are decelerating.

Qualitatively the following things are expected to happen:

(a) Since the flow is retarded, a wider area is needed for the passage of the hot gas between the shock wave and the nose, and hence the stand-off distance of the shock wave will be increased.

(b) The coefficients of skin friction and consequently heat transfer will be lowered since the free-stream velocity is diminished.

In the last two years a large number of papers have appeared in the literature dealing with different aspects of the above problem (see, for instance, references 1–9). The present work is concerned with the phenomenon (a) above. In reference 8 a numerical solution is given as a result of the digital integration of the basic conservation equations for the determination of the stand-off distance of a spherical shock wave. Numerical solutions in general give a specific answer for a particular set of flight conditions whereas they fail to reveal the meaning and the number of independent parameters describing a physical situation.

An attempt will be made here to give a closed-form answer to this problem by making use of the Newtonian approximation. It will be seen that although the shock stand-off distance depends on the ratio S_s of the ponderomotive force to the free-stream inertia force and the ratio ϵ of the mass densities across the shock wave, the important parameter is the product $S_s\sqrt{\epsilon}$. The same

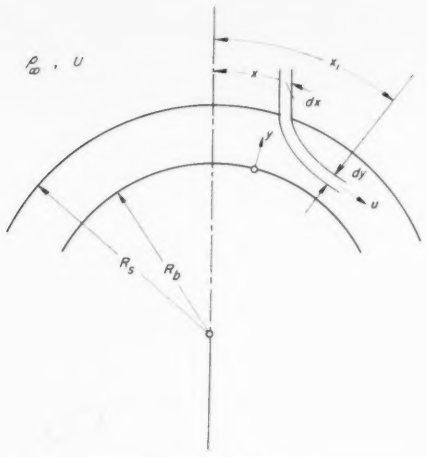

FIG. 1. Nomenclature for the basic geometry.

is true for the velocity gradient at the wall. The closed form solution obtained will be compared with the numerical, exact findings of reference 8 given only for a specific density ratio across a spherical shock, and it will be seen that the agreement is good. The case of cylindrical shocks will also be considered.

(2) Basic Equations and Approximations

The following approximations will be made in this work:

(a) The magnetic field is constant throughout the region between the shock wave and the surface of the vehicle; it remains also always perpendicular to the oncoming stream lines.

(b) The induced electric current does not distort the applied magnetic field.

(c) The shock waves are always spherical or cylindrical depending on the geometry considered.

(d) The pressure distribution in the stagnation region is not altered by the presence of the magnetic field. A Newtonian pressure distribution with constant density will be assumed.

(e) The coefficient of electric conductivity is a scalar and remains the same everywhere.

(f) Viscous effects are negligible.

Assumption (a) is difficult to realize in practice since the magnetic field will originate from a coil located coaxially with the vehicle in the neighborhood of the nose. One expects it to diminish rapidly in the outward direction. For instance the rate of reduction far away from a magnetic dipole is inversely proportional to the third power of the distance, whereas for the experimental apparatus described in reference 9 the power was found to be approximately 3.61. It was shown in reference 4 that if the assumption is made that the constant magnetic field assumed in the calculations is an average one calculated inside the shock region for the specific law of variation of the actual magnetic field, then the final result is equally acceptable.

Assumption (b) is true as long as the magnetic Reynolds number based on the body radius is much smaller than one; for most of the flight conditions in which the present theory applies this is always the case.

In the neighborhood of the stagnation point, assumption (c) is expected to be valid.* The theoretical and numerical solutions described in references 3, 7, and 8 have shown that the pressure distribution changes very little with the imposed magnetic field at least for a moderate variation of the appropriate magnetic nondimensional parameter. The success and simplicity of the Newtonian approximations in hypersonic flow are well known. The basic premises of this theory and its consequences are described very satisfactorily in reference 10. For the calculation of the nonmagnetic shock stand-off distance this assumption gives lower results than more exact numerical solutions. Nevertheless we expect a priori to find the ratio of this distance for the magnetic and nonmagnetic cases very close to the true value, since the same approximations are made for the calculation in the numerator and denominator.

Finally, assumption (e) should be understood to be valid as long as the electrical conductivity is calculated at an average temperature. The present calculations are confined to the inviscid region near the stagnation point, where this assumption becomes more plausible. On the other hand the assumption is well justified in the case of a seeded fluid within the temperature range where the electrical conductivity is insensitive to temperature variations. Its scalar character will be conserved as long as the collision frequency of the particles is much higher than the cyclotron frequency. In this case the charged particles are not free to spiral around the magnetic lines and as a result they lose the sense of a preferential direction.

In order to facilitate the reading of the present paper, use will be made, in so far as possible, of the nomenclature of reference 10. As shown in Fig. 1 the coordinate x denotes the distance of a streamline measured on the shock wave from the stagnation axis. The quantity x_1 measures in the direction x the coordinate of any point inside the shock layer lying on the same streamline.

The "Newton-Busemann" pressure laws for the cases of a sphere and a cylinder are, respectively:

$$\frac{1}{2} C_p = 1 - \frac{x_1^2}{R_s^2} - \frac{1}{3R_s^2}(x_1^2 - x^2) \qquad (1)$$

$$\frac{1}{2} C_p = 1 - \frac{x_1^2}{R_s^2} - \frac{1}{2R_s^2}(x_1^2 - x^2) \qquad (2)$$

where $$C_p \equiv (p - p_\infty)/(1/2)\rho_\infty U^2 \qquad (3)$$

The above distributions contain the Busemann cen-

* The Newtonian approximation is successful in hypersonic flow because the velocity after incidence remains tangent to the wall, since it is bounded by the thin shock layer. In this manner the momentum associated with the normal component of the incident free-stream velocity is balanced by the wall pressure. Now this last component does not interact with the radical magnetic field, since it is essentially parallel to it and therefore the pressure remains unaltered at the wall as long as the shock stand-off distance does not become too high.

trifugal pressure correction; reference 10 gives their derivation in detail.

Behind the shock wave the equation of conservation of momentum is given as follows:

$$\rho u(du/dx_1) = -(\partial p/\partial x_1) + (J \times B)x_1 \quad (4)$$

This is a generalized Bernoulli equation written along the streamline x_1. By virtue of the assumptions (a), (b) and (e) the current induced in a direction perpendicular to the plane formed by the coordinate x and the magnetic field B is given from Ohm's law:

$$J = \sigma uB \quad (5)$$

Substituting this expression into Eq. (4) we obtain:

$$\rho u(du/dx_1) = -(\partial p/\partial x_1) - \sigma B^2 u \quad (6)$$

Nondimensionalizing the velocity u by using the free-stream velocity U and the distances by using the radius of curvature of the shock, R_s, we can write the above as follows:

$$\rho \bar{u}(d\bar{u}/d\bar{x}_1) = -(\partial p/U^2 \partial \bar{x}_1) - (\sigma B^2 \bar{u}/UR_s) \quad (7)$$

At this point we define the ratio of the ponderomotive forces over the inertia forces as follows:

$$S_s \equiv \sigma B^2 R_s/\rho_\infty U \quad (8)$$

By using the above definition and definition (3) in Eq. (7) we obtain:

$$\bar{u}d\bar{u}/d\bar{x}_1 = \epsilon\{-(1/2)(\partial C_p/\partial \bar{x}_1) - S_s\bar{u}\} \quad (9)$$

where ϵ is the density ratio across the shock wave:

$$\epsilon = \rho_\infty/\rho \quad (10)$$

Integration of the basic Eq. (9) will yield the velocity $\bar{u}$ as a function of x, x_1, S_s, and ϵ. A simple application of the equation of conservation of mass will then yield the shock stand-off distance. A detailed analysis of this method for the nonmagnetic case, along with a discussion of the different assumptions involved, is given in reference 10.

(3) The Sphere

Substitution of the pressure distribution given by Eq. (1) into Eq. (9) gives:

$$\bar{u}(d\bar{u}/d\bar{x}_1) = \epsilon\{(8/3)\bar{x}_1 - S_s\bar{u}\} \quad (11)$$

This is a nonlinear homogeneous differential equation of the first order that may be solved by introducing the variable:

$$z(\bar{x}_1) = \bar{u}/\bar{x}_1 \quad (12)$$

After separation of the variables Eq. (11) becomes

$$\frac{dz}{\epsilon\{(8/3z) - S_s\} - z} = \frac{d\bar{x}_1}{\bar{x}_1} \quad (13)$$

Integration starting from the limit $\bar{x}_1 = \bar{x}$ results in

$$\left(\frac{\bar{x}}{\bar{x}_1}\right)^2 = \left(\frac{z - P}{1 - P}\right)^{1-m}\left(\frac{z - Q}{1 - Q}\right)^{1+m} \quad (14)$$

where P and Q are the positive and negative roots of the quadratic

$$z^2 + S_s\epsilon z - (8/3)\epsilon = 0 \quad (15)$$

$$P = \frac{-S_s\epsilon + \sqrt{(S_s\epsilon)^2 + (32/3)\epsilon}}{2} \quad (15a)$$

$$Q = \frac{-S_s\epsilon - \sqrt{(S_s\epsilon)^2 + (32/3)\epsilon}}{2} \quad (15b)$$

and m is defined as follows:

$$m = \frac{-P - Q}{P - Q} = \frac{1}{\sqrt{1 + (32/3S_s^2\epsilon)}} \quad (16)$$

It is not difficult to see by inspection of Eq. (15) that the absolute value of the root Q is always greater than P so that the quantity m is always a positive number. Furthermore, for zero magnetic field S_s is zero and m is equal to zero also, whereas for an infinite S_s, m asymptotically approaches the value one. It will be shown later that this parameter plays an important role in the final solution.

From Fig. 1 it is seen that the following equation of mass continuity for the case of sphere may be written:

$$\rho_\infty(2\pi x\, dx)U = \rho(2\pi x_1\, dy)u$$

Simplifying, using nondimensional quantities and integrating, we find:

$$\frac{y}{R_s} = \epsilon\int_{x=0}^{\bar{x}} \frac{\bar{x}\, d\bar{x}}{\bar{x}_1\bar{u}} \quad (17)$$

For the calculation of the above integral it is necessary to solve Eq. (14) for the velocity $\bar{u}$. It is evident that such a solution in closed form cannot be found. Instead, we differentiate Eq. (14) and by substitution in Eq. (17) it becomes possible to use the quantity z as the variable of integration. The result is surprisingly simple and is given as follows:

$$\frac{y}{R_s} = \frac{\epsilon}{(1 - P)^{1-m}(1 - Q)^{1+m}}\int_{z=P}\left(\frac{z - Q}{z - P}\right)^m dz \quad (18)^*$$

* The lower limit of integration can be understood by looking at Eq. (14); for positive values of z, x becomes zero when $z = P$.

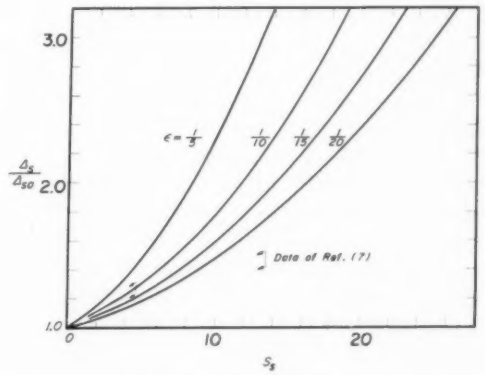

FIG. 2. The stand-off distance for a spherical shock wave versus the magnetic parameter S_s for various values of the density ratio ϵ.

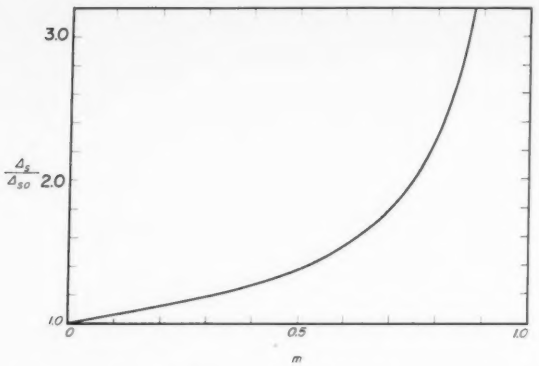

FIG. 3. The stand-off distance for a spherical shock wave versus the parameter m.

The coordinate y is measured from the stagnation point at the body; integration between the distance $R_s - R_b$ yields

$$\Delta_s = (R_s - R_b)/R_s = \frac{\epsilon}{(1-P)^{1-m}(1-Q)^{1+m}} \int_P^1 \left(\frac{z-Q}{z-P}\right)^m dz \quad (19)$$

Closed form calculation of the integral (19) is possible only if the parameter m is a rational number. This is not very much of a limitation since for all practical purposes m may be more than adequately approximated by a ratio of two natural numbers.

Values of the stand-off distance Δ_s have been calculated for four values of ϵ($^1/_5$, $^1/_{10}$, $^1/_{15}$, $^1/_{20}$) and seven values of m ($^1/_8$, $^1/_4$, $^1/_3$, $^1/_2$, $^5/_6$, $^3/_4$, $^7/_8$). For the case $m = 0$ corresponding to zero magnetic field we obtain the well-known result[10]:

$$\Delta_{s0} = \epsilon/(1 + \sqrt{8\epsilon/3}) \quad (20)$$

Fig. 2 shows the ratio Δ_s/Δ_{s0} of the stand-off distances for the magnetic and nonmagnetic cases plotted versus S_s for different density ratios ϵ. In Fig. 3 the same data are plotted, this time versus the parameter m. It is seen that the dependence on ϵ has completely disappeared at least up to the highest calculated value of m ($= 7/8$). We draw the conclusion that the ratio Δ_s/Δ_{s0} depends only on the quantity $S_s\sqrt{\epsilon}$ rather than on S_s and ϵ explicitly [see Eq. (16)]. A physical argument as to the meaning of this finding will be given in Section 5.

The data presented in reference 8 for $\epsilon = 1/10$ according to the findings of reference 7 have been recomputed in terms of the parameters S_s and Δ_s/Δ_{s0} rather than S_b and Δ_b/Δ_{b0}. The agreement with the Newtonian approximation is perfect, as shown in Fig. 2. One can also verify by comparison with reference 8 that Fig. 2 is equally valid, by merely changing the coordinate subscripts s to b.

It should be pointed out that in the work of references 6 and 8 the intensity of the magnetic field in the radial direction was varied inversely with the square of the distance away from the stagnation point; however, the solution obtained there was shown to be insensitive to different numerical values involving the coefficient of proportionality C of the inverse square law $B_r = C/r^2$.

(4) The Cylinder

For the cylindrical case the equation of conservation

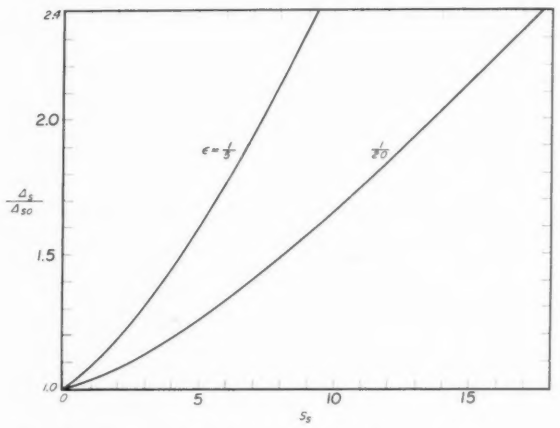

FIG. 4. The stand-off distance for a cylindrical shock wave versus the magnetic parameter S_s for various values of the density ratio ϵ.

of momentum in its nondimensional form is the following:

$$\bar{u}\, d\bar{u}/d\bar{x}_1 = \epsilon\{3\bar{x}_1 - S_s\bar{u}\} \quad (21)$$

Use was made of the pressure distribution given by Eq. (2). This differential equation is exactly the same as Eq. (11) except for the numerical coefficient characterizing the pressure distribution. As a result Eq. (14) is still valid, with the roots P and Q appearing there found from the following quadratic:

$$z^2 + S_s\epsilon z - 3\epsilon = 0 \quad (22)$$

$$P = \frac{-S_s\epsilon + \sqrt{(S_s\epsilon)^2 + 12\epsilon}}{2} \quad (22a)$$

$$Q = \frac{-S_s\epsilon - \sqrt{(S_s\epsilon)^2 + 12\epsilon}}{2} \quad (22b)$$

The quantity m is now defined as

$$m = \frac{-P-Q}{P-Q} = \frac{1}{\sqrt{1 + (12/S_s^2\epsilon)}} \quad (23)$$

The equation of conservation of mass for the cylindrical case is written as follows:

$$\rho_\infty\, dx\, U = \rho\, dy\, u \quad (24)$$

A unit length was assumed in the direction parallel to the axis of the cylinder.

Using again nondimensional quantities and integrating, we find:

$$\frac{y}{R_s} = \epsilon \int_{\bar{x}=0} \frac{d\bar{x}}{\bar{u}} \tag{25}$$

Using the same substitutions and general method applied in the case of sphere, we obtain the cylindrical shock stand-off distance

$$\Delta_s = (R_s - R_b)/R_s = \frac{\epsilon}{(1-P)^{(1-m)/2}(1-Q)^{(1+m)/2}} \int_P^1 \times \frac{dz}{(z-P)^{(1+m)/2}(z-Q)^{(1-m)/2}} \tag{26}$$

For the case $m = 0$ this integral reduces to the known expression

$$\Delta_{s0} = (\epsilon/\sqrt{1-3\epsilon}) \cosh^{-1}(1/\sqrt{3\epsilon}) \tag{27}$$

The integral (26) may always be calculated in a closed form provided m is a rational number. Such calculations have been undertaken for two values of ϵ ($^1/_5$ and $^1/_{20}$) and four values of m ($^1/_3$, $^1/_2$, $^2/_3$, $^3/_4$).

The ratio Δ_s/Δ_{s0} has been plotted versus S_s for two values of ϵ in Fig. 4. The same data plotted versus m are given in Fig. 5. It is seen that the dependence on the density ratio ϵ is again small. For instance, the difference between the values of Δ_s/Δ_{s0} at $\epsilon = 1/5$ and $1/20$ is about 2.5 percent for $m = 0.5$, whereas for $m = 0.7$ (almost a limiting value for an actual experiment), it becomes 5.0 percent. These seem to be rather small differences compared to the 400 percent change in ϵ. It is therefore in order to conclude that for all practical purposes in the cylindrical case also the ratio Δ_s/Δ_{s0} depends on the parameter m only.

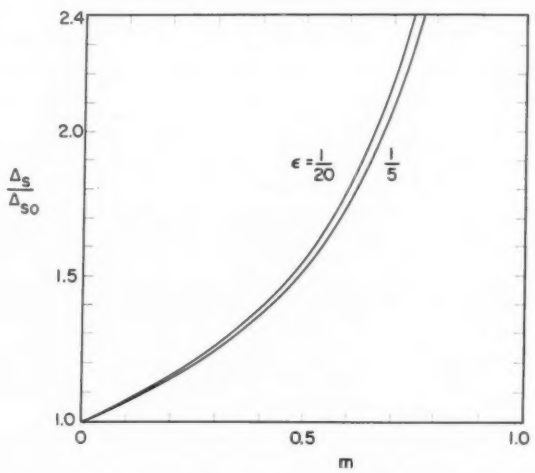

FIG. 5. The stand-off distance for a cylindrical shock wave versus the parameter m.

(5) The Velocity Gradients

The positive roots of the quadratics of Eqs. (15) and (22) have a definite physical meaning. It can be seen by inspection of Eq. (14) that P is the value of z for which $x = 0$.

$$z = \bar{u}/\bar{x}_1 = uR_s/Ux_1 = P \tag{28}$$

From this expression we conclude that the velocity gradient at the body is given as follows:

$$\partial u/\partial x_1 = (U/R_s)P \tag{29}$$

In other words, P is the nondimensional velocity gradient at the body and is given by Eqs. (15a) and (22a) for the spherical and cylindrical cases respectively.

The ratio P/P_0 comparing the velocity gradients for the magnetic and nonmagnetic cases is given as follows:

$$(P/P_0)_{\text{sph.}} = -\frac{S_s}{2}\sqrt{\frac{3\epsilon}{8}} + \sqrt{\left(\frac{S_s}{2}\sqrt{\frac{3\epsilon}{8}}\right)^2 + 1} \tag{30}$$

$$(P/P_0)_{\text{cyl.}} = -\frac{S_s}{2}\sqrt{\frac{\epsilon}{3}} + \sqrt{\left(\frac{S_s}{2}\sqrt{\frac{\epsilon}{3}}\right)^2 + 1} \tag{31}$$

For both geometries the quantity P/P_0 is given in terms of m as follows:

$$P/P_0 = \sqrt{(1-m)/(1+m)} \tag{32}$$

Eqs. (30), (31), and (32) have been plotted in Figs. 6, 7, and 8.

The above results are not new. In references 1, 2, 4, and 5 the same basic formula is given, although written in terms of another parameter which will be discussed in the following section.

For the spherical case and for $\epsilon = 1/10$ we have the results for the velocity gradient of reference 8 up to a value $S_b \approx 5$. Comparison of these data (after their transformation to values referred to the radius of the shock wave) shows that the data of Fig. 6 are higher by about 8.5 percent at $S_b = 5$. The data also show that Fig. 6 coincides completely with the digital computations of reference 8 if the coordinate subscripts are changed from s to b. This substitution apparently al-

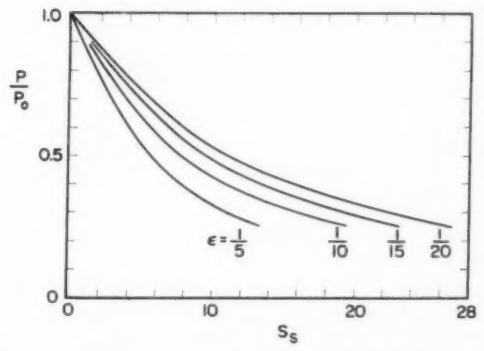

FIG. 6. The velocity gradient for a spherical shock wave versus the magnetic parameter S_s and various density ratios ϵ.

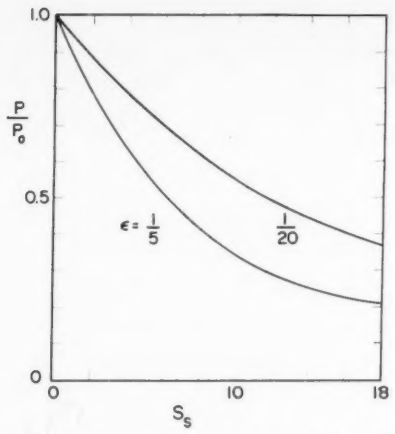

FIG. 7. The velocity gradient for a cylindrical shock wave versus the magnetic parameter S_s and various density ratios ϵ.

lows for the change of the pressure distribution in the presence of a magnetic field.

(6) Discussion

In reference 5 an approximate analysis was made of the shock stand-off distance for both steady and nonsteady hypersonic stagnation flows. An application of Bernoulli's equation at the edge of the boundary layer had shown (see references 1, 2, or 4) that the ratio of the two velocities for the magnetic and nonmagnetic cases is equal to:

$$\frac{u_e}{u_{e0}} = -\frac{\zeta}{2} + \sqrt{1 + \left(\frac{\zeta}{2}\right)^2} = \frac{P}{P_0} \equiv Z \qquad (33)$$

where $$\zeta \equiv \sigma B^2/\rho(UP_0/R_s) \qquad (34)$$

The quantity in parentheses is the velocity gradient at the body calculated for the nonmagnetic case and is always proportional to the square root of ϵ in the Newtonian approximation; it is not difficult to deduce that ζ is given as follows:

$$\zeta_{\text{sph.}} = \sqrt{3/8}\, S_s \sqrt{\epsilon} \qquad (34a)$$

$$\zeta_{\text{cyl.}} = S_s \sqrt{\epsilon}/\sqrt{3} \qquad (34b)$$

An equation for mass conservation within the thickness of the shock layer yields:

$$\rho(R_s - R_b)u_{\text{av.}} = \rho(R_s - R_b)_0 u_{\text{av.}_0} \qquad (35)$$

Assuming that Eq. (33) is valid also for the average velocities and since Δ_s and Δ_{s0} are negligibly small compared to unity we may write:

$$\Delta_s/\Delta_{s0} \approx 1/Z = (\zeta/2) + \sqrt{1 + (\zeta/2)^2} \qquad (36)$$

The above order-of-magnitude argument shows that the ratio of the stand-off distances depends solely on ζ which, in turn, has been shown to depend on $S_s\sqrt{\epsilon}$ only.

It is thus seen that use of the parameter ζ (the ratio of the ponderomotive forces to the inertia forces calculated behind the shock) is a more natural parameter than S_s, which contains the inertia forces calculated at the free stream. The approximation (36) predicts very high values as compared with the better solutions in the present work. A power-law approximation for the stand-off ratio Δ_s/Δ_{s0} versus $1/Z$, in good agreement with Eqs. (19) and (26) for values of $m < 0.5$, is given as follows:

$$(\Delta_s/\Delta_{s0})_{\text{sph.}} \approx (1/Z)^{1/2} \qquad (37)$$

$$(\Delta_s/\Delta_{s0})_{\text{cyl.}} \approx (1/Z)^{3/4} \qquad (38)$$

(7) Conclusions

The following conclusions can now be drawn. A theoretical, closed-form calculation of the shock stand-off ratio Δ_s/Δ_{s0} for spherical and cylindrical shocks is feasible within the limitations of a Newtonian nonmagnetic pressure distribution and constant electrical conductivity and density.

It is shown that this ratio depends essentially on the parameter Z which expresses the ratio of the velocity gradients at the stagnation point with and without a magnetic field. The dependence of Z on the parameter ζ, which represents the ratio of the ponderomotive force to the inertia force calculated in the shock layer, is given by Eqs. (33), (34), and (8). The above results are in good agreement with the limited results of exact numerical solutions in the literature.

The following list of ratios for the magnetic and nonmagnetic cases summarizes approximately the theoretical results:

$$(\Delta_s/\Delta_{s0})_{\text{sph.}} \approx (1/Z)^{1/2}$$

$$(\Delta_s/\Delta_{s0})_{\text{cyl.}} \approx (1/Z)^{3/4}$$

$$P/P_0 = u_e/u_{e0} \approx Z$$

$$q/q_0 \approx Z^{0.4}$$

(Continued on page 562)

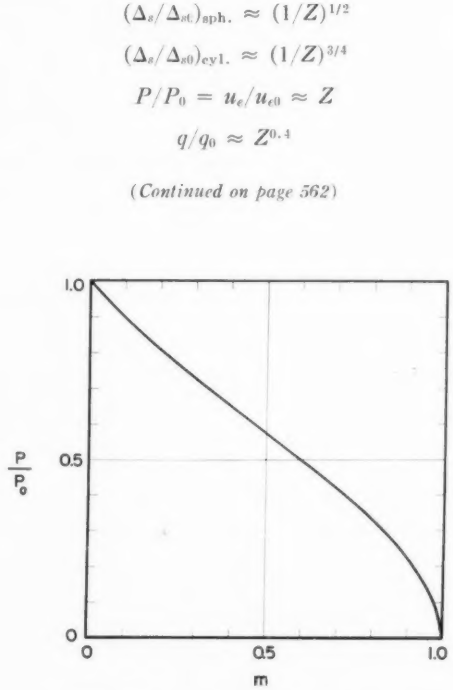

FIG. 8. The velocity gradient for both spherical and cylindrical shock waves versus the parameter m.

Body Under Lifting Wing†

C. F. CHEN* AND JOSEPH H. CLARKE**
Brown University

Summary

An investigation is made of supersonic-aircraft configurations composed of a cambered body positioned a certain distance beneath an arbitrary lifting wing. The geometry of the wing is regarded as given and the geometry of the body may be given or optimum. Expressions for the drag and lift are obtained from reverse-flow considerations; these greatly implement such a study when interference cross flows must be cancelled. The drag advantage to be gained when a given body and wing assume a given orientation is studied. Treated more extensively is the variational problem of determining the optimum wing incidence and optimum body shape, for the given volume and length, to yield the minimum drag for prescribed lift. Numerical results are provided to indicate the significance of the large number of parameters appearing in the problem. Of these, the gap between the wing and the body is found to be particularly important. It is found that at low gap moderate body distortions have a significant influence on the drag. Drag reductions of up to 44% relative to the case of no interference have been found at a Mach number of 2.24 in a configuration having a gap approximately equal to the maximum diameter of the body, and a wing chord of about three eighths of the length of the body. Comparison is made with the conventional wing-body combination including the effects of skin friction, and it is concluded that the advantage suggested by the preceding considerations is not appreciably diminished. Finally, it is shown that the configurations studied lead to bodies of fineness ratios much lower than are appropriate to conventional wing-body combinations.

Tests were made on an arrangement consisting of a Sears-Haack body located under a lifting rectangular diamond-profile wing. The Mach number was 1.6 and the Reynolds number was 9.17×10^5 based on the body length. It was found that the measured lift developed on the wing due to the flow field of the body agrees very well with the theoretical value. Downstream of the impinging shock from the wing, flow separation was observed on the exterior of the body but not in the interior. The separation is attributed not to the pressure rise across the shock but to the pressure field arising from the reflection from the body of the shock-induced cross flow. Further observations suggest that the separation can be avoided by pitching the body or by kinking the body at the shock wave to accommodate the shock-induced cross flow.

Symbols

A	= aspect ratio, or surface area of bodies
a_n	= Fourier coefficients of source distribution
B	= $\sqrt{M^2 - 1}$
b_n	= Fourier coefficients of vorticity distribution
C_D	= drag coefficient based on wing area
C_L	= lift coefficient based on wing area
c	= chord
D	= drag
F	= lineal source intensity
f	= volumetric source intensity
h	= gap distance between wing and body axis
$I_n^{(0)}$, $I_n^{(1)}$, I_n^*	= functions of n defined by Eqs. (43), (44), and (47)
$J_n^{(0)}$, $J_n^{(1)}$, J_n^*	
$I_n^{(2)}$, $J_n^{(2)}$	= functions of n, a_n, and b_n defined by Eq. (45)
$\mathbf{i}$, $\mathbf{j}$, $\mathbf{k}$	= unit vectors in the direction of x, y, z
L	= lift
l	= body length
M	= Mach number of the free stream
m	= lift-curve slope
$\mathbf{N}$	= unit outward normal vector to the section of A made by a plane x = const.
$\mathbf{n}$	= unit outward normal vector to A
p	= pressure
q	= dynamic pressure of free stream $1/2\rho U^2$
R	= body radius
S	= surface area or cross-sectional area
T	= volume enclosed by A
t	= thickness ratio
$\mathbf{U}$	= free-stream velocity
$\mathbf{V}$	= perturbation velocity
$\mathbf{W}$	= $\Phi \cdot \mathbf{V}$
u, v, w	= components of perturbation velocity
x, y, z	= Cartesian coordinates
α	= angle of attack
Γ	= lineal vorticity intensity
θ	= angular variable defined by Eq. (38)
λ	= Lagrangian multiplier
ρ	= density
Φ	= defined by Eq. (3)
$\mathbf{\Omega}$	= volumetric distribution of vorticity
$\boldsymbol{\omega}$	= bound vorticity

Subscripts

0	= free-stream conditions
1	= body
2, w	= wing
F	= forward flow
R	= reverse flow
comb	= conventional wing-body combination
iso	= isolated system
S-H	= configuration with Sears-Haack body
opt	= configuration with optimum body

Primes denote interference flow quantities.

Received March 29, 1960.

† This research was supported primarily by the United States Air Force through the Air Force Office of Scientific Research, Air Research and Development Command, under Contract No. AF 49(638)-444, Project No. 9781. Additional support was provided under Subcontract 77797 by the Johns Hopkins University, Applied Physics Laboratory, Silver Spring, Maryland, which operates under Contract NOrd 7386 with the Bureau of Weapons, Department of the Navy.

* Formerly Research Assistant. Now at Hydronautics, Incorporated.

** Associate Professor of Engineering, Division of Engineering.

(I) Introduction

MUCH HAS BEEN WRITTEN[1-8] in recent years on the subject of favorable interference in supersonic flow. Attention has been given both to a number of specific arrangements which appear to offer possibilities for reducing the inviscid drag due to volume or lift,

and to the underlying theory concerning the nature of the forces arising from a general field of disturbance to a uniform incident stream. In reference 1, a configuration composed of a mutually interfering lifting wing and slender body located underneath was proposed and analyzed, for one special case. The interference considered has three principal favorable features. The important upwash field of the body enclosing the required volume results in the appearance of an interference lift on the wing above, this lift appearing without wing incidence according to the mechanism of references 1, 2, and 3. Further, the overlapping flow fields can produce drag reductions in the manner suggested by the well-known two-dimensional biplane of reference 4. Finally, unlike the analogous interference in the biplane, the interference lift on the wing above cannot be counterbalanced by a negative lift on the body below, since the total lift on the body must vanish when it is closed.

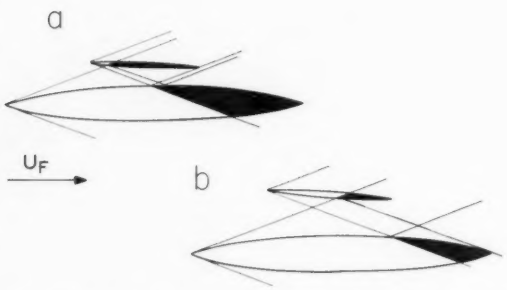

FIG. 1. Interfering configurations: (a) two-reflection case; (b) single-reflection case.

Later, as an illustrative application of a general reverse-flow relation,[5] one of the present writers presented certain expressions for the lift and drag of arbitrary arrangements of the wing and the fusiform body*; these expressions may require only limited knowledge, or no knowledge, of the interference flows needed to preserve the boundary shapes. Using these expressions, in the present paper we undertake to study the drag advantages to be gained both when a given body and wing assume a given orientation and, more extensively, when the said body is recontoured to its optimum shape for the given wing and orientation. The body may be interpreted as a fuselage, a store, etc.

The configuration analyzed then consists of a wing located above a fusiform body. Three possible formulations of the problem are of interest here: (1) wing represented by given singularities and body represented by given or optimum singularities, (2) wing with given geometry and body with given or optimum geometry, and (3) optimum wing and optimum body. In the first problem the required operations, such as optimization, are performed on the singularities representing the configuration. The geometry of the configuration is then obtained by constructing the stream surface induced by the resulting singularity distribution. This may be termed the indirect method. The optimum problem indicated has been treated by Lomax and Heaslet.[7] In the second formulation, in which both the wing and the body are given geometrically, interference fields must be added to the isolated disturbance fields to preserve the boundary shapes. Operations must be performed on the summation of these fields. This may be referred to as the direct method. (Two numerical examples are presented in this paper to compare the results given by these two different formulations.) One may, however, choose to find the optimum body in the second formulation using the indirect method, thus shifting the difficulty of determining the interference field of the body to that of subsequently determining the body geometry. But if the reverse-flow relations are used to obtain the forces, there are interesting instances in which knowledge of the interference field of the body is not needed in the direct method. Evidently the third problem can be approached by either the indirect or the direct method. In the process of optimization, one may regard the horseshoe vorticity representing the lift distribution of the wing as seeking to develop the favorable interference lift by tending to cancel the upwash field of the body and, in addition, warping the wing in an optimal way. At the same time, the body geometry is disposed to obtain maximum advantage from the wing flow field and to affect the wing favorably, much as in the other problems.

In this paper the second formulation is chosen, and interference flows are associated with both wing and body. It is believed that this formulation, in which the wing geometry is given, gives in addition an indication of what results may be expected from the most difficult third formulation. Whereas it takes no account of any advantages to be gained by warping the

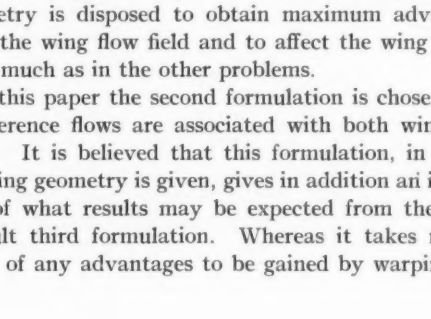

FIG. 2. Drag polar for configuration R1; $A = 1.40$, $c/l = 0.293$.

* By fusiform body is meant a body of fuselage or projectile shape which does not necessarily satisfy the smoothness property of a slender body as specified by Ward.[6]

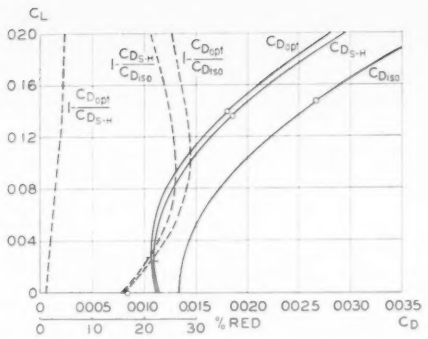

FIG. 3. Drag polar for configuration R1 − T_1; $T_1 = 0.00500/l^2$.

wing and redistributing its thickness (advantages which are well understood for isolated wings), it does account for the additional wing vorticity connected with interference lift, the effect believed to be the more important one. On the other hand, the first formulation, whatever its intrinsic interest, cannot give any indication of the results to be expected from the third, since it excludes interference lift (and the decrease in the drag of the given wing vorticity due to body upwash turns out to be much less important). The choice made also provides an ancillary advantage in that it is the one appropriate for assessment of off-design characteristics of optimal arrangements.

The problem treated is posed as follows: for a wing of given geometry, and for given gap, stagger, free-stream Mach number, and lift, (1) find the drag of the arrangement when the closed body is given, and (2) find the minimum drag when the body geometry is modified to its optimal shape for unchanged length and volume, and when the wing incidence is optimum.

First, convenient expressions for the lift and drag of the configurations are derived. The role of an extended slender-body theory in these results is discussed. After this analytic framework has been established, a physical and interpretive discussion of the interference effects is given. The variational problem is then formulated and solved with the Rayleigh-Ritz method. Numerical examples are given and results are compared to the case of no interference; these are intended to show the influence of the considerable number of geometric parameters on the phenomena. In conclusion, comparison is made with the conventional wing-body combination when the effects of skin friction are included.

(II) Expressions for Drag and Lift

We consider a steady, supersonic flow of moderate Mach number M over a wing-body configuration with inclinations to the incident stream such that linearization of the equations of motion is permitted. We introduce a Cartesian coordinate system with the x-axis in the direction of the incident stream $\mathbf{U} = U\mathbf{i}$, where $U > 0$ in forward flow and $U < 0$ in reverse flow, and the y-axis along the span of the wing. Then the perturbation velocity $\mathbf{V} = u\mathbf{i} + v\mathbf{j} + w\mathbf{k}$ is governed by

$$\nabla \cdot \mathbf{W} = f \tag{1}$$

and

$$\nabla \times \mathbf{V} = \mathbf{\Omega} \tag{2}$$

together with the definitions

$$\mathbf{W} = \Phi \cdot \mathbf{V}, \qquad \Phi = \begin{bmatrix} -B^2 & 0 & 0 \\ 0 & 1 & 0 \\ 0 & 0 & 1 \end{bmatrix} \tag{3}$$

Where $B^2 = M^2 - 1$. Exterior to source and vorticity distributions, f and $\mathbf{\Omega}$ vanish. The vorticity can be decomposed as

$$\mathbf{\Omega} = \Omega_x \mathbf{i} + \boldsymbol{\omega} \tag{4}$$

where $\boldsymbol{\omega}$, being perpendicular to the x-axis, is referred to as the bound vorticity. If $\mathbf{n}$ is the unit outward

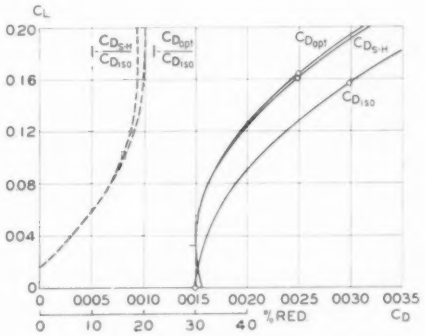

FIG. 4. Drag polar for configuration R1 − t_2; $t_2 = 0$.

normal to the surfaces A of the bodies concerned, then the tangency boundary condition in terms of $\mathbf{V}$ is

$$\mathbf{U} \cdot \mathbf{n} = -\mathbf{V} \cdot \mathbf{n} \tag{5}$$

It is understood that Eq. (5) is conveniently satisfied on the reference surface of the wing, whereas it must be satisfied on the actual surface of the body. If $\mathbf{N}$ is the unit outward normal to the section of A made by a plane $x = \text{const.}$, then $\mathbf{V} \cdot \mathbf{n}$ in Eq. (5) can be written interchangeably with any of the terms $\mathbf{V} \cdot \mathbf{N}$, $\mathbf{W} \cdot \mathbf{n}$, $\mathbf{W} \cdot \mathbf{N}$, essentially because the x-component of $\mathbf{n}$ is small. The surface pressure p in excess of that of the undisturbed stream p_0, is given by

$$(p - p_0)/\rho_0 = -\mathbf{U} \cdot \mathbf{V} - 1/2\mathbf{V} \cdot \mathbf{W} \tag{6}$$

When the pressure is evaluated on the wing, for which the approximation is $t_2 \ll 1$, t_2 being the wing thickness ratio, the last term in Eq. (6) is negligibly small. When the pressure is evaluated on the fusiform body, for which the approximation is $t_1^2 \ln t_1 \ll 1$, t_1 being the body thickness ratio, only the product of the x-components of $\mathbf{V}$ and $\mathbf{W}$ in the last term of Eq. (6) is negligible. Here we are considering a configuration consisting of two basically different bodies. We shall assume that $t_1^2 \ln t_1 = 0(t_2) \ll 1$. This establishes the

order of magnitude of each component of the perturbation velocity that arises in the configuration.

Convenient expressions for the drag and lift forces acting on the wing-body configuration have been derived in reference 5. An integral relation, the generalized reverse-flow relation, involving the forward and reverse flow over related configurations of wings and fusiform bodies is obtained therein. This reverse-flow relation is subsequently applied to the forward flow over the present configuration and the reverse flow over a related configuration chosen so as to give convenient expressions for the forces acting in the forward flow. Further applications of reverse-flow methods to interference problems are given in reference 8 for wing-body combinations with quasi-cylindrical surfaces.

Thus the perturbation velocity induced by the configuration considered in forward flow, $\mathbf{V}_F$, is the sum of the velocities induced by the isolated body and wing, $\mathbf{V}_{1F}$ and $\mathbf{V}_{2F}$, and the interference velocities associated with each member, $\mathbf{V}'_{1F}$ and $\mathbf{V}'_{2F}$, which are needed to preserve the boundary shapes. Hence

$$\mathbf{V}_F = \mathbf{V}_{1F} + \mathbf{V}_{2F} + \mathbf{V}'_{1F} + \mathbf{V}'_{2F} \tag{7}$$

We wish to compute the forces in forward flow but to avoid or reduce the labor of determining the interference flows. With this objective, we choose for the reverse flow the same arrangement of wing and body with the same isolated geometry of each as in forward flow; we do not, however, introduce interference flow

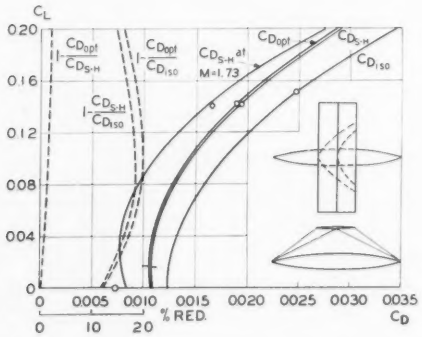

FIG. 5. Drag polar for configuration R1 — A; $A = 2.85$.

fields, so that mutual distortions of the boundaries are permitted. Therefore

$$\mathbf{V}_R = \mathbf{V}_{1R} + \mathbf{V}_{2R} \tag{8}$$

and where $\mathbf{V}_{1R}$ and $\mathbf{V}_{2R}$ satisfy the boundary conditions

$$\mathbf{U}_R \cdot \mathbf{n} = -\mathbf{V}_{1R} \cdot \mathbf{n} \qquad \text{on } A_1$$

and

$$\mathbf{U}_R \cdot \mathbf{n} = -\mathbf{V}_{2R} \cdot \mathbf{n} \qquad \text{on } A_2$$

Here $\mathbf{n}$ is the surface normal in forward flow and $\mathbf{U}_R = -\mathbf{U}_F$. By use of Eqs. (7) and (8) in the reverse-flow relation, the drag of the configuration in forward flow

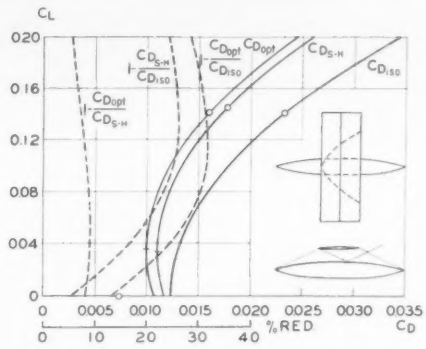

FIG. 6. Drag polar for configuration R1 — $A,h/l$; $A = 2.85$, $h/l = 0.177$.

appears expressed as a sum of the following surface integrals on the body and the wing:

$$D_F = \oint_{A_1} p_R \mathbf{n} \cdot \mathbf{i} dS + \oint_{A_2} p_R \mathbf{n} \cdot \mathbf{i} dS -$$

$$\oint_{A_1} (-\rho_0 \mathbf{U}_F \cdot \mathbf{V}_F) \frac{1}{U_R} \mathbf{V}_{2R} \cdot \mathbf{N} dS - \oint_{A_2} p_F \frac{1}{U_R} \mathbf{V}_{1R} \cdot \mathbf{N} dS$$

Evidently, the forward flow (7) is not necessarily required over the entire surface of each body. Furthermore, by re-expressing in the above the disturbance induced on the wing due to the body in reverse flow as the disturbance induced on the body due to the wing in forward flow, the surface integrals on the wing can be written[5] as a volume integral over the body T_1. Then the drag expression involves only integrations over the body plus a term expressing the drag of isolated wing in reverse flow:

$$D_F = \oint_{A_2} p_{2R} \mathbf{n} \cdot \mathbf{i} dS +$$

$$\rho_0 \int_{T_1} (\mathbf{i} \times \boldsymbol{\omega}_{1R} + f_{1R} \mathbf{i}) \cdot (\mathbf{V}_{2F} + \mathbf{V}'_{2F}) \, dT +$$

$$\oint_{A_1} p_R \mathbf{n} \cdot \mathbf{i} dS - \oint_{A_1} (-\rho_0 \mathbf{U}_F \cdot \mathbf{V}_F) \frac{1}{U_R} \mathbf{V}_{2R} \cdot \mathbf{N} dS \tag{9}$$

The first term of the right-hand member of Eq. (9) is the drag of the isolated wing in reverse flow. The volume integral is the drag due to cross flow and pressure of the wing, $\mathbf{V}_{2F} + \mathbf{V}'_{2F}$, induced on the singularities representing the body in reverse flow. We anticipate consideration of bodies that can be represented by a lineal distribution of singularities, for which this volume integral will, in the limit, become a line integral. The third term is the drag of the body in reverse flow due to the complete pressure field, which is quadratic in the complete perturbation velocity $\mathbf{V}_{1R} + \mathbf{V}_{2R}$. The last term is the drag arising from the linear part of the pressure field in forward flow supported on a fictitious slope due to the cross-flow of the wing in reverse flow. The last two integrals extend over the actual surface.

Finally, it is desirable to transform the last two surface integrals on the body in Eq. (9) into volume integrals over the body. Then, in the limit, a line

integral results. Furthermore, consideration of the full quadratic pressure and the actual surface of the body is avoided. As a consequence of this transformation, the interference effects are clearly exhibited. The surface-volume identity

$$\oint_{A_1} (\mathbf{V}_F\mathbf{W}_R\cdot\mathbf{n} + \mathbf{V}_R\mathbf{W}_F\cdot\mathbf{n} - \mathbf{V}_F\cdot\mathbf{W}_R\mathbf{n})\, dS = \int_{T_1} [\mathbf{V}_F\nabla\cdot\mathbf{W}_R + \mathbf{V}_R\nabla\cdot\mathbf{W}_F - \mathbf{W}_F\times(\nabla\times\mathbf{V}_R) - \mathbf{W}_R\times(\nabla\times\mathbf{V}_F)]dT \quad (10)$$

given by Ursell and Ward[9] and subsequently used by Ward[6] and Clarke[5] will be used to effect the desired transformation.

We begin by expanding p_R on A_1 according to Eq. (6), using the flow field given by Eq. (8), then the last two integrals of (9) become

$$\oint_{A_1} p_{1R}\mathbf{n}\cdot\mathbf{i}dS - \rho_0 \oint_{A_1} \mathbf{V}_{1R}\cdot\mathbf{W}_{2R}\mathbf{n}\cdot\mathbf{i}dS + \oint_{A_1} p_{2R}\mathbf{n}\cdot\mathbf{i}dS - \oint_{A_1} (-\rho_0\mathbf{U}_F\cdot\mathbf{V}_F)\frac{1}{U_R}\mathbf{V}_{2R}\cdot\mathbf{N}dS \quad (11)$$

The last two terms of (11) can be written in the form of the first two terms of the surface integral of Eq. (10) by applying the boundary condition on A and noting the relation $\mathbf{V}_{2R}\cdot\mathbf{N} = \mathbf{W}_{2R}\cdot\mathbf{n}$. We obtain

$$-\frac{\rho_0}{U_F}\oint_{A_1} (\mathbf{U}_F\cdot\mathbf{V}_F\mathbf{W}_{2R}\cdot\mathbf{n} - \mathbf{U}_R\cdot\mathbf{V}_{2R}\mathbf{W}_F\cdot\mathbf{n})dS \quad (12)$$

which is transformed according to Eq. (10) as

$$-\frac{\rho_0}{U_F}\int_{T_1} [\mathbf{U}_F\cdot\mathbf{V}_F f_{2R} - \mathbf{U}_R\cdot\mathbf{V}_{2R}f_F - \mathbf{U}_F\cdot\mathbf{W}_F\times\omega_{2R} + \mathbf{U}_R\cdot\mathbf{W}_{2R}\times\omega_F]\, dT - \rho_0\oint_{A_1}\mathbf{V}_F\cdot\mathbf{W}_{2R}\mathbf{i}\cdot\mathbf{n}dS \quad (13)$$

in which Eqs. (1), (2), and (4) have been used. When (13) is simplified, by noting that f_2 and ω_2 vanish in T_1, and substituted into (11), we obtain

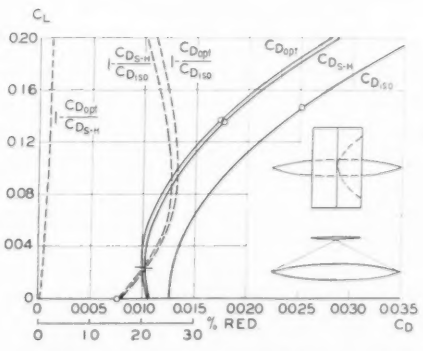

FIG. 7. Drag polar for configuration R2; $A = 1.62$, $c/l = 0.380$.

$$\oint_{A_1} P_{1R}\mathbf{n}\cdot\mathbf{i}dS - \rho_0\int_{T_1}(\mathbf{i}\times\omega_{1F} + f_{1F}\mathbf{i})\cdot\mathbf{V}_{2R}dT - \rho_0\oint_{A_1}(\mathbf{V}_F + \mathbf{V}_{1R})\cdot\mathbf{W}_{2R}\mathbf{n}\cdot\mathbf{i}dS \quad (14)$$

When the term $(\mathbf{V}_F + \mathbf{V}_{1R})\cdot\mathbf{W}_{2R}$ is evaluated by the respective components of the vectors in a local orthogonal coordinate system as in reference 5, it can be shown that the last surface integral in (14) is negligibly small. The drag formula finally becomes

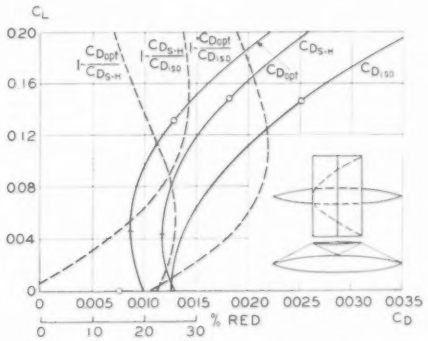

FIG. 8. Drag polar for configuration R2 — h/l; $h/l = 0.155$.

$$D_F = \oint_{A_1} P_{1R}\mathbf{n}\cdot\mathbf{i}dS + \oint_{A_\infty} P_{2R}\mathbf{n}\cdot\mathbf{i}dS + \rho_0\int_{T_1}\{(\mathbf{i}\times\omega_{1R} + \mathbf{i}f_{1R})\cdot(\mathbf{V}_{2F} + \mathbf{V}'_{2F}) - [\mathbf{i}\times(\omega_{1F} + \omega'_{1F}) + \mathbf{i}(f_{1F} + f'_{1F})]\cdot\mathbf{V}_{2R}\}dT \quad (15)$$

Knowledge only of the singularities representing the body and of the flow fields of the wing both in forward and reserve flow is explicitly required for the evaluation of D_F. Implicitly, however, the flow field of the body in forward flow is needed in order to evaluate $\mathbf{V}'_{2F}$. Let the first two terms of Eq. (15), which are the self-induced drags of the isolated body and isolated wing respectively in reverse flow, be denoted by $D_{R,11}$ and $D_{R,22}$. It has been shown that the drag of the isolated body[5] or wing[9] in either direction is the same, i.e., $D_{R,11} = D_{F,11}$ and $D_{R,22} = D_{F,22}$, aside from possible edge-force contributions in the latter case.[10]

By a similar application of the reverse-flow relation, the interference lift, L'_{2F}, produced on the wing is determined as[5]

$$L'_{2F} = -\rho_0\int_{T_1}[\mathbf{i}\times(\omega_{1F} + \omega'_{1F}) + \mathbf{i}(f_{1F} + f'_{1F})]\cdot\frac{\mathbf{V}^*_{2R}}{\alpha^*}dT \quad (16)$$

where $\mathbf{V}^*_{2R}$ is the perturbation velocity induced by a flat plate in reverse flow which is placed at an angle of incidence of α^*, and which has the same planform as that of the given wing. As previously noted, the lift on the closed body is zero. This fact can be demonstrated as follows. If we apply the momentum theo-

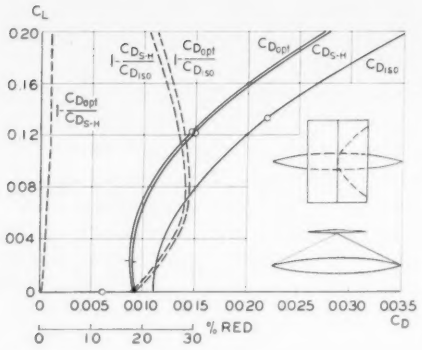

FIG. 9. Drag polar for configuration R3; $A = 1.36$, $c/l = 0.467$.

rem to a surface enclosing the configuration, the lift force is[6]

$$\mathbf{L} = \rho_0 \mathbf{U} \times \oint_A \mathbf{n} \times \mathbf{V}\, dS \tag{17}$$

Now we shrink A to include the body surface A_1, the wing surface A_2, and a tubular surface connecting the two. The integral over the tubular surface vanishes in the limit. Since the velocity $\mathbf{V}$ can be derived from a potential ϕ, the surface integrals on A_1 and A_2 can be transformed into line integrals along the trailing edges where ϕ may be discontinuous though finite. Then

$$\mathbf{L} = \rho_0 \mathbf{U} \times \left[\int_{c_1} \phi d\mathbf{s} + \int_{c_2} \phi d\mathbf{s} \right] \tag{18}$$

where $d\mathbf{s}$ is the elemental tangent vector along the path. We see then that the integral around c_1, which is proportional to the lift on the body, vanishes since the body is closed.

We shall assume throughout that the gap between the wing and the body is such that on the body the domain of influence and the domain of dependence of the wing in forward flow do not overlap (Figs. 1a and 1b depict two such situations); then the terms containing $\boldsymbol{\omega}'_{1F}$ and f'_{1F} vanish within the region of integration in both the drag and the interference lift expressions and so need never be determined. If the gap is such that the domains of influence and of dependence of the body do not overlap on the wing (Fig. 1b depicts the situation hereafter referred to as the single-reflection case), the drag formula is further simplified by the vanishing of $\mathbf{V}'_{2F}$ in the region of integration. In this case, then, the drag of the configuration is evaluated solely from a knowledge of the flow fields of the isolated wing and the singularities representing the isolated body both in forward and reverse flow. If the gap is smaller than that giving the single-reflection case (Fig. 1a depicts such a situation, hereafter referred to as the two-reflection case), $\mathbf{V}'_{2F}$ must be determined on the rear portion of the body axis. When wing edges are suitable, $\mathbf{V}'_{2F}$ is conveniently evaluated by the use of an image. More complicated wave reflection patterns will not be treated, since these seem to be adequate to this study for the Mach numbers and geometries contemplated.

Further, we shall take the bound vorticity in the direction of the y-axis because of vertical symmetry, and assume that the spatial distributions of sources and vorticity are zero everywhere except along the x-axis —i.e., we take only the first two terms of the multipole distribution which replaces the volumetric distribution when the limiting process is used. Let the lineal intensity of the sources and vorticity, F and $\mathbf{j}\Gamma$, be defined by

$$f_{1F} dT = F_{1F} dx \tag{19}$$

$$\mathbf{j}\omega_{1F} dT = \mathbf{j}\Gamma_{1F}\, dx \tag{20}$$

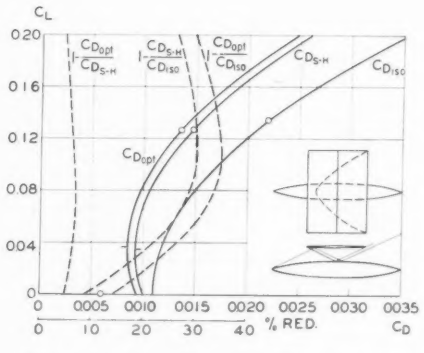

FIG. 10. Drag polar for configuration R3 — h/l; $h/l = 0.177$.

on the x-axis. If the length of the body is l, then Eqs. (15) and (16) become

$$D_F = D_{F,11}(F_{1F}, \Gamma_{1F}) + D_{F,22}(\alpha_2) + \rho_0 \int_0^l \{ [\mathbf{k}\Gamma_{1R}(x) + \mathbf{i}F_{1R}(x)] \cdot [\mathbf{V}_{2F}(x) + \mathbf{V}'_{2F}(x)] - [\mathbf{k}\Gamma_{1F}(x) + \mathbf{i}F_{1F}(x)] \cdot \mathbf{V}_{2R}(x) \} dx \tag{21}$$

$$L'_{2F} = -\rho_0 \int_0^l [\mathbf{k}\Gamma_{1F}(x) + \mathbf{i}F_{1F}(x)] \cdot \frac{\mathbf{V}^*_{2R}(x)}{\alpha^*} dx \tag{22}$$

(III) The Role of Slender-Body Theory

Since the singularities associated with only the isolated body appear in the drag expression, we now discuss briefly the flow over such a body. The singularities representing a body in forward flow are related to the geometry by the tangency boundary condition (5). When the same body appears in reverse flow, the associated singularities are implicitly related to those in forward flow by the expression

$$(\mathbf{V}_{1F} + \mathbf{V}_{1R}) \cdot \mathbf{n} = 0 \tag{23}$$

Consider in particular a lineal distribution of sources and horseshoe vorticity representing a slender body of circular cross-section $S_1(x)$ having local angle of attack

or camber $\alpha_1(x)$. If $F_1(x)$ together with its derivatives are of uniform order, and similarly for $\Gamma_1(x)$, we find

$$F_1(x) = U(d/dx)S_1(x)[1 + O(t_1^2 \ln t_1)] \quad (24)$$

$$\Gamma_1(x) = U(d/dx)[S_1(x)\alpha_1(x)][1 + O(t_1^2 \ln t_1)] \quad (25)$$

when $U \lesseqgtr 0$. The analysis is similar to that for a slender body of revolution at incidence and need not be given here. It is seen that the singularities representing a slender body in forward and reverse flow differ in sign only, when this result is substituted into Eq. (21), the expression for the interference drag is further simplified.

However, according to this slender-body approximation, the self-induced drag of the vorticity distribution is of order t_1^6, which is negligible compared to that due to the source distribution of order t_1^4. The drag expression then becomes linear in Γ_{1F}; therefore no relative minimum exists for any Γ_{1F}. Uninhibited by a self-induced drag, the vorticity distribution will grow to a point where Eq. (25) fails. Further, results indicate that the optimum vorticity distribution is sometimes insufficiently smooth to justify the use of Eq. (25) in the first place. By an extension of the slender-body theory, we can admit a less smooth vorticity distribution whose self-induced drag is not of negligible order, and, at the same time, obtain the same simple expression for the interference drag that results from use of slender-body theory; the latter is possible because the vorticity term in Eq. (21) is smaller than the source term. In anticipation of a rapidly varying

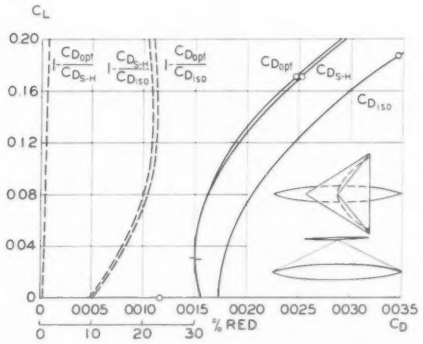

FIG. 11. Drag polar for configuration T; $A = 2.5$, $c/l = 0.5$.

$\alpha_1(x)$, we suppose the order of magnitude of $\Gamma_1(x)$ becomes larger by order $t_1^{1/2}$ for each successive derivative—i.e.,

$$\Gamma_1(x)/\Gamma_1'(x);\ \Gamma_1'(x)/\Gamma_1''(x);\ \text{etc.} = 0(t_1^{1/2}) \quad (26)$$

where the prime denotes the derivative with respect to x. By calculating the x-component of the velocity u induced by such a distribution of vorticity and applying the assumption $u \ll U$ used to derive the basic equations, one finds that $\Gamma_1(x)$ is of order $t_1^3 \ln t_1$, instead of the t_1^3 in slender-body theory. The self-induced drag becomes of order $t_1^5 \ln^2 t_1$. By applying the boundary condition in the cross-flow plane and noting the relation (26), one obtains an expression for $\Gamma_1(x)$ like Eq. (25) but with error $[1 + 0(t_1 \ln t_1)]$; therefore

$$\Gamma_{1R}(x) = \Gamma_{1F}(x)[1 + O(t_1 \ln t_1)] \quad (27)$$

Substituting Eq. (27) into the drag expression (21), and noting that $\mathbf{V}_2$ is of order $t_1^2 \ln t_1$, we obtain, just as for slender-body theory,

$$D_F = D_{F,11}(F_{1F}, \Gamma_{1F}) + D_{F,22}(\alpha_2) - \rho_0 \int_0^l [\mathbf{k}\Gamma_{1F}(x) + \mathbf{i}F_{1F}(x)] \cdot [\mathbf{V}_{2F}(x) + \mathbf{V}_{2R}(x) + \mathbf{V}'_{2F}(x)]dx + O(t_1^6 \ln t_1) \quad (28)$$

Since the second term in Eq. (28) is of order $t_1^4 \ln^2 t_1$, the last term is clearly negligible. Therefore, in evaluating the drag, $\Gamma_1(x)$ may be related to the geometry by Eq. (25) within the approximation made. On the other hand, to obtain $\alpha_1(x)$ from a computed $\Gamma_1(x)$, the term of order $t_1 \ln t_1$ in Eq. (25) is to be accounted for as follows:

$$\alpha_1(x) = \frac{1}{\pi R^2}\int_0^x \Gamma(\xi)d\xi + \frac{B^2}{2\pi}\int_0^x \Gamma''(\xi)\left[\cosh\frac{x-\xi}{BR} - \frac{1}{2}\right]d\xi + \frac{B^2}{2\pi}\Gamma'(0)\left[\cosh\frac{x-\xi}{BR} - \frac{1}{2}\right] + O(t_1^3 \ln t_1) \quad (29)$$

where R is the radius of the body.

(IV) Examination of the Lift and Drag Expressions

The nature of the interference is more easily appreciated by examining Eqs. (22) and (28) than by considering the forward flow directly. A positive interference lift generally results if the configuration is such that within the region of influence of the wing in reverse flow, the source strength is positive and the vorticity strength is negative. If the wing has neither thickness, camber, nor incidence, then lift can be developed on the wing without incurring an attendant drag. The interference drag in Eq. (28) may be de-

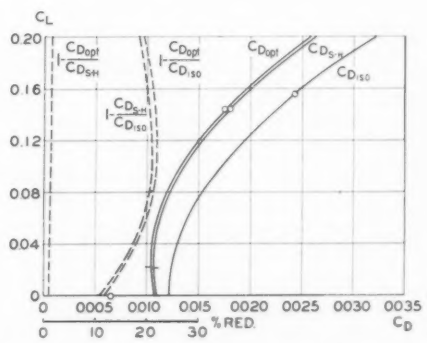

FIG. 12. Drag polar for configuration $T - T_1$; $T_1 = 0.00500l^3$.

composed into (1) that due to wing angle of attack, $\mathbf{V}_{2\alpha F} + \mathbf{V}_{2\alpha R}$, (2) that due to wing thickness and warp, $\mathbf{V}_{2tF} + \mathbf{V}_{2tR}$, and (3) that due to the interference flow, $\mathbf{V}'_{2F}$. If we consider, for purposes of illustration, a configuration with body and wing planform symmetrical about the plane $x = l/2$, then, in slender-body theory, $F_{1F}(x)$ is odd and $\Gamma_{1F}(x)$ is even with respect to the plane of symmetry. The sum of perturbation velocities $u_{2\alpha F} + u_{2\alpha R}$ is even and $w_{2\alpha F} + w_{2\alpha R}$ is odd with respect to the same symmetry plane; the interference drag due to wing angle of attack therefore vanishes. By a similar consideration, the interference drag due to wing thickness and warp can be written as

$$-2\rho_0 \int_{l/2}^{l} F_{1F} u_{2tF}\, dx - 2\rho_0 \int_{1/2}^{l} \Gamma_{1F} w_{2tF}\, dx$$

As is clear from physical considerations, a compression wave from the wing will produce a favorable effect, as will a positive α_1. Since the portion of the body affected by the interference flow from the wing has in general negative surface slope, a compressive $\mathbf{V}'_{2F}$ will contribute to the drag reduction. A consideration of these various effects is helpful for recognizing favorable orientations of the configuration considered.

When the body geometry is given, the aerodynamic forces acting on the configuration can be determined with comparative ease from Eqs. (22) and (28). (In the subsequent numerical calculations, the Sears-Haack body is taken as the given body in each of the configurations considered.) In order to exhibit the form of the polar drag curve for a configuration consisting of a given wing and a given body, which does not pitch with the wing, we write these drag and lift expressions as

$$\left.\begin{aligned} D_F &= D_{F,\,11} + \mathfrak{D}_a + \mathfrak{D}_b\alpha_2 + \mathfrak{D}_c\alpha_2^2 + \mathfrak{D}_d + \mathfrak{D}_e\alpha_2 \\ L_F &= \mathfrak{M}(\alpha_2 - \alpha_{ZL}) + L'_{2F} \end{aligned}\right\} \quad (30)$$

where $\mathfrak{D}_a$, $\mathfrak{D}_b$, $\mathfrak{D}_c$, $\mathfrak{M}$, and the angle of zero lift α_{ZL} characterize the isolated wing for given Mach number, and $\mathfrak{D}_d$ and $\mathfrak{D}_e$ characterize the interference drag. If we ignore any leading-edge singularity of the wing, then we can rewrite the above expressions in coefficient form as

$$\left.\begin{aligned} C_D &= \frac{1}{m}\left[m\alpha_2 + \frac{C_{D_b} + C_{D_e}}{2}\right]^2 + \\ &\qquad C_{D_{11}} + C_{D_a} + C_{D_d} - \frac{(C_{D_b} + C_{D_e})^2}{4m} \\ C_L &= m\alpha_2 + C'_{L_2} - m\alpha_{ZL} \end{aligned}\right\} \quad (31)$$

where m is the lift-curve slope of the isolated wing. It is seen that the effect of the body and the interference is like the effect of thickness and camber on flat-plate wing characteristics, with $C_{D_{11}}$ and C_{D_d} formally corresponding to the thickness and the warp part of C_{D_a}, respectively, C_{D_e} corresponding to C_{D_b}, and C'_{L_2} corresponding to $-m\alpha_{ZL}$; but there are possible differences in signs and magnitudes. Evidently, the effect of favorable interference is to shift the drag polar of the interfering system upward and toward the left. In the case of configurations without wing warp and with the fore-and-aft symmetry noted, the minimum C_D occurs when $\alpha_2 = 0$. The performance of such a configuration depends then on C'_{L_2} and C_{D_d}. When the latter vanishes, the total effect of the interference is to shift the polar curve upward. When the body is contoured optimally, the further reductions in drag at given C_L are due partly to a slight increase in the focal length, and partly to an additional shifting of the drag parabola.

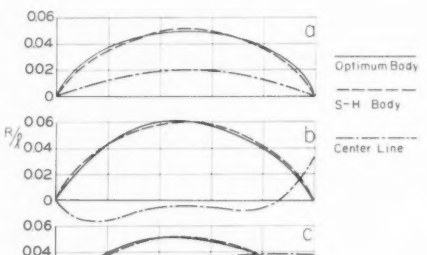

FIG. 14. Shape of optimum body; (a) configuration R1 — T_1, (b) configuration R2 — h/l, (c) configuration T — T_1.

(V) Variational Problem and Method of Solution

The variational problem requires determination of functions $F_{1F}(x)$ and $\Gamma_{1F}(x)$ which satisfy respectively the end conditions

$$F_{1F}(0) = F_{1F}(l) = 0, \quad \Gamma_{1F}(0) = \Gamma_{1F}(l) = 0 \quad (32)$$

and of α_2 such that the drag, Eq. (28), be a minimum subject to the following subsidiary conditions respectively on (1) the lift of the configuration, (2) the volume, (3) the closure, and (4) the absence of total lift on the body:

$$L = \mathfrak{M}(\alpha_2 - \alpha_{ZL}) - \rho_0 \int_0^l [\mathbf{k}\Gamma_{1F}(x) + \mathbf{i}F_{1F}(x)] \cdot \frac{\mathbf{V}^*_{2R}}{\alpha^*}\, dx \quad (33)$$

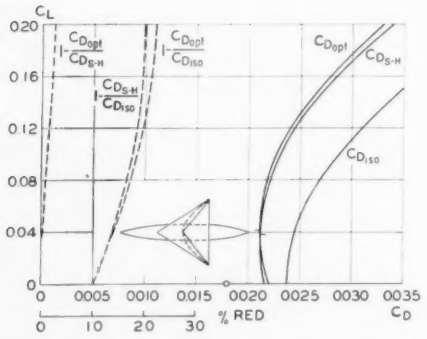

FIG. 13. Drag polar for configuration T = c/l; c/l = 0.4.

$$T_1 = \int_0^l dx \int_0^x \frac{1}{U_F} F_{1F}(\xi)\, d\xi \tag{34}$$

$$\int_0^l F_{1F}(x)\, dx = 0, \quad \text{and} \quad \int_0^l \Gamma_{1F}(x)\, dx = 0 \tag{35), (36}$$

The drag of the isolated body is[11]

$$D_{F,\,11} = -\frac{q}{2\pi}\left\{\int_0^l\int_0^l F'_{1F}(x)F'_{1F}(\xi) \times \ln|x-\xi|\,d\xi\,dx + 2B^2 \int_0^l\int_0^l \Gamma'_{1F}(x)\Gamma'_{1F}(\xi) \ln|x-\xi|\,d\xi\,dx\right\} \tag{37}$$

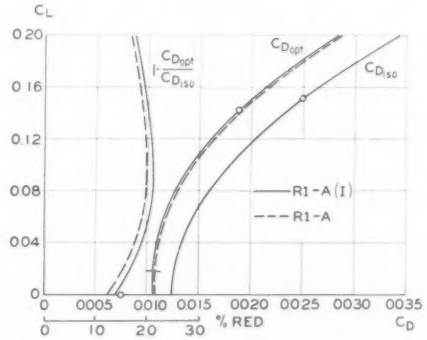

FIG. 15. Drag polar for configuration R1 — A (I).

The drag of the isolated wing can be written generally as in Eq. (30).

The direct method of Rayleigh-Ritz is used for the solution of this variational problem. For discussions of the convergence and limitations of this method, see reference 12. Then, as suggested by the technique employed in the Prandtl wing theory and later used by Sears,[13] we first transform the portion of the x-axis from $x = 0$ to $x = l$ into an angular variable θ, where

$$x = (l/2)(1 + \cos\theta) \tag{38}$$

We then choose the functions $\sin n\theta$, which satisfy the end conditions trivially, to be the coordinate functions. Expanding $F_{1F}[x(\theta)]$ and $\Gamma_{1F}[x(\theta)]$, we obtain

$$F_{1F}(\theta) = U_F \pi l \sum_{n=1}^{n} a_n \sin n\theta \tag{39}$$

and

$$\Gamma_{1F}(\theta) = U_F \pi l \sum_{n=1}^{n} b_n \sin n\theta \tag{40}$$

The subsidiary conditions (35), (36), and (34) become $a_1 = 0$, $b_1 = 0$, and

$$a_2 = -(16/\pi^2)(T_1/l^3) \tag{41}$$

respectively. Substituting Eqs. (39) and (40) together with the transformation (38) into the drag expression (28) and integrating, we obtain the drag written in coefficient form as

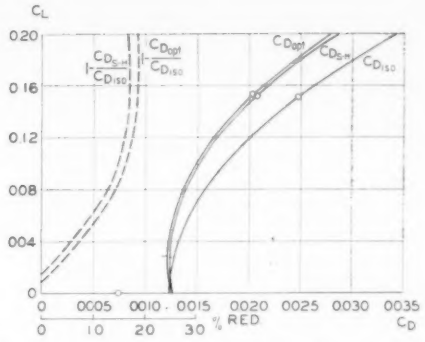

FIG. 16. Drag polar for configuration R1 — $A,h/l$ (I).

$$C_D = \frac{\pi^3 l^2}{4S_w}\sum_{n=2}^{N} n(a_n^2 + 2B^2 b_n^2) + C_{D_0} + C_{D_b}\alpha_2 + C_{D_c}\alpha_2^2 - \frac{\pi l^2}{S_w}\sum_{n=2}^{N} \times \{a_n[I_n^{(0)} + \alpha_2 I_n^{(1)} + I_n^{(2)}(a_i, b_i)] + b_n[J_n^{(0)} + \alpha_2 J_n^{(1)} + J_n^{(2)}(a_i, b_i)]\} \tag{42}$$

in which $I_n^{(0)}$ and $I_n^{(1)}$ are defined as

$$I_n^{(0)} = \frac{2}{U_F}\int_0^\pi (u_{2iF} + u_{2iR}) \sin\theta \sin n\theta d\theta \tag{43}$$

$$I_n^{(1)} = \frac{2}{U_F}\int_0^\pi (u_{2\alpha F} + u_{2\alpha R}) \sin\theta \sin n\theta d\theta \tag{44}$$

and $I_n^{(2)}$, which depends on all the a's and b's, is defined as

$$I_n^{(2)}(a_i, b_i) = \frac{2}{U_F}\int_0^\pi u'_{2F} \sin\theta \sin n\theta\, d\theta \tag{45}$$

$i = 2, 3, \ldots, N$, and $J_n^{(0)}$, $J_n^{(1)}$, and $J_n^{(2)}$ are similarly defined for $w_{2F} + w_{2R}$ and w_{2F}'. The only remaining subsidiary condition, the prescribed lift, becomes

$$C_L = m(\alpha_2 - \alpha_{ZL}) - \frac{\pi l^2}{S_w}\sum_{n=2}^{N}(a_n I_n^* + b_n J_n^*) \tag{46}$$

$$\text{where} \quad I_n^* = \frac{2}{U_F}\int_0^\pi \frac{u_{2R}^*}{\alpha^*} \sin\theta \sin n\theta\, d\theta \tag{47}$$

and J_n^* is similarly defined for w_{2R}^*/α^*. Since bodies with discontinuous surface slope and camber are not considered here, convergence of the sums $\Sigma\, n a_n^2$ and $\Sigma\, n b_n^2$ as $N \to \infty$ is assured. Terms like $\Sigma\, a_n I_n^{(0)}$ are convergent because $I_n^{(0)}$ can be regarded as the Fourier coefficient of $(u_{2iF} + u_{2iR}) \sin\theta$ and behaves like $1/n$. The drag and lift of a configuration with a Sears-Haack body are simply evaluated from Eqs. (42) and (46) by substituting a_2 according to (41), and by setting $a_n = 0$ for $n \geq 3$, and $b_n = 0$ for $n \geq 2$.

The variational problem reduces now to a problem in the ordinary calculus of maxima and minima, in terms of $2(N-1)$ variables with one subsidiary condition.

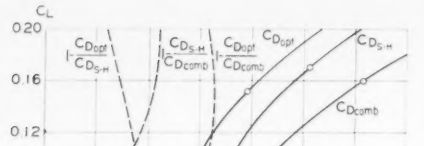

FIG. 17. Drag polar for configuration R2 = h/l with friction included.

The necessary conditions for the existence of a relative minimum give the following equations for a_n, b_n, α_2 and the Lagrangian multiplier λ:

$$(\pi^2/2)na_n + I_n^{(0)} + \alpha_2 I_n^{(1)} + (\partial/\partial a_n)[a_n I_n^{(2)}(a_i, b_i) + b_n J_n^{(2)}(a_i, b_i)] - \lambda I_n^* = 0 \quad (48)$$

$$\pi^2 B^2 n b_n + J_n^{(0)} + \alpha_2 J_n^{(1)} + (\partial/\partial b_n)[a_n I_n^{(2)}(a_i, b_i) + b_n J_n^{(2)}(a_i, b_i)] - \lambda J_n^* = 0 \quad (49)$$

$$C_{D_b} + 2\alpha_2 C_{D_c} + \frac{\pi l^2}{S_w}\sum_{n=2}^{N}(a_n I_n^{(1)} + b_n J_n^{(1)}) + \lambda m = 0 \quad (50)$$

where $n \geq 3$ in Eq. (48) and $n \geq 2$ in Eq. (49). These $2(N-1)$ equations together with the lift expression (46) will suffice to determine the optimum values of α_2, a_n (for $n = 3, 4, \ldots, N$), b_n (for $n = 2, 3, \ldots, N$), and λ. It is noted here that the optimum geometry of the body varies with the design lift. The minimum drag is obtained when these values are substituted back into Eq. (42). The sufficient condition for the existence of a relative minimum can be obtained by considering the second-order terms in the Taylor's series expansion of the drag expression about the optimum point. Having obtained the quadratic form, we find that if

$$2C_{D_c} - \frac{\pi l^2}{S_w}\left\{\sum_{n=3}^{N}\frac{(I_n^{(1)})^2}{(n\pi^2/2) + (\partial^2/\partial a_n^2)[a_n I_n^{(2)} + b_n J_n^{(2)}]} + \sum_{n=2}^{N}\frac{(J_n^{(1)})^2}{n\pi^2 + (\partial^2/\partial a_n^2)[a_n I_n^{(2)} + b_n J_n^{(2)}]}\right\} > 0$$

in which the derivatives are evaluated at the stationary point, then the stationary point is a minimum.

(VI) Numerical Results and Discussion

In this section, the results of numerical calculations for four basic configurations, three with a rectangular wing and one with a triangular wing having supersonic leading edges, are presented in order to show (1) the magnitude of the drag reduction made possible by the interference considered, (2) the further improvement resulting from the substitution of the optimum body for the Sears-Haack body, (3) the importance of the gap between the wing and the body, and (4) the effect of the Mach number and various geometrical parameters on the drag reduction. Both types of wings have symmetric diamond profiles of 5% thickness ratio with the maximum thickness at the mid-chord. The sweep angle of the triangular wing is taken to be $\tan^{-1} 0.8B$. From a qualitative consideration of the drag formula, we locate the wing centrally above the body in all configurations considered; no studies on the effect of stagger are made. The gap h, except in the low-gap studies, is taken to be $l/2B$, so that the interference flow $\mathbf{V}'_{2F}$ is not needed for calculating the drag. The lower gaps are so chosen for each wing planform that $\mathbf{V}'_{2F}$ can be determined conveniently by the method of images. The aspect ratio A of the wings is chosen such that the influence of the body is not felt on the upper side of the wing; with this choice, the flow field of the rectangular wings at the body axis is conveniently two-dimensional. For all basic configurations considered, the design Mach number is taken to be 2.24 ($B = 2$) and the given volume of the body is taken to be $0.00656l^3$, corresponding to a Sears-Haack body (referred to hereafter as the S-H body) of 12% thickness ratio. The values of geometrical parameters defining each basic configuration are listed in Table 1.

TABLE 1

Configuration	Wing planform	A	c/l
R1	Rectangular	1.40	0.293
R2	"	1.62	0.380
R3	"	1.38	0.467
T	Triangular	2.50	0.500

Modifications in the basic configurations are introduced in order to study the effect of varying a parameter; these modified configurations are designated by R1-t_2 if the wing thickness alone is changed, and so forth. The values of the modified parameters are indicated on each graph presenting the results. Extensive studies of the effects of different geometric parameters have been carried out for configuration R1; the interrelationship among these studies is exhibited in Sketch 1. The symbol (I) denotes the fact that the calculations are made by the indirect method; the results are discussed in a subsequent section.

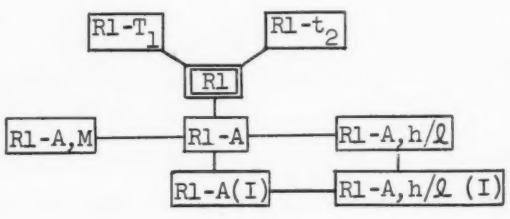

SKETCH 1.

In each configuration, the procedure of calculation is as follows: We first calculate the polar drag $C_{D_{iso}}$ of the isolated system consisting of the given wing and the S-H body in isolated flow, then the wing and the body are brought together to form an interfering configuration and its polar drag $C_{D_{S-H}}$ is evaluated. Lastly, we calculate the minimum drag $C_{D_{opt}}$ of the configuration by shaping the body optimally for each given lift. The results, reduced to coefficient form with respect to wing area, are presented in the figures in the form of these three drag polars. On each of these curves, the point of maximum ratio of lift to drag is indicated by a circle, the vertices of the $C_{D_{S-H}}$ an $C_{D_{opt}}$ curves are indicated by a horizontal dash. In addition, three curves of percentage drag reduction are presented in the same graph. The circle on the abscissa denotes the drag of the isolated S—H body. Two views of the configuration are sketched on the graphs for each of the basic configurations considered, and for those modified configurations in which the geometry of the wing or the gap is changed. The equations of the drag polars for each configuration are listed in reference 14.

The integrals involved in the calculations are evaluated in reference 14. In the single-reflection cases, the integrals are elementary for the rectangular wing and elliptic for the triangular wing. For the two-reflection cases, the value of $\mathbf{V}'_{2F}$ at the body axis is approximated by the asymptotic flow field of the image body. (When $\mathbf{V}'_{2F}$ cannot be evaluated by the method of images, it might sometimes be possible to approximate $\mathbf{V}'_{2F}$ by a flat-plate flow with the average w_{1F}/U_F determining its angle of attack.) The resulting integrals again are elliptic and are evaluated according to reference 15. All calculations are made by taking four terms—i.e., $N = 5$—in the series expansion of $F_{1F}(x)$ and $\Gamma_{1F}(x)$. The rapid convergence of the series terms in the drag expression for the single-reflection cases may be indicated by the value of $C_{D_{opt}}$ obtained in configuration R1-*A*:

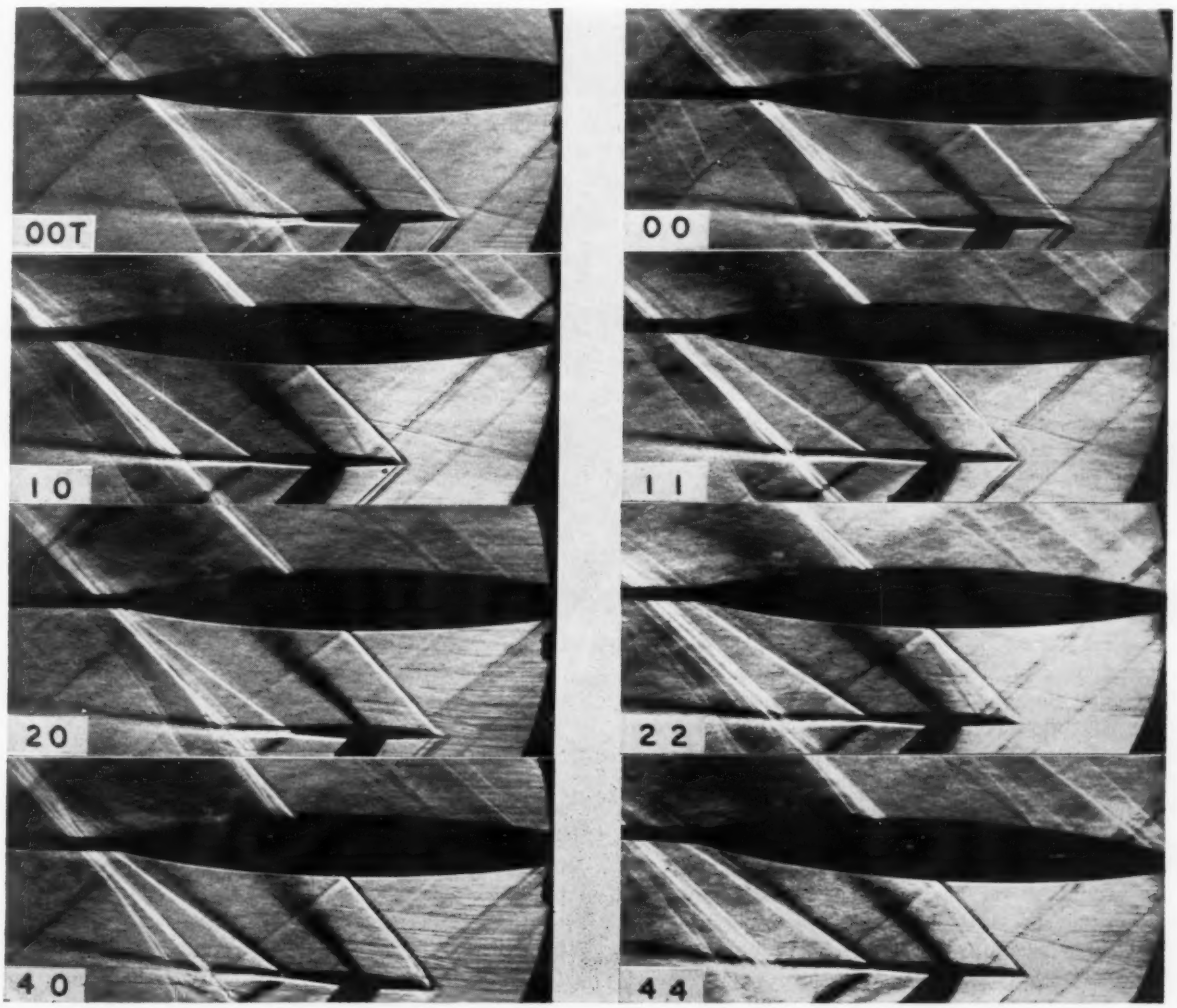

FIG. 18. Schlieren photographs of flow about wing-body configuration (knife-edge horizontal).

$$C_{D_{opt}} = 0.0107 + 0.539(C_L - 0.0178)^2 \quad \text{for } N = 20$$

$$C_{D_{opt}} = 0.0107 + 0.540(C_L - 0.0176)^2 \quad \text{for } N = 5$$

No such comparisons have been made in the case of triangular wings or in any two-reflection cases. A brief discussion of the results obtained for each of the configurations considered is presented below.

Configuration R1: All the features of favorable interference discussed previously are clearly exhibited here (see Fig. 2). The drag polar shifts when the interfering arrangement is assumed by the given wing and body. When the body is contoured optimally, the drag polar shifts again and opens up. The relative drag reduction obtainable is on the order of 25%, however, the advantage gained by contouring the body is small.

Configuration R1-T_1: The effect of changing the body volume to that corresponding to an S—H body of 10.4% thickness ratio on the drag reduction is not pronounced (see Fig. 3). Compared with the previous configuration, the maximum drag reductions from $C_{D_{two}}$ occur at a lower lift coefficient. A useful rule of thumb may be deduced here: the maximum relative drag reductions occur at a lift for which the drag of the isolated wing and body are nearly the same. The shape of the optimum body corresponding to $C_L = 0.13$ has been calculated and is presented in Fig. 14a. The body camber is calculated by the slender-body theory approximation, which is justified a posteriori. The body has fore-and-aft symmetry; its cross section is bigger at the two ends and smaller at the middle than that of the S-H body, and its centerline curves up like a circular arc with maximum camber of 2%. The large rate of increase of the cross section and the upward camber in the front result in a higher pressure acting on the rear portion of the wing, while the symmetrical geometry in the rear portion of the body provides a steeper slope for the wing pressure to act on. Of course, the distortions are limited by the self-induced drag.

Configuration R1-t_2: The effect of the wing thickness is studied here by setting the thickness ratio of the wing equal to zero. Fig. 4 shows that the interference drag vanishes by virtue of symmetry and zero thickness of wing. The reduction in drag is due solely to the interference lift, as is manifested by the absence of lateral shifting of the $C_{D_{opt}}$ and $C_{DS\text{-}H}$ curves. An interesting example is offered here. Consider the vertex of the $C_{DS\text{-}H}$ curve: it represents, an S-H body configuration with a level flat plate placed centrally above. This configuration has the drag of an S-H body, which is minimal for given volume and length, while at the same time a lift of $C_L = 0.033$ is generated on the flat plate by the flow field of the body.

Configuration R1-A: When the aspect ratio of the wing is increased, the effectiveness of the favorable interference due to the body is reduced (Fig. 5). The reasons are twofold: first, the region of interaction becomes relatively smaller as the aspect ratio is increased, and second, the wing is so efficient in carrying the lift that the optimum configuration does not require body distortions for good lift interference. The results shown in Fig. 5 are to be expected. All three relative drag reductions are smaller than in the preceeding configurations. The large aspect ratio is needed also for the off-design case, the low-gap case, and the case in which the inverse method is used. For all the configurations considered thus far, the most favorable drag reduction from that of the isolated system is on the order of one-half the drag of the isolated S-H body.

Configuration R1-A,M: To study the off-design conditions, the drag of the optimum configuration corresponding to $C_L = 0.14$ in R1-*A* is calculated at the reduced Mach number of 1.73 (Fig. 5). The polar drag of the S-H configuration is also calculated for that speed. For a meaningful comparison with the results obtained at design speed, the off-design force coefficients are normalized with respect to the original dynamic pressure and are presented also in Fig. 5, with the diamond point representing the off-design optimum configuration. Off design, this configuration evidently has a higher drag than that of the S-H configuration at the same lift because the optimum body is distorted in a special manner to give the minimum drag only for a particular design condition. When the speed is increased from that of the design condition, it is conjectured that the favorable interference decreases since the regions of interaction both on the wing and on the body become smaller.

Configuration R1-A,h/l: When the gap is reduced, the interference becomes much more favorable (see Fig. 6). All three relative drag reductions are larger than those in configuration R1-*A* except at very low lift; the maximum drag reduction for $C_{D_{opt}}$ has increased from 20% in R1-*A* to 32%. The importance of body distortions is shown by the large relative drag reduction of $C_{D_{opt}}$ from $C_{DS\text{-}H}$, with an average value of 7% and a maximum of 9%. Two factors are responsible for the more favorable effects: (1) the larger interference lift due to the larger region of influence of the body on the wing, and (2) the favorable interference drag due to $\mathbf{V}'_{2F}$. In this case, interference drag due to the wing thickness is not important.

Configuration R2: This case, given in Fig. 7, is studied primarily to provide a basis of comparison for the next study, in which the gap is reduced. The choice of parameters is such as to give the minimum gap and span under the limitations we have specified. The main features of these results resemble those of configuration R1.

Configuration R2-h/l: In this case, shown in Fig. 8, the gap is reduced to $0.155l$, or 1.3 times the maximum diameter of the body. The maximum drag reduction for the optimum configuration is increased from 26% to 44%. The favorable effects obtained by body distortions are even more pronounced than those of configuration R1-*A,h/l;* the relative drag reduction from $C_{DS\text{-}H}$ is on the order of 20% with a maximum of 26%. By comparing the $C_{DS\text{-}H}$ curve with that of the

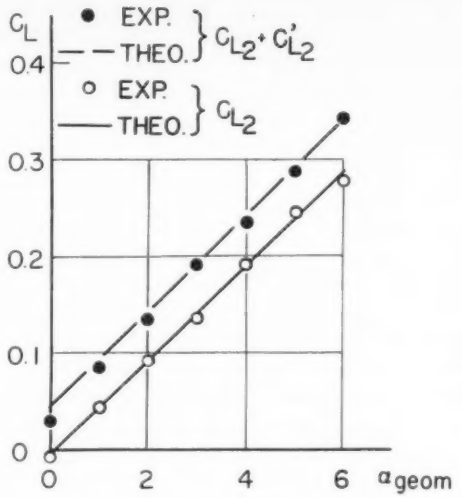

FIG. 19. Experimental lift on wing.

configuration R2 (Fig. 7), it is seen that below $C_L = 0.08$, the drag of the low-gap configuration is greater than that of the configuration with large gap. This illustrates the fact that reflecting the body flow field onto the body again is not necessarily advantageous if the body is not optimally contoured. The calculated shape of the optimum body corresponding to $C_L = 0.12$ is presented in Fig. 14b. The body is no longer symmetric about the plane $x = l/2$. The slender-body approximation is used to obtain the shape of the centerline, which is wavy and bends upward in the rear portion of the body. This shape may be affected by the asymptotic approximations for $\mathbf{V}'_{2F}$.

Configuration R3: The results of this study (see Fig. 9), together with those obtained for R1 and R2, indicate that in configurations of a body with a rectangular wing, when the gap is restricted to give a single reflection, the drag reduction from that of the isolated system is insensitive to variations of the wing chord-body length ratio c/l.

Configuration R3-h/l: Since the gap in this configuration (Fig. 10) is the same as that in configuration R1-A,h/l, the results obtained in the two configurations do not differ greatly even though the planforms are different. From the three low-gap studies, it may be concluded that the gap distance is of great importance in obtaining favorable interference, and the most favorable drag reduction is on the order of the drag of the isolated S-H body.

Configuration T: The asymmetry of the triangular wing introduces no radical changes in the results (see Fig. 11). The relative drag reduction is about 25%, and the advantages gained by body distortions are small.

Configuration T-T_1: It is seen in Fig. 12 that the effect of reducing the volume of the body is much the same as for the rectangular wing. The rule of thumb deduced from configuration R1-T_1 applies in configurations with a triangular wing also. The shape of the optimum body at $C_L = 0.14$ is calculated and presented in Fig. 14c. The slender-body approximation is used to obtain the camber. The cross section, compared with that of the S-H body, is greater over the front half and smaller over the rear half. The centerline has almost constant slope up to $x = 0.6l$, and then it becomes horizontal.

Configuration T-c/l: Except for the fact that the maximum relative drag occurs at higher lift (see Fig. 13), which is consistent with the rule of thumb, the effect of reducing the wing chord-body length ratio is not important. We see again that drag reductions are insensitive to c/l for single reflections.

(VII) Conclusions Drawn from Numerical Results

(A) For single-reflection cases involving both types of wing planforms considered, the following conclusions may be drawn:

(1) With the lift coefficient for maximum drag reduction, the drag reduction obtained through interference is about one half the drag of the S-H body in isolated flow.

(2) The advantages gained with body distortions are not important. Therefore, calculations should be made for the S-H configuration, since these are evidently very simple.

(3) When the aspect ratios of the wings are approximately the same, the relative drag reduction from $C_{D_{iso}}$ is not sensitive to variations in c/l and the body volume. However, the maximum relative drag reduction will occur at a lift for which the drag of the isolated wing is nearly the same as that of the isolated S-H body.

(4) When the Mach number of the uniform stream is lowered from the design value, the drag of the off-design optimum configuration is higher than that of the S-H configuration at the same lift.

(B) For the two-reflection cases considered, the following conclusions may be drawn:

(1) The drag reductions obtained were considerably higher than with the larger gaps. At the lift coefficient for maximum drag reduction, the drag of the optimum configuration is less than that of the isolated system by approximately the drag of the S-H body in isolated flow. Fig. 8 shows a maximum drag reduction of 44%.

(2) The effect of body distortions is very important here, although the distortions required are quite moderate. Thus at low C_L the drag of the S-H configuration may be larger for the lower gap than for the higher gap.

(3) The principal contributions to the favorable interference effects are the high interference lift generated on the wing, and the action of the interference flow of the wing $\mathbf{V}'_{2F}$ on the body.

(4) The low-gap case should be studied also for sweptback wings. The improvement obtained by in-

creasing the region of interaction on the wing suggests the possibility of sweeping the wing in such a way that the region of interaction includes the entire planform. The influence of stagger should also be studied.

(VIII) Interference With Mutual Distortion

In this section we shall consider the first formulation of the problem, as discussed in the introduction, in order to compare results. The drag of the two singularity distributions in forward flow is conveniently written according to Eq. (23) of reference 5. In this case the *same singularities* (but with different signs) appear in both flow directions. Eq. (28) results again except that $\mathbf{V}_{2F}' \equiv 0$, and $\mathbf{V}_{2R}$ is reinterpreted as above. No restrictions on orientation or smoothness now appear. The lift of the configuration is given merely by the integral of the wing vorticity. Again we expand the body singularities into four-term Fourier series and seek the optimum coefficients subject to subsidiary conditions (34), (35), and (36). For the single-reflection case R1-A(I), the results are nearly the same as those obtained with the direct formulation in Fig. 16. For the two-reflection case R1-A,h/l(1), the two principal factors responsible for good drag reduction in the direct formulation, namely, the good lift interference and the interference flow field of the wing, are absent here. The results for this case, shown in Fig. 17, are seen to be quite different from those obtained for configuration R1-A,h/l (Fig. 6). The drag reduction in this case, which is due principally to the upwash field of the body acting on the vorticity distribution of the wing, is not as great as that obtained when the direct formulation is used.

(IX) Further Considerations

Although the isolated system is the logical basis with which to compare configurations with S-H and optimum bodies, the question of practical interest is: how do the interfering configurations compare with the conventional wing-body combination? Furthermore, how does the interfering configuration perform when friction is accounted for? We shall now give some estimates for these two effects.

Without going into the details of the interference encountered in a wing-body combination, we make the simple assumption that the portion of the wing blanketed by the body does not incur thickness drag but supports the lift distribution which would normally be found there. To estimate the skin friction, we assume that separation of the boundary layer owing to interaction with the shock systems does not occur. Detailed calculations have been made for the configuration R2-h/l. The Reynolds number was assumed to be 2.65×10^6 per ft, which corresponds to $M = 2.24$ at 50,000 ft, and the length of the body was taken to be 120 ft. Data for a compressible fully turbulent boundary layer along a flat plate[16, 17] were used. It was found that the coefficient of drag due to friction is 0.0044 for the wing-body configuration and 0.0039 for the conventional wing-body combination. The results in the form of drag polars are shown in Fig. 17, where the drag of the wing-body combination $C_{D_{comb}}$, instead of $C_{D_{iso}}$, is the basis for comparison. The maximum drag reduction decreases from 44% to 33% when friction is included. Fig. 17 also shows that at low C_L the S-H configuration has more drag than the wing-body combination.

In the absence of friction, the minimum wave drag of the body of given volume and length (S-H body) decreases indefinitely as the given length is increased indefinitely at constant volume. When friction is taken into account, however, the elongation is accompanied by an increase in friction drag, and there is an optimum fineness ratio, on the order of 20. The same is evidently the case when the body is part of the isolated system and the lift is also given. However, when interference is present, the increase in body length is accompanied by a change in the interference drag which might counterbalance the improvement in the isolated (inviscid) drag of the body. It is interesting to determine whether there would exist then an inviscid minimum drag corresponding to an optimum ratio of the body length to wing chord, l/c. Such a calculation can be made using the three low-gap studies discussed, and it is found that an optimum l/c for maximum lift to drag ratio, $(L/D)_{max}$, does in fact exist. The calculations made for these low-gap cases are modified by changing the wing aspect ratio to 1.85 while keeping the body volume constant at $0.0644c^3$ for all three bodies of different lengths. For each case the polar drag of the optimum configuration is calculated, from which the maximum L/D is determined. The results obtained are shown in Table 2. It is seen that the optimum fineness ratio of the body in an interfering configuration is very much lower than that found in the isolated system or wing-body combination, and this is a decided advantage from the point of view of structural design.

TABLE 2

l/c	h/c	$(L/D)_{max}$	Approximate fineness ratio of body
2.14	0.378	9.4	8
2.63	0.407	10.6	11
3.41	0.603	7.7	17

(X) Experimental Study

The experimental investigation, performed in the Brown University 9 × 9-in. transonic-supersonic wind tunnel, has been described in more detail in reference 18. The design of the configuration tested was based essentially on that of the configuration R1-A,h/l. The rectangular wing with symmetrical diamond profile had a 5% thickness ratio, a 2.05-in. chord, and a 6.82-in. span. The aspect ratio was increased to ac-

commodate the larger nose shock cone issuing from the body at this lower Mach number. The S-H body, which had a 12% thickness ratio and a 7-in. length, was truncated at one end to provide room for a $^3/_{16}$-in. diameter sting. The wing was located centrally above the body; the gap between the centerline of the body and the wing was set at $1^7/_8$ in. The design gap, based on favorable interference considerations, was 1.95 in.; thus an error of about 0.1 in. was introduced during installation. All tests were performed at a Mach number of 1.6 and a Reynolds number of 131,000 per in.

In regard to the boundary-layer flow, no significant separation on the wing was noted for any angle of attack up to 6°, the maximum angle used. Similarly, separation was never observed on the interior side of the body. However, on the exterior side of the body the flow usually separated after interacting with the impinging shock from the wing.

A sequence of schlieren photographs showing the phenomena is presented in Fig. 18. (The pictures show some extraneous shocks due to flow nonuniformity, and, in some cases, spurious streamlines due to compressor oil on the window.) The two numbers on each photograph denote respectively the wing angle of attack and the body angle of attack. The first photograph (00) exhibits the separation discussed. The manner in which the separation occurred suggests that the flow was still laminar up to the zone of interaction. Therefore, a boundary-layer trip which was made of a loop of 0.005-in. diameter wire, was placed $2^1/_2$ in. downstream from the nose. With this trip, as shown in photograph (00T) in Fig. 18, the flow seems to have remained attached after interacting with the shock. (Note that the Prandtl-Meyer fan crosses the region of interest.) This trip was used for the remainder of the tests. When the wing angle of attack was increased to 1°, the flow separated again. As shown by the photographs in the remainder of the left column in Fig. 18, the separation became increasingly pronounced as the wing angle of attack was progressively increased.

In the next sequence of photographs, the angle of attack of both wing and body are progressively increased from zero. This arrangement eliminates cross flow due to wing angle of attack but results in cross flow due to the free stream. The flow on the exterior side of the body first separates as the angles are increased from 0° to 1°; then as the angles are increased to 4° the flow seems to stay practically the same.

The Reynolds numbers for these tests were much lower than for the flight range. At the suggestion of the authors, the Transport Division of the Boeing Airplane Company kindly ran a similar test at a higher Reynolds number (in the range of 9×10^6 based on body length) and also at the higher Mach number of 2.5. Their results were essentially the same as those reported here. It appears, however, that separation was eliminated entirely when the wing and body were pitched together. The separation which occurs when the wing alone is pitched resembles the well-defined vortex pair which appears on an isolated body at sufficiently high incidence to the stream.

It is clear from the evidence that in this case the boundary layer managed to penetrate the incident and reflected shocks on the interior side of the body without separating, and yet it separated on the exterior side where the incident pressure rise at the shock is virtually canceled locally by the reflected cross flow. From this evidence and from what is known about boundary-layer behavior on isolated bodies, one is led to examine the pressure field established on the body by the reflection of the shock-induced cross flow. Consider the equivalent problem of flow past an open-nosed body (with independent internal and external flows) set at a negative angle of attack, $-\alpha$, to the stream; this problem has been treated by Lighthill.[19] We seek the pressure gradient encountered by each fluid particle upon crossing the shock, in terms of the substantial derivative of the pressure coefficient C_p. We obtain at the shock

$$DC_n/Dt = (U\alpha/B^2R)[-\cos\delta - 2B\alpha\sin^2\delta + O(t_1^2 \ln t_1)]$$

in which δ is measured from the top-most point of the cross section. The terms of order $t_1^2 \ln t_1$ are related to the pressure coefficient of a slender body at angle of attack. It is seen that the particles entering the shock on the exterior portion of the cross section encounter a positive gradient, while particles on the interior portion encounter a favorable gradient. The adverse pressure gradient plus the accumulation of material due to the cross flow cause the flow to separate there.

We now see that the separation may be avoided in practice by kinking the body to accommodate cross flow due to wing incidence and thickness, and/or by pitching the body. We may kink the body for wing thickness and pitch the body with the wing; the latter is automatic in an actual aircraft configuration, since the body and the wing would be connected by struts. However, if the body is pitched with the wing, the separation evidenced on an isolated body at incidence to the stream may occur. Therefore it seems more advisable to kink the body for wing thickness and design angle of attack without pitch; for angles of attack other than the design angle, the wing cross flow arising from this deviation is eliminated by pitching the body with the wing.

Lift measurements on the wing, both in isolated flow and in the arrangement with the body, are presented in Fig. 19 in coefficient form as a function of geometric angle of attack $\alpha_{geom.}$ The theoretical lift coefficient for the isolated wing C_{L2} is calculated according to linear theory. The additional or interference lift on the wing due to the body flow field, C_{L2}' is calculated according to Eq. (22) as 0.05. (Estimates of the nonlinear wave propagation, which effectively shifts the range of integration in the equation, suggest that the correction is on the order of 0.005. This is

seen to be the order of discrepancy in Fig. 19.) These straight lines were shifted by about 0.1° to the true zero angle of attack. The measurements are seen to be in excellent agreement with the predicted values.

References

[1] Ferri, A., Clarke, J. H., and Ting, L., *Favorable Interference in Lifting Systems in Supersonic Flow*, Journal of the Aeronautical Sciences, Vol. 24, No. 11, pp. 791–804, November 1957.

[2] Ferri, A., *Recent Theoretical Work in Supersonic Aerodynamics at the Polytechnic Institute of Brooklyn*, pp. 341–362 of "Proceedings of the Conference on High-Speed Aerodynamics, January 20–22, 1955," Polytechnic Institute of Brooklyn, Brooklyn, N.Y., 1955.

[3] Ferri, A., Clarke, J. H., and Casaccio, A., *Drag Reduction in Lifting Systems by Advantageous Use of Interference*, PIBAL Rep. No. 272, Polytechnic Institute of Brooklyn, May 1955.

[4] Busemann, A., *Atti del V. Convego "Volta,"* Reale Accademia d'Italia, Rome, 1935.

[5] Clarke, J. H., *Reverse Flow and Supersonic Interference*, J. Fluid Mech., Vol. 6, Part 2, pp. 272–288, August 1959.

[6] Ward, G. N., *Linearized Theory of Steady High-Speed Flow*, Cambridge University Press, Cambridge, England, 1955.

[7] Lomax, H., and Heaslet, M. A., *Recent Developments in the Theory of Wing-Body Wave Drag*, Journal of the Aeronautical Sciences, Vol. 23, No. 12, pp. 1061–1074, December 1956.

[8] Clarke, J. H., *Forces on Wing-Fuselage Combinations in Supersonic Flow*, Boeing Scientific Research Laboratories, Flight Sciences Laboratory Report No. 11, August 1959. To appear in the Journal of Fluid Mechanics.

[9] Ursell, F., and Ward, G. N., *On Some General Theorems in the Linearized Theory of Compressible Flow*, Quart. J. Mech. and Appl. Math., Vol. 3, pp. 326–348, September 1950.

[10] Clarke, J. H., *On the Application of the Ursell-Ward Theorem to Wings with Edge Forces*, Readers' Forum, Journal of the Aero/Space Sciences, Vol. 26, No. 7, July 1959.

[11] Lomax, H., and Heaslet, M. A., *A Special Method for Finding Body Distortions that Reduce the Wave Drag of Wing and Body Combinations at Supersonic Speeds*, NACA Report 1282, 1956.

[12] Courant, R., and Hilbert, D., *Methods of Mathematical Physics*, Vol. I, p. 175; Interscience Publishers, New York, 1953.

[13] Sears, W. R., *On Projectiles of Minimum Wave Drag*, Quart. Appl. Math., Vol. 6, No. 4, pp. 361–366, January 1947.

[14] Chen, C. F., and Clarke, J. H., *A Study of Configurations Composed of a Body Under a Lifting Wing in Supersonic Flow*, AFOSR-TN-1276, Division of Engineering, Brown University, January 1960.

[15] Heuman, C., *Tables of Complete Elliptic Integrals*, J. Math. Phys., Vol. 20, No. 2, pp. 127–206, April 1941.

[16] Schlichting, H., *Boundary Layer Theory*, p. 439; McGraw-Hill Book Co., Inc., N.Y., 1955.

[17] Frankl, F., and Voishel, V., *Turbulent Friction in the Boundary Layer of a Flat Plate in a Two-Dimensional Compressible Flow at High Speeds*, NACA TM 1053, December 1943.

[18] Chen, C. F., *Tests of a Configuration Composed of a Body Under a Lifting Wing in Supersonic Flow*, AFOSR-TN-1275, also Technical Report WT-31, Division of Engineering, Brown University, February 1960.

[19] Lighthill, M. J., *Supersonic Flow Past a Slender Body of Revolution the Slope of Whose Meridian Section Is Discontinuous*, Quart. J. Mech. Appl. Math. Vol. 1, No. 1, pp. 90–102, 1948.

✦ ✦ ✦

The Newtonian Approximation

(*Continued from page 546*)

This last equation gives the ratio of heats transferred with and without a magnetic field at the stagnation point, and is quoted from references 1 and 2 where it was originally established in order to show the full significance of the parameter Z in both the viscid and inviscid regions.

References

[1] Lykoudis, P. S., *On a Class of Magnetic Boundary Layers*, Proceedings of the 1958 Heat Transfer and Fluid Mechanics Institute, University of California, pp. 176–186, June 1958.

[2] Lykoudis, P. S., *On a Class of Compressible Laminar Boundary Layers with Pressure Gradient for an Electrically Conducting Fluid in the Presence of a Magnetic Field*, Proceedings of the IXth International Astronautical Congress, Amsterdam, 1958; Springer Verlag, pp. 168–180.

[3] Bush, W. B., *Magnetohydrodynamic-Hypersonic Flow Past a Blunt Nose*, Journal of the Aero/Space Sciences, Vol. 25, No. 11, pp. 685–690, November 1958.

[4] Lykoudis, P. S., *The Matching of the Viscid and Inviscid Regions for the Stagnation Magnetic Flow*, Journal of the Aero/Space Sciences, Vol. 26, No. 5, pp. 315–316, May 1959.

[5] Lykoudis, P. S., and Schmitt, P. J., *Unsteady Compressible Magnetic Laminar Boundary Layers in Hypersonic Flow*, Proceedings of the Xth International Astronautical Congress, London, Springer Verlag, pp. 604–624, 1959.

[6] Kemp, H. N., *On Hypersonic Stagnation Point Flow with a Magnetic Field*, Journal of the Aeronautical Sciences, Readers' Forum, Vol. 25, No. 6, pp. 405–407, June 1958.

[7] Freeman, N. C., *On the Flow Past a Sphere at Hypersonic Speed with a Magnetic Field*, Journal of the Aero/Space Sciences, Vol. 26, No. 10, pp. 670–672, October 1959.

[8] Kemp, H. N., *Author's Reply*, Journal of the Aero/Space Sciences, Vol. 26, No. 10, p. 672, October 1959.

[9] Ziemer, R. W., *Effects of a Magnetic Field on the Hypervelocity Flow about a Blunt Body*, Space Technology Laboratories GM-TR-0165-00464, August 1958.

[10] Hayes, W. D., and Probstein, R. F., *Hypersonic Flow Theory*, pp. 150–162; Academic Press, New York, 1959.

✦ ✦ ✦

A Summary of the Supersonic Pressure Drag of Bodies of Revolution

DEANE N. MORRIS*

Douglas Aircraft Company, Inc.

Summary

A number of approximate theories for supersonic and hypersonic flow over bodies of revolution at zero angle of attack are appraised by a critical comparison with characteristics and second-order results, with the use of hypersonic similarity as a basis for the comparison. Most of the approximate theories are inadequate except over very limited ranges of fineness ratio and Mach number. The combination of second-order supersonic theory and second-order shock-expansion theory provides consistently good results throughout the supersonic speed range.

On the basis of exact (or nearly exact) supersonic solutions and a limited amount of test data and theory in the transonic region, summary design curves are developed that give the pressure drag of conical and ogive noses and conical and ogive boattails over the complete range of transonic, supersonic, and hypersonic Mach numbers. Other shapes can be analyzed in the same manner, provided that an equivalent amount of data is available.

The analysis is made with the assumption of inviscid flow, so that the effects of boundary-layer growth, shock-boundary-layer interaction, and flow separation are not included. The present correlations provide a sound basis of inviscid-flow results from which these additional viscous effects can be evaluated.

Symbols

C_{D_p} = pressure drag coefficient based on maximum cross-sectional area
C_p = pressure coefficient $= (p - p_\infty)/q_\infty$
d = maximum diameter of body
FR = fineness ratio $= l/d$
K_H = β/FR_N (see Eq. 5)
K_S = see Eq. (6)
l = length of body
M = Mach number
p = static pressure
q = dynamic pressure $= (\gamma/2)pM^2$
r = local radius of body
R = maximum radius of body
U = velocity
β = $\sqrt{M_\infty^2 - 1}$
γ = ratio of specific heats
θ_N = half-angle of body nose (see Fig. 1)

Subscripts

∞ = free-stream value
BT = boattail
C = center section
N = nose

Introduction

A FEW YEARS AGO, the problem of calculating the pressure distribution and pressure drag of a body of revolution at zero angle of attack in supersonic flow was a subject of considerable discussion among aerodynamicists. Many approximate methods of solution were proposed, but the absolute accuracy of the approximations remained in doubt. Reliable test data were lacking and, although the method of characteristics was available, the complexity of a characteristics solution was a strong deterrent to its widespread use.

Today, the fundamental problems of inviscid axially symmetric flow can be analyzed on a rational and straightforward basis. This situation is due principally to the developments of the second-order and shock-expansion theories, the use of high-speed computing machinery, and the application of the hypersonic similarity laws. It is the purpose of this paper to reappraise briefly the accuracy of the approximate supersonic theories (as well as several approximations for hypersonic flow) and to develop from the analysis a set of semiempirical curves for the pressure drag of bodies of revolution.

Hypersonic Similarity

Summaries of the hypersonic similarity law may be found in numerous articles in the current literature[1-3]; the fundamental derivation of the rules was originally presented by Tsien[39] and Hayes.[40] As applied to the pressure drag at zero angle of attack of slender bodies of revolution of the same family shape, the law states that the drag parameter $M_\infty^2 C_{D_p}$ is a function only of the hypersonic similarity parameter M_∞/FR, provided that the free-stream Mach number is large compared to one. The limits of application of the hypersonic similarity law were investigated,[2, 3] and it was established that similarity existed for much smaller Mach numbers and fineness ratios than the theoretical derivation would suggest. Later, Van Dyke[4] showed that the hypersonic and supersonic similarity rules can be combined artificially, thus extending the limits of validity of hypersonic similarity nearly to transonic speeds. This unification is accomplished simply by replacing the Mach number M_∞ in the similarity parameters by $\beta = \sqrt{M_\infty^2 - 1}$. If the pressure-drag parameter is multiplied first by the square of the hypersonic similarity parameter, the net result is:

$$C_{D_p}(FR)^2 = f(\beta/FR) \qquad (1)$$

Received April 5, 1960; based on a paper originally submitted March 18, 1958.

* Consulting Engineer, El Segundo Division, now with The RAND Corporation.

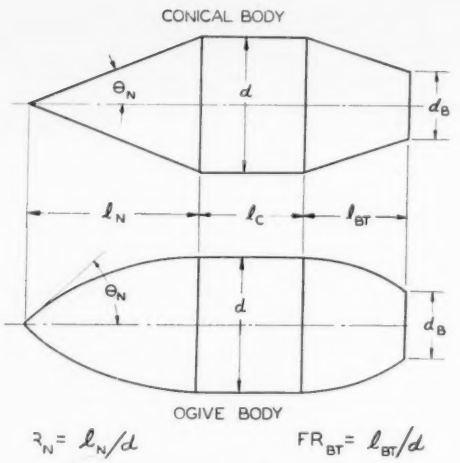

FIG. 1. Geometry of bodies of revolution.

Strictly speaking, Eq. (1) is in supersonic similarity form, but the term hypersonic similarity will be retained in order to emphasize the extension to hypersonic flow. The term β/FR will be referred to hereafter as the hypersonic similarity parameter.

On the basis of a comparison with the results of Newtonian impact theory, Van Dyke has suggested a further improvement in the hypersonic similarity rules,[6] particularly for thicker bodies. Hypersonic similarity theory indicates that the pressures (and the pressure drag) are proportional to the square of the tangent of the body-surface slope. However, impact theory assumes that the pressures are proportional to the square of the sine of the surface slope of the body. Van Dyke shows that much better correlation is obtained for cones if the hypersonic similarity rule is modified to a sine-squared variation. For cones of semivertex angle θ_N, the relations between the nose angle and the nose fineness ratio are (see Fig. 1)

$$\tan^2 \theta_N = 1/4(FR_N)^2$$

$$\sin^2 \theta_N = 1/4[(FR_N)^2 + (1/4)]$$

For cones, then, the tangent implicit in the left-hand side of Eq. (1) is replaced by the sine simply by rewriting it in the form:

$$C_{D_p}[(FR_N)^2 + (1/4)] = f(\beta/FR_N) \qquad (2)$$

In the case of ogive nose shapes, the geometry is not quite so clear-cut, but Eq. (2) would represent a sine-squared variation with regard to the nose angle of the inscribed cone. Further modifications will be discussed later.

In correlating the data, it is desirable to cover as wide a range of variables as possible in a single plot. To accomplish this without loss of accuracy, the independent variable in all plots is the hypersonic similarity parameter β/FR for a range from zero to one; then this parameter is *inverted*, to FR/β, for a range of values from one to zero. In this way the graph covers the Mach number range from one to infinity.

Conical Noses

The pressure drag of the axially symmetric cone in supersonic flow will be considered first, since exact results, in the form of the Taylor-Maccoll solutions, are readily available. A number of approximate solutions for cones are shown in Fig. 2, plotted in hypersonic similarity form. It should be noted that changes in the parameters such as the replacement of tan θ_N by sin θ_N are indistinguishable in all of the approximate theories, since the body is invariably assumed to be "slender."

The limits of validity of each of the approximate theories have usually not been specified by the authors, and in general cannot be exactly defined. Therefore, most of the theoretical curves have been terminated arbitrarily at $\beta/FR_N = 1$, although this is not meant to imply that the theories are valid to this value of the similarity parameter. The later comparisons with exact theory will allow an estimate of the regions of validity of each theoretical result.

It will be noticed also that both "linear" and "first-order" results are shown for a number of the theories. While it is now generally agreed that the linear solutions are basically incorrect, they are quite well known and it seems advisable to retain them in this comparison.

The linear slender-body theory is that presented by von Kármán.[7] Written in hypersonic similarity form, the expression for pressure drag is

$$C_{D_{pN}}(FR_N)^2 = (1/2) \ln (4FR_N/\beta) \qquad (3)$$

The first-order result is obtained directly from linear theory by retaining an additional term in the expression for the pressure coefficient. The relation for pressure drag becomes

$$C_{D_{pN}}(FR_N)^2 = (1/2) \ln (4FR_N/\beta) - (1/4) \qquad (4)$$

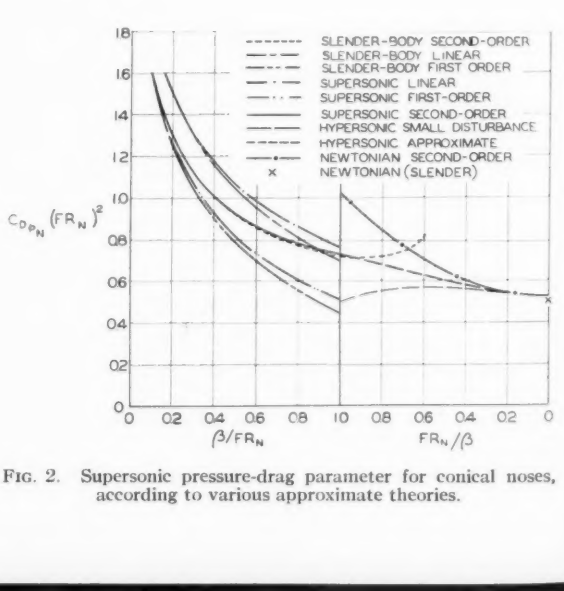

FIG. 2. Supersonic pressure-drag parameter for conical noses, according to various approximate theories.

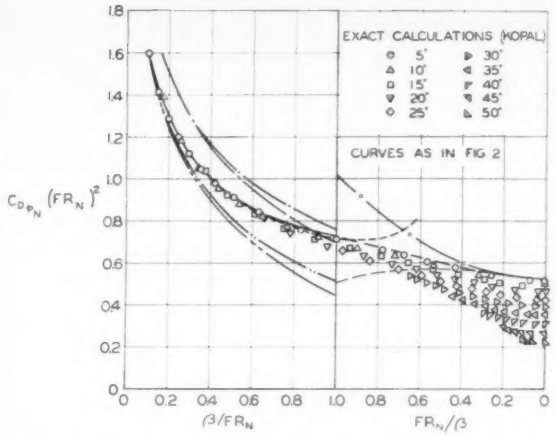

FIG. 3. Supersonic pressure-drag parameter for conical noses. Comparison of exact and approximate theories.

The second-order slender-body theory of Broderick,[41] when reduced to hypersonic similarity form, results in

$$C_{D_{pN}}(FR_N)^2 = (1/2)\ln(4FR_N/\beta) - (1/4) + (1/16)(\beta/FR_N)^2[3\ln^2(4FR_N/\beta) - 5\ln(4FR_N/\beta) + (113/20)] \quad (5)$$

The supersonic linear and first-order theories are given by the respective formulas

$$C_{D_{pN}}(FR_N)^2 = \frac{[\cosh^{-1}(2FR_N/\beta)]}{\sqrt{4 - (\beta/FR_N)^2}} \quad (6)$$

$$C_{D_{pN}}(FR_N)^2 = \frac{[\cosh^{-1}(2FR_N/\beta)]}{\sqrt{4 - (\beta/FR_N)^2}} - (1/4) \quad (7)$$

The supersonic second-order solution is derived from Van Dyke's Eqs. (13) and (14) of reference 8. Neglecting higher-order terms and assuming that $M^2 = \beta^2$ in certain places, the pressure drag of a cone can be written (with $K_H = \beta/FR_N$)

$$C_{D_{pN}}(FR_N)^2 = \frac{10}{7K_H^2}\left\{1 + \frac{K_H^2}{5}\left[\frac{2K_H^2}{4 - K_H^2} \times \left(1 - \frac{3K_H^2}{10}\right)\left(\frac{\operatorname{sech}^{-1} K_H/2}{\sqrt{4 - K_H^2}}\right)^2 + \left(1 - \frac{K_H^2(40 + K_H^2)}{16(4 - K_H^2)}\right) \times \frac{\operatorname{sech}^{-1} K_H/2}{\sqrt{4 - K_H^2}} + \left(\frac{59K_H^2}{40(4 - K_H^2)} - 1\right)\right]\right\}^{7/2} - \frac{10}{7K_H^2} \quad (8)$$

The hypersonic small-disturbance theory is that presented by Van Dyke[5] in the form of a numerical solution.

The hypersonic approximate theory was proposed by Lees[9] on the basis of an expansion of the conical-flow equations when the shock lies close to the body. The result is:

$$\left.\begin{aligned} C_{D_{pN}}(FR_N)^2 &= \frac{K_S^2 - 4}{(\gamma+1)K_H^2} + \frac{1}{2}\left(\frac{K_S}{K_H} - 1\right)^2\left[\frac{\gamma+1}{\gamma - 1 + (8/K_S^2)}\right] \\ K_S &= \frac{\gamma+1}{\gamma+3}K_H + \sqrt{\left(\frac{\gamma+1}{\gamma+3}\right)^2 K_H^2 + \frac{8}{\gamma+3}} \end{aligned}\right\} \quad (9)$$

where the notation is changed slightly from that of Lees.

In the Newtonian approximation it is assumed that the fluid momentum normal to the surface is entirely lost upon impact, so that the pressures are proportional to the square of the sine of the body-surface slope. For slender cones, this results in:

$$C_{D_{pN}}(FR_N)^2 = 1/2 \quad (10)$$

The second-order Newtonian theory has been proposed by Cole[10] to account for the effect of a value of γ different from one. The formula for the pressure-drag coefficient of cones is:

$$C_{D_{pN}}(FR_N)^2 = \frac{1}{2}\left[1 + \frac{\gamma - 1}{4(\gamma + 1)} + \left(\frac{FR_N}{\beta}\right)^2\right] \quad (11)$$

This is plotted in Fig. 2 for $\gamma = 1.4$.

It should be noted that all of the approximate theories presented above require that the flow be completely supersonic—i.e., that the shock be attached to the cone and that the Mach number behind the shock be greater than one.

It is apparent in Fig. 2 that, plotted in this form, the various approximate theories give considerably different results. The approximate theories are shown again in Fig. 3, and the exact calculations for cones made by Kopal[11] have been plotted on the figure. For moderate supersonic Mach numbers the data for the more slender cones correlate well with the second-order

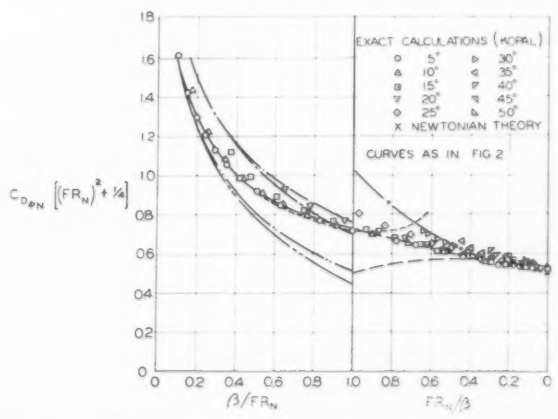

FIG. 4. Supersonic pressure-drag parameter (modified) for conical noses. Comparison of exact and approximate theories.

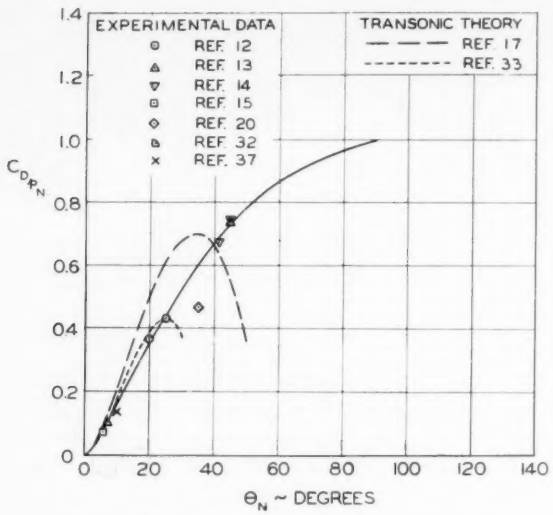

FIG. 5. Pressure drag of conical noses at $M = 1.0$.

theory. At the higher Mach numbers, however, and particularly for the blunter cones, the data diverge into a family of curves. In Fig. 4, the ordinate has been modified to the sine-squared variation represented by Eq. (2), and the calculations of Kopal replotted with the new parameters. The improvement is apparent; the correlation is almost perfect, particularly at the higher Mach numbers. The exact results follow closely the theoretical curves obtained from the second-order and the hypersonic small-disturbance theories, and coincide with Newtonian theory at infinite Mach number.

It would appear that the remaining divergence shown in the figure, which occurs as the Mach number approaches that for shock detachment for a given cone angle, cannot be removed by further changes in the parameters. In this regard it should be noted that the lowest Mach number shown for each cone angle is that at which the surface Mach number is equal to one. In order to obtain the pressure drag for Mach numbers less than this value, it is necessary to resort to experimental data or to transonic theory.

The available data for the pressure-drag coefficients of cone-cylinders at a Mach number of one are plotted in Fig. 5 versus the nose semivertex angle θ_N. The points from references 12–14 have been obtained by extrapolation from results at higher or lower Mach number by use of the principle of stationarity of local Mach number in the transonic region (see below). The result from reference 15 is a value calculated by the relaxation method for a Mach number of one, corrected for an error as discussed in reference 16. The dashed curves in Fig. 5 are the transonic slender-body theories of Miles[17] and Spreiter and Alksne.[33] The solid curve follows the slender-body result of Spreiter and Alksne as far as it appears to be applicable, and then has been faired through the data and terminated at a pressure-drag coefficient of 1.0 for $\theta_N = 90°$, which is a reasonable estimate for the force coefficient at sonic speed on the end of a circular cylinder in axial flow.

These results for a Mach number of one can be extended into the supersonic range by means of the principle of stationarity of flow near a Mach number of one.[18] This principle states that the local flow conditions (Mach number, static pressure) remain constant as the free-stream Mach number varies through a value of one. Neglecting changes in total pressure, the local pressure coefficient at any point on the body is given by

$$C_p = \frac{2}{\gamma M_\infty^2}\left\{\left[1 + \frac{\gamma - 1}{2} M_\infty^2\left(1 - \frac{U^2}{U_\infty^2}\right)\right]^{\gamma/(\gamma-1)} - 1\right\} \quad (12)$$

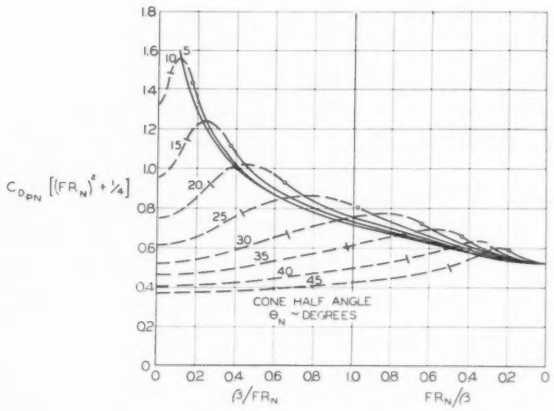

FIG. 6. Supersonic pressure-drag parameter of conical noses.

It is convenient to convert this expression from a relation based on local velocity to one based on local Mach number. By use of the compressible-flow relations,[19] either for isentropic flow or for flow behind a normal shock, the local velocity ratio is given in terms of Mach number by

$$\left(\frac{U}{U_\infty}\right)^2 = \left(\frac{M}{M_\infty}\right)^2 \frac{M_\infty^2 + 5}{M^2 + 5}$$

Then Eq. (12) becomes ($\gamma = 1.4$)

$$C_p = \frac{10}{7M_\infty^2}\left[\left(\frac{M_\infty^2 + 5}{M^2 + 5}\right)^{7/2} - 1\right] \quad (13)$$

The pressure-drag coefficient of an axially symmetric nose of arbitrary shape (based on maximum frontal area) is given by

$$C_{D_{pN}} = \int_0^1 C_p \, d\left(\frac{r}{R}\right)^2 \quad (14)$$

Substituting Eq. (13) into Eq. (14) gives

$$C_{D_{pN}} = \frac{10}{7M_\infty^2}\left[\int_0^1 \left(\frac{M_\infty^2 + 5}{M^2 + 5}\right)^{7/2} d\left(\frac{r}{R}\right)^2 - 1\right] \quad (15)$$

For a free-stream Mach number of one, this becomes

$$(C_{D_{pN}})_{M_\infty = 1} = \frac{10}{7}\left[\int_0^1 \left(\frac{6}{M^2+5}\right)^{7/2} d\left(\frac{r}{R}\right)^2 - 1\right]_{M_\infty = 1} \quad (16)$$

Now, Eq. (15) can be rewritten and expanded in series:

$$C_{D_{pN}} = \frac{10}{7M_\infty^2}\left\{\int_0^1 \left[\left(\frac{6}{M^2+5}\right)^{7/2} + \frac{7}{2}\left(\frac{M_\infty^2-1}{M^2+5}\right)\left(\frac{6}{M^2+5}\right)^{5/2} + \ldots\right] d\left(\frac{r}{R}\right)^2 - 1\right\}$$

$$= \frac{10}{7M_\infty^2}\left\{\left[1 + \frac{7}{12}(M_\infty^2 - 1)\right] \times \int_0^1 \left(\frac{6}{M^2+5}\right)^{7/2} d\left(\frac{r}{R}\right)^2 - 1\right\} \quad (17)$$

where terms of order $(M_\infty^2 - 1)^2$ have been neglected. If it is accepted that the local Mach number is invariant

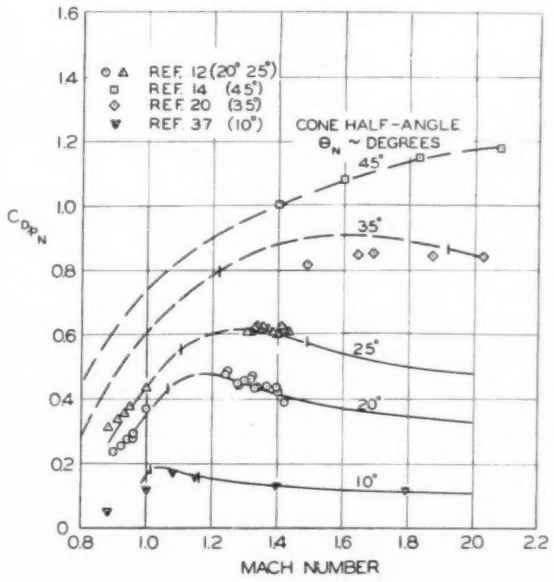

FIG. 7. Comparison of calculated and experimental values of the pressure drag of conical noses.

for free-stream Mach numbers near one, then the integral of Eq. (16) may be substituted into Eq. (17), giving finally

$$C_{D_{pN}} = \frac{7M_\infty^2 + 5}{12\,M_\infty^2}(C_{D_{pN}})_{M_\infty = 1} + \frac{5}{6M_\infty^2} \times (M_\infty^2 - 1) + O[(M_\infty^2 - 1)^2] \quad (18)$$

This result agrees with that of Bryson,[18] in that the slope of the drag curve at a Mach number of one is given by

$$\left(\frac{dC_{D_{pN}}}{dM_\infty}\right)_{M_\infty = 1} = \frac{4}{\gamma+1} - \frac{2}{\gamma+1}(C_{D_{pN}})_{M_\infty = 1} = \frac{5}{3} - \frac{5}{6}(C_{D_{pN}})_{M_\infty = 1} \quad (19)$$

The expansion of Eq. (17) can be extended to the second order in terms of $(M_\infty - 1)$ for comparison with the result of Guderley.[38] This gives

$$C_{D_{pN}} = \left[1 - \frac{5}{6}(M_\infty - 1) + \frac{125}{72}(M_\infty - 1)^2\right] \times (C_{D_{pN}})_{M_\infty = 1} + \left[\frac{5}{3}(M_\infty - 1) - \frac{65}{36} \times (M_\infty - 1)^2\right] + O[(M_\infty - 1)^3] \quad (20)$$

This expression differs from that of Guderley in the coefficient of the third term of the first bracket and in the sign of the second term of the second bracket.

The Mach number region of validity of Eq. (18) is uncertain. On the basis of the limited information available from transonic theory and experiment, it appears that the flow conditions should be approximately invariant for values of the transonic similarity parameter (βFR_N) less than about 1/2. By means of Eq. (18), values of the pressure-drag coefficients for cones from Fig. 5 have been extrapolated into the supersonic range up to the limiting Mach number defined by $\beta FR_N = 0.50$. The results are plotted in Fig. 6 in the modified hypersonic similarity form discussed above, these extrapolations extending from the left axis up to the small tick marks on the curves. Curves for the exact calculations of Kopal in Fig. 4 are shown as solid lines, and the intermediate portions of the

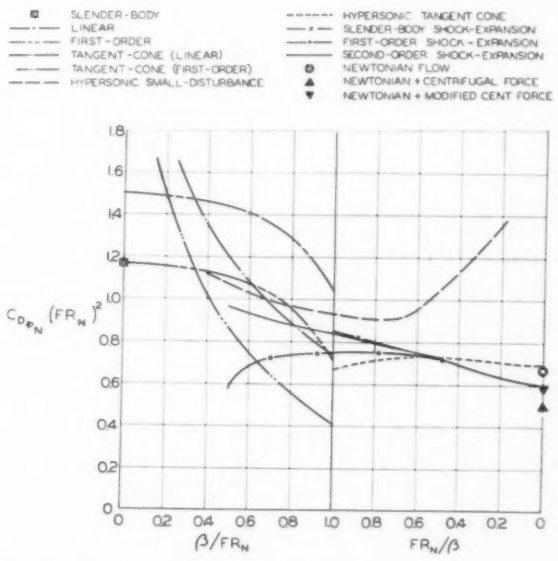

FIG. 8. Supersonic pressure-drag parameter for ogive noses, according to various approximate theories.

curves have been faired. It can be expected that Fig. 6 will give quite accurate values of the pressure-drag coefficient for cones of semivertex angles from 5° to 45°, and for Mach numbers from one to the order of infinity. Of course, at the very high Mach numbers it is necessary to consider effects such as the interaction of the shock wave and the boundary layer, but these considerations are outside the scope of this analysis.

The calculations of Kopal have been compared many times with experimental data for the pressure drag of cones with attached shocks. The general validity and accuracy of these theoretical results are well established, and further comparisons will not be made here. Unfortunately, there are very few reliable results for cones tested in the Mach number range for a detached shock wave. A family of curves for the predicted pressure-drag coefficient of cones is shown in Fig. 7, along with the only test data available (obtained from measured pressure distributions) for the detached shock régime.[12, 14, 20, 37] As a matter of interest, the calculated curves have been extended into the subsonic region as far as the arbitrary limit $\beta FR_N = 0.50$, with the use of the principle of stationarity of flow as given by Eq. (18).

Ogive Noses

The general procedures developed for cones will now be applied to the determination of the pressure drag of ogive noses. Curves for a number of approximate theories for pressure drag of ogives are plotted in Fig. 8 in the standard hypersonic similarity form. In general, closed-form analytic solutions are difficult to obtain

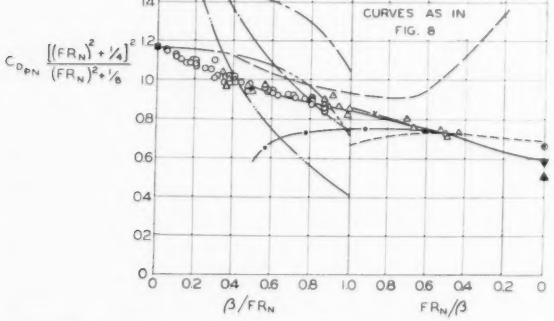

FIG. 9. Supersonic pressure-drag parameter for ogive noses Comparison of exact and approximate theories.

from any of the approximate theories, and most of the results are determined from numerical solutions. All of the approximate treatments (except the Newtonian flow theory) are based on the assumption of a reasonably slender shape, so the differences between a true ogive (circular arc) and an approximate ogive (parabolic arc) are negligible.

The supersonic linear theory, based on linearized source-sink methods, is given by Jones and Margolis[21] for a parabolic-arc body of revolution. The supersonic first-order theory is obtained directly from the linear results by the usual modification of the approximate expression for pressure coefficient, with the result that the pressure-drag parameter from first-order theory is less than that from linear theory by a constant term (1/3).

The supersonic and hypersonic tangent-cone theories have been proposed by Probstein and Bray.[22] The

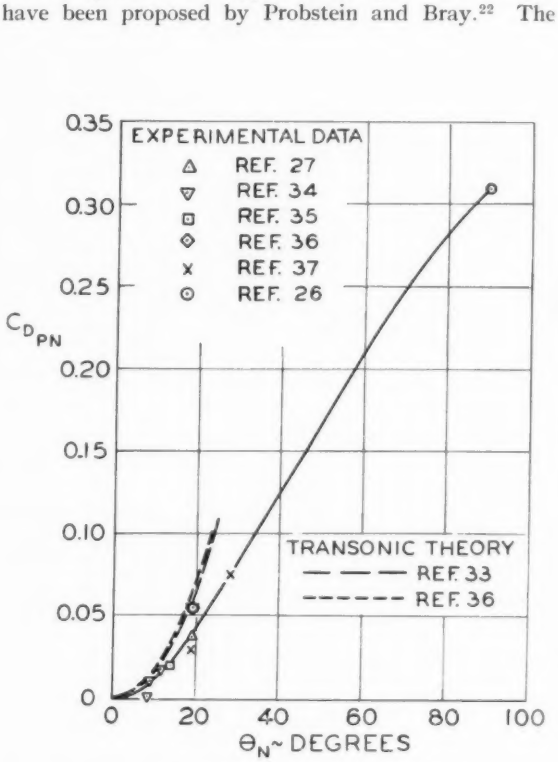

FIG. 10. Pressure drag of ogive noses at $M = 1.0$.

tangent-cone approximation is applied to slender parabolic-arc noses using the results for cones from the supersonic linear theory of von Kármán, Eq. (3), and the hypersonic approximate theory of Lees, Eq. (9). The supersonic first-order result follows in the usual way.

The first-order shock-expansion method was developed by Eggers and Savin.[23] The shock-expansion theory is not limited to slender bodies, but it is specified that the hypersonic similarity parameter (β/FR_N) should be somewhat greater than one. In its complete form the theory cannot be expressed in terms of the hypersonic similarity parameters above, but a slender-body approximation does reduce to hypersonic similarity form. Both results have been plotted in Fig. 8, with the complete theory shown for an average of the computations for nose fineness ratios of 3 and 6.

The second-order shock-expansion theory is given by Syvertson and Dennis.[24] By use of the numerical

methods presented in the reference, the pressure drag of ogives of fineness ratios 3 and 6 has been computed for Mach numbers from 3 to 10. Excellent correlation was obtained between the two sets of computations using the hypersonic similarity parameters, and the resultant curve is that shown in Fig. 8.

The hypersonic small-disturbance theory of Van Dyke[5, 6] has been given in series form for ogive noses, but only the first three coefficients of the series solution have been calculated. Van Dyke has concluded that this is an insufficient number of terms to give satisfactory results, and the relative divergence of the hypersonic small-disturbance curve in Fig. 8 bears out this conclusion.

The slender-body approximation of von Kármán[7] is shown at a Mach number of one, as given by the formula

$$C_{D_{pN}}(FR_N)^2 = 7/6 \tag{21}$$

Newtonian flow theory has been applied to ogive noses at very high Mach Numbers by Young and Huntzicker,[25] Ivey, Klunker, and Bowen,[30] and Eggers, Resnikoff, and Dennis.[31] A direct application of Newtonian (or impact) theory to ogives results in a formula for pressure drag as follows:

$$C_{D_{pN}} = \frac{2}{3}\,\frac{(FR_N)^2 + (1/8)}{[(FR_N)^2 + (1/4)]^2} \tag{22}$$

It has been pointed out by the above authors that the effects of centrifugal force around the curved meridian line have been neglected in this result. If it is assumed that the shock wave lies parallel to the body surface, centrifugal force effects are easily included, and it is

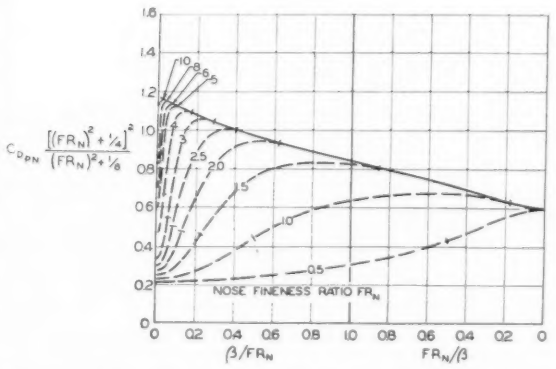

FIG. 11. Supersonic pressure-drag parameter of ogive noses.

found that the predicted drag is just one half of that given by Eq. (22). However, this application results in pressures over parts of the nose that are less than zero. If it is then assumed that a vacuum exists in this region—i.e., that the shock "separates" from the body—Eq. (22) will be modified to give, approximately,

$$C_{D_{pN}} = \frac{1}{2}\,\frac{(FR_N)^2 + (1/8)}{[(FR_N)^2 + (1/4)]^2} \tag{23}$$

Eggers, Resnikoff, and Dennis[31] have presented a modified approach to the inclusion of centrifugal forces in which it is not assumed that the shock is parallel to the body surface, and they thereby avoid the problem of a vacuum and "shock separation." For ogive noses, their result gives

$$C_{D_{pN}} = \frac{2}{3}\,\frac{(FR_N)^2 + (1/8)}{[(FR_N)^2 + (1/4)]^2} \times \left[1 - \frac{1}{8}\,\frac{(FR_N)^2 + (1/20)}{(FR_N)^2 + (1/8)}\right] \tag{24}$$

This is very similar to the results obtained from Young

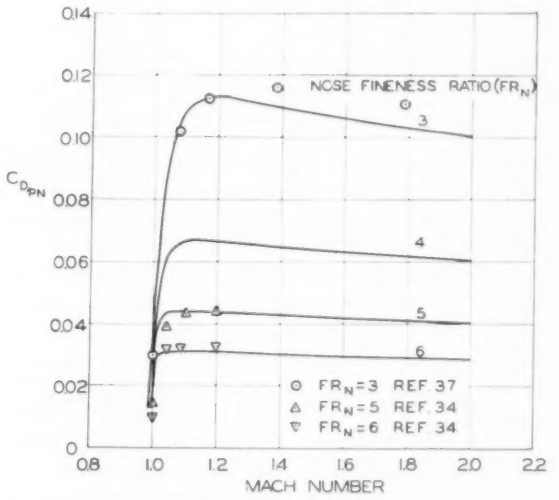

FIG. 12. Comparison of calculated and experimental values of the pressure-drag coefficient of ogive noses.

and Huntzicker's "Case 5".[25] For slender bodies this reduces to

$$C_{D_{pN}} = \frac{7}{12}\,\frac{(FR_N)^2 + (1/8)}{[(FR_N)^2 + (1/4)]^2} \tag{25}$$

Eqs. (22), (23), and (25) have been shown in Fig. 8. It is not yet clear which of these expressions should be used.

The form of Eqs. (22)–(25) suggests that the hypersonic correlation factor for ogives should be modified to $[(FR_N)^2 + (1/4)]^2/[(FR_N)^2 + (1/8)]$. This factor provides the same property for ogives as the factor $1/\sin^2\theta_N = (FR_N)^2 + 1/4$ does for cones, namely, that perfect correlation for all fineness ratios is obtained as the Mach number becomes large.

Just as in the case of the cone solutions, the various approximate theories in Fig. 8 show an appreciable variance in the prediction of pressure drag. In Fig. 9, the approximate theories are compared with exact calculations by the method of characteristics (from published literature) and with calculations made for the present report using Van Dyke's second-order theory. These exact (or nearly exact) calculations

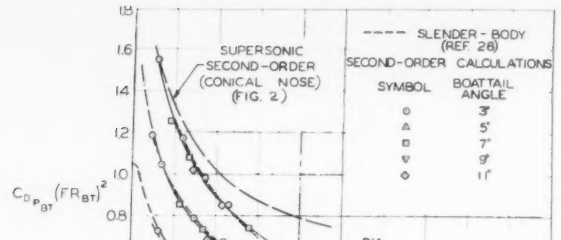

FIG. 13. Supersonic pressure-drag parameter for conical boattails, according to various theories.

have been correlated in the figure by using the modified hypersonic similarity parameter for ogives which was discussed above. A single well-defined correlation curve is obtained which does not agree well with any of the approximate supersonic theories, but is in good agreement with the hypersonic second-order shock-expansion theory.

It is somewhat surprising to note that the exact correlation curve appears to approach the result of slender-body theory at the left axis. The exact calculations are applicable only if the local Mach number behind the attached shock at the nose is supersonic; consequently, the correlation curve at the far left applies only to very slender noses (the last points shown for second-order theory were calculated for ogive noses of fineness ratio 15). Just as for the conical noses, the pressure drag for Mach numbers in the detached-shock region must be obtained from experimental data or transonic theory.

Measured pressure-drag coefficients for ogive noses[26, 27, 34–37] at a Mach number of one are shown in Fig. 10. A faired curve has been drawn through the experimental points, using the transonic slender-body theory of Spreiter[33] as a guide for the more slender noses.

The pressure-drag coefficients at a Mach number of one, obtained from the faired curve of Fig. 10, have been extended into the supersonic region by means of the sonic-stationarity principle represented by Eq. (18). These results are shown in Fig. 11, where the transonic extrapolation extends up to the tick marks on the dashed curves. The solid line is the single correlation curve through the exact calculations shown in Fig. 9, and the dashed curves have been faired into the solid curve at values corresponding to the Mach number for local sonic velocity behind the attached shock wave. Except for the uncertainty regarding the detailed values at a Mach number of one, Fig. 11 will give accurate pressure-drag coefficients for ogive noses of fineness ratios from 0.5 (hemisphere) to 10 and for Mach numbers from one to the order of infinity.

Representative curves of pressure-drag coefficient versus Mach number are shown in Fig. 12, as obtained from the design curves of Fig. 11.

Other Nose Shapes

For application to nose shapes other than the cone and ogive, the correlations of exact and approximate theory have indicated that the second-order supersonic method is reliable for the lower supersonic Mach numbers with attached shock and that the second-order shock-expansion theory provides valid results at the higher Mach numbers. With a few reliable measurements of pressure distribution in the detached-shock region, similar sets of design curves can be prepared for other families of nose shapes.

Boattail

The pressure drag of isolated boattails has been estimated by Fraenkl,[28] who used slender-body theory. In view of the deficiencies of slender-body theory for the prediction of the pressure drag of nose shapes at Mach numbers much above one, it was considered to be desirable to compute the pressure-drag coefficients of isolated boattails using the second-order theory. (In the present context, "isolated boattail" refers to a boattail attached to the rear of a cylinder that extends forward to infinity.)

The results of the second-order calculations for conical boattails are presented in Fig. 13 for various ratios of base diameter to maximum body diameter (some of these data were taken from reference 29). The usual hypersonic similarity parameters have been used, since there appeared to be no theoretical or numerical justification for the sine-squared modification. Also shown in the figure is the curve for a conical nose (supersonic second-order theory) from Fig. 2, the curve representing a vacuum over the entire boattail, and Fraenkl's slender-body results for several diameter ratios. The slender-body theory is surprisingly accurate over a large

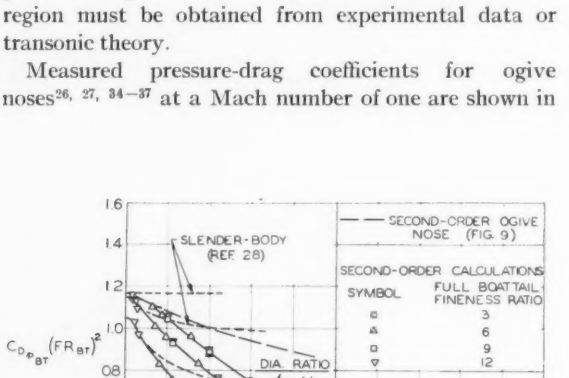

FIG. 14. Supersonic pressure-drag parameter for ogive boattails, according to various theories.

Mach number range. The curves for various diameter ratios in Fig. 13 have been faired tentatively into a Mach number of one ($\beta/FR_{BT} = 0$) but the extrapolations are only speculative at this time.

Similar calculations have been made for ogive boattails and are presented in Fig. 14. It will be noticed that the Fraenkl slender-body theory for boattails is seriously in error except for very slender bodies near a Mach number of one. As in the case of the conical boattails, there are no theoretical or experimental results for boattails with finite diameter ratios at sonic speed, and it is necessary to make tentative extrapolations of the curves to the left axis.

The faired curves of Figs. 13 and 14 are presented without the calculated points in Figs. 15 and 16, which may be considered as design curves for boattail pressure drag. With regard to the parameters used in the figures, it should be noted that the boattail fineness ratio is based on the length from the start of the boattail to the blunt base, and the drag coefficient is based on the maximum cross-sectional area of the body.

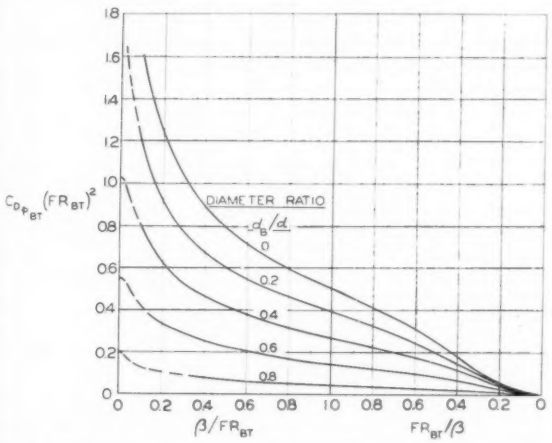

FIG. 15. Supersonic pressure-drag parameter of conical boattails.

It should be borne in mind that viscous effects will often produce large effects on boattail pressures and therefore on pressure drag, and that even the results of second-order theory do not always agree well with the small amount of experimental data that is available on boattails. Whether this disagreement is a result of viscous effects, deficiencies in the theory, or errors in the test data is not clear.

Nose-Boattail Interference

Design curves have been presented for the pressure drag of isolated noses and isolated boattails. It remains to determine the interaction effects for the finite body of revolution—i.e., the nose-boattail interference drag. This subject has been investigated by Fraenkl[28] by use of slender-body theory. Since the previous results have shown that slender-body theory is accurate

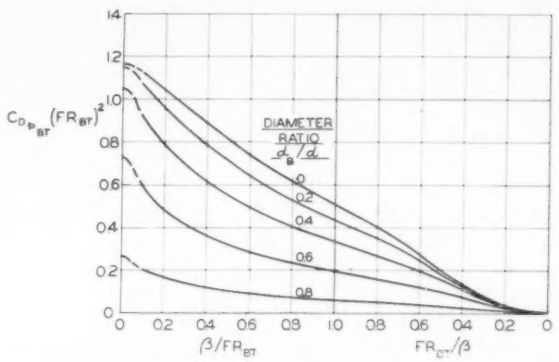

FIG. 16. Supersonic pressure-drag parameter of ogive boattails.

only near a Mach number of one, further investigation by a more nearly exact theory is required. This work has not been completed, but a sample of the type of curve which is obtained is shown in Fig. 17. The drag coefficient $\Delta C_{D_{pBT}}$ represents the additional drag acting upon the boattail due to the presence of the nose. The data were calculated by second-order theory for an ogive-boattail combination with no cylindrical center-section, and are presented for several values of the ratio of boattail length to nose length (this is an extreme case, and the interference drag is larger than might normally be encountered). The curves have been faired into the values obtained from Fraenkl's results at the left side of the graph. Because of the great number of variables involved, many similar figures would be required in order to give a complete presentation of the results.

Conclusions

The summary curves presented in this paper give the pressure drag of conical and ogive noses and conical and ogive boattails over the complete range of transonic, supersonic, and hypersonic Mach numbers. Other shapes can be analyzed in the same manner provided that an equivalent amount of transonic experimental data is available. The analysis has been made with the assumption of inviscid flow, so that the effects of boundary-layer growth, shock-boundary-layer inter-

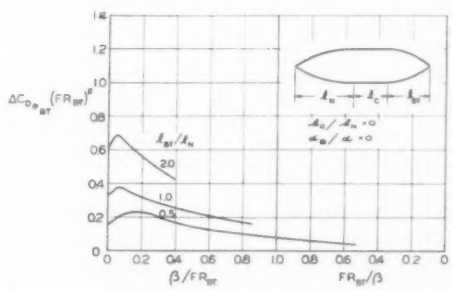

FIG. 17. Supersonic nose-boattail interference-drag parameter for ogive shapes.

action and flow separation are not included in the results. Regions of separated flow will be present to some extent over the rear of most boattail configurations and will affect the pressure drag. At the higher supersonic Mach numbers, interaction between the nose shock wave and the boundary layer will exert an influence on the pressure drag of the nose. However, the present results provide a reliable basis for evaluating the effects of these viscous flow phenomena.

References

[1] Hamaker, F. M., Neice, S. E., and Wong, T. J., *The Similarity Law for Hypersonic Flow and Requirements for Dynamic Similarity of Related Bodies in Free Flight*, NACA Report 1147, 1953.

[2] Ehret, D. M., Rossow, V. J., and Stevens, V. I., *An Analysis of the Applicability of the Hypersonic Similarity Law to the Study of Flow About Bodies of Revolution at Zero Angle of Attack*, NACA TN 2250, December 1950.

[3] Rossow, V. J., *Applicability of the Hypersonic Similarity Rule to Pressure Distributions Which Include the Effects of Rotation for Bodies of Revolution at Zero Angle of Attack*, NACA TN 2399, June 1951.

[4] Van Dyke, M. D., *The Combined Supersonic-Hypersonic Similarity Rule*, Journal of the Aeronautical Sciences, Vol. 18, No. 7, pp. 499–500, July 1951.

[5] Van Dyke, M. D., *A Study of Hypersonic Small-Disturbance Theory*, NACA TN 3173, May 1954.

[6] Van Dyke, M. D., *Applications of Hypersonic Small-Disturbance Theory*, Journal of the Aeronautical Sciences, Vol. 21, No. 3, pp. 179–186, March 1954.

[7] von Kármán, T., *The Problem of Resistance in Compressible Fluids*, Proceedings of the Fifth Volta Congress, Rome, pp. 210–271, 1935.

[8] Van Dyke, M. D., *Practical Calculation of Second-Order Supersonic Flow Past Non-Lifting Bodies of Revolution*, NACA TN 2744, July 1952.

[9] Lees, L., *Note on the Hypersonic Similarity Law for an Unyawed Cone*, Journal of the Aeronautical Sciences, Vol. 18, No. 10, pp. 700–702, October 1951.

[10] Cole, J. D., *Newtonian Flow Theory for Slender Bodies*, The RAND Corporation, Research Memorandum RM-1633, February 1956.

[11] Kopal, Z., *Tables of Supersonic Flow Around Cones*, MIT Department of Electrical Engineering, Center of Analysis, Technical Report No. 1, Cambridge, 1947.

[12] Solomon, G. E., *Transonic Flow Past Cone Cylinders*, NACA TN 3213, September, 1954. Also see Cole, J. D., Solomon, G. E., and Willmarth, W. W., *Transonic Flow Past Simple Bodies*, Journal of the Aeronautical Sciences, Vol. 20, No. 9, pp. 627–634, September 1953.

[13] Seiff, A., and Sommer, S. C., *Experimental Investigation of the Drag of 30°, 60°, and 90° Cone Cylinders at Mach Numbers Between 1.5 and 8.2*, NACA RM A52A14b, April 1952.

[14] Drougge, G., *The Flow Around Conical Tips in the Upper Transsonic Range*, Aeronautical Research Institute of Sweden, FFA Report No. 25, 1948.

[15] Yoshihara, H., *On the Flow Over a Cone-Cylinder Body at Mach Number One*, WADC TR 52-295, November 1952.

[16] Heaslet, M. A., and Spreiter, J. R., *Three-Dimensional Transonic Flow Theory Applied to Slender Wings and Bodies*, NACA TN 3717, July 1956.

[17] Miles, J. W., *On the Sonic Drag of a Slender Body*, Journal of the Aeronautical Sciences, Vol. 23, No. 2, pp. 146–154, February 1956.

[18] Bryson, A. E., Jr., *An Experimental Investigation of Transonic Flow Past Two-Dimensional Wedge and Circular-Arc Sections Using a Mach-Zehnder Interferometer*, NACA Report 1094, 1952.

[19] Ames Research Staff, *Equations, Tables, and Charts for Compressible Flow*, NACA Report 1135, 1953.

[20] Bergdolt, V. E., *Airflow About Cone-Cylinders with Curved Shock Waves*, Journal of the Aeronautical Sciences, Vol. 20, No. 11, pp. 751–756, November 1953.

[21] Jones, R. T., and Margolis, K., *Flow Over a Slender Body of Revolution at Supersonic Velocities*, NACA TN 1081, August 1946.

[22] Probstein, R. F., and Bray, K. N. C., *Hypersonic Similarity and the Tangent-Cone Approximation for Unyawed Bodies of Revolution*, Journal of the Aeronautical Sciences, Vol. 22, No. 1, pp. 66–68, January 1955.

[23] Eggers, A. J., Jr., and Savin, R. C., *Approximate Methods for Calculating the Flow About Non-Lifting Bodies of Revolution at High Supersonic Airspeeds*, NACA TN 2579, December 1951.

[24] Syvertson, C. A., and Dennis, D. H., *A Second-Order Shock-Expansion Method Applicable to Bodies of Revolution Near Zero Lift*, NACA TN 3527, January 1956.

[25] Young, G. B. W., and Huntzicker, J. H., *A Hypersonic Approximation of the Pressure Forces on Ogives*, The RAND Corporation, Research Memorandum RM-770, January 1952.

[26] Sommer, S. C., and Stark, J. A., *The Effect of Bluntness on the Drag of Spherical-Tipped Truncated Cones of Fineness Ratio 3 at Mach Numbers 1.2 to 7.4*, NACA RM A52B13, April 1952.

[27] Danforth, E. C. B., and Johnston, J. F., *Pressure Distribution Over a Sharp Nose Body of Revolution at Transonic Speeds by the NACA Wing Flow Method*, NACA RM L7K12, March 1948.

[28] Fraenkl, L. E., *The Theoretical Wave Drag of Some Bodies of Revolution*, Royal Aircraft Establishment Report No. Aero 2420, May 1951.

[29] Jack, J. R., *Theoretical Pressure Distributions and Wave Drags for Conical Boattails*, NACA TN 2972, July 1953.

[30] Ivey, H. R., Klunker, E. B., and Bowen, E. N., *A Method for Determining the Aerodynamic Characteristics of Two- and Three-Dimensional Shapes at Hypersonic Speeds*, NACA TN 1613, July 1948.

[31] Eggers, A. J., Resnikoff, M. M., and Dennis, D. H., *Bodies of Revolution Having Minimum Drag at High Supersonic Airspeeds*, NACA TN 3666, February 1956.

[32] Page, W. A., *Experimental Study of the Equivalence of Transonic Flow About Slender Cone-Cylinders of Circular and Elliptic Cross Section*, NACA TN 4233, 1958.

[33] Spreiter, J. R., and Alksne, A. Y., *Slender-Body Theory Based on Approximate Solution of the Transonic Flow Equation*, NASA Report 2, 1959.

[34] Taylor, R. A., and McDevitt, J. B., *Pressure Distributions at Transonic Speeds for Parabolic-Arc Bodies of Revolution Having Fineness Ratios of 10, 12, and 14*, NACA TN 4234, 1958.

[35] Drougge, G., *Some Measurements on Bodies of Revolution at Transonic Speeds*, Ninth International Congress of Applied Mechanics, Vol. II, pp. 70–77.

[36] Oswatitsch, K., and Keune, F., *The Flow Around Bodies of Revolution at Mach Number One*, Proceedings of the Conference on High-Speed Aeronautics, Polytechnic Institute of Brooklyn, pp. 113–131, 1955.

[37] Morris, D. N., and Grobli, B. L., *Analysis of Pressure Tests on Sharp- and Blunt-Nosed Bodies of Revolution for Mach Numbers from 0.2 to 3.5*, El Segundo Division, Douglas Aircraft Company Inc., Report No. ES 29700, March 1960.

[38] Guderley, K. G., *Theorie Schallnaher Strömungen*, Springer Verlag, Berlin, 1957.

[39] Tsien, H. S., *Similarity Laws of Hypersonic Flows*, J. Math. & Phys., Vol. 25, No. 3, p. 247, 1946.

[40] Hayes, W. D., *On Hypersonic Similitude*, Quart. J. Appl. Math., Vol. 5, No. 1, p. 105, 1947.

[41] Broderick, J. B., *Supersonic Flow Round Pointed Bodies of Revolution*, Quart. J. Mech. & Appl. Math., Vol. 2, Part 1, pp. 98–120 March 1949.

✦ ✦ ✦

Buckling of a Finite-Length Cylindrical Shell Under a Circumferential Band of Pressure†

B. O. ALMROTH,* AND D. O. BRUSH**

Lockheed Missiles and Space Division

Summary

This paper is concerned with buckling of a circular cylinder of finite length subjected to a symmetrical band of external pressure. Both experimental and theoretical results are presented. The experimental data were obtained from tests of three thin-walled steel cylinders subjected to external pressure by a pneumatic tube encircling the test cylinder at mid-length. The theory is based on the principle of minimum potential energy, and the Rayleigh-Ritz procedure is used to expand the displacement components in trigonometric series.

Theoretical results are given in the form of graphs which show buckling pressure as a function of the following ratios:

Cylinder radius/thickness
Cylinder length/radius
Pressure bandwidth/cylinder length

Theoretical results are in close agreement with existing solutions to special cases in which (1) the pressure is applied over the entire lateral surface, and (2) the pressure is concentrated along a circumferential line. The theoretical results are also in agreement with the test results.

Symbols

a	= mean radius of undeformed shell
h	= thickness of shell
L	= length of shell
b	= width of pressure band
α	= L/a
γ	= a/h
δ	= $b/2a$
E	= Young's modulus
ν	= Poisson's ratio
p	= external pressure
p_{cr}	= critical external pressure
U_m	= membrane strain energy
U_b	= bending strain energy
Ω	= potential energy of external forces
V	= total potential energy ($U_m + U_b + \Omega$)
x, z, ϕ	= dimensionless cylindrical coordinates (see Fig. 1)
$\epsilon_x, \epsilon_\phi, \gamma_{x\phi}$	= strains at a point in the shell's middle surface
$\chi_x, \chi_\phi, \chi_{x\phi}$	= changes of curvature at a point in the shell's middle surface
u, v, w	= dimensionless axial, tangential, and radial displacements of a point in the shell's middle surface. The corresponding distances are au, av, aw. w is positive inward.
ξ, η, ζ	= virtual increments in u,v,w, respectively
A_p	= dimensionless displacement parameters [Eq. (7)]
u_p, v_p	= dimensionless displacement parameters [Eq. (7)]
n, q, p, k	= see Eqs. (6), (7), and (8)
K_{pk}	= see Eq. (12)
$J_1(p, k, n)$, $J_2(p, k)$, $\delta(p, k)$	= see Eq. (10)
λ	= $p_{cr}(1 - \nu^2)/\pi^2 E$
X_n	= prebuckling deflection parameter

Subscripts x or ϕ on displacement components denote partial differentiation.

Introduction

IN MISSILE APPLICATIONS, large-diameter cylindrical shells must be designed to resist loads introduced by handling-and-storage support frames. It is frequently undesirable and sometimes impossible to add internal stiffeners in the shell at the point of load application. In the absence of stiffeners, compressive hoop stresses resulting from the support frame loads can cause the structure to fail by buckling.

This paper presents the results of a theoretical and experimental investigation of the buckling of a circular cylindrical shell subjected to an axially symmetrical band of external pressure. The problem was treated theoretically in reference 1. In that analysis, however, the shell was assumed to be infinitely long, and as a consequence the stabilizing effect of end rings was not included. Shells of finite length are considered here.

The present theoretical analysis is related also to the analysis in reference 2. In that analysis, a more general loading was considered in that the external pressure was not restricted to an axially symmetrical band. The present paper explores more fully the results of the theory for the symmetrical loading than did reference 2, and also includes the results of experimental investigation.

Only a small-displacement buckling theory is considered. The shell is assumed to be quite thin (say, $a/h \geqq 100$) and stresses are assumed to be elastic.

Experiments

In the experimental investigation, three thin-walled steel cylinders were subjected to pressure applied by means of a pneumatic tube encircling the test cylinder at mid-length. Prebuckling stresses as well as buckling mode and critical pressure were observed.

Received April 20, 1960. Revised and received August 18, 1960.

† The experimental portion of this investigation was sponsored by the US Navy Bureau of Ordnance under Contract NOrd 18780(FBM). The authors gratefully acknowledge the able assistance of Mr. H. W. Lutz, Test Engineer, Lockheed Missiles and Space Division, Van Nuys, Calif., who supervised the tests in conjunction with this investigation.

* Research Specialist, Structures Department.

** Staff Scientist, Structures Department.

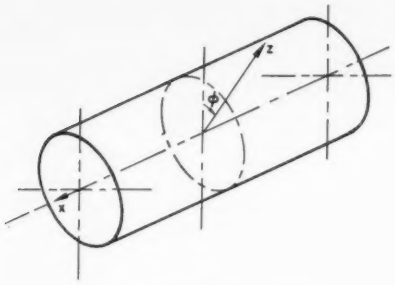

FIG. 1. Coordinate system.

Test Equipment

The test cylinders were fabricated from 4130 steel sheet formed into cylinders 22.00 in. in diameter and 36.0 in. long, and welded with one longitudinal seam. Bulkheads were tack welded in place 1 in. from either end.

The measured wall-thickness of Cylinder Nos. 1 and 2 was approximately 0.035 in. The seam weld on these two cylinders were ground flush. Cylinder No. 3 was fabricated subsequent to completion of tests of the first two cylinders. The measured wall-thickness of this cylinder was approximately 0.029, and the seam weld was not ground. The test setup is illustrated in Fig. 2.

A pneumatic tube made of natural, pure gum rubber was used to apply an axially symmetric band of fluid pressure to the outside of the shell at mid-length. The width of this pressure band was 5 in. The tube was backed up by a restraining frame. A cross section through the tube and backup frame is illustrated in Fig. 3. Air was used to apply pressure after the tube had been filled with water. Forty $^1/_4$-in. SR4, constantan foil, epoxy-backed strain gages were applied to Cylinder No. 2 at the locations shown by Fig. 4.

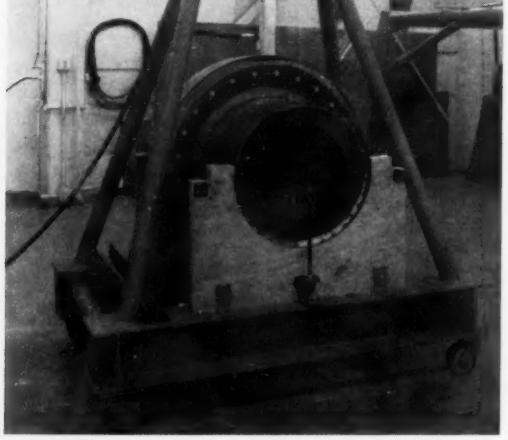

FIG. 2. Test setup.

Test Procedure and Results

The first test cylinder was not instrumented with strain gages. Pressure applied through the pneumatic tube was increased slowly until buckling occurred. The first buckle formed in an area adjacent to the weld at a pressure of 14.7 psi. Three additional buckles formed on the opposite side of the cylinder at 21.5 psi. By 30.0 psi, a complete series of ten equally spaced buckles had formed. A photograph of the buckled shell under a pressure of 30 psi is shown in Fig. 5.

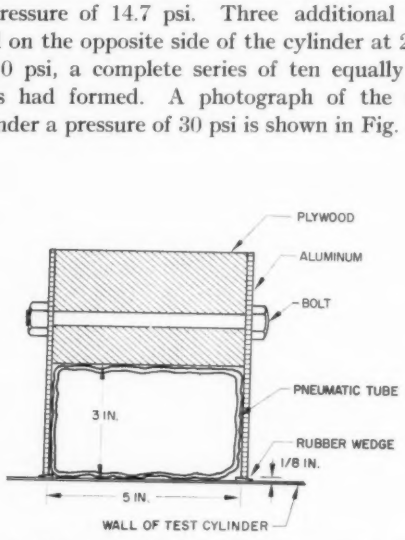

FIG. 3. Typical cross section through pneumatic tube and backup frame.

The second cylinder was instrumented with strain gages (Fig. 4). Pressure was increased slowly, and strain gage readings were recorded at pressure increments of about 5 psi. Recorded circumferential membrane strains at test pressures of 5, 10, and 15 psi are shown in Fig. 8. The first buckle formed near the weld seam at 15.5 psi. A second buckle formed at 19.8 psi, a third at 21.5 psi and a fourth at 22.4 psi. By 30 psi, five additional buckles had formed. The portion of the cylinder in the region of gages 33–34 did not buckle. Pressure/strain plots for two pairs of back-to-back gages which were located at the centers of buckles are shown in Fig. 6.

The third cylinder, unlike the others, was loaded to buckling three times. Between loadings, the applied pressure was reduced to zero and the cylinder was rotated relative to the test equipment. In the first loading, three buckles appeared at 9.8 psi, and a fourth at 10.8 psi. One of the first three was in the region of the seam weld. In the second loading, three buckles again appeared at 9.8 psi. These three, however, were in a different portion of the cylinder circumference from the first three, and the region of the seam weld was not included. In the third load application, the buckles of the preceding loading reappeared, together with a fourth one, at between 9.0 and 9.1 psi.

In all of the tests the buckles extended only a small

distance outside the pressure band and were of uniform size. Each buckle popped in abruptly. The measured pressure was the same immediately before and after each buckle formed. The cylinders continued to accept increased pressure in the post-buckling range. When pressure was removed, the buckles disappeared.

Theory

A theoretical solution to the problem is derived from the same general theory as was used in references 1 and 2. The stability criterion is based on the principle of minimum potential energy. Nonlinear terms necessary for a buckling analysis are introduced in the basic geometric relationships, and the Rayleigh-Ritz procedure is used to reduce the second variation of the potential energy to a quadratic form in the virtual displacement components.

The Potential-Energy Expression

With the notations u,v,w for prebuckling middle-surface displacement components, and ξ,η,ζ for incremental virtual displacements, the strains and changes of curvature in terms of displacements are

$$\left.\begin{aligned}
\epsilon_x &= u_x + \xi_x + {}^1/_2\zeta_x{}^2 = \nu w + \xi_x + {}^1/_2\zeta_x{}^2 \\
\epsilon_\phi &= -w + \eta_\phi - \zeta + {}^1/_2(\eta + \zeta_\phi)^2 \\
\gamma_{x\phi} &= \xi_\phi + \eta_x + \zeta_x(\eta + \zeta_\phi) \\
\chi_x &= w_{xx} + \zeta_{xx} \\
\chi_\phi &= w + \zeta_{\phi\phi} + \zeta \\
\chi_{x\phi} &= \zeta_{x\phi}
\end{aligned}\right\} \quad (1)$$

These expressions are based on Eqs. (5) and (6) in reference 1. In deriving them it is assumed that prebuckling displacements are determined accurately enough by linear theory; thus, second-order terms containing u,v,w and their derivatives are omitted. Furthermore, advantage is taken of the fact that prebuckling displacements are axially symmetrical and that axial stresses before buckling are zero.

The customary expression is used for the total potential energy of the system:

$$V = \Omega + U_m + U_b \quad (2)$$

where Ω is the potential energy of the external forces, and U_m and U_b are the membrane and bending strain energies, respectively. The latter are given by the equations

$$\left.\begin{aligned}
U_m &= \frac{Ea^2h}{2(1-\nu^2)} \times \\
&\qquad \iint\left[\epsilon_x{}^2 + \epsilon_\phi{}^2 + 2\nu\epsilon_x\epsilon_\phi + \frac{1-\nu}{2}\gamma_{x\phi}{}^2\right] dx\, d\phi \\
U_b &= \frac{Ea^2h}{2(1-\nu^2)}\frac{1}{12\gamma^2} \times \\
&\qquad \iint[\chi_x{}^2 + \chi_\phi{}^2 + 2\nu\chi_x\chi_\phi + 2(1-\nu)\chi_{x\phi}{}^2]\, dx\, d\phi
\end{aligned}\right\} \quad (3)$$

For the present analysis, Ω is based on Eq. (10) of reference 1. Integration by parts with respect to ϕ in that equation yields

$$\Omega = pa^2 \int\int [-w + {}^1/_2(w^2 + 2vw_\phi + v^2)]\, dx\, d\phi \quad (4)$$

where v and w represent total displacement components. Introduction of η, $w + \zeta$, and ζ_ϕ, respectively, for u, w, and w_ϕ yields

$$\Omega = pa^3 \int\int \{-(w+\zeta) + {}^1/_2[(w+\zeta)^2 + 2\eta\zeta_\phi + \eta^2]\} dx\, d\phi \quad (5)$$

Insertion of Eqs. (1), (3), and (5) into Eq. (2) yields an expression for the total potential energy from which the second variation is readily obtained in terms of the prebuckling displacement w and the virtual increments ξ,η,ζ.

Trigonometric Expansion of Displacement Components

The prebuckling displacement w may be determined from Eqs. (1) through (4) by use of the principle of stationary potential energy. Expanding w in trigonometric series, and observing that the vector $(\xi,\eta,\zeta) \equiv 0$ before buckling, we obtain

$$w = \frac{p_{cr}}{\pi E} \sum_{n=1,3,5}^{\infty} X_n \cos\left(\frac{n\pi}{\alpha}x\right) \quad (6)$$

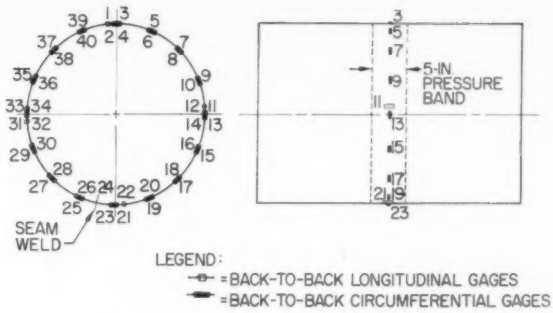

FIG. 4. Strain gage locations.

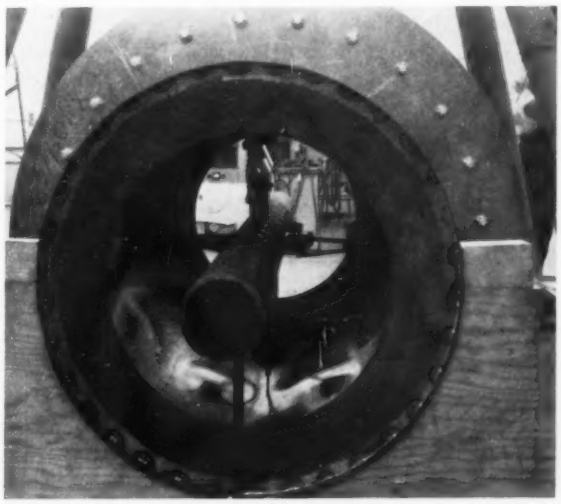

FIG. 5. Buckled shell.

where $X_n = A_n/B_n$

and $A_n = 4(1 - \nu^2)\gamma(1/n) \sin(n\pi\delta/\alpha)$

$B_n = 1 - \nu^2 + (1/12\gamma^2)(n\pi/\alpha)^4$

For the virtual displacement components, the following forms are assumed:

$$\left.\begin{aligned} \xi &= \cos(q\phi) \sum_{p=1,3,5}^{\infty} u_p A_p \sin\left(\frac{p\pi}{\alpha} x\right) \\ \eta &= \sin(q\phi) \sum_{p=1,3,5}^{\infty} v_p A_p \cos\left(\frac{p\pi}{\alpha} x\right) \\ \zeta &= \cos(q\phi) \sum_{p=1,3,5}^{\infty} A_p \cos\left(\frac{p\pi}{\alpha} x\right) \end{aligned}\right\} \quad (7)$$

These expressions are periodic in ϕ, and they satisfy the forced boundary conditions $\eta = \zeta = 0$ at $x = \pm\alpha/2$. They also satisfy the natural boundary conditions $\zeta_{xx} + \nu\zeta_{\phi\phi} = \xi_x + \nu(\eta_\phi - \zeta) = 0$ at $x = \pm\alpha/2$. The parameter q is an integer greater than one; $q = 0$ and $q = 1$ represent respectively axially symmetric buckling and buckling of the cylinder as a column with undistorted cross section. These two cases are not included in the analysis.

Insertion of Eq. (7) into the expression for the total potential energy yields for the second variation the quadratic form

$$\delta^2 V = \sum_{p,k=1,3,5}^{\infty} \sum K_{pk}(p) A_p A_k \quad (8)$$

In the following, the two differential equations expressing equilibrium in the plane of the shell surface are used to determine u_p and v_p. This procedure reduces the size of the final matrix considerably. The source of these equations is discussed in reference 2. They are:

$$\left.\begin{aligned} \nabla^4\xi &= \nu\zeta_{xxx} - \zeta_{x\phi\phi} \\ \nabla^4\eta &= (2 + \nu)\zeta_{xx\phi} + \zeta_{\phi\phi\phi} \\ \text{where} \quad \nabla^4 &= [(\partial^2/\partial x^2) + (\partial^2/\partial\phi^2)]^2 \end{aligned}\right\} \quad (9)$$

Then, with Eq. (9) and the relations

$$\left.\begin{aligned} J_1(p,k,n) &= (-1)^{(p+k+n-1)/2} \times \frac{4pkn}{(p^4 + k^4 + n^4) - 2[(pk)^2 + (kn)^2 + (np)^2]} \\ J_2(p,k) &= \begin{cases} (\pi\delta/\alpha) + [\sin(2p\pi\delta/\alpha)/(2p)] & \text{if } p = k \\ \dfrac{\sin[(p+k)(p\delta/\alpha)]}{p+k} + \dfrac{\sin[(p-k)(p\delta/\alpha)]}{p-k} & \text{if } p \neq k \end{cases} \\ \delta(p,k) &= \begin{cases} 1 & \text{if } p = k \\ 0 & \text{if } p \neq k \end{cases} \end{aligned}\right\} \quad (10)$$

and $$\lambda = p_{cr}(1 - \nu^2)/\pi^2 E \quad (11)$$

we have

$$K_{pk} = \delta(p,k)\left\{\left(u_p\frac{p\pi}{\alpha}\right)^2 + (qv_p - 1)^2 + 2\nu\frac{p\pi}{\alpha}u_p(qv_p - 1) + \frac{1-\nu}{2}\left(qu_p + \frac{p\pi}{\alpha}v_p\right)^2 + \frac{1}{12\gamma^2}\left[\left(\frac{p\pi}{\alpha}\right)^4 + (q^2-1)^2 + 2\left(\frac{p\pi}{\alpha}\right)^2(q^2 - \nu)\right]\right\} - \lambda\left\{2(q - v_p)(q - v_k)\sum_{n=1,3,5}^{\infty} X_n J_1(p,k,n) - 2\pi\gamma[1 - q(v_p + v_k) + v_p v_k]J_2(p,k)\right\} \quad (12)$$

The solution to the buckling problem is thus reduced to finding the eigenvalue, λ, of a matrix of infinite order.

Numerical Analysis

For numerical analysis the matrices must be reduced to a reasonable size. Accordingly, the sequence of values p and k is truncated as follows:

$$p,k = 1, 3, 5, \ldots P$$

where P is chosen to give sufficient accuracy in the final result. The numerical analysis shows that good accuracy is generally obtained with a matrix of rather moderate size.

For each q we have one lowest eigenvalue, λ_q. The smallest of all the λ_q represents the solution of the problem.

In the general expression for the coefficients of the eigenvalue problem [Eq. (12)], an infinite summation of prebuckling deflection parameters appears. It was shown through several numerical examples that, within the range of parameters investigated, extension of this

Table 1

COMPARISON OF RESULTS FROM DIFFERENT ANALYSES FOR b/L = 1

		$10^6\ \gamma\ p_{cr}/E$			
			Present Analysis		
α	γ	Flügge (Ref. 4)	Column A*	Column B**	Batdorf (Ref. 5)
8π	100	32.80	32.87	43.86	40.70
8π	400	4.972	4.974	5.596	5.503
8π	1000	1.111	1.111	1.250	1.161
2π	100	157.7	158.0	168.6	165.9
2π	400	18.11	18.12	18.88	18.52
2π	1000	4.610	4.611	4.743	4.664
$\pi/4$	100	1395	1377	1397	1400
$\pi/4$	400	159.9	159.6	160.4	160.2
$\pi/4$	1000	38.94	38.93	39.06	39.00

* Column A. Second-order terms of Eq. (4) included in potential energy of external forces.
** Column B. Second-order terms of Eq. (4) not included.

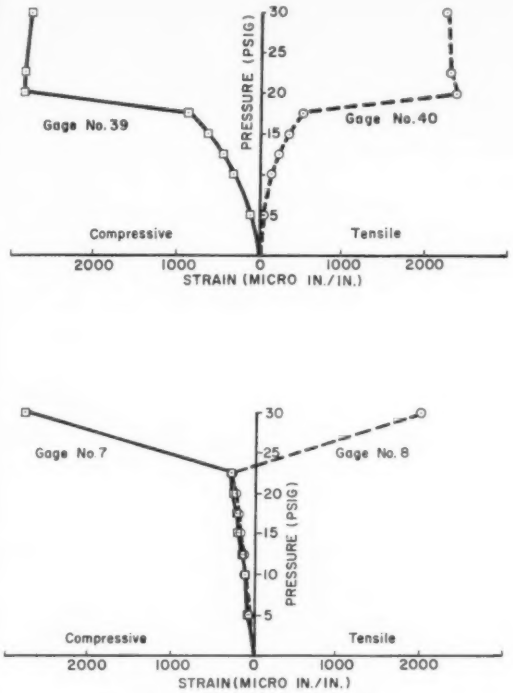

FIG. 6. Pressure/strain plots.

summation beyond the twelfth term has practically no effect on the final result of the computations. Consequently, in the numerical analysis the sequence $n = 1, 3, 5 \ldots$ was limited to $n = 23$.

The most accurate solution to the buckling problem is represented by a matrix of infinite order. The computed buckling pressure decreases with increasing size of matrix. By successively increasing P to a point where the buckling pressure is not significantly affected, we can determine an acceptable minimum size of the matrix. For the same accuracy in the final results, the order of the matrix increases with increasing cylinder length and decreasing pressure bandwidth. In the limiting case $b/L = 1$, the buckling pattern is purely sinusoidal in the axial direction (one half wave over the entire length).

A parameter study based upon this formulation has been performed. A digital computer (Remington Rand 1103A) was used for the numerical work. Results are given in Figs. 7a–7c for the parametric range

$$\pi/4 \leqq \alpha \leqq 8\pi \qquad 100 \leqq \gamma \leqq 1{,}000$$

$$0.01 \leqq b/L \leqq 1.0$$

For smaller values of b/L, the buckling pressure is inversely proportional to the pressure bandwidth.

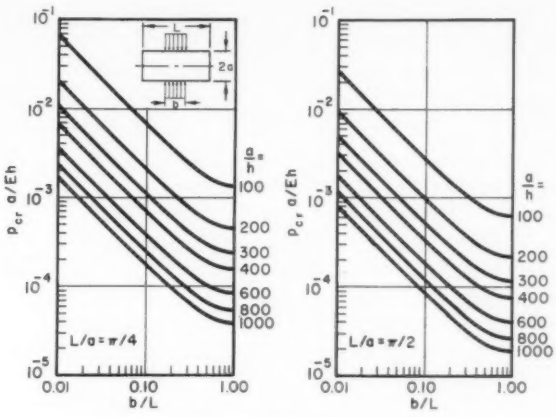

FIG. 7a. Buckling pressures.

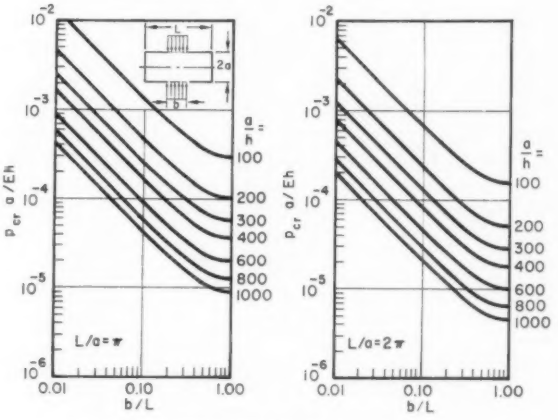

FIG. 7b. Buckling pressures.

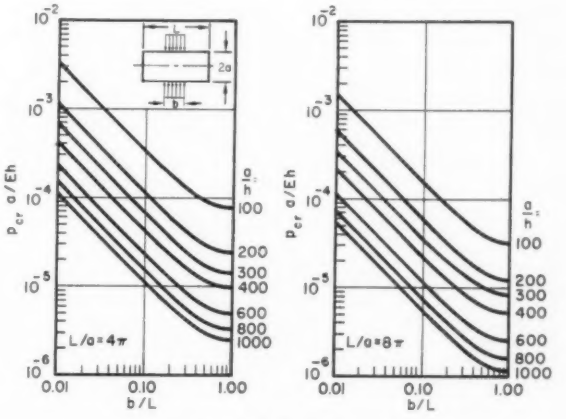

FIG. 7c. Buckling pressures.

Discussion

Present theoretical results for the prebuckling displacement w [Eq. (6)] were compared with corresponding results based on an analysis in reference 3, page 397, and were found to be in close agreement. The theories indicate that the compressive hoop stress is essentially uniform in the loaded region and that it drops to zero at an extremely short distance outside the loaded region.

The circumferential distribution of the prebuckling circumferential membrane strain ϵ_ϕ is shown in Fig. 8 for the cylinder cross section under the middle of the pressure band. Theoretical values [based on Eqs. (1) and (6)] and test data are shown. Except for two points along the circumference of the cylinder, test data and theory are in close agreement. The disagreement at 25–26 may be attributed to the nearness of the weld. The second discrepancy (at gages 33–34) was at the one region in the cylinder circumference which did not buckle (see above).

In the test of Cylinders No. 1 and 2, a buckle formed in the region of the seam weld at about 15 psi, and three additional buckles formed in a region remote from the weld at about 21 psi. The theoretical buckling pressure for these cylinders is found from Fig. 7 to be 15.9 psi. The sequence of formation of buckles in these two tests suggests that geometric irregularities in the welded region may have precipitated buckling in that region at a reduced pressure. Furthermore, other tests have shown that objects which limit outward bulging of the shell during buckling tend to exert a stabilizing influence on the shell, and the two rubber wedges shown in Fig. 3 partially restrict such bulging

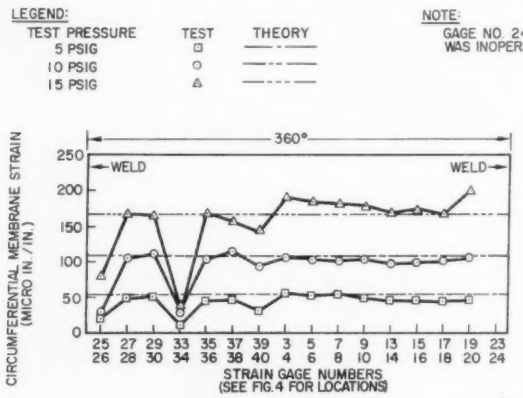

FIG. 8. Circumferential membrane strain distribution.

at the edges of the pressurized zone. Consequently, Cylinder No. 3 was fabricated and tested with the rubber wedges omitted from the loading device.

As noted above, the third cylinder buckled twice at 9.8 psi, and a third time at about 9.0 psi. Furthermore, three or more buckles appeared simultaneously each time, and the welded region did not participate in the initial buckling in the last two load applications. The theoretical buckling pressure for Cylinder No. 3 is found from Fig. 7 to be 10.0 psi. Therefore, the theoretical and experimental values for the buckling pressure are concluded to be in reasonably close agreement.

Results of the theoretical analysis were compared with available solutions of related problems. In the

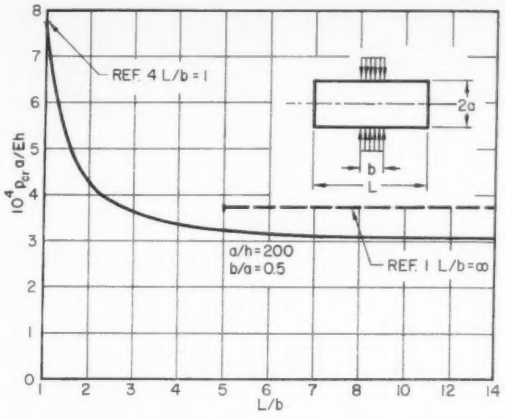

FIG. 9. Effect of end-ring restraint for a typical example.

case where the pressure extends over the entire lateral surface of the cylinder ($b/L = 1$), the solutions obtained are in close agreement with those by Flügge.[4] The solutions are compared in Table 1. Also shown are results based on Batdorf's analysis[5] (the Donnell equations).

The solution of a second limiting case is available in Hahne's analysis of the buckling of a circular cylinder subjected to a radial, circumferential line load.[6] An approximate line-load solution is obtained from the present analysis if, in a case where the pressure band is narrow, the buckling pressure is multiplied by the pressure bandwidth. For the example $\alpha = 4$, $\gamma = 100$, we have the buckling load $4.2 \times 10^{-4}\, Eh$ pounds/inch of circumference. Hahne found this value to be $4.6 \times 10^{-4}\, Eh$.

Out of curiosity, the final equations in the present analysis were also developed without the inclusion of quadratic terms in (v,w) in the potential energy of the external forces [Eq. (4)]. Such terms are frequently omitted in cylindrical shell analyses but are known to be important in the analysis of a circular ring subjected to uniform external pressure (see reference 7). A few values for the case $b/L = 1$ were computed by use of these simplified equations. Results of the calculations are shown in Table 1, Column B. It may be seen that deletion of these second-order terms increases the buckling pressure of the longer shells.

Fig. 9 shows, for comparison, certain results of the analysis in reference 1 for infinitely long cylinders and corresponding results from the present analysis. It is seen that the buckling pressure from reference 1 is about 20 percent higher than the value shown by the present analysis for long cylinders. This difference reflects the fact that in applying the Rayleigh-Ritz procedure, more degrees of freedom were used in the displacement functions of the present analysis than were used in the analysis in reference 1.

The restraining effect of end-rings is also illustrated in Fig. 9. The ratio $L/b = 1$ represents the load case

(*Continued on page 592*)

Readers' Forum

BRIEF REPORTS of investigations in the aerospace sciences and discussions of papers published in the JOURNAL are presented in this special department. Entries must be restricted to a maximum of 1,300 words or the equivalent of one JOURNAL page including formulas and illustrations. Publication is completed as soon as possible after receipt of the material. The Editorial Committee does not hold itself responsible for the opinions expressed by the correspondents.

Contents

Integral-Method Compressible Boundary-Layer Calculations for Strong Favorable Streamwise Pressure Gradients Over an Insulated Surface.... MARTIN H. STEIGER 579

On a Generalized Solution for the Torsion of a Prismatical Beam of Any Convex Polygonal Cross Section..... HOWARD E. BRANDT 580

Effect of Thermal Radiation from a Hot Gas Layer on Heat of Ablation..... ROBERT T. SWANN 582

Transformation of Coordinate Axis Systems of Aircraft..... HERBERT L. ROTHMAN AND MURRAY PITTEL 583

The Propagation of a Plane Shock Wave Into a Moving Fluid..... ROY M. GUNDERSEN 584

Surface Streamlines in Three-Dimensional Hypersonic Flows..... E. A. BRONG AND D. C. LEIGH 585

A Generator of Stable Smoke..... DONALD F. CLAUSEN 587

Effect of Stability Augmentation on Frequency Response of an Aircraft in Atmospheric Turbulence..... HERBERT L. ROTHMAN AND MAX CHERNOFF 587

An Approximate Solution of the Lifting Problem of Thin Airfoils at Sonic Speed..... IWAO HOSOKAWA 588

Comment on "Torsion Analysis of Multicell Tubes"..... W. H. WITTRICK 590

Author's Reply..... F. W. NIEDENFUHR 590

On the Maximum Static-Temperature Rise in Subsonic Flow..... H. E. BRANDMAIER 590

Centerline Flow Gradients in Axisymmetric Ducts..... SOLOMON CIOLKOWSKI 591

Addendum to "The Characteristics of Two-Dimensional Sails in Hypersonic Flow"..... WALTER DASKIN AND LEWIS FELDMAN 592

Integral-Method Compressible Boundary-Layer Calculations for Strong Favorable Streamwise Pressure Gradients Over an Insulated Surface*

Martin H. Steiger
Research Associate, Polytechnic Institute of Brooklyn, Freeport, N.Y.

November 17, 1960

THE CALCULATIONS of constant-density, laminar-boundary-layer properties under strong favorable pressure gradients by means of a one-parameter integral method has been treated by Steiger in reference 1. In that paper a discussion was held on the relation of the integral-method solution, as given, to other suggested methods of analysis, such as that of local similarity and the "cold-wall" approximation. The breakdown of the usual polynomial-profile assumption was also discussed.

This paper presents an extension of the method of reference 1 to the compressible case for insulated surfaces. It was considered of interest to compare some of the results with the existing "cold-wall" estimates given by the method of Lees,[2] and the techniques of local similarity.[2, 3] Experimental evidence[4, 5] has shown that the cold-wall approximation is reasonably satisfactory even under conditions for which the ratio of surface to local inviscid temperature is not much less than one. The present analysis, which does not utilize the cold-wall restriction-thus provides an interesting comparison with the cold-wall analysis in a case which is distinctly not in the cold-wall category.

* This work was carried out under Contract AF 33(616)-6118, Project No. 7064, which is administered by the Aeronautical Research Laboratory of ARDC and partially supported by the Air Force Ballistic Missile Division.

The author wishes to express his appreciation to Professor Martin H. Bloom for many stimulating discussions about this work, and also, he wishes to thank Mr. Joseph Shang for his assistance with the calculations.

Contributors Please Note

Readers' Forum items must be confined to the equivalent of one page in the *Journal*. Contributions that exceed this limit will be returned to the authors for condensation and rewrite. To avoid inconvenience and delay, please adhere to the following specifications:

(1) Five, double-spaced, typewritten, manuscript pages (8½ by 11 in.), including wide margins, equations, and headings, equal one printed page.

(2) For every illustration, deduct at least one-half or as much as one manuscript page, depending on the size of the illustration.

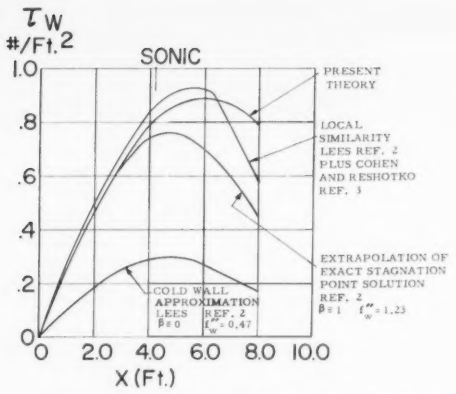
τ_w #/Ft.2
SONIC
PRESENT THEORY
LOCAL SIMILARITY LEES REF. 2 PLUS COHEN AND RESHOTKO REF. 3
EXTRAPOLATION OF EXACT STAGNATION POINT SOLUTION REF. 2 $\beta=1$ $t'_w=1.23$
COLD WALL APPROXIMATION LEES REF. 2 $\beta=0$ $t'_w=0.47$
X (Ft.)

FIG. 1. Surface skin friction. Flow past a circular cylinder. U_∞ = 20,000 ft/sec at 200,000 ft. Nose radius 5 ft.

The pertinent comparison is made for the surface shear stress.

The case of Prandtl number equal to unity is considered here to permit the use of the Crocco integral relation, which in the pressure gradient case specifies that the stagnation enthalpy is constant throughout the flow field. The nomenclature is that used by Schlichting.[6]

By introducing a Dorodnitsyn transformation, the momentum-integral differential equation that governs a two-dimensional, compressible boundary layer in the transformed plane is given by

$$\frac{d\vartheta}{dx} + \frac{d \ln \rho_1 u_1^2}{dx} + \delta^* \frac{d \ln u_1}{dx} = \frac{\nu_1}{u_1}\left(\frac{\rho\mu}{\rho_1\mu_1}\right)_w \left[\frac{\partial u/u_1}{\partial N}\right]_w \left(\frac{1}{\delta_\eta}\right) \quad (1)$$

where
$$(\rho/\rho_1)dy = \delta_\eta\, dN \quad (1a)$$

The boundary conditions are

$$y = 0, \quad N = 0, \quad u = 0, \qquad \left[\frac{\rho\mu}{\rho_1\mu_1}\frac{\partial u/u_1}{\partial N}\right]_N + \frac{\delta_\eta^2 \rho_1}{\rho_w \nu_1}\frac{du_1}{dx} = 0 \quad (2a)$$

$$y \to \delta, \quad N = 1, \quad u = u_1, \quad \partial u/\partial N = \partial^2 u/\partial N^2 = 0 \quad (2b)$$

Let
$$u/u_1 = 1 - (1 - N)^a \quad (3a)$$

Condition (2a) yields

$$a(a - 1) = \Lambda + a\left[\frac{\partial \ln(\rho\mu/\rho_1\mu_1)}{\partial N}\right]_w \quad (3b)$$

where
$$\Lambda = \frac{\delta_\eta^2 \rho_1}{\rho_w \nu_1 (\rho\mu/\rho_1\mu_1)_w}\frac{du_1}{dx} \quad (3c)$$

while (2b) yields
$$2 < a \leq \infty \quad (3d)$$

However, since the surface is insulated

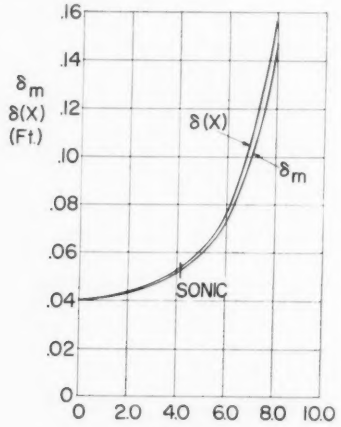

FIG. 2. Boundary-layer thickness. Flow past a circular cylinder. U_∞ = 20,000 ft/sec at 200,000 ft. Nose radius 5 ft.

$$h_s = h + (u^2/2) = \text{constant throughout} \quad (4)$$

it follows
$$\Lambda = a(a - 1) \quad (5a)$$

$$\vartheta/\delta_\eta = a/[(2a + 1)(a + 1)] > 0 \quad (5b)$$

$$\delta^*/\delta_\eta = (h_s/h_1)\{(3a + 1)/[(2a + 1)(a + 1)]\} - \vartheta/\delta_\eta \quad (5c)$$

$$\delta/\delta_\eta = (h_s/h_1) - a/[(2a + 1)(a + 1)](u_1^2/h_1) \quad (5d)$$

The present theory is shown to agree very closely with the exact solution in the stagnation region of a blunt body.[7]

The analysis is applied to the flow about a cylinder. The free-stream flight conditions are U_∞ = 20,000 fps at 200,000 ft and a 5-ft nose radius. The solution is presented in the following figures. It should be noted that there were no difficulties with regard to singularities in the solution.

For a further discussion of this analysis see reference 7.

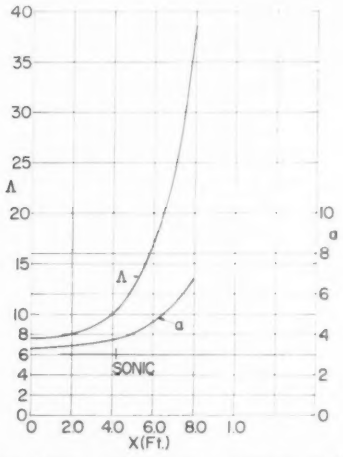

FIG. 3. Shape factor. Flow past a circular cylinder. U_∞ = 20,000 ft/sec at 200,000 ft. Nose radius 5 ft.

REFERENCES

[1] Steiger, Martin H., *Integral-Method Boundary-Layer Calculations for Strong Favorable Streamwise Pressure Gradients*, Polytechnic Institute of Brooklyn, Rept. 613, ARL TN 60-137, July 1960.

[2] Lees, Lester, *Laminar Heat Transfer Over Blunt-Nosed Bodies at Hypersonic Flight Speeds*, Jet Propulsion, Vol. 26, No. 4, pp. 259–269, April 1956.

[3] Cohen, C. B., and Reshotko, E., *Similar Solutions for the Compressible Laminar Boundary Layer with Heat Transfer and Pressure Gradient*, NACA TN 3325, 1955.

[4] Cresci, R. J., MacKenzie, D. A., and Libby, P. A., *An Investigation of Laminar, Transitional and Turbulent Heat Transfer on Blunt-Nosed Bodies in Hypersonic Flow*, Journal of the Aero/Space Sciences, Vol. 27, No. 6, pp. 401–414, June 1960.

[5] Broglio, L., and Buongiorno, C., *An Experimental Technique to Measure Heat Transfer Fluxes at High Speeds: Turbulent Heat Transfer Data on a Blunt Body at M = 3.98*, Universita Degli Studi Di Roma, April 1960.

[6] Schlichting, H., *Boundary Layer Theory*, McGraw-Hill Book Co., Inc., 1955.

[7] Steiger, Martin H., *Integral-Method Compressible Boundary-Layer Calculations for Strong Favorable Streamwise Pressure Gradients Over an Insulated Surface*, Polytechnic Institute of Brooklyn, Rept. 621, ARL TN 60-149, September 1960.

On a Generalized Solution for the Torsion of a Prismatical Beam of Any Convex Polygonal Cross Section

Howard E. Brandt
Massachusetts Institute of Technology, Cambridge, Mass.

September 27, 1960

RECENTLY, the author published a paper concerning the torsion of a prismatical bar whose cross section is a regular

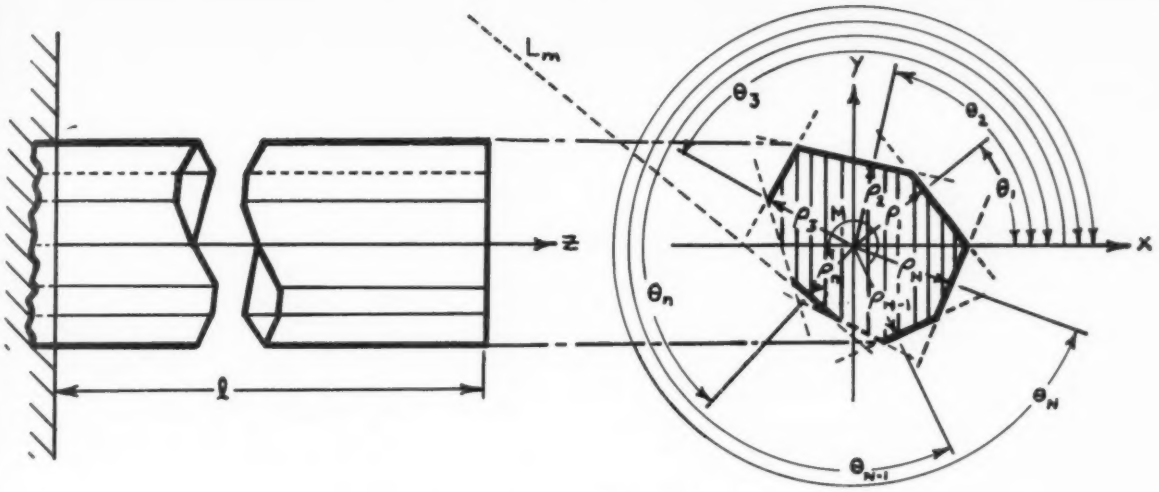

FIG. 1. Geometry of the section.

N-sided polygon.[1] This paper is a generalization of the theory there presented to any convex polygonal cross section—e.g., trapezoidal, rectangular, etc. This generalization is a result of the topological character of the stress function in the Prandtl sense and is associated with the properties of the Laplacian operator.

MATHEMATICAL FORMULATION OF THE PROBLEM AND ITS SOLUTION

The solution will be found by means of the Prandtl stress function, applying the Galerkin method. This method for determining stress and displacement fields was outlined by Stanišić and Shirely.[2]

The Prandtl stress function is of the form

$$\Psi(x, y) = \sum_{m=1}^{n} A_m \eta_m(x, y), \qquad (m = 1, 2, 3, \ldots, n) \quad (1)$$

and the Galerkin form of the problem becomes

$$\iint_S \nabla^2[\Psi(x, y) + 2]\eta_r(x, y)dS = 0, \qquad (r = 1, 2, 3, \ldots, n) \quad (2)$$

where $\eta_r(x, y)$ are coordinate functions which must be found, such that the boundary condition, $\Psi(\Gamma) = 0$, is satisfied on the boundary Γ of the polygon; A_m are constants satisfying Eq. (2); and S is the domain of integration.

A function, $\Psi(x, y)$, must first be found which satisfies the boundary condition. Refer to Fig. 1. The convex polygonal cross section has N sides which divide it into N-triangular surfaces, $S_1, S_2, \ldots, S_{N-1}, S_N$. The equations of the respective N sides, L_m, must be expressed with respect to a coordinate system, so chosen that the point of intersection of the first and Nth side of the polygon is a point on the positive x-axis; the equations are then expressed as functions of their perpendicular distances, ρ_m, from the origin and the angles, θ_m, which these perpendiculars make with the positive x-axis. It is readily shown that

$$L_m \equiv x \cos\theta_m + y \sin\theta_m - \rho_m = 0, \qquad (m = 1, 2, 3, \ldots, N) \quad (3)$$

Thus $\Psi(x, y)$ will take the following form:

$$\Psi(x, y) = A_1 \prod_{n=1}^{N} [x \cos\theta_n + y \sin\theta_n - \rho_n] \quad (4)$$

where A_1, is a constant of first approximation to be determined later and Π denotes the product of expressions with indicated index. Eq. (2) becomes

$$\iint_S [A_1\nabla^2\eta_1(x, y) + 2]\eta_1(x, y)dS = 0 \quad (5)$$

where $$\eta_1(x, y) = \prod_{n=1}^{N} [x \cos\theta_n + y \sin\theta_n - \rho_n] \quad (6)$$

Solving for A_1, one finds

$$A_1 = -2 \frac{\sum_{m=1}^{N} \iint_{S_m} \prod_{n=1}^{N} \phi_n(x, y)dS}{\sum_{m=1}^{N} \iint_{S_m} \prod_{n=1}^{N} \phi_n(x, y)\,\nabla^2 \prod_{n=1}^{N} \phi_n(x, y)dS} \quad (7)$$

where the integrals are evaluated over the respective triangles, S_m, and

$$\phi_n(x, y) = x \cos\theta_n + y \sin\theta_n - \rho_n \quad (8)$$

But it is readily shown that

$$\nabla^2 \prod_{n=1}^{N} \phi_n(x, y) = \prod_{n=1}^{N} \phi_n(x, y) \left\{ -\sum_{n=1}^{N} \phi_n^{-2}(x, y) + \left[\sum_{n=1}^{N} \frac{\cos\theta_n}{\phi_n(x, y)}\right]^2 + \left[\sum_{n=1}^{N} \frac{\sin\theta_n}{\phi_n(x, y)}\right]^2 \right\} \quad (9)$$

The limits of integration for S_m in polar coordinates, r, θ, are easily determined. The lower and upper limits with respect to r for each S_m are clearly $r_{mL} = 0$ and $r_{mu} = R \sec[\theta - \theta_m]$, respectively.

The lower and upper limits with respect to θ are (note $\theta_0 = \theta_N$ and $\rho_0 = \rho_N$)

$$\theta_{mL} = \tan^{-1}\left(\frac{\rho_m \cos\theta_{m-1} - \rho_{m-1} \cos\theta_m}{\rho_{m-1} \sin\theta_m - \rho_m \sin\theta_{m-1}}\right)$$

and $$\theta_{mu} = \tan^{-1}\left(\frac{\rho_{m+1} \cos\theta_m - \rho_m \cos\theta_{m+1}}{\rho_m \sin\theta_{m+1} - \rho_{m+1} \sin\theta_m}\right)$$

respectively. Eq. (8) in polar coordinates becomes

$$\phi_n(\theta, r) = r \cos(\theta - \theta_n) - \rho_n \quad (10)$$

Hence Eqs. (4), (7)–(11) imply

$$\Psi(x, y) = 2 \frac{\left\{ \sum_{m=1}^{N} \int_{\theta_{mL}}^{\theta_{mu}} \int_{0}^{R \sec(\theta - \theta_m)} r \prod_{n=1}^{N} \phi_n(\theta, r) dr d\theta \right\} \prod_{n=1}^{N} \phi_n(x, y)}{\sum_{m=1}^{N} \int_{\theta_{mL}}^{\theta_{mu}} \int_{0}^{R \sec(\theta - \theta_m)} r \left[\prod_{n=1}^{N} \phi_n(\theta, r) \right]^2 \left\{ \sum_{n=1}^{N} \phi_n^{-2}(\theta, r) - \left(\sum_{n=1}^{N} \frac{\cos \theta_n}{\phi_n(r, \theta)} \right)^2 - \left(\sum_{n=1}^{N} \frac{\sin \theta_n}{\phi_n(r, \theta)} \right)^2 \right\} dr\, d\theta} \quad (11)$$

Evidently the stress and displacement field are uniquely determined (see Eqs. 14–17).[1]

The torsional rigidity is given by

$$D = 2G \sum_{m=1}^{N} \int_{\theta_{mL}}^{\theta_{mu}} \int_{0}^{R \sec(\theta - \theta_m)} r \Psi(r, \theta) dr d\theta \quad (12)$$

where $\Psi(r, \theta)$ is obtained from Eq. (11) by substituting $x = r \cos \theta$, $y = r \sin \theta$; and G is the shear modulus.

References

[1] Brandt, H. E., *On a Generalized Solution to a Torsion Problem in Linear Elasticity*, Journal of the Aerospace Sciences, Readers' Forum, Vol. 28, No. 5, pp. 422–424, May 1961.

[2] Shirely, L. K., and Stanišić, M. M., *On the Torsion of a Cylindrical Beam Having a Trapezoidal Cross Section*, Journal of the Aero/Space Sciences, Readers' Forum, Vol. 26, No. 7, pp. 462–464, July 1959.

[3] Stanišić, M. M., Hauck, C. A., and Mathias, R. A., *Concerning the Torsion of Prismatic Bars Having a Hexagonal Cross-Section*, Journal of the Aerospace Sciences, Readers' Forum, Vol. 27, No. 8, pp. 631–633, August 1960.

[4] Brandt, H. E., *On the Torsion of a Rectangular Beam With Diametrically Opposite Sides of the Form ax^n*, Journal of the Aerospace Sciences, Readers' Forum, Vol. 28, No. 6, pp. 503–505, June 1961.

Effect of Thermal Radiation From a Hot Gas Layer on Heat of Ablation

Robert T. Swann

Aeronautical Research Engineer, NASA Langley Research Center, Langley Field, Va.

October 6, 1960

Symbols

C = stagnation-point velocity gradient
H = enthalpy
H_A = heat of ablation
Δh = heat required to inject unit weight into boundary layer
$\dot{m}$ = rate of mass injection
Nu = Nusselt number
q = aerodynamic heating rate
q_r = net radiant heating rate to surface
Re = Reynolds number
S = Sutherland constant
T = temperature
ρ = density
μ = coefficient of viscosity

Subscripts

e = external flow condition
0 = no injection
w = wall value

THERMAL RADIATION from the hot gas layer may constitute an appreciable fraction of the total heat input to the stagnation area of a vehicle entering a planetary atmosphere from supercircular velocity. Unless the gaseous products of ablation are opaque to thermal radiation, the ablative mechanism provides no shielding against radiant heating, and the heat of ablation will be less for combined aerodynamic and radiant heating than for aerodynamic heating only.[1] The purpose of this note is to indicate the effect of radiant heating on heat of ablation for the special case in which the gaseous products of ablation are similar to air. Results for other transparent gaseous products may be inferred from this case.

The heat of ablation will be defined as the rate of heat transfer to the surface with no injection, divided by the rate of injection, i.e.,

$$H_A = (q_0 + q_r)/\dot{m} \quad (1)$$

The rate of injection is determined from an energy balance at the surface to be as follows:

$$\dot{m} = (q + q_r)/\Delta h \quad (2)$$

The aerodynamic heating rate is related to the rate of injection through the boundary-layer equations.[2] Exact solutions of the boundary-layer equations for a highly cooled axisymmetric stagnation point with air injection are shown in Table 1 in terms of dimensionless parameters. [The wall temperature has little effect on the heat of ablation defined by Eq. (1).]

The heat of ablation was calculated from Eqs. (1) and (2) and Table 1 for a range of values of q_r/q_0, and the results are plotted on Fig. 1. With no net radiative heat transfer, the heat of ablation is somewhat less than the value predicted by the usual linear theory. When radiation to the surface is present, the heat of ablation has the limiting value, $\Delta h[1 + (q_0/q_r)]$, approached for large values of $(H_e - H_w)/\Delta h$, corresponding to complete blocking of the aerodynamic heating. Note that the limiting value of the heat of ablation is independent of the properties of the injected gas. Since radiation from a hot gas layer will normally be significant only when the enthalpy difference across the boundary layer is large, the properties of the injected gas are diminished in importance when radiation from a hot gas layer is significant. Therefore, the choice of an ablating

TABLE I

Heat Transfer as a Function of Mass Injection Rate
$T_w/T_e = 0.05$ $S/T_e = 0.02$

$\dot{m}/\sqrt{2\rho_w\mu_w C}$	$Nu/\sqrt{Re}$
0	0.4096
0.25	0.2526
0.50	0.1271
0.60	0.0882
0.70	0.0568
0.80	0.0332
0.90	0.0175
1.00	0.0091

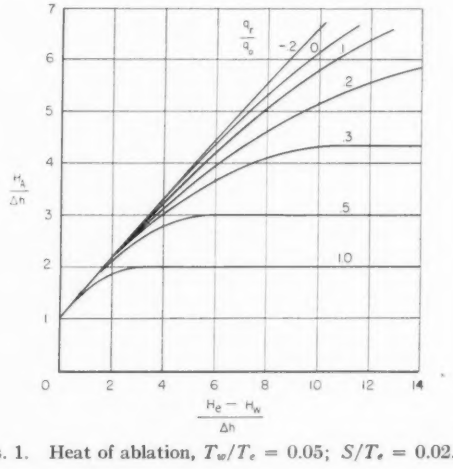

FIG. 1. Heat of ablation, $T_w/T_e = 0.05$; $S/T_e = 0.02$.

material for such an application may be based on other considerations.

Radiation from a hot gas layer to an ablating surface not only increases the total heat input to the surface, but also reduces the efficiency of ablation in blocking and absorbing the heat input. Radiation to an ablating surface is thus a much more serious problem than is indicated by the percentage increase in total heat input. For example, consider a case with air injection for which

$$(H_e - H_w)/\Delta h = 10$$

If $q_r/q_0 = 0.2$, the heating rate is increased by 20 percent, but the mass injection rate is increased by 44 percent. If $q_r/q_0 = 1.0$, the heating rate is increased by 100 percent, but the injection rate is increased by over 500 percent.

These increased rates of mass injection will cause large increases in the required weight of ablating material. However, there are several possibilities for reducing the radiant flux to the body, such as changes in vehicle configuration and selection of ablating materials having favorable values of absorptivity and emissivity in both the solid and gaseous states.

References

[1] Swann, Robert T., and South, Jerry, *A Theoretical Analysis of the Effects of Ablation on Heat Transfer to an Arbitrary Axisymmetric Body*, NASA TN D-741.

[2] Beckwith, Ivan E., *Similar Solutions for the Compressible Boundary Layer on a Yawed Cylinder with Transpiration Cooling*, NASA TN 4345, September 1958.

Transformation of Coordinate Axis Systems of Aircraft

Herbert L. Rothman, and Murray Pittel,
Sr. Engineer, and Design Specialist, Respectively, Republic Aviation Corporation, Farmingdale, N.Y.

October 10, 1960

Symbols

θ = attitude angle, angle between the x axis of the airplane and its projection on the horizontal
ψ = heading angle, angle between the initial heading (x axis of the airplane) and the projection of the x axis on the horizontal
ϕ = bank angle, angle between the y axis of the airplane and a horizontal line in the y-z plane.
α = angle of attack, angle between the x axis and the projection of the wind vector on the plane of symmetry
β = angle of sideslip, angle between the wind vector and its projection on the plane of symmetry
η = angle of attack of longitudinal principal axis
$[\ ]$ = matrix
$[\ ]^{-1}$ = inverse of matrix
$[L_w]$ = matrix rotation from wind axis system to earth axis system
$[\eta']$ = matrix rotation from principal axis system to body axis system
$[\alpha']$ = matrix rotation from body axis system to stability axis system
$[\beta']$ = matrix rotation from stability axis system to wind axis system
X, Y, Z = components along the X, Y, Z axes, respectively

Subscripts

e = refers to earth axis system
p = refers to principal axis system
s = refers to stability axis system
w = refers to wind axis system
B = refers to body axis system

THERE are primarily five coordinate axis systems in which an airplane's dynamic motions can be described: earth axis, body axis, stability axis, principal axis, and wind axis (see reference 1 and 2 for a description of these axis systems). They are related to each other by orthogonal transformations.[3] Since analysis of the dynamic motions of an airplane in various degrees of freedom usually require changes of coordinate systems, this note presents a general matrix equation which relates in a single equation the five coordinate axis systems of an airplane. The general transformation equation can be written in the following form

$$\begin{bmatrix} X_e \\ Y_e \\ Z_e \end{bmatrix} = [L_w][\eta'][\alpha'][\beta'] \begin{bmatrix} X_p \\ Y_p \\ Z_p \end{bmatrix} \tag{1}$$

which expresses the transformation from the principal axis system to the earth axis system. The first four matrices on the right-hand side of Eq. (1) are:

$$[L_w] = \begin{bmatrix} \cos\theta\cos\psi & \sin\phi\sin\theta\sin\psi - \cos\psi\cos\phi & \cos\psi\cos\phi\sin\theta + \sin\psi\sin\phi \\ \cos\theta\sin\psi & \sin\psi\sin\theta\sin\phi + \cos\psi\cos\phi & \sin\psi\cos\phi\sin\theta - \sin\psi\sin\phi \\ -\sin\theta & \sin\phi\cos\theta & \cos\phi\cos\theta \end{bmatrix} \tag{2}$$

$$[\eta'] = \begin{bmatrix} \cos\eta & 0 & \sin\eta \\ 0 & 1 & 0 \\ -\sin\eta & 0 & \cos\eta \end{bmatrix} \tag{2a}$$

$$[\alpha'] = \begin{bmatrix} \cos\alpha & 0 & \sin\alpha \\ 0 & 1 & 0 \\ -\sin\alpha & 0 & \cos\alpha \end{bmatrix} \tag{2b}$$

$$[\beta'] = \begin{bmatrix} \cos\beta & \sin\beta & 0 \\ -\sin\beta & \cos\beta & 0 \\ 0 & 0 & 1 \end{bmatrix} \tag{2c}$$

and

$$[L_w][\eta'][\alpha'][\beta'] = \begin{bmatrix} A_{11} & A_{12} & A_{13} \\ A_{21} & A_{22} & A_{23} \\ A_{31} & A_{32} & A_{33} \end{bmatrix} \tag{3}$$

where:

$$\begin{aligned} A_{11} = {} & \cos\theta_w\cos\psi_w\cos\beta\cos\alpha\cos\eta \\ & -\cos\theta_w\cos\psi_w\cos\beta\sin\alpha\sin\eta \\ & -\sin\phi_w\sin\theta_w\cos\psi_w\sin\beta\cos\alpha\cos\eta \\ & +\sin\phi_w\sin\theta_w\cos\psi_w\sin\beta\sin\alpha\sin\eta \\ & +\sin\psi_w\cos\phi_w\sin\beta\cos\alpha\cos\eta \\ & -\sin\psi_w\cos\phi_w\sin\beta\sin\alpha\sin\eta \\ & -\cos\psi_w\cos\phi_w\sin\theta_w\sin\alpha\cos\eta \\ & -\cos\psi_w\cos\phi_w\sin\theta_w\cos\alpha\sin\eta \\ & -\sin\psi_w\sin\phi_w\sin\alpha\cos\eta \\ & -\sin\psi_w\sin\phi_w\cos\alpha\sin\eta \end{aligned}$$

$$\begin{aligned} A_{12} = {} & \cos\theta_w\cos\psi_w\sin\beta + \sin\phi_w\sin\theta_w\cos\psi_w\cos\beta - \\ & \sin\psi_w\cos\phi_w\cos\beta \end{aligned}$$

$$\begin{aligned} A_{13} = {} & \cos\theta_w\cos\psi_w\cos\beta\cos\alpha\sin\eta \\ & +\cos\theta_w\cos\psi_w\cos\beta\sin\alpha\cos\eta \\ & -\sin\phi_w\sin\theta_w\cos\psi_w\sin\beta\cos\alpha\sin\eta \\ & -\sin\phi_w\sin\theta_w\cos\psi_w\sin\beta\sin\alpha\cos\eta \\ & +\sin\psi_w\cos\phi_w\sin\beta\cos\alpha\sin\eta \\ & +\sin\psi_w\cos\phi_w\sin\beta\sin\alpha\cos\eta \\ & -\cos\psi_w\cos\phi_w\sin\theta_w\sin\alpha\sin\eta \\ & +\cos\psi_w\cos\phi_w\sin\theta_w\cos\alpha\cos\eta \\ & -\sin\psi_w\sin\phi_w\sin\alpha\sin\eta \\ & +\sin\psi_w\sin\phi_w\cos\alpha\cos\eta \end{aligned}$$

$$\begin{aligned} A_{21} = {} & \cos\theta_w\sin\psi_w\cos\beta\cos\alpha\cos\eta \\ & -\cos\theta_w\sin\psi_w\cos\beta\sin\alpha\sin\eta \\ & -\sin\psi_w\sin\theta_w\sin\phi_w\sin\beta\cos\alpha\cos\eta \\ & +\sin\psi_w\sin\theta_w\sin\phi_w\sin\beta\sin\alpha\sin\eta \\ & -\cos\psi_w\cos\phi_w\sin\beta\cos\alpha\cos\eta \end{aligned}$$

$$
\begin{aligned}
&+ \cos\psi_w \cos\phi_w \sin\beta \sin\alpha \sin\eta \\
&- \sin\psi_w \cos\phi_w \sin\theta_w \sin\alpha \cos\eta \\
&- \sin\psi_w \cos\phi_w \sin\theta_w \cos\alpha \sin\eta \\
&+ \cos\psi_w \sin\phi_w \sin\alpha \cos\eta \\
&+ \cos\psi_w \sin\phi_w \cos\alpha \sin\eta
\end{aligned}
$$

$$
\begin{aligned}
A_{22} = {} & \cos\theta_w \sin\psi_w \sin\beta \\
& + \sin\psi_w \sin\theta_w \sin\phi_w \cos\beta \\
& + \cos\psi_w \cos\phi_w \cos\beta
\end{aligned}
$$

$$
\begin{aligned}
A_{23} = {} & \cos\theta_w \sin\psi_w \cos\beta \cos\alpha \sin\eta \\
& + \cos\theta_w \sin\psi_w \cos\beta \sin\alpha \cos\eta \\
& - \sin\psi_w \sin\theta_w \sin\phi_w \sin\beta \cos\alpha \sin\eta \\
& - \sin\psi_w \sin\theta_w \sin\phi_w \sin\beta \sin\alpha \cos\eta \\
& - \cos\psi_w \cos\phi_w \sin\beta \cos\alpha \sin\eta \\
& - \cos\psi_w \cos\phi_w \sin\beta \sin\alpha \cos\eta \\
& - \sin\psi_w \cos\phi_w \sin\theta_w \sin\alpha \sin\eta \\
& + \sin\psi_w \cos\phi_w \sin\theta_w \cos\alpha \cos\eta \\
& + \cos\psi_w \sin\phi_w \sin\alpha \sin\eta \\
& - \cos\psi_w \sin\phi_w \cos\alpha \cos\eta
\end{aligned}
$$

$$
\begin{aligned}
A_{31} = {} & - \sin\theta \cos\beta \cos\alpha \cos\eta \\
& + \sin\theta \cos\beta \sin\alpha \sin\eta \\
& - \sin\phi_w \cos\theta_w \sin\beta \cos\alpha \cos\eta \\
& + \sin\phi_w \cos\theta_w \sin\beta \sin\alpha \sin\eta \\
& - \cos\phi_w \cos\theta_w \sin\alpha \cos\eta \\
& - \cos\phi_w \cos\theta_w \cos\alpha \sin\eta
\end{aligned}
$$

$$
A_{32} = -\sin\theta_w \sin\beta + \sin\phi_w \cos\theta_w \cos\beta
$$

$$
\begin{aligned}
A_{33} = {} & - \sin\theta \cos\beta \cos\alpha \sin\eta \\
& - \sin\theta_w \cos\beta \sin\alpha \cos\eta \\
& - \sin\phi_w \cos\theta_w \sin\beta \cos\alpha \sin\eta \\
& - \sin\phi_w \cos\theta_w \sin\beta \sin\alpha \cos\eta \\
& - \cos\phi_w \cos\theta_w \sin\alpha \sin\eta \\
& + \cos\phi_w \cos\theta_w \cos\alpha \cos\eta
\end{aligned}
$$

The inverse of Eq. (1) is

$$
\begin{bmatrix} X_p \\ Y_p \\ Z_p \end{bmatrix} = [L_w]^{-1} [\eta']^{-1} [\alpha']^{-1} [\beta']^{-1} \begin{bmatrix} X_s \\ Y_s \\ Z_s \end{bmatrix} \tag{4}
$$

In Eq. (1),

$[\eta']$ rotates $\begin{bmatrix} X_p \\ Y_p \\ Z_p \end{bmatrix}$ to $\begin{bmatrix} X_B \\ Y_B \\ Z_B \end{bmatrix}$

$[\alpha']$ rotates $\begin{bmatrix} X_B \\ Y_B \\ Z_B \end{bmatrix}$ to $\begin{bmatrix} X_s \\ Y_s \\ Z_s \end{bmatrix}$

$[\beta']$ rotates $\begin{bmatrix} X_s \\ Y_s \\ Z_s \end{bmatrix}$ to $\begin{bmatrix} X_w \\ Y_w \\ Z_w \end{bmatrix}$

and $[L_w]$ rotates $\begin{bmatrix} X_w \\ Y_w \\ Z_w \end{bmatrix}$ to $\begin{bmatrix} X_e \\ Y_e \\ Z_e \end{bmatrix}$

Similarly in Eq. (4),

$[L_w]^{-1}$ rotates $\begin{bmatrix} X_e \\ Y_e \\ Z_e \end{bmatrix}$ to $\begin{bmatrix} X_w \\ Y_w \\ Z_w \end{bmatrix}$

$[B']^{-1}$ rotates $\begin{bmatrix} X_w \\ Y_w \\ Z_w \end{bmatrix}$ to $\begin{bmatrix} X_s \\ Y_s \\ Z_s \end{bmatrix}$

$[\alpha']^{-1}$ rotates $\begin{bmatrix} X_s \\ Y_s \\ Z_s \end{bmatrix}$ to $\begin{bmatrix} X_B \\ Y_B \\ Z_B \end{bmatrix}$

and $[\eta']^{-1}$ rotates $\begin{bmatrix} X_B \\ Y_B \\ Z_B \end{bmatrix}$ to $\begin{bmatrix} X_p \\ Y_p \\ Z_p \end{bmatrix}$

Therefore from Eq. (1) and its inverse, Eq. (4), the transformation between any two of the five axis systems considered can be obtained by setting the appropriate angles equal to zero. For example:

(1) If we want the coordinates X_B, Y_B, Z_B in terms of X_s, Y_s, Z_s, then set $\theta = \phi = \psi = \beta = \eta = 0$ in Eq. (4).

(2) If we want the coordinates X_w, Y_w, Z_w in terms of X_B, Y_B, Z_B, then set $\eta = \theta = \phi = \psi = 0$ in Eq. (1).

References

[1] Howe, R. M., *Coordinate Systems For Solving the Three-Dimensional Flight Equations*, WADC TN 55-747, June 1956.

[2] Schuler, J. M., *Analytical Study of Airplane Dynamics and Tail Loads in Rolling Pull-Out Maneuvers*, WADC TR 56-403, September 1956.

[3] Doolin, B. F., *The Application of Matrix Methods to Coordinate Transformations Occurring in Systems Studies Involving Large Motions of Aircraft*, NACA TN 3968, May 1957.

The Propagation of a Plane Shock Wave Into a Moving Fluid*

Roy M. Gundersen
Associate Professor of Mathematics,
Illinois Institute of Technology, Chicago, Ill.

October 13, 1960

By the use of a linearization based on small area variations, the perturbation of a plane shock wave propagating through a tube of varying cross-sectional area into an ideal compressible fluid at rest was determined by Chester,[1] and also by the present author[2]; the former started with the full three-dimensional theory, and then used an averaging process, while the latter used a one-dimensional analysis. In the present note, these results are generalized to the case that the flow in front of the shock is a uniform state and thus applicable to an initially stationary shock.

When the equations, which govern the one-dimensional, unsteady flow of an inviscid ideal compressible gas in a tube of variable cross-sectional area, are linearized in the neighborhood of a known (isentropic) solution, the general solution for an initially uniform state is:

$$
\begin{aligned}
A \equiv {} & u_1/2 + c_1/(\gamma - 1) = F[x - (u_0 + c_0)t] + \\
& c_0^{-1} R(x - u_0 t) - u_0 c_0 E_1/2E_0(u_0 + c_0) \\
B \equiv {} & -u_1/2 + c_1/(\gamma - 1) = G[x - (u_0 - c_0)t] + \\
& c_0^{-1} R(x - u_0 t) - u_0 c_0 E_1/2E_0(u_0 - c_0) \\
H_0 \equiv {} & c_0^2 s_{1x}/c_v \gamma(\gamma - 1) = 2R'(x - u_0 t)
\end{aligned} \tag{1}
$$

where u, c, s, E_0, E_1, and γ are the particle velocity, local speed of sound, specific entropy, original uniform cross-sectional area, area perturbation, and ratio of the specific heats at constant pressure c_p and at constant volume c_v. The subscript zero denotes the basic (known) flow, the subscript 1 the terms of first-order and F, G, and R are arbitrary functions of one variable.

Let a shock of arbitrary strength be propagating along the tube of varying cross section, and let the flow in front of the shock be denoted by subscript 1 and the flow behind by subscript 2. Denote perturbations of a base quantity by a bar. Let P denote the pressure, w the shock velocity, $v = w - u$, $m = u/c$, $M = v/c$, so that the following relations hold:

$$u_2 = u_1 + 2M_1 c_1 (1 - M_1^{-2})/(\gamma + 1) \tag{2a}$$

$$c_1/c_2 = (\gamma + 1)M_2/M_1 (\gamma - 1 + 2M_1^{-2}) \tag{2b}$$

$$P_2/P_1 = 2\gamma M_1^2/(\gamma + 1) - (\gamma - 1)/(\gamma + 1) \tag{2c}$$

$$M_2^2 = (\gamma - 1 + 2M_1^{-2})/[2\gamma - (\gamma - 1)M_1^{-2}] \tag{2d}$$

* This work was supported by a grant from the National Science Foundation.

$$m_2 = (\gamma + 1)M_2m_1/M_1(\gamma - 1 + 2M_1^{-2}) + 2(1 - M_2^2)/M_2(\gamma + 1) \quad (2e)$$

$$(\gamma + 1)v_2 = M_1c_1(\gamma - 1 + 2M_1^{-2}) \quad (2f)$$

From the formulation of the problem—i.e., with the shock coming from minus infinity, so to speak, the contribution given by F is not included for there is no mechanism downstream of the shock which could give rise to such a term. Thus, setting $F \equiv 0$ in the second of Eqs. (1) gives:

$$\tilde{u}_2/2c_2 + \tilde{c}_2/c_2(\gamma - 1) - \tilde{s}_2/2c_v\gamma(\gamma - 1) + m_2E_1/2E_0\,(1 + m_2) = 0 \quad (3)$$

Replacing the second two terms of Eq. (3) by their equivalent $\bar{P}_2/2\gamma P_2$, determining $\tilde{u}_2/c_2$ from Eq. (2a), c_1/c_2 from (2b), $\overline{M}_1$ from (2c) gives:

$$\bar{P}_2 = -(\gamma + 1)(P_2 - P_1)\tilde{u}_1/M_1c_1(1 - M_1^{-2}) \times (1 + 2M_2 + M_1^{-2}) + (\gamma + 1)(1 + M_1^{-2}) \times (P_2 - P_1)\bar{P}_1/2\gamma P_1(1 - M_2^2)\,(1 + 2M_2 + M_1^{-2}) - 2(P_2 - P_1)\tilde{c}_1/c_1(1 + 2M_2 + M_1^{-2}) - (\gamma + 1)(P_2 - P_1) \times m_2M_2E_1(x)/E_0(1 + m_2)\,(1 - M_2^2)(1 + 2M_2 + M_1^{-2}) \quad (4)$$

Since it follows from (2e) that

$$(\gamma + 1)m_2M_2/(1 - M_2^2) = 2 + (\gamma + 1)m_1/M_1(1 - M_1^{-2})$$

Eq. (4) may be written as:

$$\bar{P}_2 = -(\gamma + 1)(P_2 - P_1)\tilde{u}_1/M_1c_1(1 - M_1^{-2}) \times (1 + 2M_2 + M_1^{-2}) + (\gamma + 1)(P_2 - P_1) \times (1 + M_1^{-2})\bar{P}_1/2\gamma P_1(1 - M_2^2)(1 + 2M_2 + M_1^{-2}) - 2(P_2 - P_1)\tilde{c}_1/c_1(1 + 2M_2 + M_1^{-2}) - (\gamma + 1)m_1 \times (P_2 - P_1)E_1(x)/E_0(1 + m_2)M_1(1 - M_1^{-2}) \times (1 + 2M_2 + M_1^{-2}) - 2(P_2 - P_1)E_1(x)/E_0(1 + m_2) \times (1 + 2M_2 + M_1^{-2}) \quad (5)$$

If the area variations are restricted to a finite length of the tube, the ultimate effect is to produce a change in shock strength and the shock again becomes uniform.

For the case that the state one is an unperturbed rest state, $m_1 = 0$, $M_1 = w/c_1$, etc., all terms on the right-hand side of Eq. (5) vanish except the last so that

$$\bar{P}_2 = -2(P_2 - P_1)E_1(x)/E_0(1 + m_2)(1 + 2M_2 + M_1^{-2}) \equiv -K(P_2 - P_1)E_1(x)/E_0$$

which is the result first obtained by Chester. The parameter K is a monotonic decreasing function of the shock strength defined as the pressure ratio P_2/P_1, and varies between 0.5 for a very weak shock to an asymptotic limit of 0.3941 (for $\gamma = 7/5$).

To complete the present solution, the arbitrary function G of Eq. (1) must be determined. This is done most readily by noting that the system (1) may be written as:

$$\tilde{u}_2/c_2 + \bar{P}_2/\gamma P_2 + m_2E_1(x)/E_0(1 + m_2) = 0$$
$$-\tilde{u}_2/c_2 + \bar{P}_2/\gamma P_2 + m_2E_1(x)/E_0(m_2 - 1) = 2G[x - (u_2 - c_2)t]/c_2$$

By addition, it follows that

$$\bar{P}_2 = -m_2^2(P_2 - P_1)[2\gamma - (\gamma - 1)M_1^{-2}]E_1(x)/2(m_2^2 - 1) \times (1 - M_1^{-2})E_0 + [2\gamma - (\gamma - 1)M_1^{-2}](P_2 - P_1)G[x - (u_2 - c_2)t]/2c_2(1 - M_1^{-2}) \quad (6)$$

Evaluating this on the shock, $x = wt$, and replacing $\bar{P}_2$ by its equivalent from Eq. (5) gives:

$$G(\lambda)/c_2 = m_2[2M_2 + m_2(1 + M_1^{-2})]\,E_1(\tau\lambda)/(m_2^2 - 1) \times (1 + M_1^{-2} + 2M_2)E_0 - 2(\gamma + 1)\tilde{u}_1[\tau\lambda, \lambda/c_2(1 + M_2)] \div M_1c_1[2\gamma - (\gamma - 1)M_1^{-2}](1 + M_1^{-2} + 2M_2) - 4(1 - M_1^{-2})\tilde{c}_1[\tau\lambda, \lambda/c_2(1 + M_2)]/(2\gamma - (\gamma - 1)M_1^{-2}]\,(1 + M_1^{-2} + 2M_2) + (1 + M_1^{-2}) \times \bar{P}_1[\tau\lambda, \lambda/c_2(1 + M_2)]/\gamma P_1(1 + M_1^{-2} + 2M_2) \quad (7)$$

where

$$\tau = (M_2 + m_2)/(1 + M_2), \qquad \lambda = x - (u_2 - c_2)t$$

Thus substituting Eq. (7) into Eq. (6) and noting that

$$[2\gamma - (\gamma - 1)M_1^{-2}]/2(1 - M_1^{-2}) = (\gamma + 1)/2(1 - M_2^2) = \{m_2M_2 + (\gamma + 1)m_1/M_1[2\gamma - (\gamma - 1)M_1^{-2}]\}^{-1}$$

the complete solution for $\bar{P}_2$ is:

$$\bar{P}_2/(P_2 - P_1) = (\gamma + 1)m_2[2M_2 + m_2(1 + M_1^{-2})] \times E_1(\tau\lambda)/2(1 - M_2^2)(m_2^2 - 1)(1 + M_1^{-2} + 2M_2)E_0 - m_2^2(\gamma + 1)E_1(x)/2E_0(m_2^2 - 1)(1 - M_2^2) - (\gamma + 1)\,\tilde{u}_1[\tau\lambda, \lambda/c_2(1 + M_2)]/M_1c_1(1 - M_1^{-2}) \times (1 + M_1^{-2} + 2M_2) - 2\tilde{c}_1[\tau\lambda, \lambda/c_2(1 + M_2)]/c_1(1 + M_1^{-2} + 2M_2) + (\gamma + 1)(1 + M_1^{-2})\bar{P}_1[\tau\lambda,\lambda/c_2(1 + M_2)]/2\gamma P_1(1 - M_2^2)(1 + M_1^{-2} + 2M_2) \quad (8)$$

For the case that state one is an unperturbed rest state, all terms on the right-hand side of (8) vanish except the first two so that

$$\bar{P}_2/(P_2 - P_1) = [2M_2 + m_2(1 + M_1^{-2})]\,E_1(\tau\lambda)/E_0M_2(m_2^2 - 1) \times (1 + M_1^{-2} + 2M_2) - m_2E_1(x)/E_0M_2(m_2^2 - 1) \equiv -NE_1(\tau\lambda)/E_0 - m_2E_1(x)/E_0M_2(m_2^2 - 1)$$

which is Chester's result. He has calculated the values of the parameters τ and N and found that the parameter τ was a monotonic decreasing function of the shock strength and took, respectively, the values 2, 1, and 0.6076, when the shock was very weak, when the flow behind the shock was sonic, and when the shock strength became infinite. For subsonic flow behind the shock, he found that N increased rapidly from a value of 0.5 for a very weak shock and became singular when the flow behind the shock was sonic. For supersonic flow, N became negative (singular at $m_2 = 1$) and increased monotonically to an asymptotic limit of -0.1550.

In the region directly behind the shock, the pressure change is given by Eq. (5). When the flow behind the shock is subsonic, a disturbance will be reflected downstream of the shock, and the pressure perturbation is given by Eq (8). If the area perturbation is such that $E_1(x) = 0$ for $x < 0$ (say), the second term on the right-hand side will ultimately become zero.

When the flow behind the shock is supersonic, this disturbance will propagate upstream of the shock, and the pressure perturbation is given by the entire Eq. (8).

REFERENCES

[1] Chester, W., *The Quasi-Cylindrical Shock Tube*, Philos. Mag., Ser. 7, Vol. 45, p. 1293, 1954.

[2] Gundersen, R., *The Flow of a Compressible Fluid with Weak Entropy Changes*, J. Fluid Mech., Vol. 3, Pt. 6, p. 553, 1958.

Surface Streamlines in Three-Dimensional Hypersonic Flows†

E. A. Brong* and D. C. Leigh**
Missile and Space Vehicle Dept., General Electric Co., Philadelphia, Pa.

October 18, 1960

THE COMPUTATION of boundary layers generally is most conveniently carried out along the surface streamlines of the inviscid flow.[1,2] This, of course, requires an a priori knowledge of

† Based on work performed under the auspices of the U.S. Air Force, Ballistic Missile Division, Contract AF 04(647)-269.

* Engineer, Theoretical Aerodynamics.

** Consultant and Assistant Professor of Mechanical Engineering, Princeton University.

the shape of these streamlines—a knowledge which at best is very difficult to obtain by exact mathematical solution even for most simple geometrical configurations. The object of this paper is to compare the results of three approximate methods of determining streamlines to the results from one of the few available exact solutions.

The first of the approximate methods is based on a result obtained by the Newton-Busemann theory of hypersonic flows.[3, 4] This result is that a particle in the shock layer is acted upon only by forces normal to the body surface and thus follows a geodesic trajectory. Therefore the inviscid flow in contact with the surface determines streamlines which are the family of geodesics originating from the stagnation point with assigned initial directions.

In the second method the direction of a streamline is in the plane containing the normal to the surface and the direction of the free-stream flow.[5] Streamlines determined in this way denote the family of paths of steepest descent from the stagnation point with respect to the direction of the flow at infinity. This method will, therefore, be called the steepest-descent method. Note that in the Newton-Busemann theory the initial direction of a particle entering the shock layer is along a path of steepest descent.

The third method utilizes some of the exact flow-field equations to determine streamline shapes from a known or assumed pressure distribution—e.g., the modified Newtonian sine-squared law. The relevant equations are the energy equation relating fluid velocity to pressure along the isentropic body surface,

$$1/2u^2 + h(p, S_0) = h_0 \tag{1}$$

the thermodynamic state relation giving density,

$$\rho = \rho(p, S_0) \tag{2}$$

and the component Euler equation,

$$\rho u^2 \kappa = -\partial p/\partial \eta \tag{3}$$

where $d\eta$ is an elemental distance in the body surface normal to the streamlines and κ is the surface component of streamline curvature. This method is called the pressure method.

Application to a Swept Cylinder-Wedge

Consider a wedge with cylindrical leading edge and swept at an angle Ω with the free-stream flow. Dimensionless plots of the streamlines for two wedge angles are shown for an exact calculation as well as for the three approximate methods in Fig. 1. The exact solution was determined by superimposing a constant spanwise velocity on the velocity distribution obtained from a two-dimensional flow field.[6]

Since the stagnation point is at an infinite distance along the leading edge, there is some question about how the geodesic method is applied. It can be reasoned that along the planar wedge surface the direction of the geodesic and the path of steepest-descent coincide. Since the surface is developable, the geodesic is a straight line on the developed surface of the cylinder as well as on the wedge.

The equation of the path of steepest descent on the cylinder is

$$y/D \tan \Omega = 1/2 \ln \tan (x/D) \tag{4}$$

where y is the distance along the leading edge, x is the distance along the developed surface, and D is the diameter of the cylinder. On the wedge of half-angle β the path of steepest descent is the straight line given by $y/\tan \Omega = x/\cos \beta$.

Using modified Newtonian pressures in the pressure method, we have

$$p = p_\infty + (p_0 - p_\infty) \cos^2(2x/D) \tag{5}$$

on the cylinder and an equivalent formula with $\cos^2 (2x/D)$ replaced by $\sin^2 \beta$ on the wedge. The leading-edge pressure p_0 and surface entropy S_0 are determined by the normal-shock equations as functions of p_∞, ρ_∞, and $U_\infty \cos \Omega$, so that $p(x/D)$ is known. Since p is a function only of x/D, an integral of Eq. (3) is obtained as

$$\left\{\frac{[d(y/D)/d(x/D)]^2}{1 + [d(y/D)/d(x/D)]^2}\right\}^{1/2} = \frac{\text{const.}}{u[p(x/D), S_0]} \tag{6}$$

The conditions that $u = U_\infty \sin \Omega$ and $d(y/D)/d(x/D) \to \infty$ as $x \to 0$ give the value of the constant in Eq. (6); viz., const. $= U_\infty \sin \Omega$, and Eq. (6) may be integrated numerically to give $y/(D \tan \Omega)$ as a function of x/D.

Conclusion

The geodesic method does not give the indicated physical behavior at the leading edge. Considering for the moment a cone at angle of attack, geodesics from the vertex are simply the straight generators and there is no three-dimensional effect, whereas the other methods do give three-dimensional effects. The Newton-Busemann theory in general, leads to many anomalous results.[4]

Both the steepest-descent and pressure methods display the essential three-dimensional effects for the swept cylinder-wedge. The pressure method agrees more closely with the exact solution than does the steepest-descent method. The pressure method

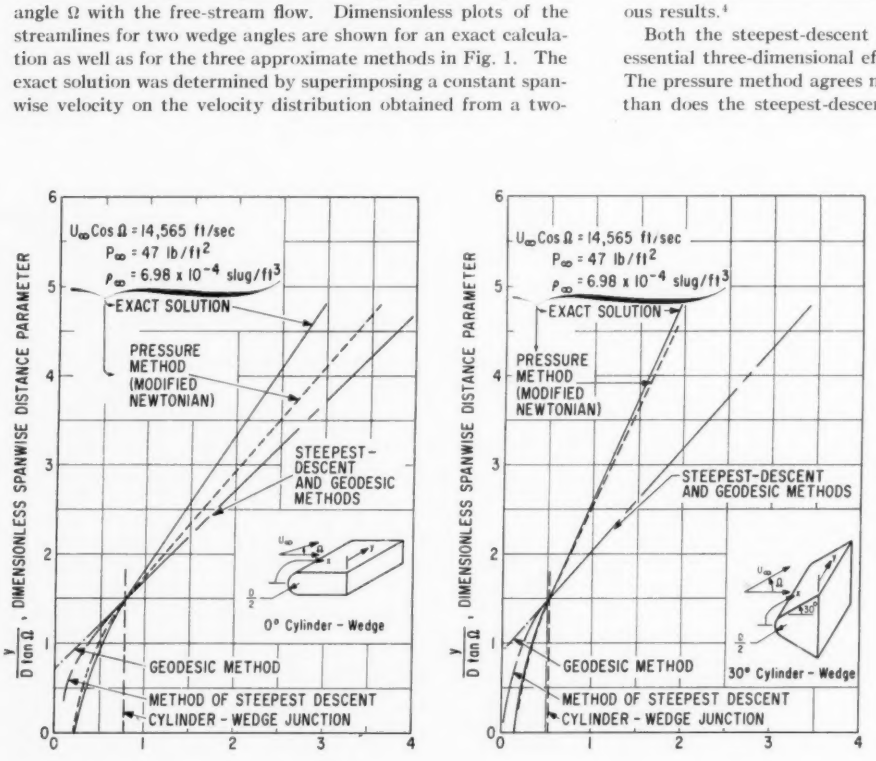
$U_\infty \cos \Omega$ = 14,565 ft/sec
P_∞ = 47 lb/ft^2
ρ_∞ = 6.98 x 10^{-4} slug/ft^3
EXACT SOLUTION
PRESSURE METHOD (MODIFIED NEWTONIAN)
STEEPEST-DESCENT AND GEODESIC METHODS
0° Cylinder - Wedge
GEODESIC METHOD
METHOD OF STEEPEST DESCENT
CYLINDER - WEDGE JUNCTION
$\frac{y}{D \tan \Omega}$, DIMENSIONLESS SPANWISE DISTANCE PARAMETER
30° Cylinder - Wedge

FIG. 1. (a) *left*, (b) *right*. X/D, dimensionless distance along the developed surface. Comparison of solutions by pressure, geodesic, and steepest-descent methods with an exact solution.

improves with increasing wedge angle and is very close indeed for the 30° wedge. The steepest-descent method increasingly diverges from the exact solution with increasing wedge angle. The pressure method is somewhat more complicated to apply to the blunt wedge than the steepest-descent method, and both are correspondingly more complicated for more complex bodies.

References

[1] Hayes, W. D., *The Three-Dimensional Boundary Layer*, NAVORD Report 1313, NOTS 384, May 1951.

[2] Cooke, J. C., *An Axially Symmetric Analogue for General Three-Dimensional Boundary Layers*, RAE, Aero. TN 2625, June 1959.

[3] Freeman, N. C., *The "Newtonian" Theory of Hypersonic Flow for Any Three-Dimensional Body*, ARC TR C.P. No. 439 (20, 344), August 1958.

[4] Hayes, W. D., and Probstein, R. F., *Hypersonic Flow Theory*—1st Ed.; Academic Press, New York, 1959.

[5] Leigh, D. C., *Notes on the Calculation of Three-Dimensional Compressible Laminar Boundary Layers—Part I*, Aero. Memo. No. 69, G-E MSVD, July 1958.

[6] Gravalos, F. G., Edelfelt, I. H., and Emmons, H. W., *Supersonic Flow About a Blunt Body of Revolution for Gases at Chemical Equilibrium*, TIS R58SD245, General Electric Co., June 1958.

A Generator of Stable Smoke*

Donald F. Clausen
Research Associate, Dept. of Physiology, University of Minnesota, Minneapolis

October 19, 1960

IT WAS DEEMED DESIRABLE to study at low Reynolds numbers some of the properties of aerosols made of biological materials. Under these conditions, a well-known instability of gas flow may be observed such that separation of aerosol particles according to size becomes impossible. Since smoke streamers are useful as indicators of the state of the flow of a gaseous system, smoke from various sources such as burning tobacco or tar was injected into the aerosol stream according to suggestions offered by members of the Departments of Aeronautical and Mechanical Engineering of the University of Minnesota.

Unfortunately, moisture and tars from these smokes soon plugged the metal tubes used for the injection and also covered the inside of the apparatus with deposits. Therefore, a smoke generator was designed and built to produce quantities of clearly visible smoke, free from tars and water, which is obtainable from one charge for at least two hours.

Design of Smoke Generator

As shown in Fig. 1, the generator consists of a metal pot made of welded, heavy-gauge sheet metal, 10 in. in diameter and 14 in. high, capped by a 6-in. pipe nipple, of which the cap can be tightened by means of a metal rod thrust through pairs of metal eyelets welded to it. A rubber gasket provides for a gas-tight fit. The upper four inches of the pot is cooled, to protect the gasket and to allow for handling, by means of a coil of 1/4-in. copper tubing soldered to the pot wall and through which cold water passes. The same water flow cools a 24-in. metal condenser through which the smoke passes, and which removes water of combustion and some tars, both of which can finally be drained from the bottom of the condenser by means of a petcock. The partially cleaned smoke is forced through a water scrubber several inches deep (not shown) to remove remaining tars and then through a second (glass) condenser (also not shown) to remove water introduced by the scrubber. Rubber tubing conducts smoke around the room to points of use. The smoke is injected into the aerosol stream by means of short lengths of metal tubing either 0.5 mm or 1.0 mm in. inside diameter.

* This investigation was supported in part by Public Health Service Grant C-3583 from the National Cancer Institute of the Public Health Service.

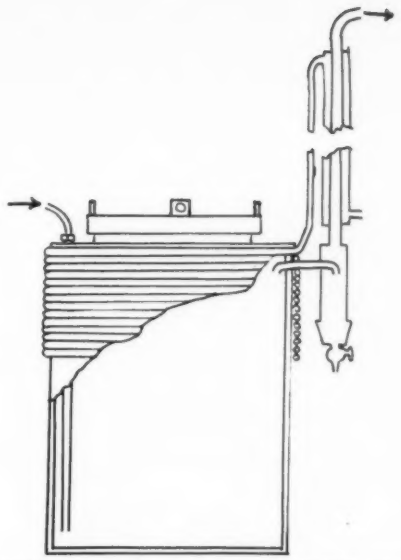

FIG. 1. Smoke generator. Entrance of nitrogen and exit of smoke are shown by means of arrows.

The pot is heated by a 6-in. gas hot plate. Because it was felt that oxygen in the presence of heated combustibles might lead to an explosion in the pot, the incoming gas, originally air, was changed to tank nitrogen without noticeable effect on the yield of smoke. The stream of nitrogen is conducted to the bottom of the pot by means of a length of 3/8-in. copper tubing run through a packing gland.

Operation of Smoke Generator

The pot is packed with about 400 g. of either sanitary wipes (Kleenex-type tissues) or surgical sponges (gauze) weighted down by means of eight 4-in. spirals of plumber's tape to prevent unburned material from remaining as an elevated dome over the ash of burned material. The pot cover is tightened in place, water is run through both condensers and the cooling coil around the top of the pot, and the gas hot plate is turned on full force. Smoke is available in quantity within five minutes. By adjustment of the level of the flame of the hot plate and of the nitrogen flow, generous supplies of smoke are obtainable for at least two hours. By means of a T-tube in the rubber tubing used to conduct smoke to the site of use, excess smoke is shunted into a fume hood. No tars have clogged the system over months of use, and no deposits form on the inside of equipment. Yet the smoke is visible enough to visualize the gas flow easily, particularly if the room is darkened and if a flashlight is used. Infrequently, very small drops of water will form on the end of the metal injection tubing, but these seem to evaporate spontaneously in the aerosol stream.

Effect of Stability Augmentation on Frequency Response of an Aircraft in Atmospheric Turbulence

Herbert L. Rothman, and Max Chernoff,
Senior Engineer and Principal Engineer, Respectively, Republic Aviation Corp., Farmingdale, N.Y.

October 14 1961

Symbols

ω = angular frequency, rad/sec
$C(\omega)$ = $F + iG$, Theodorsen function, represents the change

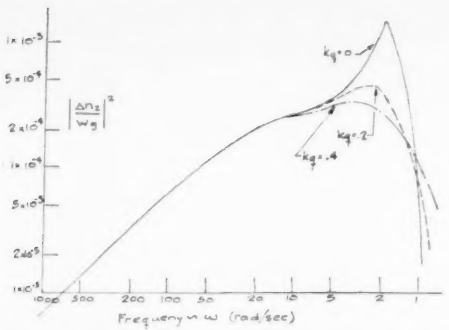

FIG. 1. Frequency response functions for incremental normal load factor for typical fighter-bomber airplane for varying values of the pitch-damper gain.

in static lift forces acting on an airfoil when it is performing harmonic oscillations

F = standard notation for real part of Theodorsen function
G = standard notation for imaginary part of Theodorsen function
$\phi(\omega)$ = Sears function, represents the change in static lift forces due to the sinusoidal gust
w = vertical component of total airplane velocity, ft/sec
w_g = vertical component of gust velocity, ft/sec
θ = body-axis attitude angle, rad.
q = pitch velocity, y component of body-axis angular velocity, $\dot{\theta}$, rad/sec
i_T = deflection of horizontal tail, rad.
V = total aircraft velocity, ft/sec
Δn_z = incremental normal load factor from 1 "g" trim at the c.g.
k_q = pitch-damper gain, sec
$\cdot$ = d/dt, time-rate-of-change operator, sec^{-1}
$||^2$ = modulus squared

AN ANALYSIS of the response of an airplane due to vertical atmospheric gusts is presented to show the effects of stability augmentation in relieving the dynamic motions of the airplane. The longitudinal two-degree-of-freedom (pitch acceleration and vertical acceleration) dynamic equations of motion can be written in the following form:

$$(\dot{w} - V\dot{\theta}) - Z_w C(\omega)w - Zq C(\omega)q - Zi_T C(\omega)i_T = Z_w\phi(\omega)w_g \quad (1)$$

$$\ddot{\theta} - M_w C(\omega)w - Mq C(\omega)q - Mi_T C(\omega)i_T = M_w\phi(\omega)w_g \quad (2)$$

where the horizontal-tail deflection (i_T) is a function of the pitch velocity (q) and the pitch-damper gain (kq) of the stability-augment system—i.e.,

$$i_T = k_q\, q \quad (3)$$

Therefore Eqs. (1) and (2) can be rewritten as

$$(\dot{w} - V\dot{\theta}) - Z_w C(\omega)w - (Zq + Zi_T k_q)C(\omega)q = Z_w\phi(\omega)w_g \quad (4)$$

$$\ddot{\theta} - M_w C(\omega)w - (Mq + Mi_T k_q)C(\omega)q = M_w\phi(\omega)w_g \quad (5)$$

From Eqs. (4) and (5), and the auxiliary equation

$$\Delta n_z = -\frac{1}{g}(\dot{w} - V\dot{\theta}) \quad (6)$$

the modulus squared incremental normal load factor per unit gust velocity can be derived; it is given by the equation:

$$\left|\frac{\Delta n_z}{w_g}\right|^2 = \left|\frac{\phi(\omega)}{g^2}\right|^2 \left\{\frac{\omega^2[(AF)^2 + (\omega Z_w + AG)^2]}{[\omega BF + G(2AF + E)]^2 + [\omega(-\omega + BG) + (G^2 - F^2)A - EF]^2}\right\} \quad (7)$$

where

$$A = M_w(Zq + Zi_T k_g) - Z_w(Mq + Mi_T k_q)$$
$$B = (Mq + Mi_T k_q) + Z_w \qquad E = M_w V \quad (7a)$$

Eq. (7) is plotted in Fig. 1 for a typical fighter-bomber aircraft, $0.9M$ at 35,000 feet and $k_q = 0.2$. Two additional curves are plotted in Fig. 1, for $k_q = 0.4$ and $k_q = 0$, in order to show the effects of doubling the pitch-damper gain and having no stability-augment system.

It is clear from the three curves in Fig. 1 that stability augmentation has a significant effect in reducing the dynamic motions of an airplane responding to atmospheric gusts.

REFERENCES

Flodin, K., and Sundstrom, M., *Investigation of the Response to Random Wind Gusts of a Typical Subsonic Fighter Aircraft in Level Flight with Mach Number 0.9 at Sea Level*, KTH Aero TN47, Stockholm, 1958.

An Approximate Solution of the Lifting Problem of Thin Airfoils at Sonic Speed*

Iwao Hosokawa
National Aeronautical Laboratory, Tokyo, Japan
March 14, 1961

SYMBOLS

U_∞, M_∞ = velocity and Mach number, respectively, of the free stream parallel to the x-axis
γ = ratio of specific heats
Φ = perturbation velocity potential divided by U_∞, which is governed by the equation

$$(1 - M_\infty{}^2)\Phi_{xx} + \Phi_{yy} = (\gamma + 1)M_\infty{}^2\Phi_x\Phi_{xx} \quad (1)$$

φ = linearized potential due to Oswatitsch and Maeder, which satisfies

$$(1 - M_\infty{}^2)\varphi_{xx} + \varphi_{yy} = K\varphi_x \quad (K: \text{ const.}) \quad (2)$$

α = $K/2\beta^2$ or $-K/2m^2$
β^2 = $-m^2 = 1 - M_\infty{}^2$
K_0, I_0 = modified Bessel functions of the zeroth order
$F(x)$ = distribution of the cross-sectional area of the airfoil, whose chord length is assumed unity
$s(x)$ = slope of the camber-line of the airfoil
Δ = symbol which means the difference of the subsequent quantity between the two surfaces of the airfoil
c^* = sonic point of the flow on the symmetric airfoil
t = thickness ratio of the airfoil
θ = incidence angle of the airfoil
$\bar{C}_p$ = reduced pressure coefficient

DUE to the recent development of the linearized transonic flow theory,[1,2] the analysis of the transonic flow around airfoils may be possible. Spreiter's recently published work,[3] particularly, showed results in striking agreement with experiments in sonic flow case ($M_\infty = 1$). The present author, on the other hand, devised another method of approach for solving the nonlinear transonic-flow equation near the obstacle, making use of the results of the linearized transonic-flow theory as a starting point.[4] [Eq. (13) is a final formula given by the method.] This method has an advantage over Spreiter's in covering the whole transonic range of M_∞ and in predicting the

* The same problem was treated in a similar manner by the author at the 10th National Congress for Applied Mechanics, Japan 1960. However, the previous work should be replaced by the present one, as the former included an unnecessary approximate procedure and some erroneous calculations were made with it.

occurrence of a sort of shock wave. Here some results on the lifting problem of two-dimensional airfoils at sonic speed will be reported.

In order to develop the author's method for this problem, it is necessary at first to know φ in the lifting case. As is well known, the doublet method is the most convenient approach to the linear theory of the thin airfoil with an arbitrary camber. This can be applied also in the present case although Eq. (2) is not a Laplace type; application of the extended Green's theorem leads to

$$\varphi(x, y) = -\frac{1}{2\pi}\int_0^\infty e^{\alpha(x-\xi)}\left\{F'(\xi) + \Delta\varphi(\xi)\frac{\partial}{\partial y}\right\}\frac{K_0[\alpha\{(x-\xi)^2+\beta^2y^2\}^{1/2}]}{\beta}\,d\xi,\ M_\infty \leqq 1 \tag{3}$$

$$= -\frac{1}{2}\int_0^{x-m|y|} e^{\alpha(x-\xi)}\left\{F'(\xi) + \Delta\varphi(\xi)\frac{\partial}{\partial y}\right\}\frac{I_0[|\alpha|\{(x-\xi)^2-m^2y^2\}^{1/2}]}{m}\,d\xi,\ M_\infty \geqq 1 \tag{4}$$

and particularly to

$$\varphi(x, y) = -\frac{1}{2\sqrt{\pi K}}\int_0^x\left\{F'(\xi) + \Delta\varphi(\xi)\frac{\partial}{\partial y}\right\}\frac{\exp[-Ky^2/4(x-\xi)]}{\sqrt{x-\xi}}\,d\xi,\ M_\infty = 1 \tag{5}$$

The first term in the integrand is symmetric with respect to the x-axis; while the second is antisymmetric, and hence $\Delta\varphi$ should be determined so as to fulfil the boundary condition regarding the camber of the airfoil (including the incidence). But, generally speaking, this is not easy except in the purely subsonic case ($K = 0$). Here the integral sign with a shilling fraction symbol signifies the finite part of the Hadamard integral.

However, the exact conversion formula which follows can be found in the case of $M_\infty = 1$. Then,

$$s(x) = \lim_{y\to 0}\frac{\partial}{\partial y}\left\{-\frac{1}{2\sqrt{\pi K}}\int_0^x \Delta\varphi(\xi)\frac{\partial}{\partial y}\frac{\exp[-Ky^2/4(x-\xi)]}{\sqrt{x-\xi}}\,d\xi\right\},\ 0 \leqq x \leqq 1 \tag{6}$$

$$= \frac{1}{4}\sqrt{\frac{K}{\pi}}\int_0^x \Delta\varphi(\xi)\frac{d\xi}{(x-\xi)^{3/2}},\ 0 \leqq x \leqq 1 \tag{7}$$

Taking into account the continuity of φ at the leading edge:

$$\Delta\varphi(0) = 0 \tag{8}$$

Eq. (7) is reduced to

$$s(x) = \frac{1}{2}\sqrt{\frac{K}{\pi}}\int_0^x\{-\Delta\varphi'(\xi)\}\frac{d\xi}{\sqrt{x-\xi}},\quad 0 \leqq x \leqq 1 \tag{9}$$

Fortunately, Eq. (9) is the well known Abel's integral equation, and so the converse transform can be made immediately as follows:

$$-\Delta\varphi'(\xi) = \frac{1}{\pi}\frac{d}{d\xi}\int_0^\xi \frac{(2\sqrt{\pi/K})s(x)}{\sqrt{\xi-x}}\,dx,\quad 0 \leqq \xi \leqq 1 \tag{10}$$

Therefore,

$$-\Delta\varphi(\xi) = \frac{2}{\sqrt{\pi K}}\int_0^\xi \frac{s(x)}{\sqrt{\xi-x}}\,dx,\quad 0 \leqq \xi \leqq 1 \tag{11}$$

Here it should be noted that this conversion be unique so that another physical condition such as the Kutta-Joukowsky condition in subsonic flow need not be imposed; but also no infinite pressure appears at the trailing edge. Particularly, in the case of $s(x) = -\theta$, we have

$$\Delta\varphi(x) = (4/\sqrt{\pi K})\theta\sqrt{x},\quad 0 \leqq x \leqq 1 \tag{12}$$

Now, in order to formulate the lift distribution $\Delta\bar{C}_p$ in terms of $\Delta\varphi$, we can use the resulting formula which was established in the previous work[4]:

$$\bar{C}_p = \frac{(\gamma+1)^{1/3}}{t^{2/3}}(-2\Phi_x) =$$

$$\pm\frac{(\gamma+1)^{1/3}}{t^{2/3}}\,2\sqrt{\frac{2K}{(\gamma+1)}\{\varphi(x)-\varphi(c^*)\}}$$

for $M_\infty = 1$ (13)

where the double sign corresponds to $x \lessgtr c^*$. Hence

$$\Delta\bar{C}_p = \frac{1}{2}\bar{C}_p\frac{\Delta K}{K} + \left\{\frac{4K}{t^{4/3}(\gamma+1)^{1/3}}\right\}\frac{1}{\bar{C}_p}\{\Delta\varphi(x)-\Delta\varphi(c^*)\} \tag{14}$$

and further, based on the relation between K and c^*,[4]

$$\Delta K/K = \{-\varphi_{xxx}(c^*)\Delta\varphi_x(c^*) + \varphi_{xx}(c^*)\Delta\varphi_{xx}(c^*)\}/\varphi_{xx}^2(c^*) \tag{15}$$

Thus, these results constitute the basic formulas giving the characteristics of the lifting airfoil. The pressure coefficient in the lifting case is given by the sum of $\bar{C}_p$ for the symmetric airfoil and its deviation due to the camber $(\pm 1/2)\Delta\bar{C}_p$. (But in order that this treatment of approximation be valid, it is necessary that the airfoil have a much smaller camber ratio in comparison with the thickness ratio.)

For a symmetric circular-arc airfoil at small incidence, we have

$$\Delta\bar{C}_p = \frac{4}{\sqrt{\pi}}\left[\frac{1}{a^3}\,\bar{C}_p + 4a\,\frac{\{\sqrt{x}-(1/2)\}}{\bar{C}_p}\right]\left(\frac{\theta}{t}\right) \tag{16}$$

in which

$$\bar{C}_p = \pm 4\,\frac{a^{1/2}}{\pi^{1/4}}\sqrt{\left(\frac{8}{3}x^{3/2}-2x^{1/2}\right)\Big|_{1/4}^{x}}\quad (c^* = 1/4) \tag{17}$$

and

$$a^3 = K^{3/2}/\{t(\gamma+1)\} = 16/\sqrt{\pi}\quad \text{(a similarity constant)} \tag{18}$$

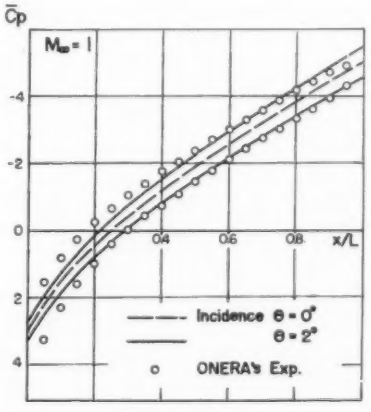

FIG. 1. Pressure distribution on the two surfaces of a circular-arc airfoil at incidence 2°.

as easily derived from reference 4. Eq. (16) shows that the lift distribution should be essentially influenced by the thickness effect (through a and $\bar{C}_p$) in the case of $M_\infty = 1$, as a result of the nonlinearity. As an example, a result from these formulas [Eqs. (16)–(18)] is shown in Fig. 1, which is in comparatively good agreement with the Michel-Sirieix experiment (at ONERA).[5]

REFERENCES

[1] Oswatitsch, K., and Keune, F., *The Flow Around Bodies of Revolution at Mach Number 1*, Proc. Conf. on High-Speed Aeronautics, Polytech. Inst. Brooklyn, January 1955.

[2] Maeder, P. F., and Thommen, H. U., *Some Results of Linearized Transonic Flow About Slender Airfoils and Bodies of Revolution*, Journal of the Aeronautical Sciences, Readers' Forum, Vol. 23, No. 2, pp. 187–188, February 1956.

[3] Spreiter, J. R., and Alksne, A. Y., *Thin Airfoil Theory Based on Approximate Solution of the Transonic Flow Equation*, NACA TN 3970, May 1957.

[4] Hosokawa, I., *A Refinement of the Linearized Transonic Flow Theory*, Phys. Soc. Japan J., Vol. 15, No. 1, pp. 149–157, January 1960.

[5] Michel, R., and Sirieix, M., *Répartitions Expérimentales du Nombre de Mach Local sur Différents Profiles d'Ailes en Écoulement Sonique*, ONERA TM 17, 1959.

Comment on "Torsion Analysis of Multicell Tubes"

W. H. Wittrick*
Lawrence Hargrave Professor of Aeronautics, University of Sydney, Australia

October 21, 1960

NIEDENFUHR[1] has derived, theoretically, equations for the shear stresses and for the torsional rigidity of a multicell torque tube of rectangular section containing an arbitrary number of identical and equally spaced internal webs. This same problem was previously solved by the writer[2] with essentially the same results.

It should be pointed out, however, that Niedenfuhr's Eqs. (12) and (13) can be simplified appreciably if it is noted that the product of the two roots of Eq. (6) is unity. In fact, the two equations [(12)–(13)], reduce to the following:

$$\delta_x = G\theta h t_f \{1 - [(\beta^x + \beta^{N+1-x})/(1 + \beta^{N+1})]\}$$

$$T = 2G\theta h^2 l t_f \{N - [2\beta(\beta^N - 1)]/[(\beta - 1)(\beta^{N+1} + 1)]\}$$

where β may be either β_1 or β_2.

The tube considered in reference 2 was slightly more general than that of Niedenfuhr in that the two outer webs were assumed to have a thickness different from that of the internal webs. With this in mind, however, the two equations above are essentially the same as Eqs. (10) and (11) of the writer's paper.

REFERENCES

[1] Niedenfuhr, F. W., *Torsion Analysis of Multicell Tubes*, Journal of the Aero/Space Sciences, Vol. 27, No. 4, pp. 308–309, April 1960.

[2] Wittrick, W. H., *Torsion of a Multi-webbed Rectangular Tube*, Aircraft Eng., Vol. 25, No. 298, p. 372, December 1953.

Author's Reply

F. W. Niedenfuhr
Associate Professor, The Ohio State University Columbus, Ohio

November 19, 1960

IT IS A PLEASURE to receive Professor Wittrick's very useful comment on the simplification which can be achieved in the equations, [(12) and (13)] as well as to acknowledge his priority in publication. I regret that his earlier work had not come to my attention sooner.

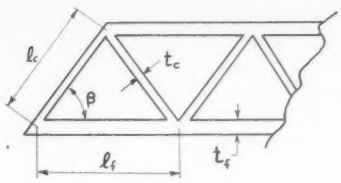

FIG. 1.

Various other modifications of the problem can be made in addition to the one he suggests. It is simple, for instance, to consider a cross section, like that shown in Fig. 1, in which the webs are at an angle β to the face sheets. The governing difference equation is then

$$-2G\theta A(t_c/t_f) = \delta_x - (2 + l_f t_c/l_c t_f)\delta_{x+1} + \delta_{x+2}$$

where A is the area enclosed by each cell. The rest of the analysis then proceeds as in the original example.

* At present, Visiting Professor, College of Aeronautics, Cranfield, Bletchley, Buckinghamshire, England.

On the Maximum Static-Temperature Rise in Subsonic Flow

H. E. Brandmaier
Chief Project Engineer, Curtiss-Wright Corporation, Wright Aeronautical Div., Wood-Ridge, N.J.

November 2, 1960

FLOW PROPERTIES resulting from subsonic, one-dimensional heat addition to a gas or mixture of gases can be determined from a simultaneous solution of the usual mass, momentum, and energy equations, the area rate of heat addition, the equation of state, and a relation between enthalpy, entropy and two of the state variables, say, pressure and temperature. Since enthalpy, entropy, and the state equation are generally not explicit functions of pressure P, and temperature T, the solution of these equations without the aid of a digital computer is generally a long, tedious process. However, if only order-of-magnitude answers are required, limiting values may suffice. It is the purpose of this technical note to show that the maximum static-temperature conditions depend only on the initial conditions and the equation of state.

Designating initial conditions by subscript 1 and maximum static-temperature conditions by subscript 2, and assuming no mass addition, conservation of mass can be written as

$$\rho_1 A_1 V_1 = \rho_2 A_2 V_2 \tag{1}$$

where ρ is the mass density, A is the one-dimensional flow area, and V the corresponding velocity. Assuming an equation of state of the form,

$$P = f(P,T)\rho RT \tag{2}$$

where R is the universal gas constant, Eq. (1) can be written as

$$\delta(T_2/T_1) = \beta(P_2/P_1)(V_2/V_1) \tag{3}$$

where $\delta = f(P_2,T_2)/f(P_1,T_1)$ and $\beta = A_2/A_1$. A maximum value of $\delta T_2/T_1$ can be found by differentiating Eq. (3) with respect to V_2/V_1. Thus,

$$(d\,\delta T_2/T_1)/(d\,V_2/V_1) = \beta(P_2/P_1) + (V_2/V_1)(d\,P_2/P_1)/(d\,V_2/V_1) \tag{4}$$

P_2/P_1 can be found from momentum considerations as follows: Conservation of momentum between stations 1 and 2 can be

TABLE 1

Limiting Values of V_2/V_1, $\delta T_2/T_1$, P_2/P_1, A_2/A_1

	V_2/V_1		P_2/P_1		$\delta T_2/T_1$		A_2/A_1	
ϵ / α	1	2	1	2	1	2	1	2
0.0	∞	∞	0.5000	0.2500	∞	∞	1	2
0.1	5.500	10.50	0.5500	0.2756	3.025	5.513	1	1.905
0.2	3.000	5.500	0.6000	0.3025	1.800	3.025	1	1.818
0.3	2.167	3.833	0.6500	0.3306	1.408	2.204	1	1.739
0.4	1.750	3.000	0.7000	0.3600	1.225	1.800	1	1.667
0.5	1.500	2.500	0.7500	0.3906	1.125	1.563	1	1.600
0.6	1.333	2.167	0.8000	0.4225	1.067	1.409	1	1.538
0.7	1.214	1.929	0.8500	0.4556	1.032	1.302	1	1.481
0.8	1.125	1.750	0.9000	0.4900	1.013	1.225	1	1.429
0.9	1.056	1.611	0.9500	0.5256	1.003	1.168	1	1.379
1.0	1.000	1.500	1.0000	0.5625	1.000	1.125	1	1.333

written as

$$\frac{W}{g}(V_1 - V_2) = \int_1^2 A\,dp \tag{5}$$

Assuming a pressure-area relation of the form suggested by Crocco,[1]

$$P_2/P_1 = \beta^{\epsilon/(1-\epsilon)} \tag{6}$$

Eq. (5) becomes

$$(W/g)(V_1 - V_2) = \epsilon(P_2A_2 - P_1A_1) \tag{7}$$

Thus, $\epsilon = 1$ is equivalent to constant-area flow, and $\epsilon = 0$ to constant-pressure flow. Letting $\alpha = WV_1/gP_1A_1$, Eq. (7) becomes

$$\beta(P_2/P_1) = 1 - (\alpha/\epsilon)[(V_2/V_1) - 1] \tag{8}$$

Substituting Eq. (8) and its derivative with respect to V_2/V_1 into Eq. (4) yields

$$(d\,\delta T_2/T_1)/(d\,V_2/V_1) = [1 + (\alpha/\epsilon)] - 2(\alpha/\epsilon)(V_2/V_1) \tag{9}$$

Since $V_2/V_1 = 1$ for $\epsilon = 0$ the static-temperature function rise is directly proportional to the area ratio β, and Eq. (9) does not apply. In addition, ϵ must be positive.

Setting Eq. (9) equal to zero yields the maximum velocity ratio

$$V_2/V_1 = (\epsilon + \alpha)/2\alpha \tag{10}$$

Substituting Eq. (10) into (8) yields

$$P_2/P_1 = (\alpha/\beta\epsilon)[(\epsilon + \alpha)/2\alpha] \tag{11}$$

or, after substituting Eq. (6) for β,

$$P_2/P_1 = (\alpha/\epsilon)^{\epsilon}[(\epsilon + \alpha)/2\alpha]^{\epsilon} \tag{12}$$

Conversely, the area ratio is found to be

$$\beta = (\alpha/\epsilon)^{1-\epsilon}[(\epsilon + \alpha)/2\alpha]^{1-\epsilon} \tag{13}$$

Inserting Eq. (10) into Eq. (3),

$$\delta(T_2/T_1) = (\alpha/\epsilon)[(\epsilon + \alpha)/2\alpha]^2 \tag{14}$$

If δ can be assumed independent of pressure, these equations define conditions for the maximum static-temperature ratio. For a real gas δ is the ratio of compressibility factors, Z_2/Z_1; for a mixture of dissociating ideal gases, it is the ratio of mixture molecular weights, M_1/M_2, and for an ideal gas or constant-composition mixture of ideal gases, it equals 1.

Knowing ϵ and α, the limiting values of V_2/V_1, P_2/P_1, $\delta T_2/T_1$, and A_2/A_1 can be found from Eqs. (10), (12), (13), and (14).

In conclusion, Table 1 gives these limiting values as functions of α for $\epsilon = 1$ and 2.

REFERENCE

[1] Emmons, H. W. (ed.), *Fundamentals of Gas Dynamics*, Vol. 3, High Speed Aerodynamics and Jet Propulsion, p. 105, Princeton University Press, Princeton, N.J., 1958.

Centerline Flow Gradients in Axisymmetric Ducts

Solomon Ciolkowski
Research Scientist, Grumman Aircraft Engineering Corp., Bethpage, N.Y.
October 20, 1960

IN STUDYING nonviscous, compressible-fluid flows through axisymmetric ducts of variable cross section, it is often desirable to describe the flow behavior along and away from the axis of symmetry. The gradients of the Mach number and flow angularity are often required to determine the usefulness of these ducts. This note is concerned with the analysis of the angularity and Mach-number gradients along the centerline of axisymmetric ducts of variable cross section. Axisymmetric wind-tunnel nozzles, rocket exhaust nozzles, shock tubes, and shock-tube wind tunnels are all examples of these ducts.

ANALYSIS OF THE PROBLEM

The equations describing the isentropic flow of a compressible fluid are

$$(\partial\rho/\partial t) + \nabla\cdot(\rho\mathbf{q}) = 0 \tag{1}$$

$$\rho(\partial\mathbf{q}/\partial t) + \rho(\mathbf{q}\cdot\nabla)\mathbf{q} + \nabla p = 0 \tag{2}$$

$$p = p(\rho) \tag{3}$$

where ρ is the density, p the pressure, and $\mathbf{q}$ the velocity vector.

This note treats steady axisymmetric flows. The coordinate system used is formed by the streamlines and the curves normal to them with the x-axis as the axis of symmetry. Because of symmetry, the x-axis is a streamline. Let ξ be the distance along the streamline, and η the distance normal to the direction of ξ.

The equations in this coordinate system become (see reference 1)

$$q(\partial\rho/\partial\xi) = -\rho[(\partial q/\xi) + q(\partial\theta/\partial\eta + \sin\theta/r)] \tag{4}$$

$$q(\partial q/\partial\xi) = -(1/\rho)(\partial p/\partial\xi) \tag{5}$$

$$q^2(\partial\theta/\partial\xi) = -(1/\rho)(\partial p/\partial\eta) \tag{6}$$

$$p = p(\rho) \tag{7}$$

where θ is the angle between the streamline and the x-axis, q is the absolute velocity, and r is the distance from the x-axis.

On the centerline—i.e., the x-axis—the equations become

$$q(\partial\rho/\partial x) = -\rho[(\partial q/\partial x) + 2q(\partial\theta/\partial r)] \tag{8}$$

$$q(\partial q/\partial x) = -(1/\rho)(\partial p/\partial x) = -(a^2/\rho)(\partial\rho/\partial x) \tag{9}$$

$$q^2(\partial\theta/\partial x) = -(1/\rho)(\partial p/\partial r) \tag{10}$$

Combining Eqs. (8) and (9),

$$[1 - (1/M^2)](\partial\rho/\partial x) = -2\rho(\partial\theta/\partial r) \tag{11}$$

Thus a density gradient along the centerline will result in an angularity gradient normal to the centerline and vice versa.

Since on the centerline $\theta = 0$, Eq. (10) results in the relation

$$\partial p/\partial r = 0 \tag{12}$$

Thus, the pressure gradient normal to the centerline is zero, and therefore the Mach-number gradient normal to the centerline is zero.

DUCTS OF VARYING CROSS SECTION, ONE-DIMENSIONAL APPROXIMATION

Making use of Eq. (9), Eq. (11) may be written in the form

$$(M^2 - 1)(1/q)(\partial q/\partial x) = 2(\partial\theta/\partial r) \tag{13}$$

If the flow is analyzed using one-dimensional theory to relate area change dA/dx to change in flow velocity q, it is found that

$$(1/A)(dA/dx) = -(1 - M^2)(1/q)(\partial q/\partial x) \tag{14}$$

Accordingly, after substitution of Eq. (14) into (13),

$$\partial\theta/\partial r = (1/2)(1/A)(\partial A/\partial x) \tag{15}$$

Since $A = \pi R^2$, with R equal to the radius of the duct,

$$\partial\theta/\partial r = R_x/R = \tan\theta_{wall}/R \tag{16}$$

where θ_{wall} is the local angle between the walls of the duct and the x-axis. Eq. (14) results in

$$\frac{dM}{dx} = \frac{1}{(M^2-1)}\frac{q}{(\partial q/\partial M)}2\frac{1}{R}\frac{dR}{dx} \tag{17}$$

Conical Nozzle

For the case of a conical nozzle, Eq. (16) becomes simply

$$\partial\theta/\partial r = 1/L \tag{18}$$

where L is the length of the cone from its generating apex. Thus, the angularity gradient is a function only of the length of the conical nozzle.

For a perfect gas, the Mach-number gradient can be obtained by using the relationship

$$q^2 = \frac{a_0^2}{(\gamma-1)/2 + (1/M^2)}$$

and Eq. (17). It follows that

$$\frac{dq}{dM} = \frac{1}{q}\frac{a_0^2}{[(\gamma-1)/2 + (1/M^2)]^2}\frac{1}{M^3} \tag{19}$$

so that using Eq. (17)

$$dM/dx = 2[M^2/(M^2-1)][(\gamma-1)/2 + (1/M^2)](1/R)(dR/dx) \tag{20}$$

so that for large M one obtains the approximate relationship

$$dM/dx \approx (\gamma-1)M(1/R)dR/dx$$

Accordingly, $$dM/dx \approx (\gamma-1)(M/L)$$

In order to provide some feeling for the magnitude of the angularity and Mach-number gradients, consider a conical nozzle with exit diameter of 1.5 ft and 12.5° semiangle with exit $M = 10$, $\gamma = 1.4$. Neglecting the boundary layer, this nozzle will have an angularity gradient at the centerline of $\partial\theta/\partial r = 1.41°$ per in. The Mach-number gradient is approximately $dM/dx = 0.099$ per in.

Reference

[1] Chu, Boa-Teh, *Wave Propagation and the Method of Characteristics in Reacting Gas Mixtures with Applications to Hypersonic Flow*, WADC TN-57-213, ASTIA Doc. AD118350, 1957.

Addendum to "The Characteristics of Two-Dimensional Sails in Hypersonic Flow"

Walter Daskin and Lewis Feldman
Scientific Supervisors, General Applied Science Laboratories, Inc., Westbury, L.I., N.Y.
February 16, 1961

The authors would like to point out that the steady shape assumed by a flexible member under the sine-squared law of forces which we displayed in reference 1 has been previously published. The hypersonic sail[1] is equivalent to a towing cable, a balloon cable, a kite string, or a paravane cable. Published work on the shapes assumed by these devices and the forces acting on them appeared before either of the authors were born. It is our pleasure to acknowledge that references 2–5 contain the essentials of reference 1; some of these go further to include body forces, oscillations about the equilibrium position, and friction. These venerable tomes, lightly sprinkled with the dust of decades, wrestled successfully with the intricate problems of hypersonic aerodynamics of the space age.

References

[1] Daskin, W., and Feldman, L., *The Characteristics of Two-Dimensional Sails in Hypersonic Flow*, Journal of the Aeronautical Sciences, Vol. 25, No. 1, pp. 53–55, January 1958.

[2] McLeod, A. R., *On the Action of Wind on Flexible Cables, With Applications to Cables Towed Below Aeroplanes, and Balloon Cables*, Brit. Advisory Comm. Aero., R&M 554, October 1918.

[3] Glauert, H., *The Stability of a Body Towed by a Light Wire*, Brit. Advisory Comm. Aero., R&M 1312 (Ae 451), February 1930.

[4] Glauert, H., *The Form of a Heavy Flexible Cable Used for Towing a Heavy Body Below an Aeroplane*, Brit. Advisory Comm. Aero., R&M 1592 (T. 3498), February 1934.

[5] Landweber, L., and Protter, M. H., *The Shape and Tension of a Light Flexible Cable in a Uniform Current*, J. Appl. Mech., Vol. 14, No. 2, pp. A121–126, June 1942.

✦ ✦ ✦

Buckling of Cylindrical Shell

(*Continued from page 578*)

in which the pressure is applied over the entire lateral surface. It may be seen that the end-rings in this example have little effect if the cylinder length is more than about five times the bandwidth.

References

[1] Brush, D. O., and Field, F. A., *Buckling of a Cylindrical Shell Under a Circumferential Band Load*, Journal of the Aero/Space Sciences, Vol. 26, No. 12, pp. 825–830, December 1959.

[2] Almroth, B. O., *Buckling of a Cylindrical Shell Subjected to a Saddle-Type Load*, LMSD-288242, Lockheed Missiles and Space Division, Sunnyvale, Calif., April 1960.

[3] Timoshenko, S., *Theory of Plates and Shells*, McGraw-Hill, New York, 1940.

[4] Flügge, W., *Statik und Dynamik der Schalen*, 2nd ed., Julius Springer, Berlin, 1957.

[5] Batdorf, S. B., *A Simplified Method of Elastic-Stability Analysis for Thin Cylindrical Shells*, NACA Report No. 874, 1947.

[6] Hahne, H. V., *A Stability Problem of a Cylindrical Shell Subject to Direct and Bending Stresses*, unpublished Ph.D. Thesis, Stanford University, July 1954.

[7] Boresi, A. P., *A Refinement of the Theory of the Buckling of Rings Under Uniform Pressure*, J. Appl. Mech., Vol. 22, No. 1, pp. 95–102, March 1955.

An Authorized Binding for
Journal of the Aerospace Sciences

Arrangements have been made by the Institute of the Aerospace Sciences for members and subscribers to have their Journals bound carefully and economically. Simply write for details to:

Publishers' Authorized Bindery Service Ltd., 430 West Erie St., Chicago 10, Ill.

REQUIREMENTS *for* CONTRIBUTIONS
to the publications of the
INSTITUTE *of the* AEROSPACE SCIENCES

The Institute of the Aerospace Sciences invites both members and nonmembers from any country to submit papers for publication in the JOURNAL OF THE AEROSPACE SCIENCES and AEROSPACE ENGINEERING. The Institute, following the practice of other societies, does not pay for contributions.

The following directions for the preparation of papers, if followed by authors, will save correspondence, avoid the return of papers for changes, minimize the work of preparation for the printer, and save the expense due to the charges made for "author's corrections."

MANUSCRIPTS: The original typewritten copy of the paper is desired. **To expedite review, an additional copy of both the manuscript and figures should be submitted.** The manuscript must be double or triple spaced on one side of white paper sheets, consecutively numbered. There should be wide margins to allow for the marking of directions to the printer. Correcting, changing, or adding to papers after they are in type is costly. It is, therefore, imperative that papers submitted be in final form. Typographical errors may be corrected on proofs, but if authors wish to add material, they may do so at their own expense. In mailing, drawings may be rolled, but manuscripts should be sent flat. Send by first-class mail (register if you wish for your own protection) to the Editorial Office, Institute of the Aerospace Sciences, 2 East 64th Street, New York 21, N.Y. All manuscripts will be examined by the Editorial Committee and by the Editor. Authors will be advised as promptly as possible whether the paper is acceptable for publication.

TITLES: The title of the paper should be brief. The name and initials of the author should be written as he prefers. The use of the full name of an author is advocated because of the frequent duplication of initials and surnames which sometimes makes it difficult to establish the identity of the author. This is particularly important for large annual indexing and abstracting services. All titles and degrees or honors are omitted. The name of the organization with which the author is associated should be placed after his name on a separate line. The date on which the paper is received will be inserted by the Editor. The author's title or position should be indicated in a footnote.

SUMMARIES OR ABSTRACTS: An abstract to be printed at the beginning should accompany each article. It should be adequate as an *index* and as a *summary*. It should contain a statement of major conclusions reached, since summaries in many cases constitute the only source of information used in compiling scientific reference indexes. Abstracts printed in other journals, especially foreign, in most cases consist of summaries from printed papers. The summary should explain as adequately as possible the major conclusions to a nonspecialist in the subject and should contain from 100 to 300 words, depending on the length of the paper.

SUBHEADINGS: Subheadings should be inserted by the author at frequent intervals. The work of editorial preparation will be simplified by the author's provision of many subheadings.

MATTER USUALLY DELETED: Photographs or illustrations of little technical interest and not showing advances in general practice. Too detailed tabular matter (general results of such tables may be included in the text). Lengthy descriptions of materials or processes or of preliminary experiments or theories that preceded final results; salient features only are of interest.

REFERENCES: References should be numbered consecutively and grouped together at the end of the manuscript, with only the corresponding number being mentioned in the text. The arrangement should be as follows. For books: [1]Durand, W. F., *Aerodynamic Theory*, 1st Ed., Vol. 1, p. 23; Julius Springer, Berlin, 1934. For magazines: [1]England, C. R., Crawford, A. B., and Mumford, W. W., *Some Results of a Study of Ultra-Short-Wave Transmission Phenomenon*, Proc. IRE, Vol. 20, No. 12, pp. 481–482, March, 1933. Please give author, title, edition, volume, number, page, publisher, and place and date of publication as indicated. Omission of one required fact causes much extra editorial work and possible inaccuracies.

ILLUSTRATIONS: Illustrations should accompany manuscripts, and each should always be referred to in the text by number. Drawings or graphs should not be larger than 12 × 16 inches, and must be made with jet black India ink on white paper or tracing cloth, the latter being preferred. *Do not use typewriter for lettering.* The smallest lettering on 8 × 10 inch figures should be no less than $^1/_4$ inch high. Cross-section paper (white with black lines) may be used, but it should not have more than 4 lines per inch. If finer ruled paper is used, the major division lines should be drawn in with black ink, omitting the finer divisions. In the case of finely ruled paper, only blue-lined paper can be accepted. *Tracing paper and blueprints* are not acceptable. Lettering and all markings must be large enough to be readable after reduction to single-column width ($3^5/_{16}$ in.). Mail rolled or flat; never fold. Drawings that cannot be reproduced (including pencil drawings) will be returned to the author for redrawing, thus delaying publication of the paper. Photographs should be distinct and show clear black and white contrasts. They must be on glossy white paper. Avoid round or oval photographs.

CAPTIONS AND LEGENDS: Legends or captions must accompany each drawing or photograph submitted. If written on the drawing or photograph they should be placed below and well outside the part to be reproduced. Each table should have a caption such as Table 1, Table 2, Table 3, etc. Captions should be complete in themselves so as to make the data intelligible to the reader without reference to the text. A duplicate list of captions for figures should be included as the last page of the manuscript. Use "Fig. 1" (not Figure 1), "Figs. 3 and 4," etc., in both the text and the numbering of illustrations. In the text, "Eq. (1)" or "Eqs. (1) and (2)" is used, not "Equation (1)." In captions, legends, and in table headings, write all words in full; do not abbreviate, except for "Fig." and "Eq."

MATHEMATICAL WORK: Formulas may be typewritten or carefully written in pen and ink, the writing to be large enough so that it can be marked for the printer. Considerable space for marking should be allowed above and below all equations. All complicated equations should be repeated on separate sheets with adequate space left for marking. The solidus should be used for simple fractions appearing within the text. Make all expressions clear to the typesetter. Greek letters used in formulas should be clearly designated by name in the margin of the manuscript. The difference between capital and lower-case letters should be clearly distinguished and care taken to avoid confusion between zero (0) and the letter (o), between the numerical (one) and the letter (ell) and the prime (′), between alpha and a, kappa and k, u and mu, v and nu, n and eta. All subscripts and exponents should be clearly distinguished. Avoid complicated exponents and subscripts. Dots and bars over letters or mathematical expressions should also be avoided. When it is necessary to repeat a complicated expression, it should be represented by some convenient symbol.

SYMBOLS AND ABBREVIATIONS: The symbols recommended in the American Standard Association "Letter Symbols for Aeronautical Sciences," ASA Y10.7—1954, should be used wherever practicable. All symbols should be clearly written and carefully checked. Standard abbreviations should be used, and it should be noted that most abbreviations are lower case.

CORPORATE MEMBERS

OF THE

INSTITUTE OF THE AEROSPACE SCIENCES

AC SPARK PLUG DIVISION, GENERAL MOTORS CORPORATION

ACADEMY OF AERONAUTICS

AEROJET-GENERAL CORPORATION

AERONCA MANUFACTURING CORPORATION

AERONUTRONIC, DIVISION OF FORD MOTOR COMPANY

AEROSPACE CORPORATION

AGAWAM AIRCRAFT PRODUCTS, INC.

AIRBORNE INSTRUMENTS LABORATORY, DIVISION OF CUTLER-HAMMER, INC.

ALLIED RESEARCH ASSOCIATES, INC.

ALLISON DIVISION, GENERAL MOTORS CORPORATION

AMERICAN AIRLINES, INC.

AMERICAN BOSCH ARMA CORPORATION

AMERICAN OIL COMPANY

AMOCO CHEMICALS CORPORATION

ARDE ASSOCIATES

ARO, INC.

ASTRO-ELECTRONIC PRODUCTS DIVISION, RADIO CORPORATION OF AMERICA

AVCO-EVERETT RESEARCH LABORATORY

AVCO CORPORATION, RESEARCH AND ADVANCED DEVELOPMENT DIVISION

AVIEN, INC.

BEECH AIRCRAFT CORPORATION

BELL AEROSPACE CORPORATION

THE BENDIX CORPORATION

THE BOEING COMPANY

BOOZ, ALLEN APPLIED RESEARCH, INC.

BULOVA RESEARCH & DEVELOPMENT LABORATORIES, DIVISION OF BULOVA WATCH COMPANY, INC.

CANADAIR, LTD.

CHANCE VOUGHT CORPORATION

THE CHASE MANHATTAN BANK

CHICAGO AERIAL INDUSTRIES, INC.

CONTINENTAL MOTORS CORPORATION

CORNELL AERONAUTICAL LABORATORY, INC.

COX & COMPANY, INC.

CURTISS-WRIGHT CORPORATION

DANIEL, MANN, JOHNSON, & MENDENHALL

THE DECKER CORPORATION

DEFENSE ELECTRONIC PRODUCTS DIVISION, RADIO CORPORATION OF AMERICA

DEFENSE SYSTEMS DIVISION, GENERAL MOTORS CORPORATION

DEL MAR ENGINEERING LABORATORIES

DELCO-RADIO DIVISION, GENERAL MOTORS CORPORATION

DELCO-REMY DIVISION, GENERAL MOTORS CORPORATION

DOAK AIRCRAFT COMPANY, INC.

DOUGLAS AIRCRAFT COMPANY, INC.

DZUS FASTENER COMPANY, INC.

EASTERN AIR LINES, INC.

EATON MANUFACTURING COMPANY

EDO CORPORATION

ELASTIC STOP NUT CORPORATION OF AMERICA

ENGINEERING SUPERVISION COMPANY

FAIRCHILD CAMERA AND INSTRUMENT CORPORATION

FAIRCHILD ENGINE AND AIRPLANE CORPORATION

THE GARRETT CORPORATION

GENERAL APPLIED SCIENCE LABORATORIES, INC.

GENERAL DYNAMICS CORPORATION

GENERAL ELECTRIC COMPANY

GENERAL PRECISION, INC.

THE B. F. GOODRICH COMPANY

GOODYEAR AIRCRAFT CORPORATION

GRUMMAN AIRCRAFT ENGINEERING CORPORATION

HOFFMANN AIRCRAFT COMPANY

HUGHES AIRCRAFT COMPANY

INSURANCE COMPANY OF NORTH AMERICA COMPANIES

INTERNATIONAL BUSINESS MACHINES CORPORATION FEDERAL SYSTEMS DIVISION

THE INTERNATIONAL NICKEL COMPANY, INC.

ITT FEDERAL LABORATORIES, A DIVISION OF INTERNATIONAL TELEPHONE AND TELEGRAPH CORPORATION

ANITROL AIRCRAFT DIVISION, MIDLAND-ROSS CORPORATION

JOHNS-MANVILLE SALES CORPORATION

KOLLSMAN INSTRUMENT CORPORATION

LAVELLE AIRCRAFT CORPORATION

LEAR, INCORPORATED

C. W. LEMMERMAN, INC.

THE LIQUIDOMETER CORPORATION

ARTHUR D. LITTLE, INC.

LOCKHEED AIRCRAFT CORPORATION

THE MARQUARDT CORPORATION

THE MARTIN COMPANY

McDONNELL AIRCRAFT CORPORATION

MELETRON CORPORATION

MINNEAPOLIS-HONEYWELL REGULATOR COMPANY

MOBIL OIL COMPANY

NATIONAL CREDIT OFFICE, INC.

NORTH AMERICAN AVIATION, INC.

NORTHROP CORPORATION

PAN AMERICAN WORLD AIRWAYS, INC.

THE RALPH M. PARSONS COMPANY

PIASECKI AIRCRAFT CORPORATION

POLY INDUSTRIES, INC.

REPUBLIC AVIATION CORPORATION

ROHR AIRCRAFT CORPORATION

RYAN AERONAUTICAL COMPANY

SHELL OIL COMPANY

SIMMONDS PRECISION PRODUCTS, INC.

SOLAR AIRCRAFT COMPANY

SOUTHWEST PRODUCTS COMPANY

SPACE TECHNOLOGY LABORATORIES, INC.

R. DIXON SPEAS ASSOCIATES

SPERRY GYROSCOPE COMPANY, DIVISION OF SPERRY RAND CORPORATION

STANDARD-THOMSON CORPORATION

STANLEY AVIATION CORPORATION

THERM, INCORPORATED

THIOKOL CHEMICAL CORPORATION

THOMPSON RAMO WOOLDRIDGE INC.

TRANS WORLD AIRLINES, INC.

UNION CARBIDE METALS COMPANY, DIVISION OF UNION CARBIDE CORPORATION

UNITED AIR LINES, INC.

UNITED AIRCRAFT CORPORATION

UNITED STATES AVIATION UNDERWRITERS, INC.

VEHICLE RESEARCH CORPORATION

WESTERN GEAR CORPORATION

WESTINGHOUSE ELECTRIC CORPORATION